Universiteit
Leiden
The Netherlands

The colours of the extreme universe

Calistro Rivera, G.

Citation
Calistro Rivera, G. (2019, January 10). *The colours of the extreme universe*. Retrieved from https://hdl.handle.net/1887/68466

Version:	Not Applicable (or Unknown)
License:	Licence agreement concerning inclusion of doctoral thesis in the Institutional Repository of the University of Leiden
Downloaded from:	https://hdl.handle.net/1887/68466

Note: To cite this publication please use the final published version (if applicable).

Cover Page

Universiteit Leiden

The handle http://hdl.handle.net/1887/68466 holds various files of this Leiden University dissertation.

Author: Calistro, Rivera G.
Title: The colours of the extreme universe
Issue Date: 2019-01-10

THE COLOURS OF THE EXTREME UNIVERSE

The Colours of the Extreme Universe

Panchromatic studies of star forming galaxies
and accreting black holes

Proefschrift

ter verkrijging van
de graad van Doctor aan de Universiteit Leiden,
op gezag van Rector Magnificus prof.mr. C. J. J. M. Stolker,
volgens besluit van het College voor Promoties
te verdedigen op donderdag 10 January 2019
klokke 11.15 uur

door

Gabriela Calistro Rivera

geboren te Lima, Perú
in 1990

Promotiecommissie

Promotor:	Prof. dr. Huub Röttgering	
Co-promotor:	Dr. Jacqueline Hodge	
Overige leden:	Prof. dr. Paul van der Werf	
	Prof. dr. David Alexander	(Durham University)
	Prof. dr. Marijn Franx	
	Dr. Vernessa Smolčić	(University of Zagreb)
	Dr. Rychard Bouwens	

ISBN 978-94-028-1344-9

Cover: drawing by Gabriela Calistro Rivera. Two artistic perspectives of a female dancer doing a pirouette. In the front cover the dancer is viewed from above, where the colourful dress and hair movement evokes the main topics of the thesis, colours and galaxies. In the back cover, the dancer is viewed from a perspective at eye-level, where the side view of the dress reveals a galaxy's spectral energy distribution.

A mi papá,
por su entusiasmo contagioso
por la física y el Universo

Contents

1

Introduction

1.1 The Building Blocks of the Observable Universe

You are reading these lines on some spot on Earth, one of the eight planets that orbit our closest star, the Sun. The Sun is in turn one element in a structure of a few hundreds of billions of stars[1] bound by gravity and defined as a galaxy, our galaxy, the Milky Way. Such as the Milky Way, trillions of galaxies[2] of a large diversity of sizes, shapes and masses are the building blocks of our vast observable Universe. The exploration of the observable Universe is an endeavour inherent to the human nature and thus from ancient times human civilizations have targeted their skills and imagination to observe and map the skies. However, the scientific study of the observable Universe has seen an unprecedented development only recently, after the telescope constructed by Galileo Galilei evolved, hand in hand with technology, into magnificent machines of exploration. These machines do not only deepen our view to look into inconceivable distances, but also broaden the spectrum allowing us to see and understand the Universe through colours not even humanly perceivable. In this thesis we will make parallel use of most kinds of these machines and portray the early Universe at different colours. We will show how the study of the panchromatic emission of galaxies will provide us with a more complete physical understanding of the extreme and distant Universe.

Galaxies beyond our own and their central black-holes

The existence of other galaxies beyond our own, and extragalactic astronomy as such, is a concept that first came into inception no more than hundred years ago. In the 1920s, using the new 100 inch Mt. Wilson optical telescope, Edwin Hubble confirmed that many of the nebulae or clouds reported by previous observations were too distant to belong to our own galaxy. This was the final remark in a long and complex path of this discovery of a extragalactic Universe. As most breakthroughs in astronomy, this discovery was a long process, involving a large number of observations (such as the 'nebulae' catalogs of Charles Messier and William Herschel) and centuries of debate, to finally confirm the nature of these nebulae as extragalactic objects.

E. Hubble himself would then portray the morphological diversity of galaxies through a classification scheme used till today, which divides galaxies into spirals, ellipticals and irregulars. Soon after, it would be discovered that observing galaxies with two or more colour filters, and comparing the different measurements in a magnitude-colour diagram, could separate them principally into blue and red galaxies. Blue galaxies being galaxies actively growing through the formation of stars, and red galaxies having primordially old stellar populations, undergoing a quiescent state with no significant star formation. Later on, observing the skies with telescopes that probe different parts of the electromagnetic spectrum of light, new galaxy

[1] GAIA DR2 (Gaia Collaboration et al. 2018)
[2] Conselice et al. (2016)

populations would be discovered, entirely invisible or barely detectable at optical wavelengths, revealing the complexity and panchromatic nature of galaxies.

The first evidence that some galaxies were hosting highly-luminous nuclei in their centers was found in the 1940s by Carl Seyfert, when he detected unexpectedly bright and broad emission lines in the central regions of nearby galaxies (Seyfert 1943). Around 20 years later, the discovery of enigmatic quasi-stellar radio sources (quasars) using optical spectra and radio continuum observations (e.g., Schmidt 1963), would then revolutionize our notion of galaxies. These observations put forward the concept that the large nuclear luminosities observed in these galaxies were produced by massive nuclear black-holes feeding matter and growing through a luminous accretion process. Later observations would then show that most galaxies, if not all, host massive black holes in their centres (Lynden-Bell 1969), a concept that represents now one of the pillars of extragalactic astronomy. Indeed, a strangely immobile radio source, of a luminosity similar to our own Sun, would be discovered some years later in the center of our own galaxy revealing that even our own Milky Way hosted a massive black hole in its centre, which was called Sagittarius A* (Lynden-Bell & Rees 1971). The fact that the Sagittarius A* galactic nucleus is a weaker radio/ X-ray source by 5–10 orders of magnitude[3] than the earlier discovered quasars would also demonstrate the existence of a large variety of galactic nuclei. Indeed, while most galaxies host massive and super-massive black holes in their centers, these are experiencing different activity levels.

This thesis focuses on characterizing the most extreme epoch of cosmic history, where most of galaxy growth took place. As will be discussed in detail in Section 1.3, growing BHs are ubiquitous in the centers of galaxies populating this period. Indeed, one of the most important discoveries around galaxies and their active galactic nuclei is the finding of a tight correlation between the masses of the galaxy spheroids and those of the central black holes in the local Universe (e.g., Kormendy & Richstone 1995; Magorrian et al. 1998; Marconi & Hunt 2003; Gültekin et al. 2009). While this finding suggests a symbiotic relation between the host galaxy and its central nucleus, this is a surprising observation due to the extremely different scales inhabited by host galaxies and black holes: the stellar and gas content in a galaxy is distributed on scales of $1-100$ kpc, while the black-hole accretion occurs only on scales of < 1 pc. These observations suggest that physical mechanisms should be in place which transport gas onto those small scales. However, these mechanisms are still not understood and the galaxy-black hole co-evolution remain an intriguing question that sparkles lively discussions in the astronomical community.

The formation of stars in the Universe appears to be very inefficient if we notice that the fraction of baryons which make up stars and stellar remnants in the present day Universe has been observed to be $< 6\%$ of the total baryon content of the Universe (e.g., Fukugita & Peebles 2004). The large radiative energies emitted in the process of black hole accretion place quasars and other active galactic nuclei as the most probable candidates to be the regulators of galaxy growth. This occurs through feedback processes that heat or expel the gas from the interstellar medium of galaxies, preventing the formation of stars. Cosmological simulations (e.g., EAGLE, IllustrisTNG), which use numerical recipes to mimic galaxy formation and evolution from the Big Bang till the present day, use this 'AGN feedback' in order to calibrate the cosmic star formation history of the Universe, so that it matches the observed present-day stellar content. Understanding the co-evolution of galaxies and AGN is thus a crucial element to characterize the build-up of matter in the Universe.

[3] Sgr A* has a bolometric luminosity of less than $L_{bol} = 10^{37}$ erg s^{-1}

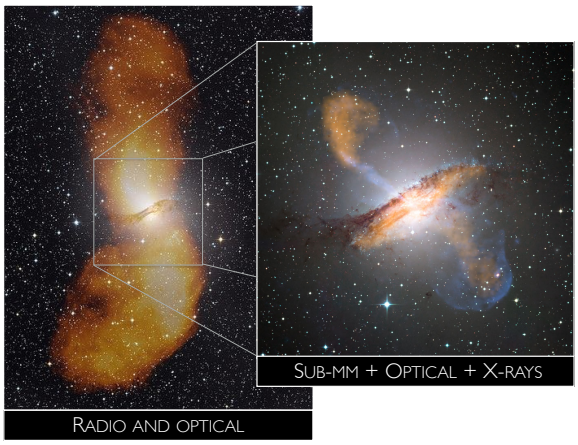

Figure 1.1: Multiwavelength emission of the galaxy NGC 5128, known as Centaurus A. The *left panel* shows a composition of the radio emission of the outer-lobes extending ∼a million light-years from the galaxy and the optical galaxy emission. (Credit: Capella Observatory (optical), CSIRO/ATNF, ASTRON, MPIfR (radio)). The *right panel* shows a zoom-in view on the inner-lobes and the central galaxy, as a composition . of sub-mm, X-ray and optical emission (Credit: ESO/A. Weiss et al.; NASA/CfA/R.Kraft)

Observing galaxies and black-holes across cosmic time

Light is the main source of information when observing galaxies in the Universe. Any description that involves distances travelled by light and time scales over a significant fraction of cosmic time, including the age of the Universe, are highly dependent on the cosmological framework chosen. The current standard model of Big Bang cosmology is the Λ-cold dark matter model (ΛCDM). ΛCDM prescribes the formation of structure in the Universe based on the equations of general relativity (Einstein 1916), while being able to explain the observed early structure formation imprinted on the cosmic microwave background (Planck Collaboration et al. 2014). Based on ΛCDM, the energy content in the Universe is dominated by dark energy (69.2%, parametrized by Λ) and cold dark matter (26.8%), while baryons represent only 4%, from which only 6% are visible. While dark matter is a form of matter that interacts with baryonic matter only through gravity, dark energy is the cosmological constant that determines that the Universe is expanding in an accelerated manner, as confirmed by observations (Riess et al. 1998; Perlmutter et al. 1999),

The constant speed of light at $c = 3 \times 10^8$ m s^{-1} is of great value to galaxy evolution studies since it allows us to look back in time. Due to its constant velocity, light produced at early times of cosmic history would reach us only now, allowing us to witness these early events. Additionally, light travelling towards us is 'stretched' to longer wavelengths by the expansion of the Universe, in a phenomenon call redshift. The accelerated expansion of the Universe produces a redshift that is higher at earlier epochs, serving as a tag for the time when an event has occurred. For instance, the galaxy NGC 5128 shown in Figure 1.1, better known as Centaurus A, is one of the closest radio AGN to us and is located at a distance 3.8 ± 0.1 Mpc (Harris et al. 2010).To arrive to us from that distance, light has travelled ∼ 10 million years (10 Myr). Since this is a negligible amount of time, compared to the age of the Universe (13.8 Gyr from the Big Bang), Centaurus A is at redshift $z \sim 0.0006$. The light of a galaxy observed at redshift $z = 2$ – the median redshift of the galaxies studied in this thesis – would have travelled towards us for 10.5 Gyrs; and at redshift $z = 4$, only 1.5 Gyrs had passed since the Big Bang.

Albeit the emission we can observe from Centaurus A has originated fairly 'recent', the formation and evolution of that galaxy is expected to have started > 10 Gyr ago, based on

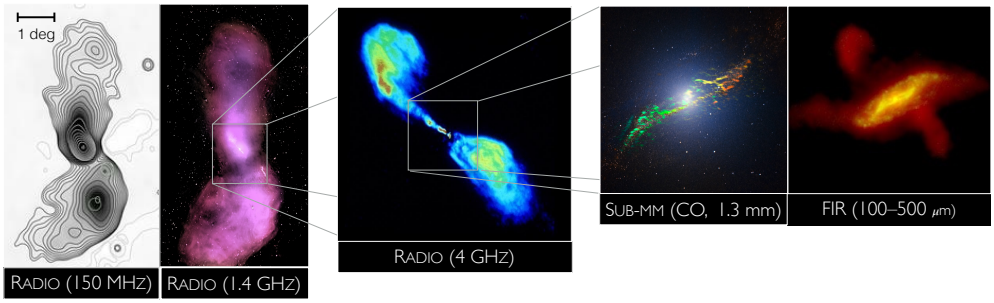

Figure 1.2: Multiwavelength radio–infrared emission of Centaurus A. Credit: PAPER array, Stefan et al. 2013(150 MHz), Morganti et al. 1999, Feain et al. 2011 (1.4 GHz), VLA Burns & Price, 1983 (4 GHz), ALMA/ESO (sub-mm), ESA/Herschel/PACS/SPIRE/C.D Wilson (FIR)

theoretical modelling of the stellar populations in its halo (Rejkuba, M. et al. 2011). Indeed, due to the cosmological time scales implied in the formation and life-time of a galaxy, it is impossible for humans to directly follow galaxy evolution. To characterize galaxy evolution through observations, astronomers thus require large unbiased samples of galaxies populating different epochs across cosmic time. Observing galaxies at different redshifts would then allow us to connect galaxy populations (of similar fundamental properties) across a single evolutionary path in order to test theoretical evolutionary models. However, most methods used to study galaxy evolution are limited by properties of light that need to be taken into account. The intensity of light decreases as a function of the inverse square of the luminosity distance it has travelled towards the observer, where the luminosity distance is a function of $\propto (1+z)^{-2}$. This implies a decrease of the flux density as measured by instruments of $\propto (1+z)^{-4}$. It is thus challenging to detect the most distant galaxies at earlier epochs, largely biasing galaxy samples to contain only the most luminous galaxies. Since most observational campaigns can sample only the most luminous and thus massive galaxies across all redshifts, *the most extreme sources are an ideal laboratory to trace galaxy evolution.*

Similarly, the observed angular sizes of galaxies decreases as a function of the inverse square of the distance, preventing the angular resolution of current instruments from resolving the detailed morphology of the sources. Additionally, high-resolution observations need to detect low-surface brightness emission and thus require larger exposure times and become highly expensive. The advent of recent and future high-resolution and sensitivity telescopes, such as the Hubble Space telescope (*HST*), the Atacama Large Millimeter Array (*ALMA*) and the mid-infrared James Webb Telescope (*JWST*), will make it possible to study galaxy evolution from a resolved perspective. In this thesis we will present some exceptional examples of high-resolution multiwavelength studies using these new-generation instruments.

The emission of a galaxy across the electromagnetic spectrum is very complex since a large variety of physical processes, probing different spatial scales, contribute simultaneously to the emission. Observations from single telescopes at given wavelengths are thus always biased for or against certain properties or structured within galaxies, as can be seen in different views of Centaurus A achieved across the electromagnetic spectrum in Figures 1.2 and 1.3. Moreover, the emission of some galaxy populations at given redshifts might be so weak at certain wavelengths that they would remain entirely undetected in these observations. Observing galaxies at single wavelengths, even when these are detectable, is thus commonly not enough to understand the physics or the initial conditions producing the emission. *Multiwavelength approaches are thus essential to have a full description of galaxy physics.*

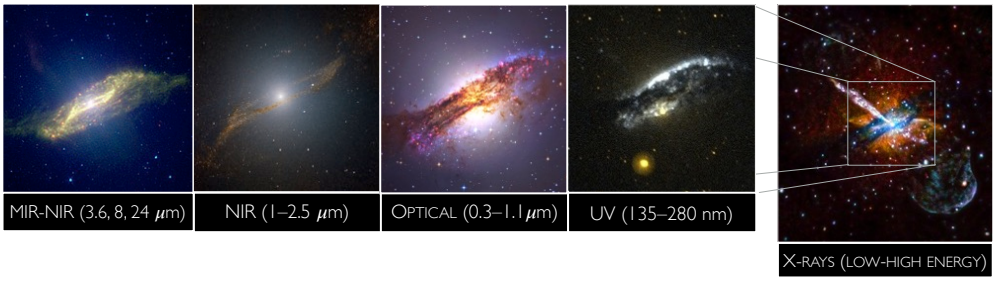

Figure 1.3: Multiwavelength infrared–X-rays emission of Centaurus A. Credit: IRAC(at 3.6 and 8 μm) and MIPS (24 μm)/Spitzer/NASA-JPL (mid-infrared); J, H and K bands, SOFI at NTT/ESO (near-infrared); NASA/ESA/STScI/ESO/Robert Gendler/Roberto Colombari (optical); NASA/Chandra X-ray Observatory (X-rays).

1.2 The Panchromatic Nature of Galaxies and AGN

Figures 1.2 and 1.3 illustrate the different views of the radio galaxy Centaurus A (star forming and AGN), achieved observing at some of the parts of the electromagnetic spectrum covered by this thesis. In Centaurus A, structures probed at different wavelengths can be characterized in detail, since this source is one of the closest and brightest galaxies in the Universe. For galaxies at redshifts $z \sim 2$, however, resolving any galaxy structure becomes almost impossible at these wavelengths using current instruments (see exceptional cases in Chapter 4 and 5 of this thesis). Fortunately, integrated emission averaged across the entire galaxy can provide valuable insight on the properties of sources in the early Universe when combined with theoretical models.

A representation of the complexity of the electromagnetic spectrum emitted by galaxies can be achieved through the sampling of the galaxy's spectral energy distribution (SED). The SED is the distribution of energy over frequency or wavelength and is usually constructed using broadband photometric observations of a galaxy across the spectrum. All physical processes responsible for the radiative emission of galaxies, including those from the galactic nuclei, are imprinted in the shape of the SED. Historically, early versions of SED models were mostly limited to fitting stellar emission in the UV-NIR regime (e.g, Bolzonella et al. 2000; Brinchmann & Ellis 2000). The last decade has seen significant development in the modelling of other parts of the spectrum providing SED-fitting approaches that model the infrared and radio regimes as well (e.g., Burgarella et al. 2005; da Cunha et al. 2008). In Figure 3.4 we summarize the panchromatic emission of galaxies that has been studied in this thesis. Below, we describe the physics behind the integrated panchromatic emission of galaxies, starting from the high-energy regime (X-rays) to the low-energy end (radio) of the spectrum covered by this thesis.

High energy black-hole physics: optical, UV and X-rays

The **optical/UV** regime of the integrated SED of a galaxy hosting an AGN is typically dominated by the nuclear emission. This is a product of the *accretion of gas* onto the gravitational potential of its central massive black hole. An optically thick accretion disk of material (Shakura & Sunyaev 1973) is formed as the black hole grows, producing a luminous and broad thermal continuum emission at temperatures around 105 K, commonly known as the "big blue bump". The observed shape of the accretion disk SED is further altered by dust attenuation at

nuclear or galactic scales. While its integrated emission is prominent, the accretion disk is too small to be spatially resolved even in local galaxies since it is expected to surround the black-hole at scales of around few light-days for local Seyfert and less than a few light-years for quasars. Apart from the continuum, the nuclear optical-UV emission is also characterized by the presence of broad (∼1000 km/s) and narrow (300–1000 km/s) emission lines, originated from gas clouds distributed at scales of less than 1 and a few hundred pc around the accretion disk, respectively. In bright star-forming galaxies, with weak or highly obscured AGN, the optical-UV part of the SED can be dominated by the emission of stellar populations as will be discussed below. Surrounding the accretion disk, a corona of hot electrons is responsible for the intrinsic **X-ray emission** through *inverse Compton scattering of the accretion disk UV-photons*, producing a power-law shaped X-ray continuum. This intrinsic emission is then altered by the interaction with other nuclear components, such as photo-electric absorption, reflection and scattering. The X-ray emission in most galaxies is dominantly originated in the AGN and is thus often used as one of the most reliable AGN tracers and the largest and arguably less-biased AGN surveys have been selected based on detections in X-ray surveys (see Brandt & Alexander 2015, for a review). However, as X-ray surveys go deeper, the weak X-ray emission detected starts tracing the weak emission of stellar X-ray binaries that are X-rays luminous, contrary to the majority of stellar populations.

The stellar emission: NIR, optical and UV

Historically, the most studied part of the galaxy SED is the **near-infrared, optical and UV** emission emitted by the *stellar populations* that compose the galaxy. The stellar SED is shaped by the physical properties of the stellar populations composing the galaxy, including the star formation history, the metal content in stars, the dust distributions and the interstellar radiation. The galaxy SEDs are commonly studied using stellar population synthesis modelling, which rely on stellar evolution theory to determine the ensemble of possible stellar types at a given age and metallicity that is needed to explain the shape of the SED (see Conroy 2013, for a review.). The building blocks of such a model are Simple Stellar Populations (SSP), which are single populations of stars of equal metallicity and undergoing equal stellar evolution. The 'mock' galaxy emission from a SSP is produced as a superposition of empirical and theoretical stellar spectral libraries following the distribution dictated by an assumed initial mass function (IMF). The total galaxy stellar SED is then constructed as the composite of different SSPs, of different ages and metallicities, as determined by the SFH and the metallicity evolution of the galaxy, respectively. Generally speaking, the blue end of the optical-UV emission of the stellar SED is then dominated by the emission of young stellar populations of recent star formation. The intensity of the blue end is thus largely determined by the star-formation history of the galaxy and is essential to *determine the star formation rate* of the galaxy in the optical/UV regime. The near-infrared end of the stellar SED, on the other side, is dominated by the reddest, more massive and oldest stars, being thus crucial for the *estimation of stellar mass* of the galaxy.

The intrinsic emission from the different stellar populations and the shape of the optical/UV SED can be largely attenuated and absorbed by dust distributions typical of star forming regions. This emission is reprocessed and re-emitted by the dust at infra-red wavelengths, as will be explained below. Dust attenuation is a determining factor for the capability of the optical/UV SED as a tracer of star formation, since corrections for dust attenuation can be uncertain, preventing robust measurement of the intrinsic young stellar emission. In contrast, the NIR part is less affected by obscuration and thus stellar masses are usually a fairly well-constrained quantity in SED-fitting (within a relative error of 0.1-0.2 dex, Muzzin et al. (2009)). However, although less discussed in the literature, the NIR emission of the stellar

population can be contaminated by the emission of nuclear host dust, when the galaxy host AGN. This emission can produce overestimated stellar masses when is not taken into account. This thesis will explore the effect of including AGN in the panchromatic modelling.

The hot nuclear dust and molecules at galactic scales: MIR

AGN can emit considerable fractions of their total energy output in **mid-infrared and near-infrared** wavelengths. This component originates in the nuclear obscuring material, composed of *hot gas and dust* at scales of few parsecs (e.g., Alonso-Herrero et al. 2011; Ichikawa et al. 2015), which is heated by the high-energy accretion disk emission. The obscuring material has been historically believed to be shaped in the form of a torus. Recent results suggest that a clumpy toroidal structure is a more accurate description (Nenkova et al. 2002), albeit the distribution is not well constraint due to the lack of observational evidence. The gas is the principal obscuring material of the X-ray part of the nuclear emission, and the dust attenuates mainly the optical-UV emission. This material is distributed closely around the accretion disk, at a distance defined by the sublimation temperature of dust, where dust grains and gas molecules can be formed. The morphology and orientation of this obscuring torus play an important role for the diversity of AGN. The presence or absence of broad-lines in the optical spectra of AGN, which classified them into type 1 and 2, respectively, is considered to be closely related to the viewing angle of the observer to the torus, whether it was face-on or edge-on, respectively. We will discuss AGN obscuration in detail in Chapter 2 of this thesis.

The MIR part of the SED of star forming galaxies and AGN is also characterized by hosting **poly-cyclic aromatic hydrocarbons (PAHs)** (e.g., Tielens 2008), which are large molecules emitting the brightest emission lines across the spectrum and are thus a prominent component of the MIR emission of galaxies. PAHs are abundant in galaxies with metallicities close to solar and since they typically populate star-forming regions in galaxies, they are usually used as tracers of star formation. Strong peaks that compose the feature complexes of PAHs can usually fall around $6-8\,\mu$m and $11.2-12.7\,\mu$m. Due to their large luminosities and widths, the PAH contribution and the strength of the hot dust continuum are parameters that are often degenerate, in particular when only broadband photometry is available. Degeneracies, correlations and other statistical challenges in the modelling of the multiwavelength SEDs will be investigated in Chapter 2 of this thesis.

The interstellar medium: FIR and sub-mm

The far-infrared and sub-millimeter regime in a galaxy's SED is dominated by the **continuum emission of cold dust** distributed in the interstellar medium of star forming regions. The emission originates in dust that is heated by the UV and optical stellar emission, in particular by the young and short lived stellar population of red giant stars. The FIR emission is thus an indirect indicator of the recent star formation and is used as a *reliable star formation rate tracer*. The FIR SED is a thermal emission, composed as a superposition of black-bodies at different temperatures whose shape is described by Planck's law. The temperatures of each black-body is determined by parameters such as the dust distributions around the heating source, and the size of the dust grains, where small grains are usually heated faster and produce higher-energy thermal emission than large grains. The total SED has then a characteristic peak that gives the mean temperature of the dust in the system, usually around 30-40 K (e.g., Casey et al. 2014), which is a characteristic temperature for the heating of molecular clouds by star formation activity. The low-energy, submillimeter end of the SED is consistent with the Rayleigh Jeans (RJ) tail, which provides the FIR SED with a remarkable property, the negative K-correction. A K-correction describes the change of the intensity at a given wavelength as

a product of redshift, since the SED shifts towards lower energies as the redshift increases. Since the shape of the RJ tail (positive slope) counteracts the flux density dimming by the increased distance to the observer (negative slope), the observed sub-millimeter flux density remains almost constant for galaxies at redshifts $1 - 8$ (Casey et al. 2014). This thesis benefits from this negative K-correction and studies the high-redshift Universe targeting sub-mmm-selected galaxies in Chapters 4 and 5.

The sub-millimetre regime of a galaxy's emission is also characterized by tracing the emission of **molecular and atomic gas** in the interstellar medium (ISM). Molecular gas is predominantly distributed in the ISM within molecular clouds of sizes up to 50 pc, as has been observed in the Milky way and nearby galaxies (e.g., Carilli & Walter 2013) The most abundant molecule in the ISM is molecular hydrogen (H_2), but is undetectable due to its lack of rotation-vibrational transitions. Carbon, on the other hand, does not only play an important role in the ISM as the main provider of free electrons, but provides some of the brightest emission lines in the sub-mm regime. The carbon monoxide molecule (CO) ($\sim 10^{-4}$ as abundant as H_2) and the fine-structure line of the carbon ion [C II] are among the main tracers of the molecular gas and the most luminous emission lines in the sub-mm, being able to contribute up to $20 - 40\%$ of the total sub-mm flux (Smail et al. 2011). Chapters 4 and 5 of this thesis studies the emission of these two lines at high-resolution in order to characterize the ISM in detail.

Interacting plasma: radio

The emission at intermediate and low radio frequencies (<10 GHz) is dominated by synchrotron emission. Synchroton emission is generally produced by the interaction of ultra-relativistic ($E \ll m_e\ c^2$) electrons with a magnetic field, in this case the magnetic field of the galaxy. The sources of accelerated electrons, or plasma, in galaxies are related to both AGN and star-formation processes.

In AGN, and specifically radio galaxies and radio quasars, immense relativistic collimated streams of plasma, called radio jets, are emitted from the accretion process of the black hole. These radio jets can extend to scales even larger than the host galaxy and the details around the origin and conditions in which these form are still open questions in astronomy. Historically, the low sensitivity of radio telescopes assured that these radio AGN with luminosities that can reach $P_{1.4\ \mathrm{GHz}} \sim 10^{27}$ were the only sources detectable at radio frequencies (thus the general nomenclature of 'radio galaxy'). The radio was thus used as a tracer of black hole activity.

However, the interstellar medium of galaxies is also pervaded of interstellar plasma, produces by the acceleration of electrons in supernova remnants. Since supernova remnants are direct products of the short-lived massive stars (with stellar masses of $M \leq 8\ M_\odot$), the interstellar synchroton emission is used as a tracer of recent massive star formation in galaxies. The interstellar synchroton emission, however, produces usually luminosities below $P_{1.4\ \mathrm{GHz}} \sim 10^{24}$, populating the low end of the radio luminosity function (Condon 1992; Padovani 2016). These luminosities have become detectable only recently, with the advent of radio interferometer such as the low frequency array (LOFAR), and star forming galaxies have been included in radio-selected galaxy samples only recently. A key property of radio emission from star-forming galaxies is that it presents a tight correlation with the far-infrared emission, also a tracer of star formation. This correlation is a fundamental instrument to disentangle the radio emission arising from the AGN to that from the galaxy, which are otherwise indistinguishable, since both have been observed to present a fairly similar SED simplied as a steep negative power-law with a spectral index of $\alpha \sim -0.7$. In this thesis we will explore in detail both the far-infrared radio correlation and the radio SED at low-frequencies (150 MHz) for the first time (Chapter 3). At high frequencies ($\nu > 30$ GHz) the radio emission in

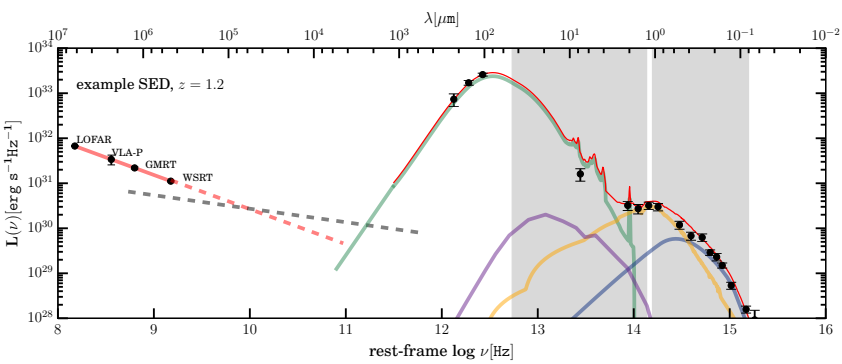

Figure 1.4: Example SED of dusty star forming galaxy at $z = 1.2$. The data points are representative of the photometric data covered in this thesis. The photometry is modelled and decomposed into physical components of the host galaxy and the AGN. The dashed red and grey lines correspond to the synchroton and thermal contributions to the radio emission, respectively. The green line corresponds to the FIR and sub-mm dust continuum emission from star forming regions, while the yellow line represents the NIR/optical emission from stellar populations. The purple line represent the hot dust emission from the nuclear obscuring medium or 'torus'. Finally the blue line represents the accretion disk emission of the AGN, attenuated by obscuration. The thin red line represents the total fitted SED.

star forming galaxies starts to be dominated by a thermal flat free-free component, which isc directly related to the rate of ionizing photons arising from newly formed massive stars. This part of the spectrum, however, is outside the scope of this thesis.

1.3 The Epoch of Extreme Galaxy and Black-hole Growth

Based on observations across the electromagnetic spectrum of light, fundamental properties have been learned and new questions have been posed about the nature of galaxies and black holes. Galaxies grow through the transformation of gas (mostly molecular) into stars, and indeed, the star formation rate (SFR) and the stellar mass are the main integrated properties that describe the evolutionary state of a galaxy. Efforts to characterize galaxy evolution have demonstrated that the position of a galaxy on this sequence, or the specific star formation rate (sSFR), is a fundamental property and decisive for the galaxy's fate. Based on these properties, studies have found that most of star-forming galaxies at a given redshift follow a '**main sequence**' (Brinchmann et al. 2004; Whitaker et al. 2012), which is defined as a relatively tight distribution (<0.3 dex) in star formation rate versus stellar mass. Although this relation evolves as a function of redshift, where main sequence galaxies at a fixed mass present higher SFR at higher redshifts, a main sequence is found to exist at both low and high redshifts. Indeed, the star formation rates of some of the most massive main sequence galaxies in the early Universe can reach values up to a few 100 $M_{\odot}yr^{-1}$.

The total **cosmic star formation history of the Universe** can be characterized based on the integrated properties measured for large samples of galaxies selected across the spectrum, and on unresolved measurements of the cosmic background at different wavelengths. A key finding was that both, the cosmic star formation history and BH evolution evolves as a function of redshift, increasing from the local Universe towards the past, peaking at redshifts $z \sim 2$, when the Universe was 3 Gyrs old, declining again at earlier epochs (See Figure 1.5). This

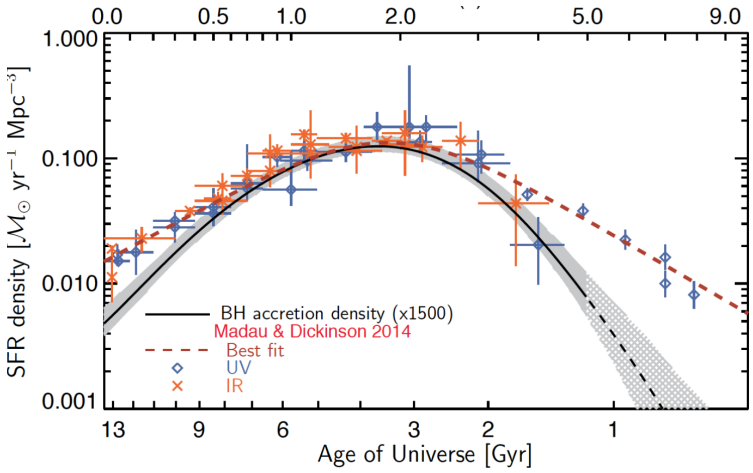

Figure 1.5: Co-evolution of galaxies and black holes. Adapted from Aird et al. (2015). The dots represent the observed SFR density per unit volume versus cosmic time using the tracers indicated in the legend. The dashes line indicates the best fitting relation to these observations (Madau & Dickinson 2014). The solid line shows the accretion rate density from observations of X-ray selected AGNs (Aird et al. 2015), re-normalized by a factor of 1500. The peak and shape of the distribution of both the SFR and accretion rate densities across cosmic time show a remarkable similarity.

epoch of galaxy assembly – which is the focus of this thesis – represents a key phase of galaxy evolution, since most of the stars in the present day Universe are believe to be formed in this phase. Furthermore, the observation that the peaks of both processes are coincidental is a strong support for the tight galaxy-BH co-evolution scenario, and suggest that this epoch is a good laboratory for the study of the apparent symbiotic and enigmatic relation between the galaxies and their nuclei.

Based on observations of galaxies and AGN at this epoch, the **probability of finding AGN in the centers of star forming galaxies** has been studied extensively (Kirkpatrick et al. 2012; Rosario et al. 2013, 2015; Aird et al. 2018). Clearly, the AGN fraction within a galaxy population depends strongly on the wavelength of selection and flux limits probed. Selections at wavelengths where the AGN features in the SED are more prominent, such as the MIR, UV and X-rays (Figure 3.4), would deliver larger AGN fractions than other regimes, where galaxy emission dominates. Another important factor that affect the probability of finding a luminous AGN hosted by a galaxy is the different time-scales probed by star formation and BH accretion, since AGN activity can vary by a factors of $\sim 0.1 - 1$ Myr timescales (Volonteri et al. 2015), whereas star formation time scales can achieve time scales of a few Gyr. Remarkably, recent unbiased studies of mass-selected samples of galaxies have shown that the probability of finding significant emission originated in AGN accretion increases as a function of stellar mass, star formation rate and redshift (Fig. 1.6, e.g. Aird et al. (2018)). In particular, at $z \sim 2 - 3$ – on which this thesis is focused – the probability of black hole growth within galaxies at all masses and star formation rates achieves its peak. The ubiquity of accreting black holes in highly star forming galaxies is thus an important factor to take into account, even for galaxy populations with emission dominated by star formation.

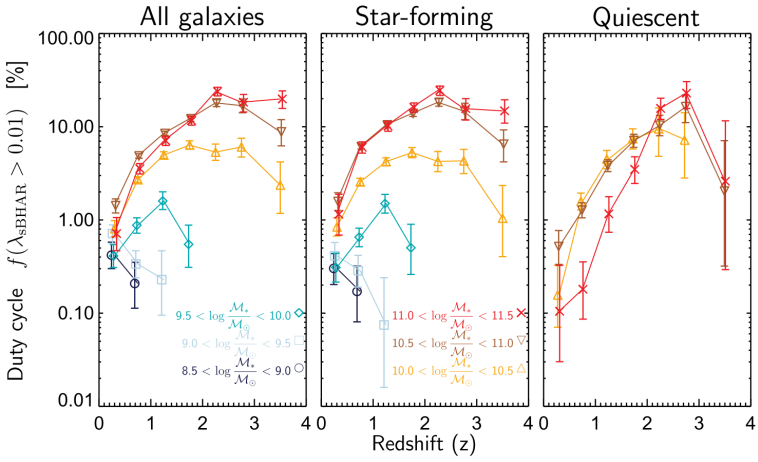

Figure 1.6: The evolution of the fraction of galaxies hosting AGN (duty cycle) as a function of redshift, stellar mass, and SFR. From Aird et al. (2018).

An extreme and obscured epoch

A key finding that revolutionized our understanding of galaxy evolution was that an important fraction of the star formation occurring during this epoch is invisible to optical wavelengths since it is enshrouded by dust. Most critically, observations of the COsmic Background Explorer (COBE) revealed that the cosmic extragalactic background at infrared wavelengths was comparable to that at optical wavelengths. This was a strong suggestion that around half the extragalactic emission, originated from galaxies and AGN, must be enshrouded by dust. Indeed, later observations with the Herschel telescope would confirm that at early epochs ($0.5 < z < 3$) about 70% of the co-moving star formation rate density (SFRD) is obscured by dust (Chary & Elbaz 2001). This refocused the main approaches of galaxy formation studies, since it high-lightened the strict need of parallel FIR observations to fully characterize galaxy evolution. An important challenge for such studies is the low resolution of commonly used FIR and sub-mm instruments, such as Herschel (beams or 4-10 arcsec) and single-dish sub-millimeter telescopes (beams of 1–4 arcmin), thus with high-changes of confusion, e.g., measuring several sources blended within one resolution element. This challenge has been overcome thanks to de-blending approaches using prior knowledge from higher-resolution observations at related wavelengths, such as 24 μm priors, or radio interferometric observations, and especially thanks to the advent of new sub-mm interferometers such as ALMA.

Black-hole accretion has been observed to be in great part obscured by dust and gas as well, however the origin of AGN obscuration is less well understood and is still a source of debate in the extragalactic community. Historically, AGN obscuration was thought to be an inclination effect, based on detections of polarized broad lines in obscured sources (Antonucci & Miller 1985). Since the obscuring material is assumed to be distributed in the shape of a torus, the obscured fraction would therefore be determined by the viewing angle; while a face-on view would allow a direct glimpse into the accretion disk and broad line region, producing an unobscured AGN or Type 1, an edge-on view would observe the AGN through the toroidal structure that would cover the broad line region, producing an obscured or Type 2 AGN. While it is widely accepted that AGN obscuration is produced in part by inclination, it has been shown that obscuration is a more complex phenomenon. Luminosity is known to

play an important role, where more luminous objects have been observed to be less obscured by being capable of pushing the obscuring medium by radiation pressure (receeding torus model Ricci et al. 2017). Evolutionary models of massive galaxies suggest that obscuration in AGN would be related to a short phase, right after a starburst event, assuming that both star formation and AGN activity are promoted by a galaxy merger event (Hopkins et al. 2008). Obscuration by dust and gas plays a fundamental role in galaxy and black-hole evolution across cosmic history. Chapters 2 and 5 will explore in depth this property for AGN and star forming galaxies, respectively.

Extreme sources

The increase of the galaxy 'main sequence' as a function of redshift, implies that at a given stellar mass, the star formation rates expected for 'typical' galaxies can increase by a factor 20 when going from $z = 0$ towards the peak at $z \sim 2$ (Sargent et al. 2012). Therefore, the most spectacular and extreme sources in both star formation and black-hole accretion are more likely to be found at $z \sim 2$. Here, I will shortly present some of the galaxy populations investigated in this thesis.

Active Galactic Nuclei (AGN): The AGN phenomenon is a complex concept since although AGNs are generally defined as accreting black-holes hosted in galaxy centers, this definition might apply as well for galaxies with small black-hole masses or accretion rates so low, that the intrinsic emission is not detectable or outshone by the host galaxy emission. In this thesis, by AGN are generally meant nuclear sources with bolometric luminosities from $L_{bol} \sim 10^{41} - 10^{48}$ erg s^{-1}and black-hole masses of a few $10^6 - 10^{10}$ $M_\odot$. Since historically all galaxies and AGN have been classified by their observational characteristics rather than their physical ones, some of the most common AGN types are: *Seyfert galaxies type 1 and 2*, the most common unobscured and obscured AGN in the local Universe, respectively; *radio galaxies*, bright radio sources typically associated with large relativistic jets (see disambiguation with radio-selected galaxy below); and *quasars*, the most luminous distant continuously-emitting sources in the early Universe. Although all these sources present overlaps in their intrinsic properties, and the different mass bins and redshifts probed might be the main source of diversity, the question whether other fundamental physical differences exist among them is still a matter of discussion. In this thesis, we will explore this question and recover physical intrinsic properties by modelling their multiwavelength emission. The second and third chapter of this thesis focus on AGN of two different selections: X-ray selected AGN and radio selected AGN, respectively. Both AGN populations cover redshift ranges of $z = 0.5 - 2.5$, including Seyfert 1 and 2; radio AGN; and QSO 1 and 2.

Dusty star-forming galaxies (DSFGs), starbursts, and submillimeter galaxies (SMGs):

Star-forming galaxies have been classified into several types based on their selection, which can sometimes be confusing due to the large overlap of the intrinsic physical properties of these classes. A large population of star forming galaxies, key in the phase of galaxy assembly, are dusty star forming galaxies (DSFGs, Casey et al. 2014). DSFGs are generally defined to be galaxies with prominent infrared emission and large amount of dust attenuation. As explained in Section 1.3, DSFGs likely represent the majority of star forming galaxies since dust distributions are a main by-product of the star formation process itself. These galaxies are sometimes also referred to as starburst galaxies, which have however a more strict definition: their star formation histories are characterized by short-lived intense periods of star formation; and they lay above the main sequence, forming a second component in the SFR-M* plot with a factor 4 to 10 times higher star formation rates than galaxies on the main sequence. Early observations with infrared telescopes have detected such galaxies in the local Universe and called them ultra-luminous (ULIRGs, $\log(LIR[L_\odot]) \geq 12$) and luminous

(LIRGs, $11 \leq \log(\mathrm{LIR}[L_\odot]) \leq 12$) infrared galaxies, where LIR is the total IR luminosity from $8 - 1000\ \mu$m (see Sanders & Mirabel 1996, for a review). *Sub-millimeter galaxies* are interesting DSFGs at high redshift, defined as galaxies strongly detected by sub-mm instruments. SMGs were initially discovered in the late 1990s with the SCUBA[4] and MAMBO[5] instruments. Due to the shift of the FIR SED to sub-mm wavelengths, the redshift distribution of SMGs is centered at $z \sim 2$. It is important to note, that although SMGs are highly star-forming and originally considered to strictly lay above the main sequence, some of the most massive SMGs may actually be main sequence galaxies due to their large masses at $z \sim 2$.

Radio-selected galaxies, were historically defined as a class of AGNs, since the low sensitivity of radio telescopes, before the advent of radio interferometres, probed almost exclusively AGN-originated radio emission. However, as discusses in Section 1.2, the increasing sensitivity of radio telescopes (such as the VLA and LOFAR) has started to probe lower luminosities, largely populated by star forming galaxies. Chapter 3 in thesis studies as well a sample of radio-selected star forming galaxies, which at high redshifts imply star-forming galaxies of SFR$> 500\ M_\odot$/yr given the sensitivity of the instruments used.

1.4 This Thesis

This thesis presents pioneering work on the panchromatic emission of some of the most luminous sources in the early Universe: star forming galaxies and active galactic nuclei. Using state-of-the-art statistical methods and new-generation radio-to-optical instruments, this thesis builds up on the current knowledge presented above to expand the parameter space covered by current multi-wavelength studies. In particular, this thesis pushes three different frontiers: the statistical frontier, the wavelength frontier and the resolution frontier. This study focuses on star-forming galaxies, AGN and composite galaxies at redshifts $z \sim 1 - 3$, all with rich ancillary multi-wavelength coverage from the radio-to-X-rays.

In **Chapter 2** we push **the statistical frontier** by exploring the complex parameter spaces needed to model the multiwavelength emission of galaxies and their AGN. In particular, we developed the probabilistic tool AGN*fitter* to consistently model the panchromatic emission of galaxies and accreting black-holes using physical semi-empirical and theoretical models from the UV to the sub-millimetre. We explore the statistical challenges associated with sampling such a complex parameter space, prone to correlations and degeneracies, and address these challenges by using a sophisticated Bayesian approach based on the Markov Chain Monte Carlo method. We apply the code to study the panchromatic emission of X-ray selected obscured and unobscured AGN from the COSMOS field. In this chapter, we show that our method is able to recover the entire probability density functions, including the mean values and, most crucially, the uncertainties of all physical parameters, such as stellar masses, star formation rates, AGN bolometric luminosities, reddening parameters, AGN obscuration, and AGN fraction. Finally, we test the capability of our multi-wavelength SED-fitting tool to recover the obscuration properties of the nuclear AGN region through comparisons with optical spectroscopy. Despite the ~7 order of magnitude difference between the scales probed by the AGN and those of the integrated galaxy emission, we show that AGN*fitter* is able to robustly classify the AGN into obscured and unobscured AGN by modelling the photometric data with 80% reliability. These results were presented in Calistro-Rivera et al. (2016).

In **Chapter 3** we push **the wavelength frontier** and present the first galaxy and AGN

[4]Sub-millimetre Common User Bolometer Array
[5]MAx-Planck Millimetre BOlometer

evolution study, as seen from the new frequency window opened by the Low Frequency ARray (LOFAR). Thanks to the combination of resolution and sensitivity achieved by LOFAR, we are able to build an unprecedented statistical sample of low-frequency radio-selected galaxies and AGN till redshifts of $z \sim 2.5$. We connect the low-frequency radio emission at 150 MHz to the FIR-UV SED by reconstructing the radio SED from low-to-high frequencies, using ancillary radio data, and by applying the method presented in Chapter 2 to reconstruct the panchromatic SED. We build the deepest sample of radio SEDs of galaxies and AGN from low-to-high frequencies, finding a significant difference in the shapes of the star-formation (SF) dominated sources as compared to the AGN-dominated ones, where the SF dominated galaxies tend to flatten towards lower frequencies. Focussing on the sub-sample of star forming galaxies, in this chapter we investigate for the first time the far-infrared-radio correlation for the low-frequency radio. Our results suggest that the FIR-radio correlation at high and low frequencies is not constant as suggested by previous literature, but evolve as a function of redshift. Finally, we present the first calibration of the radio emission at 150 MHz as a star-formation tracer, and provide a fitting function for the radio-SFR relation at 150 MHz. These results were presented in Calistro-Rivera et al. (2017).

In **Chapter 4** we push **the resolution frontier** by studying the multiwavelength emission at subarsecond resolution of four dusty star-forming galaxies at $z \sim 2-3$, selected in the sub-millimeter regime. Exploiting the unparalleled combination of depth and resolution of the ALMA interferometer, together with imaging from the *Hubble Space Telescope* (*HST*), we investigate the spatial and physical properties of the insterstellar medium, as seen from the molecular gas and dust continuum emission, and of the stellar emission of these galaxies. We observe the molecular gas as traced by the ^{12}CO($J = 3-2$) emission, and investigate the dynamical properties of the galaxies based on kinematic modelling, finding that these sources are consistent with disk rotation to first order. The high-resolution multiwavelength emission shows that the resolved spatial distributions of the dust continuum emission and, most remarkably, the molecular gas emission, can both be entirely offset to the stellar emission.We apply a statistical analysis of the observed sizes based on stacking of the molecular gas, dust continuum and stellar emission components of a larger sample of dusty star forming galaxies. We find that the cool molecular gas emission in these sources (radii$\sim 5-14$ kpc) is clearly more extended than the rest-frame ~ 250 μm dust continuum by a factor > 2. Assuming a constant dust-to-gas ratio, we find that this apparent difference in sizes can be explained by temperature and optical-depth gradients alone. The results of this chapter suggest that caution must be exercised when extrapolating morphological properties of dust continuum observations to conclusions about the molecular gas phase of the ISM. These results were presented in Calistro-Rivera et al. (2018).

In **Chapter 5** we complement the study of the interstellar medium at high resolution presented in Chapter 4, by studying the [C II] emission of two of the dusty star-forming galaxies in our previous sample. In particular, we compare ALMA measurements of gas emission line [C II] at 0.15 arcsecond resolution to the cool molecular gas emission traced by the ^{12}CO($J = 3-2$), presented above. We find that the [C II] surface brightness distribution is dominated by a compact core $\sim$1 kpc in radius, a factor of 2–3 smaller than the CO (3–2) emission, embedded in an extended, low surface-brightness [C II] component. We find that galaxies exhibit a strong [C II]/FIR deficit, with FIR surface brightness–[C II]/FIR slope steeper than in local star-forming galaxies. We compare our [C II]/CO(3–2) observations from Chapter 4 and 5 with PDR models, finding that a strong FUV radiation field ($G_0 \sim 10^4$) and moderate density (n(H) $\sim 10^3$ cm^{-3}) in the centre of the galaxies. We find that the pronounced [C II]/FIR deficit in these sources is probably a thermal saturation of the C$^+$ fine-structure lev-

els, and a significantly reduced heating of the gas via the photoelectric effect. These results have been submitted and will be presented in Rybak, Calistro-Rivera et al. (2018)[6].

[6]This chapter is part of this PhD Thesis due to my significant contribution to this project at all levels. The main result of this chapter is based on the comparison of the [C II] data to the CO observations presented in Chapter. I have been active in both the realization and discussion of this comparative analysis. Additionally, I have carried out the kinematic modelling of the [C II] data presented in section 2.3 and have written the description of the process in this chapter. Finally, I have proof-read and edited different versions of this chapter, and have led the ALMA Cycle 4 proposal to complete the [C II] observations for the two remaining sources from Calistro-Rivera et al. (2018).

1

Bibliography

Aird, J., Coil, A. L., & Georgakakis, A. 2018, MNRAS, 474, 1225

Aird, J., Coil, A. L., Georgakakis, A., et al. 2015, MNRAS, 451, 1892

Alonso-Herrero, A., Ramos Almeida, C., Mason, R., et al. 2011, ApJ, 736, 82

Antonucci, R. R. J., & Miller, J. S. 1985, ApJ, 297, 621

Bolzonella, M., Miralles, J.-M., & Pelló, R. 2000, A&A, 363, 476

Brandt, W. N., & Alexander, D. M. 2015, A&A Rev., 23, 1

Brinchmann, J., Charlot, S., White, S. D. M., et al. 2004, MNRAS, 351, 1151

Brinchmann, J., & Ellis, R. S. 2000, ApJ, 536, L77

Burgarella, D., Buat, V., & Iglesias-Páramo, J. 2005, MNRAS, 360, 1413

Carilli, C. L., & Walter, F. 2013, ARA&A, 51, 105

Casey, C. M., Narayanan, D., & Cooray, A. 2014, Phys. Rep., 541, 45

Condon, J. J. 1992, ARA&A, 30, 575

Conroy, C. 2013, ARA&A, 51, 393

Conselice, C. J., Wilkinson, A., Duncan, K., & Mortlock, A. 2016, ApJ, 830, 83

da Cunha, E., Charlot, S., & Elbaz, D. 2008, MNRAS, 388, 1595

Einstein, A. 1916, Annalen der Physik, 354, 769

Gaia Collaboration, Brown, A. G. A., Vallenari, A., et al. 2018, A&A, 616, A1

Gültekin, K., Richstone, D. O., Gebhardt, K., et al. 2009, ApJ, 698, 198

Harris, G. L. H., Rejkuba, M., & Harris, W. E. 2010, Publications of the Astronomical Society of Australia, 27, 457

Hopkins, P. F., Hernquist, L., Cox, T. J., & Kereš, D. 2008, ApJS, 175, 356

Ichikawa, K., Packham, C., Ramos Almeida, C., et al. 2015, ApJ, 803, 57

Kirkpatrick, A., Pope, A., Alexander, D. M., et al. 2012, ApJ, 759, 139

Kormendy, J., & Richstone, D. 1995, ARA&A, 33, 581

Lynden-Bell, D. 1969, Nature, 223, 690

Lynden-Bell, D., & Rees, M. J. 1971, MNRAS, 152, 461

Madau, P., & Dickinson, M. 2014, ARA&A, 52, 415

Magorrian, J., Tremaine, S., Richstone, D., et al. 1998, AJ, 115, 2285

Marconi, A., & Hunt, L. K. 2003, ApJ, 589, L21

Muzzin, A., Marchesini, D., van Dokkum, P. G., et al. 2009, ApJ, 701, 1839

Nenkova, M., Ivezić, Ž., & Elitzur, M. 2002, ApJ, 570, L9

Padovani, P. 2016, A&A Rev., 24, 13

Perlmutter, S., Aldering, G., Goldhaber, G., et al. 1999, ApJ, 517, 565

Planck Collaboration, Ade, P. A. R., Aghanim, N., et al. 2014, A&A, 571, A16

Rejkuba, M., Harris, W. E., Greggio, L., & Harris, G. L. H. 2011, A&A, 526, A123

Ricci, C., Trakhtenbrot, B., Koss, M. J., et al. 2017, Nature, 549, 488

Riess, A. G., Filippenko, A. V., Challis, P., et al. 1998, AJ, 116, 1009

Rosario, D. J., Trakhtenbrot, B., Lutz, D., et al. 2013, A&A, 560, A72

Rosario, D. J., McIntosh, D. H., van der Wel, A., et al. 2015, A&A, 573, A85

Sanders, D. B., & Mirabel, I. F. 1996, ARA&A, 34, 749

Sargent, M. T., Béthermin, M., Daddi, E., & Elbaz, D. 2012, ApJ, 747, L31

Schmidt, M. 1963, Nature, 197, 1040

Seyfert, C. K. 1943, ApJ, 97, 28

Shakura, N. I., & Sunyaev, R. A. 1973, A&A, 24, 337

Smail, I., Swinbank, A. M., Ivison, R. J., & Ibar, E. 2011, MNRAS, 414, L95

Tielens, A. G. G. M. 2008, ARA&A, 46, 289

Volonteri, M., Capelo, P. R., Netzer, H., et al. 2015, MNRAS, 449, 1470

Whitaker, K. E., van Dokkum, P. G., Brammer, G., & Franx, M. 2012, ApJ, 754, L29

2

The Statistical Frontier: A Bayesian MCMC Approach to Fitting Spectral Energy Distributions of AGN

We present AGNfitter, a publicly available open-source algorithm implementing a fully Bayesian Markov Chain Monte Carlo method to fit the spectral energy distributions (SEDs) of active galactic nuclei (AGN) from the sub-mm to the UV, allowing one to robustly disentangle the physical processes responsible for their emission. AGNfitter makes use of a large library of theoretical, empirical, and semi-empirical models to characterize both the nuclear and host galaxy emission simultaneously. The model consists of four physical emission components: an accretion disk, a torus of AGN heated dust, stellar populations, and cold dust in star forming regions. AGNfitter determines the posterior distributions of numerous parameters that govern the physics of AGN with a fully Bayesian treatment of errors and parameter degeneracies, allowing one to infer integrated luminosities, dust attenuation parameters, stellar masses, and star formation rates. We tested AGNfitter's performance on real data by fitting the SEDs of a sample of 714 X–ray selected AGN from the XMM–COSMOS survey, spectroscopically classified as Type1 (unobscured) and Type2 (obscured) AGN by their optical-UV emission lines. We find that two independent model parameters, namely the reddening of the accretion disk and the column density of the dusty torus, are good proxies for AGN obscuration, allowing us to develop a strategy for classifying AGN as Type1 or Type2, based solely on an SED-fitting analysis. Our classification scheme is in excellent agreement with the spectroscopic classification, giving a completeness fraction of $\sim$ 86% and $\sim$ 70%, and an efficiency of $\sim$ 80% and $\sim$ 77%, for Type1 and Type2 AGNs, respectively .

G. Calistro Rivera, E. Lusso, J. F. Hennawi, D. W. Hogg
ApJ, **Volume 833**, Issue 1, p. 98-120 (2016)

2.1 Introduction

Active galaxies host in their nuclei (AGN) the most efficient energy sources in the universe: accreting supermassive black holes (SMBHs) that convert significant fractions of the accreted material rest-mass energies into powerful electromagnetic radiation. The evolution and properties of the host-galaxies of AGN are closely connected to the formation and growth of the SMBHs, as supported by both observational evidence (Magorrian et al. 1998; Marconi & Hunt 2003) and cosmological simulations (Springel et al. 2005; Hopkins et al. 2006). The study of the SMBH/host-galaxy co-evolution demands a proper characterisation of their properties; for instance the intrinsic AGN luminosity, the covering factor of nuclear obscuring medium, the stellar mass and star formation rate (SFR) of the host galaxies and the amount of this emission that is reprocessed by dust. These physical parameters are all encoded in the observed spectral energy distributions (SED) of the sources. In order to constrain these physical parameters and to place AGN into the context of galaxy evolution, it is fundamental to disentangle the contribution of the AGN from the host-galaxy in the observed SED.

The AGN SED covers the full electromagnetic spectrum from radio to X-rays. The most prominent features are the "infrared bump" at $\sim 10 - 20\,\mu$m, and an upturn in the optical-UV, the so-called "big-blue bump" (BBB; Sanders et al. 1989; Elvis et al. 1994; Richards et al. 2006a; Shang et al. 2011; Elvis et al. 2012; Krawczyk et al. 2013). The BBB is thought to represent the emission from the accretion disk surrounding the SMBH, while the mid-infrared bump is due to the presence of dust that re-radiates a fraction of the optical-UV disc photons at infrared wavelengths. The presence of this screen of gas and dust surrounding the accretion disc (dusty torus) is the foundation of the unified model for AGN (Antonucci 1993; Urry & Padovani 1995), which explains the differences in their spectral characteristics as an effect of viewing angle with respect to a dusty obscuring torus. These spectral differences classify AGN into unobscured (Type1) and obscured (Type2) due to the presence or absence respectively of broad emission lines in their optical spectra. While in Type1 AGN the observer has a direct view into the ionized gas clouds Doppler-broadened by the SMBH potential (the broad line region), in Type2 AGN the line emission of these clouds is completely or partially extincted depending on the inclination angle respective to the torus, leaving only the narrow line emission to be observed.

An obvious complication in the study of the host galaxy properties in AGN is that the emission of the central nuclei outshines the galaxy light, therefore it becomes extremely difficult to derive constraints on the stellar populations. On the other hand, for obscured AGN the host-galaxy light may be the dominant component in the optical/near-infrared SED, making it challenging to estimate the intrinsic nuclear power.

A common approach to tackle this problem is to fit the SED with different combinations of theoretical models and/or empirical templates for each individual emission component (eg. da Cunha et al. (2008)). The complexity of the models increases as a more accurate description of the underlying physics is needed. In this way, the number of unknown parameters increases as well, including the unavoidable existence of degeneracies and correlations among them. The best statistical approach for dealing with parameter degeneracies are Bayesian methods, which also allows the user to obtain reliable confidence ranges for parameter estimates. The importance of a Bayesian study for general SED fitting has provoked the development of several Markov Chain Monte Carlo (MCMC)-based algorithms in the last years, principally in SED studies of quiescent galaxies (e.g. Acquaviva et al. (2011), Serra et al. (2011), Pirzkal et al. (2012), Johnson et al. (2013)). These algorithms sample the space to infer galaxy parameters, which have been derived from stellar population synthesis models.

Parallel AGN studies at single wavelength regimes have demonstrated that no monochromatic diagnostic can achieve a complete characterisation of AGNs (Juneau et al. 2013) and

combined multi-wavelength approaches are necessary for a comprehensive exploration of the physics of active galaxies (Lusso et al. 2012). To date, the publicly available SED fitting codes in the literature do not include any modelling of the broad-band AGN emission in a panchromatic approach, but have focused their analysis exclusively at infrared wavelengths (Sajina et al. (2006), Han & Han (2012), Berta et al. (2013) and Hernán-Caballero et al. (2015)).

We have thus developed AGNfitter: a probabilistic SED-fitting tool based on Markov Chain Monte Carlo sampling. This code is designed to simultaneously disentangle the physical components of both AGN and host galaxy from optical-UV to sub-mm wavelengths and to infer the posterior distribution of the parameters that govern them. Our Bayesian method allows us to robustly perform this inference in order to recover the parameters with a complete description of their uncertainties and degeneracies through the calculation of their probability density functions (PDFs). The MCMC technique allows us to probe the shape of these PDFs, and the correlations among model parameters, giving far more information than just the best fit and the marginalized values for the parameters. The efficiency and speed of the algorithm makes it capable of treating large samples of AGN and galaxies, enabling statistical studies of nuclear obscuration in the context of AGN classification. The current version of AGNfitter is publicly available on /github-link.

This paper is structured as follows. In §2.2 we describe the construction of the total AGN and host galaxy models used in the code. In §2.3 we will explain the technical details of the code and the MCMC implementation used. For an illustration of the astrophysical capabilities of AGNfitter, we show in Section 2.4 the results of the application of the code on synthetic data. In Sections 2.5 and 2.6 we describe the sample selection of Type1 and Type2 AGN of the XMM–COSMOS survey and show the results of AGNfitter on this sample.

We adopt a concordance flat Λ-cosmology with $H_0 = 70\,\mathrm{km\,s^{-1}\,Mpc^{-1}}$, $\Omega_\mathrm{m} = 0.3$, and $\Omega_\Lambda = 0.7$ (Komatsu et al. (2009), Planck Collaboration et al. (2014)).

2.2 The code AGNfitter

AGNfitter produces independent samples of the parameter space to fit the observational data, which is constituted by photometric fluxes ranging from the optical-UV to the sub-mm. Following Lusso et al. (2013) we consider four independently modelled components, which cover in total a rest-frame frequency range of $\log\nu = 11 - 16$ ($\lambda = 0.01 - 100\mu$m). These models are specifically the accretion disk emission (BBB), the hot dust surrounding the accretion disk (the so-called torus), the stellar population of the host galaxy, and emission from cold dust in galactic star-forming regions. We make the assumption that the broad band SED can be constructed as a linear combination of these components with their relative contribution depending on the nature of the source. In order to properly mimic the observed fluxes, the emission templates F_λ need to be integrated against the telescope response curves $S(\lambda)$ corresponding to the spectral bands used, following

$$F_\mathrm{S} = \frac{\int \lambda F_\lambda S(\lambda)\, d\lambda}{\int \lambda S(\lambda)\, d\lambda}, \tag{2.1}$$

where F_S is the resulting filtered flux. Depending on the photometric data available, the corresponding filter curves can be chosen from the filter library included in AGNfitter, which is a compilation of COSMOS filters published in `http://www.astro.caltech.edu/~capak/filters/index.html`. New filters that are not available in this list can be easily added by the user.

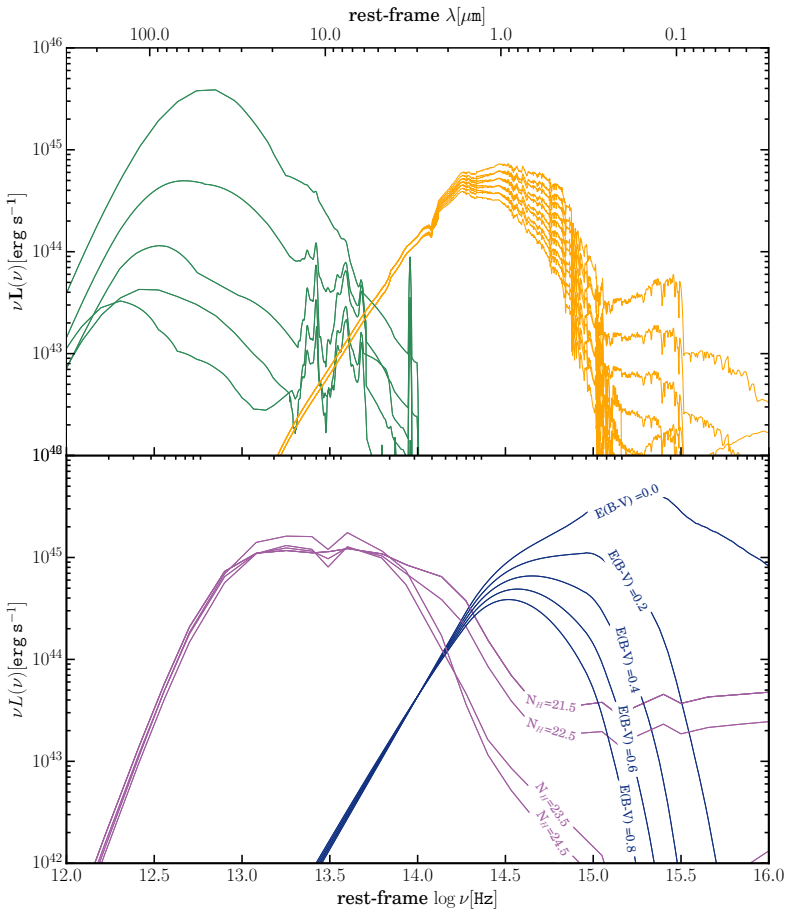

Figure 2.1: Examples of templates employed in AGNfitter, which models AGN SEDs considering four different components. *Upper panel*: The green and the orange solid lines correspond to different templates of the starburst and host-galaxy components, respectively. *Lower panel*: The purple and blue solid lines correspond to the hot-dust emission at different column density values log N_H and the BBB templates with increasing reddening $E(B-V)_{bbb}$, respectively.

2.2.1 Accretion disk emission (Big Blue Bump)

The most prominent feature in the AGN SED is the BBB, which is produced by the thermal radiation emitted by matter accreating into the central SMBH (Richstone & Schmidt 1980). AGNfitter models this emission using a modified version of the empirical template constructed by Richards et al. (2006b).

This template is a composite spectrum of 259 Type1 QSO SEDs selected from the Sloan Digital Sky Survey (SDSS, York et al. 2000). Given that the mid-infrared region of the SED will be modelled by independent warm dust templates in AGNfitter, we have neglected the near-infrared regime originally included in the Richards et al. SEDs. We extrapolated the BBB template from 1μm to longer wavelengths assuming $F_\nu \propto \nu^{-2}$ (i.e. Rayleigh-Jeans tail of a black body). Our BBB component is modelled by a single template and the only adjustable parameter is a normalization factor called 'BB' (see Table 2.1) determining its amplitude.

The emitted BBB spectrum can be altered by extinction from dust along the line of sight. We model this effect by applying the Prevot et al. (1984) reddening law for the Small Magellanic Clouds (SMC, which seems to be appropriate for Type-1 AGN, Hopkins et al. 2004; Salvato et al. 2009) to the template of the emitted BBB SED in our model. Corresponding to the dust screen model, the extinguished flux $\mathrm{f_{red}}$ is given by

$$\mathrm{f_{red}}(\lambda) = \mathrm{f_{em}}(\lambda) \times 10^{-0.4\mathrm{A}_\lambda}, \tag{2.2}$$

where $\mathrm{f_{em}}$ is the emitted flux. The value A_λ depends directly on the Prevot reddening law $k(\lambda)$ and the reddening parameter $\mathrm{E(B-V)_{bbb}}$, which is an input parameter in AGNfitter, following

$$\mathrm{A}_\lambda = \mathrm{k}(\lambda)\mathrm{E(B-V)_{bbb}}. \tag{2.3}$$

The exact function we use for the Prevot's law is

$$k(\lambda) = 1.39(10^{-4}\lambda)^{-1.2} - 0.38. \tag{2.4}$$

where λ are in μm.

AGNfitter explores a discrete grid of reddening values in the range of $0 \leq \mathrm{E(B-V)_{bbb}} \leq 1$ in steps of 0.05 and uses equation (2.4) to construct the reddening function. Since the MCMC requires a continuous parameter space, we overcome the discrete distribution of the reddening values through a k-Nearest Neighbour Interpolation (kNN), associating any $\mathrm{E(B-V)_{bbb}}$ in the sampling to the nearest $\mathrm{E(B-V)_{bbb-grid}}$ of our templates. A sub-sample of our BBB templates with different reddening levels is presented in Figure 2.1 (blue solid lines).

2.2.2 Hot dust emission (torus)

The nuclear hot-dust SED models are taken from Silva et al. (2004). These empirical templates were constructed from a large sample of Seyfert galaxies having reliable observations of the nuclear intrinsic NIR and MIR emission and are corrected by carefully removing any galaxy contribution. The photometric data obtained from the Seyfert infrared observations were then interpolated based on a radiative transfer code GRASIL (Silva et al. 1998) to obtain full AGN infrared SEDs. This code simulates the emission of dust contents heated by a central source, which has a typical AGN intrinsic spectrum. The infrared SEDs are divided into 4 intervals of absorption: $N_\mathrm{H} < 10^{22}$ cm^{-2} for Seyfert 1s (Sy1), $10^{22} < N_\mathrm{H} < 10^{23}$ cm^{-2}, $10^{23} < N_\mathrm{H} < 10^{24}$ cm^{-2}, and $N_\mathrm{H} > 10^{24}$ cm^{-2} for Seyfert 2s (Sy2) . As explained in Silva et al. (2004), the main difference between the SEDs as a function of N_H is the increment of absorption in the near-IR at $\lambda < 2\mu$m and some mild silicate absorption at 9.7 μm for larger N_H values. A slight increase of the overall IR emission can be also observed at $N_\mathrm{H} > 10^{24}$

cm^{-2}, as a product of a higher covering factor of the circumnuclear dust at these N_H values. In the context of the unified AGN model, the increasing N_H values arise from different viewing angles with respect to the torus. We expect thus to observe Type1 AGNs of low N_H values with hot dust emission at near-infrared wavelengths, while in the case of Type2 AGN this near-IR emission may be extincted by the dust distribution of high N_H values. The four templates employed in the code are plotted in Fig. 2.1 with the purple solid line. In order to reduce the degree of discreteness in our parameter space due to the small number of torus templates, we performed a further interpolation in between these four templates. We then constructed an empirical function f(N_H) which produces a finer parameter grid for the torus models. Our final SED grid consist on 80 templates corresponding to a range of log N_H = [21,25] in intervals of $\Delta N_H = 0.05$. Also here, we overcome the discreteness of the N_H parameter through a k-Nearest Neighbour Interpolation (kNN), associating any N_H in the sampling to the nearest N_{H-grid} of our templates. A further parameter adjusting this contribution is the corresponding amplitude parameter 'TO' as listed in Table 2.1.

2.2.3 Stellar emission

To construct the library of templates for the stellar emission of the host galaxy we follow the standard approach and use the stellar population synthesis models by Bruzual & Charlot (2003). These models predict the rest-frame flux of single stellar populations (SSPs) at different ages and for different star formation rates. The evolution of the stellar population is computed by assuming a constant metallicity, leaving as free parameters both the age of the galaxy (*age*) and the star-formation history time-scale (τ).

We have assumed a Chabrier (2003) initial mass function (IMF) and an exponentially declining star formation history modulated by the time scale τ as $\psi(age) \propto e^{-age/\tau}$. For the purposes of this analysis a set of galaxy templates representative of the entire galaxy population from passive to star forming is selected. To this end, 10 exponentially decaying star formation histories (SFHs) with characteristic times ranging from $\tau = 0.1$ to 10 Gyr and a model with constant star-formation rate are included.

For each SFH, a subsample of ages is selected, to avoid both degeneracy among parameters and to speed up the computation. The grid of ages used to calculate the galaxy templates covers ages from 0.2 to 11 Gyr in steps of log $age \sim 0.1$. In particular, early-type galaxies, characterized by a small amount of ongoing star formation, are represented by models with values of τ smaller than 1 Gyr and ages larger than 2 Gyr, whereas more actively star forming galaxies are represented by models with longer values of τ and a wider range of ages from 0.1 to 10 Gyr. An additional constraint on the age implies that for each source, the age has to be smaller than the age of the universe at the redshift of the source.

Altogether, 90 different stellar emission templates from the Bruzual & Charlot (2003) models are included in AGNfitter. A small subsample of these templates is shown in the upper panel of Fig. 2.1 with the orange solid line. Since the MCMC requires a continuous parameter space, we overcome the discrete distribution of the galaxy templates parameters through a k-Nearest Neighbour Interpolation (kNN). In this way we choose from the grid the nearest combination (τ_{grid}, age_{grid}) corresponding to any pair of parameter values (τ, *age*). Additionally, since stellar emission may be altered by extinction along the line of sight, the templates are reddened according to the Milky Way-like reddening law derived in Calzetti et al. (2000). The reddening values $E(B-V)_{gal}$ range between 0 and 0.5 with a step of 0.05. Including the extinction effect on the Bruzual & Charlot (2003) SED templates, the total AGNfitter stellar library is composed by 900 stellar templates. Finally, the amplitude of the stellar contribution on the total SED is adjusted by the normalizing parameter 'GA'.

2.2.4 Cold Dust Emission from Star-Forming Regions

AGNfitter models the emission of cold dust in star forming regions using the semi-empirical starburst template libraries by Chary & Elbaz (2001) and Dale & Helou (2002). These template libraries represent a wide range of SED shapes and luminosities and are widely used in the literature.

The Chary & Elbaz (2001) template library consists of 105 templates based on the SEDs of four prototypical starburst galaxies (Arp220 (ULIRG); NGC 6090 (LIRG); M82 (starburst); and M51 (normal star-forming galaxy)). They were derived using the Silva et al. (1998) models with the mid-infrared region replaced with ISOCAM observations between 3 and 18μm (verifying that the observed values of these four galaxies were reproduced by the templates). These templates were then interpolated between the four prototypical starburst galaxies to generate a more diverse set of templates.

The Dale & Helou (2002) templates are updated versions of the widely used Dale et al. (2001) templates. These models involve three components, large dust grains in thermal equilibrium, small grains semistochastically heated, and stochastically heated PAHs. They are based on IRAS/ISO observations of 69 normal star-forming galaxies in the wavelength range 3–100μm. Dale & Helou (2002) improved upon these models at longer wavelengths using SCUBA observations of 114 galaxies from the Bright Galaxy Sample (BGS, see Soifer et al. 1989), 228 galaxies observed with ISOLWS (52–170μm; Brauher 2002), and 170μm observations for 115 galaxies from the ISOPHOT Serendipity Survey (Stickel et al. 2000).

Altogether, the total far-infrared library used in AGNfitter is composed by 169 templates, which are parametrized by their different IR (8–1000μm) luminosities in the range IRlum= $10^8 - 10^{12} L_\odot$. The IRlum values were already pre-computed for each template in the original library provided by Chary & Elbaz (2001) and Dale & Helou (2002). It is important to note, that the IRlum parameter is used in AGNfitter solely with the aim of indexing the templates in the library, hence it does not have any physical relevance, and it should not be confused with the computed total infrared luminosity of the sources (denoted as $L_{IR,8-1000\,\mu m}$, see § 2.4.4). Also here, we overcome the discrete parametrization of this component through a k-Nearest Neighbour Interpolation, associating any IRlum value required by the sampling to the nearest $IRlum_{grid}$ of our templates. The amplitudes of this component's contributions are further adjusted by the normalization parameter 'SB'. A small subsample of starburst templates are plotted in Figure 2.1 with green solid lines.

2.2.5 Parameter Space

The parameter space describing the total active galaxy emission in AGNfitter is 10-dimensional, as given by the number of parameters listed in Table 2.1. It is composed by two different types of parameters: (1) physical parameters, which determine the shape of the templates and hence represent non-linear dependencies, and (2) amplitude parameters, on which the model depends linearly and re-scale the contribution strength of each component. The ranges that we assume each parameters to reside in is listed in Table 2.1.

2.3 The MCMC Algorithm

The Bayesian approach in SED-fitting implies that given the observed photometric data, the posterior probability of the parameters that constitute the model $\vec{\rho}$, is given by

$$P(\vec{\rho}|data) = \frac{P(data|\vec{\rho})P(\vec{\rho})}{P(data)}, \tag{2.5}$$

Table 2.1: Parameter space in AGNfitter: Description of the parameters and their value ranges. The value of age(z) is the limiting maximal age for a galaxy at redshift z, given by the age of the universe at that redshift according to the chosen cosmology.

Component	Parameter ρ_i	Description	Range
BBB emission	BB	BBB normalization	[0,20]
BBB emission	$E(B\text{-}V)_{bbb}$	BBB reddening	[0,1.0]
torus emission	log N_H [log cm^{-2}]	torus column density	[21,25]
torus emission	TO	torus normalization	[0,20]
stellar emission	τ[Gyr]	exponential SFH time scale	[0.1,3.0]
stellar emission	log *age* [log yr]	age of the galaxy	[10^5,age(z)]
stellar emission	GA	galaxy normalization	[0,20]
stellar emission	$E(B\text{-}V)_{gal}$	galaxy reddening	[0,0.5]
cold dust emission	log IRlum [log $L_\odot$]	parametrization of starburst templates	[7,15]
cold dust emission	SB	starburst normalization	[0,20]

where $\vec{\rho}$ is the ten dimensional vector that includes the parameters listed in Table 2.1. The function $P(\vec{\rho})$ represents our prior knowledge on the distribution of parameters previous to the collection of the data, while the factor $P(data)$ can be regarded as a constant of proportionality, since it is independent of the parameters. The function $P(data|\vec{\rho})$ is the likelihood of the data being observed given the model $\mathcal{L}(data, \vec{\rho}) \equiv P(data|\vec{\rho})$.

Provided that the individual photometric measurements are independent and their uncertainties are Gaussian distributed, the likelihood function is given by

$$\mathcal{L}(data, \vec{\rho}) \propto \prod_{i=0}^{n} \exp\left[-\frac{[data_i - f(\vec{\rho}|\nu)]^2}{2\sigma_i^2}\right], \tag{2.6}$$

where $f(\vec{\rho})$ is defined to be the total active galaxy model (linear combination of the four model templates presented in §2.2). One of the main advantages of the Bayesian approach is the possibility of calculating the posterior PDFs of a specific subset of parameters of interest, ignoring other nuisance parameters, in a process referred to as marginalization. The PDF of a single parameter ρ_i is then calculated by integrating over all possible values of the nuisance parameters, propagating their uncertainties into the final result on $P(\rho_i)$,

$$P(\rho_i) = \int^{k\neq i} d\rho_1 ... d\rho_k \;\; P(\vec{\rho}|data). \tag{2.7}$$

Though the Bayesian approach presents many advantages in theory, AGNfitter requires integrations of a high-dimensional parameter space with parameters related in non-linear functions and it can be extremely computationally intensive in practice. This can be overcome using numerical power, through informed sampling of the parameter space using MCMC algorithms.

Following the Bayesian assumption that unknown parameters can be treated as random variables, the MCMC algorithm produces independent samples of the parameters' posterior PDFs in an efficient way through a random walk in the parameter space. The sequence of visited points in the walk is called a *chain*, where each chain is a Markov process. The 'Markov' property ensures that every Monte Carlo (random) step is dependent only on the last visited point having no memory of previous steps.

The random walk is initialised at a position ρ_0, which we describe in detail in §2.3.2 for the case of AGNfitter. The transition steps between visited points will be decided from a proposal distribution P and the chosen step will be accepted or rejected based on the comparison of the probability of the previous and next trial points. This probability is computed depending on the priors and the likelihood of the model at the current visited point, which results from the calculation of Eq. 2.6. The chosen proposal distribution P is an important factor in the efficiency of the sampling, since it can lead the chain to regions of convergence or to make them diverge towards regions of mainly rejected steps producing heavily correlated samples.

2.3.1 Emcee

The MCMC core embedded in AGNfitter is the Python package Emcee (Foreman-Mackey et al. 2013), which is a pure-python implementation, slightly modified from the affine-invariant MCMC ensemble sampler developed by Goodman & Weare et al. (2010). In comparison to codes based of the Metropolis-Hastings (MH) algorithm (Metropolis et al. 1953; Hastings 1970), one advantage of Emcee is its affine-invariance property, which implies the clever choice of a proposal distribution which is invariant under any linear transformation of the posterior distribution to sample. This makes the proposal distribution independent on any possible covariances among the parameters, requiring the hand-tuning of only 1 or 2 parameters rather than $\sim N^2$ for a traditional (MH) algorithm in an N-dimensional parameter space. The fact that the efficiency of Emcee is independent of the dimensionality of the model used is a clear advantage for treating a complex problem as the one tackled by AGNfitter.

A further property of the Emcee implementation is that the parameter space is explored through a set of chains (*walkers*) that evolve in parallel as an ensemble, rather than through a single chain. This implies that at each step each walker is randomly assigned to a partner walker, moving along lines which connect the single chains to each other. This allows two great features of the code. On one side this makes the exploration of the parameter space extremely efficient, since the proposal distribution of each current walker is based on the information gained by the rest of the chains. On the other side, Emcee used the parallel evolution of the chain to allow the distribution of the processes into parallel computing taking advantage of multi-core processors. Finally, the simple Python interface of Emcee allows more flexibility in its use. A brief discussion comparing several Python statistical packages which supports our choice of Emcee can be found in VanderPlas (2014).

2.3.2 Initialization and burn in steps

In AGNfitter all walkers start in a random position in a region of very small radius around the central values of the parameter ranges (see Table 2.1). Before running the MCMC sampling, which should return the right PDFs, the walkers need to arrive to the region of interest, around which the maximum likelihood should be located. There is a certain number of steps used for this aim, and the period needed for this initial convergence is called *burn in*. The burn in steps will be neglected for the purposes of sampling the posterior probability distribution of the parameters.

Achieving the convergence of the chains is an important condition for the correct sampling of the target distribution and different methods on judging convergence are discussed in the literature (e.g. Gelman & Rubin 1992; Mary Kathryn Cowles 1996; Lewis & Bridle 2002). As explained in detail in Foreman-Mackey et al. (2013), a good convergence diagnostic consists in measuring the autocorrelation function and more specifically, the integrated autocorrelation time of the chains. The inverse of the autocorrelation time estimates the fraction of the total sample which has converged into the relevant regions, i.e. the effective fraction, which samples of the target distribution. As a feature of Emcee, AGNfitter includes the option to calculate the autocorrelation time using the Python module acor2. The longer the autocorrelation time, the more samples that are needed during the burn-in face to ensure independent samples of the target density. A good convergence test recommended for AGNfitter chains consists in verifying than the autocorrelation time for each parameter is at least a factor of ~ 32 shorter than the chain length.

One recurring issue in parallel evolving chain-ensembles, is that some of the chains can get trapped in some uninteresting local but not global maxima. In order to deal with this problem, we have introduced multiple burn-in processes. The basic idea is that, after each single burn-in sampling, all walkers are relocated to the point of the highest likelihood (global maximum) visited during the last set, restarting a new sampling set and avoiding that some of the walkers remain in regions of local maxima. This process is iterated ideally until the region of interest (i.e. around the location of the maximum likelihood value) is achieved. Unfortunately, there is no established theory for how long the burn in process should be, and this must instead be determined empirically for the problem at hand. The number of burn-in sets, as well as the number of steps in each burn in, can be set by the user. For the size of the AGNfitter parameter space, we recommend at least two burn-in sets of 10,000 steps each.

2.3.3 MCMC steps

After the burn-in period all further samples are included in the calculations of the posterior PDFs. The length needed for the sampling depends on several factors such as the size and dimension of the parameter space, the quality of the data (number of data points, error sizes), whether the convergence of the chains has been achieved previously in the burn-in process, and the density of the sampling desired. For the latter, the number of sampling points used for the distribution is not only determined by the number of MCMC steps but also by the number of walkers used for the parameter space exploration.

2.3.4 Running AGNfitter

We set AGNfitter to use a number of 80 walkers and two burn-in sets each of 5,000 steps as default values. This can be freely changed based on the user's preferences. After the burn-in phase, the PDFs are sampled with a number of 10,000 steps during the MCMC procedure. For this default configuration, the SED-fitting process takes in total about 5 minutes per source of computational time in a Macbook Pro with a 2.8 GHz Intel Core i5 processor, using only one core. It should be noted that the time needed for sampling the PDFs is both source and data dependent, as the parameter space exploration time depends on how often the proposed steps are accepted or neglected. Since the consideration of each proposed step involves likelihood calculations, the time may increase for sources which are difficult to fit.

For the case of large catalogs, AGNfitter provides the possibility of fitting several sources simultaneously using the multiprocessing Python package, which distributes automatically several fitting processes into an specified number of computer cores. The availability of a multi-core computer would largely increase the efficiency of the code.

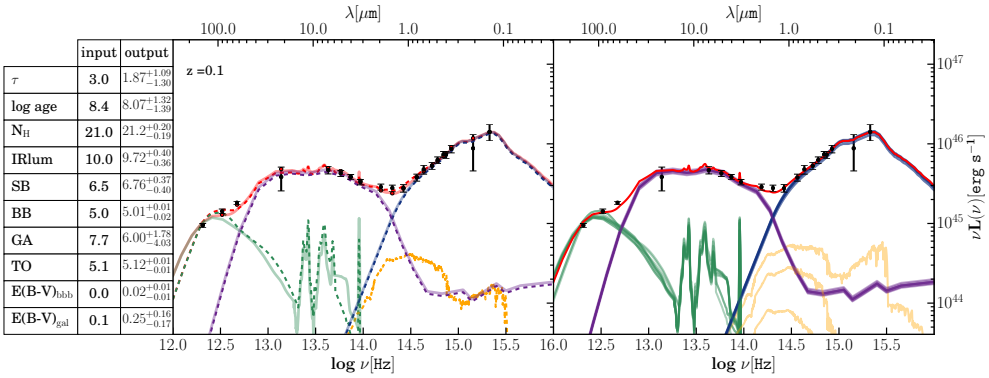

	input	output
τ	3.0	$1.87^{+1.09}_{-1.30}$
log age	8.4	$8.07^{+1.32}_{-1.39}$
N_H	21.0	$21.2^{+0.20}_{-0.19}$
IRlum	10.0	$9.72^{+0.40}_{-0.36}$
SB	6.5	$6.76^{+0.37}_{-0.40}$
BB	5.0	$5.01^{+0.01}_{-0.02}$
GA	7.7	$6.00^{+1.78}_{-4.03}$
TO	5.1	$5.12^{+0.01}_{-0.01}$
$E(B\text{-}V)_{bbb}$	0.0	$0.02^{+0.01}_{-0.01}$
$E(B\text{-}V)_{gal}$	0.1	$0.25^{+0.16}_{-0.17}$

Figure 2.2: SED output of a synthetic Type1 AGN: The colours of the component SED shapes are assigned similarly to Figure 2.1, while the linear combination of these, the 'total SED', is depicted as a red line. *The table* provides the initial input values used for the construction of the mock AGN and the median values of the parameters' PDFs resulting from the fitting with the respective 16th and 84th percentiles. For the aim of comparison, we plot the SEDs as given by the input parameter values and the output best-fit values in the *left panel*. The dashed lines are the SEDs corresponding to the input values and the solid transparent lines are the SED produced with the output best-fit parameters. In the *right panel* we randomly pick eight different realizations from the posterior PDFs and over-plot the corresponding component SEDs in order to visualize the dynamic range of the parameters values included in the PDF. The total SEDs from the realizations are constructed and the mean is depicted as a red line.

2.3.5 Prior on the galaxy luminosity

One of the problems we faced while fitting the optical-UV region of the SED of Type 1 AGN was the degeneracy between the BBB and galaxies with very bright and young stellar populations. A luminous Type 1 AGN ($L_{\rm bol} \sim 10^{45-46}$ erg s^{-1}) can be either modelled with a BBB with zero reddening and negligible galaxy contribution, or with a highly reddened BBB (e.g., E(B–V)$\gtrsim$ 0.5) and a star-forming galaxy with significant contribution by the young stellar population. However, such galaxies will have exceptionally high luminosities, much higher than typically observed. Part of this degeneracy is due to lack of flexibility for the BBB template currently employed: the shape of the BBB (at zero reddening) is fixed, and it does not change with black hole mass[1]. On the other hand, stellar population synthesis models are much more flexible, since their shape depends on several parameters (e.g., *age*, τ, metallicity, etc.). To overcome this issue, in AGNfitter we have implemented a simple prior on the galaxy luminosity based on the galaxy luminosity function. Specifically, we considered the redshift evolution of galaxy Schechter luminosity functions. As estimated by Iovino et al. (2010, see also Kovač et al. 2010), after fitting this redshift evolution, the characteristic absolute magnitude in the B-band of the stellar population M^*_B has the following functional form:

$$M^*_B = -20.3 - 5\log(h_{70}) - 1.1 \times z. \tag{2.8}$$

M^*_B includes a redshift evolution of roughly 1 magnitude between $z = 0.1$ and $z = 1$ (see their § 4 for further details), and it represents the characteristic absolute magnitude of a galaxy at a given redshift. For each fit we computed the absolute magnitude from the galaxy template in

[1]Our BBB template is representative of an optically selected AGN population with an average black hole mass of about 5×10^8 $M_\odot$ (Richards et al. 2006a).

the B-band ($M_{\rm B,fit}$). This magnitude is then compared with the expected value from equation (2.8) at the source redshift. We set the likelihood to zero if $M_{\rm B,fit}$ is a factor of 10 times brighter than $M^*_{\rm B}$. The choice of the threshold factor is rather arbitrary (and it can be changed by the user), but it provides a simple and effective way of preventing possible degeneracies between reddened BBBs and unphysically luminous stellar populations in Type 1 AGN.

2.3.6 IGM absorption

Significant amount of effort has been devoted in determining the AGN SED in the UV (Zheng et al. 1997; Telfer et al. 2002; Scott et al. 2004; Shull et al. 2012). To estimate the *intrinsic* shape of the BBB one must take into account the intergalactic medium (IGM) absorption by neutral hydrogen along the line of sight (Stevans et al. 2014; Lusso et al. 2015; Tilton et al. 2016). Absorption from intergalactic H I, blueward of Ly α emission in the AGN rest frame, attenuates the source flux both in the Lyman series (creating the so-called H I forest), and in the Lyman continuum at rest $\lambda_{\rm r} < 912$ Å (e.g. Moller & Jakobsen 1990). Therefore, we should consider this effect while modelling AGN SEDs. To correct for the intervening Ly α forest and continuum absorption, one possibility is to employ a set of IGM transmission functions (T_λ) calibrated from multiple quasar absorption line observables (Lusso et al. 2015, see also Stevans et al. 2014; Tilton et al. 2016 for a different approach) over a wide range of redshifts. Such functions can be estimated statistically given the stochasticity of Lyman limit systems (e.g. Worseck & Prochaska 2011; Prochaska et al. 2014) and critically depends on the parametrization of the H 1 column density distribution (Madau 1995; Meiksin 2006; Inoue et al. 2014; Prochaska et al. 2014). Given that observations of the IGM are not present to constrain T_λ at all redshifts, this implementation is problematic. Although we recognise the importance of correcting broad-band photometry for IGM absorption, in order not to largely increase the model's complexity, we have been rather conservative and simply neglected all rest-frame data at wavelengths[2] shorter than 1250 Å (i.e. $\log \nu/{\rm Hz} > 15.38$).

2.4 Analysis of synthetic data

2.4.1 Synthetic SEDs

In order to test the response of AGNfitter to AGN of different obscuration properties, we construct two synthetic SEDs that mimic typical Type1 and Type2 AGN. These prototypes are built using four model templates of known input parameters. The parameter values are chosen from representative values for the AGN populations and are shown in tables in the left panel of Figure 2.2 for the Type1 AGN and of Figure 2.3 for the Type2 AGN. In the middle panels of these figures, the four model templates that correspond to those input parameter values are plotted as dashed lines of different colors, where the colors correspond to different physical components similar to Figure 2.1. The red dashed line is the total model calculated as a linear combination of these four templates. The total model SEDs are integrated against the broad band filter curves that are included in the COSMOS photometry library to produce mock photometric data points. The uncertainties in the photometry are mimicked through the addition of Gaussian random noise of a standard deviation appropriate from typical uncertainties of each band of the COSMOS photometry (see §2.5). These mock photometric data are plotted in the central and right panels as black dots with error bars.

[2]For simplicity, we have considered the effective wavelength for each photometric band, neglecting their width.

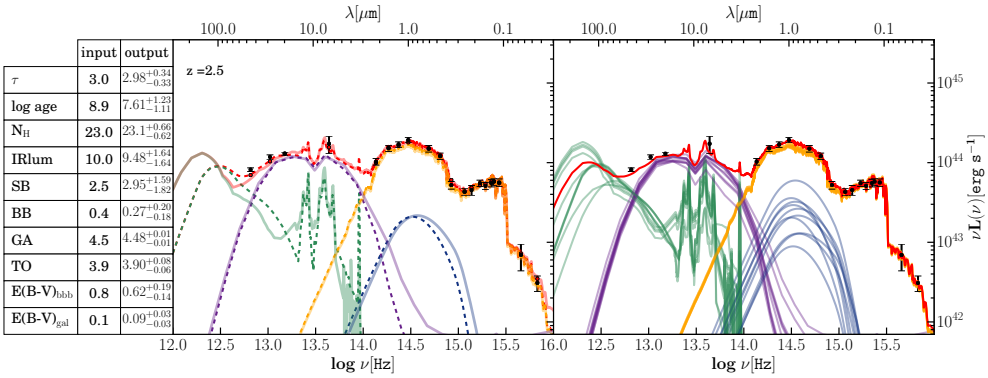

	input	output
τ	3.0	$2.98^{+0.34}_{-0.33}$
log age	8.9	$7.61^{+1.23}_{-1.11}$
N_H	23.0	$23.1^{+0.66}_{-0.62}$
IRlum	10.0	$9.48^{+1.64}_{-1.64}$
SB	2.5	$2.95^{+1.59}_{-1.82}$
BB	0.4	$0.27^{+0.20}_{-0.18}$
GA	4.5	$4.48^{+0.01}_{-0.01}$
TO	3.9	$3.90^{+0.08}_{-0.06}$
$E(B\text{-}V)_{bbb}$	0.8	$0.62^{+0.19}_{-0.14}$
$E(B\text{-}V)_{gal}$	0.1	$0.09^{+0.03}_{-0.03}$

Figure 2.3: SED output of a synthetic Type2 AGN: The colours of the component SED shapes are assigned similarly to Figure 2.1, while the linear combination of these, the 'total SED', is depicted as a red line. *The table* provides the initial input values used for the construction of the mock AGN and the median values of the parameters' PDFs resulting from the fitting with the respective 16th and 84th percentiles. For the sake of comparison, we plot the SEDs as given by the input parameter values and the output best-fit values in the *left panel*. The dashed lines are the SEDs corresponding to the input values and the solid transparent lines are the SED produced with the output best-fit parameters. In the *right panel* we randomly pick eight different realizations from the posterior PDFs and over-plot the corresponding component SEDs in order to visualize the dynamic range of the parameters values included in the PDF. The total SEDs from the realizations are constructed and the mean is depicted as a red line.

MOCK Type1 AGN

The mock Type1 AGN is constructed using the input parameter values specified in the Table of Figure 2.2 . Since the optical-UV regime of the prototypical Type1 SED is dominated by the direct accretion disk emission, we choose a reddening value of $E(B-V)_{bbb}$= 0, following the observation that Type1 AGN do not exhibit large amounts of extinction at these wavelengths (Lusso et al. (2012), Merloni et al. (2014)). As obscuring media is not abundant in Type1s, the mid-IR/sub-mm regime is mimicked by a starburst (cold dust) and a torus template (warm dust) normalized to lower luminosities. We choose these luminosities accordingly to the obscuring fraction for Type1 AGN in XMM-COSMOS, which has been observed to approximately follow the relation $L_{tor} = 0.5\times L_{bbb}$ (Lusso et al. 2013; Merloni et al. 2014). Considering the low optical depth medium observed for Type1 tori (Hatziminaoglou et al. 2008), the torus template is chosen to have the minimum column density of $\log N_H = 21.0$. The galaxy template chosen is determined by parameter values of $\tau = 3$ and $\log age = 8.4$ ($age = 0.251$ Gyrs). Because of the small stellar contribution to the total emission in Type1 AGNs, the values assumed for the *age* and τ parameters do not play a significant role in modelling the shape of the total SED. Following these conditions we have modelled the MOCK Type 1 to be a redshift 0.1 bright, unobscured QSO, with direct BBB luminosity $L_{bbb,1-0.1\mu m} = 2.0 \times 10^{46}$ erg s^{-1}and torus luminosity $L_{tor,1-40\mu m} = 1.0 \times 10^{46}$ erg s^{-1}, where these luminosities are calculated by integrating over the wavelength ranges specified in the subscripts.

MOCK Type2 AGN

The synthetic Type2 AGN is constructed following the definition that Type2s lack or have low accretion disk emission in the optical/UV, since this is obscured on nuclear scales. Therefore two properties have to be accounted for: (1) The dominant contribution to the total optical/UV luminosity is the stellar emission of the host galaxy, since the AGN contribution (BBB) is obscured. (2) The AGN emission obscured by the hot dust of the torus is reemitted in the IR, and thus the torus emission is expected to represent a large fraction of the accretion disk luminosity in a Type1 AGN (according to the AGN unified model(Antonucci 1993; Urry & Padovani 1995)).

Following condition (1), the BBB template is normalized to a lower luminosity than the Type1 example, producing a total observed luminosity of $L_{bbb-red,1-0.1\mu m} = 4.4 \times 10^{43}$ erg s^{-1}after being extincted according to a reddening parameter of $E(B-V)_{bbb} = 0.2$. If we correct for dust extinction, the mock Type 2 AGN present a dereddened BBB luminosity of $L_{bbb-dered,1-0.1\mu m} = 1.59 \times 10^{44}$ erg s^{-1}. The dominant contribution of the stellar emission is chosen to be $L_{gal,1-0.1\mu m} = 1.9 \times 10^{44}$ erg s^{-1}corresponding to $\sim 81\%$ of the total optical/UV contribution. The host galaxy chosen for the mock Type 2 is a galaxy of regular stellar mass $M_* = 5.77 \times 10^{10} M_\odot$, intermediate age ($\log\ age = 8.9, age = 0.79$ Gyrs) and following an exponential SFH with $\tau = 3.0$.

Following condition (2), we model the mock Type 2 torus emission to have the luminosity $L_{tor,1-40\mu m} = 7.0 \times 10^{43}$ erg s^{-1}, which corresponds to about 52% of the total MIR luminosity. The chosen template represents a torus of large column density ($\log N_H = 23$), which includes dust self-absorption, meaning that the emission from the inner, hotter part of the torus, emitting at shorter wavelength is highly absorbed (eg. Silva et al. (1998), Hatziminaoglou et al. (2008)).

Following these conditions, we have modelled the mock Type2 AGN as a redshift z = 2.5 obscured active galaxy, with an intrinsic luminosity corresponding to $L_{bbb-dered,1-0.1\mu m} = 1.59 \times 10^{44}$ erg s^{-1}.

2.4.2 Recovery of parameters

After running the code, the comparison between the columns in the tables of Figure 2.2 and Figure 2.3 shows a close agreement between the input and output values of the fitting parameters within the uncertainty ranges. This shows clearly the capability of AGNfitter in recovering accurate parameter values as well as error estimates which encompasses both the noise of the data and the degeneracies among the model parameters.

This can also be seen visually in the middle panels of Figures 2.2 and 2.3 where the dashed lines represent the input SEDs used to create the synthetic data points and the solid lines represent the output best-fit SEDs. As shown here, both curves overlap almost completely, showing excellent agreement between the input and output SEDs. Here, we have chosen to plot the best-fit result as output SED, which is the SED given by the output parameter values of highest likelihood. This result is comparable to the output obtained through other customary SED-fitting tools that use the χ^2-minimization method. In both examples of Figures 2.2 and 2.3 the best fit solution recovers almost perfectly the input SED shape of each AGN model component.

2.4.3 Posterior PDFs

One of the primary quality assessments products of the algorithm are the PDFs of the fitting parameters. These are summarized in the PDF-triangle of each source and contain a wealth of

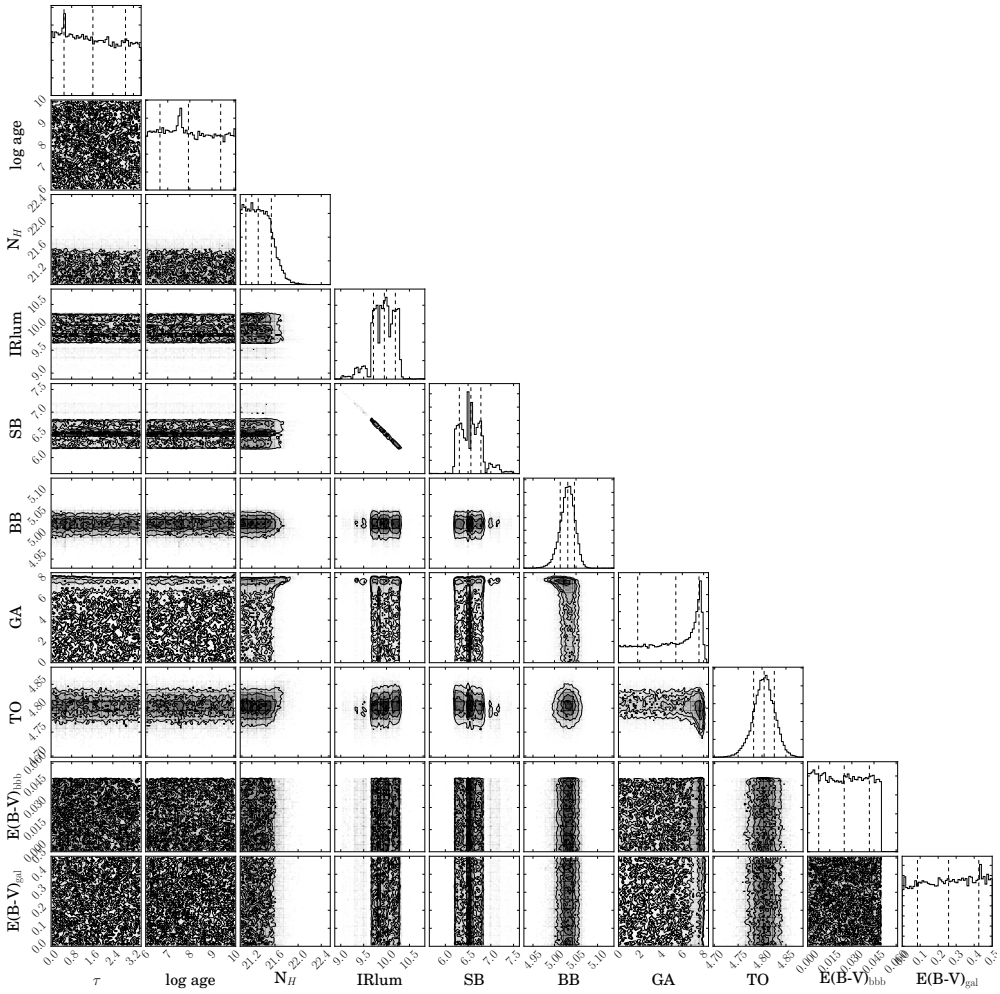

Figure 2.4: PDF triangle of the synthetic Type 1 AGN shown in Figure 2.2: 1- and 2 dimensional PDFs of the components of the parameter space explored by AGNfitter. The outer part of the triangle shows the 1-dimensional PDFs for each parameter as histograms. The lines indicate the medium and 1 σ uncertainties. The inner part of the triangle shows the 2-dimensional PDFs for pairs of parameters as contours. The different contours shades represent the 0.5, 1, 1.5 and 2 σ.

information on the parameter dependencies.

In Figure 2.4 the PDF triangle produced from the fitting of the synthetic Type1 AGN is presented as an example. One-dimensional and two-dimensional PDFs of all parameters are depicted in the border and interior parts of the diagram, respectively. The median value (50th percentile) and 16th and 84th percentiles of the PDF are reported by the dashed black lines. The two-dimensional PDFs are shown as probability surfaces, with contours corresponding to 38th, 68th, 88th and 95th percentiles (equivalent to 0.5, 1, 1.5 and 2 σ for Gaussian distributions).

The shapes of the 1-D and 2-D PDFs are a good indicator of the quality of the inference of a given parameter and hints to the existence of covariances among parameters. As can be noticed for the mock Type1 AGN in Figure 2.2, parameters associated with the galaxy contribution (τ, *age*, GA, E(B-V)$_{\rm gal}$) have very noisy and nearly flat PDFs. This is a consequence of the lack of recognisable galaxy features in the total SED of a Type1 AGN (total SED: red line in 2.2) and thus, the stellar properties cannot be very accurately constrained. Nonetheless an upper limit for the normalisation parameter of this template (parameter GA) is well defined and a maximum contribution to the total luminosity can be infered. Parameters determining the AGN contributions ($\log {\rm N_H}$, BB, TO, E(B − V)) on the contrary show more defined posterior distributions and the resulting parameter values, as given by the percentiles, present smaller uncertainties.

As mentioned before, we interpolate between discrete model templates using Nearest-Neighbor interpolations in order to have a continuous parameter space. This has also an effect on the 1-dimensional PDFs of discrete parameters (in this example IRlum and E(B-V)$_{\rm bbb}$ in Figure 2.4), which sometimes show abrupt cut-offs on the regions outside the nearest neighborhoods of the discrete values chosen (in this example: IRlum = 10 and E(B − V)$_{\rm bbb}$ = 0).

The 2-dimensional PDF allows the recognition of covariances of the parameters. This can be clearly observed for instance in Figure 2.4 for the parameters IRlum and SB. This strong covariance between these parameters occurs by construction, since as explained in § 2.2.4 both the parameters SB and IRlum are normalization parameters of the same model. While SB is a normalization parameter introduced in AGNfitter, IRlum was predefined by the authors of the models to parametrize the SED shapes of the cold dust library based on their total luminosities.

Similarly, complex shaped 2D posterior distributions can result from non-linear dependencies on model parameters. As an example, Figure 2.5 presents the PDF triangle of the integrated luminosities of the synthetic Type2 AGN. The 2D posterior of the integrated luminosities $L_{\rm bbb,\ 0.1-1\ \mu m}$ and $L_{\rm gal,\ 0.1-1\ \mu m}$ show slightly twisted banana shaped contours, revealing that the estimation of the two parameters are degenerate. This can be easily understood observing the physical components from which these luminosities are computed in the right panel of Figure 2.3. Even though the galaxy templates dominates the SED, both the reddened BBB and the galaxy template peak around 1μm, such that both can contribute to the observed SED around this wavelength. This naturally results in a slight degeneracy in their respective integrated luminosities. See §2.4.6 for a more detailed description of the SED plot.

One of the main advantages in estimating the parameters' PDFs is that robust uncertainties on the parameter inference can be now calculated. As describe above, AGNfitter estimates credible intervals from the PDFs (50th, 16th and 84th percentiles). Following our Bayesian approach we quote only these uncertainty values from now on in this paper. If requested by the user, AGNfitter returns as well the best-fit values for the parameters, which should be the one with the highest likelihood computed in the chain in the case of convergence. Nonetheless, if the posterior distribution inferred by the sampling is not symmetric, the best fit value will differ from the median value.

All in all, the true values used for the construction of the mock Type-1 and Type-2 AGN are robustly recovered by the median values and uncertainties of the parameters posteriors estimated by AGNfitter.

2.4.4 Integrated luminosities

Integrated luminosities are estimated in order to probe the total power produced by a given radiative process. AGNfitter presents a set of functions, which can be easily adjusted by the user to obtain the preferred integration ranges. In the default version of AGNfitter we calculate four integrated luminosities over frequency ranges, which are key to the decomposition of host galaxy/AGN contributions ($L_{\rm bbb}, L_{\rm gal}, L_{\rm sb}, L_{\rm tor}$), as well as two integrated luminosities which can be converted to key parameters for the physical description of the sources ($L_{\rm bol}$, $L_{\rm IR}$). Consistent with our Bayesian approach, AGNfitter computes the total posterior PDFs of the integrated luminosities and returns their median values and percentiles as representative values. Since integration algorithms are computationally expensive, the chains can be additionally 'thinned' (e.g. by a factor k), which means we discard all but every k-th observation with the goal of reducing the computational time.

$L_{\rm bbb,\ 0.1-1\ \mu m}$, $L_{\rm gal,\ 0.1-1\ \mu m}$: We calculate the integrated accretion disk luminosity (BBB) and the integrated host galaxy emission in the frequency range from 0.1-1 μm, in the $\log\nu$ - $\log(\nu L_\nu)$ frame. This interval is chosen due to the simultaneous emission of AGN and host galaxy, which allows the study of their relative contribution.

$L_{\rm tor,\ 1-40\ \mu m}$, $L_{\rm sb,\ 1-40\mu m}$: Several studies have shown that the mid-infrared regime offers a good laboratory for the study of the ratio of AGN and galaxy contribution to total luminosity (e.g. Lacy et al. 2004; Stern et al. 2005; Donley et al. 2012; Ciesla et al. 2015). AGNfitter computes MIR-luminosities for both the torus and cold dust (starburst) emission components integrating within the relevant wavelength range ($1-40\mu$m).

$L_{\rm bol,\ 0.1\mu m-1KeV}$: An important probe for the intrinsic power of an AGN is its bolometric luminosity, which we calculate integrating the rest-frame AGN direct emission (BBB) within the frequency interval from 0.1 μm - 1 keV , in the $\log\nu$ - $\log(\nu L_\nu)$ frame. We only consider the BBB template and omit the torus template for the integration, since nearly all photons emitted at infrared wavelengths are reprocessed optical/UV/soft X-ray photons emitted into other directions and re-radiated isotropically. Thus, adding the torus emission to the $L_{\rm bbb}$ calculation would amount to double counting these contributions to the luminosity (e.g. Marconi et al. (2004); Lusso et al. (2012)). The X-ray emission would also contribute ~20% to the total bolometric budget but we omit this contribution since the fitting of X-ray data is not currently implemented in AGNfitter.

$L_{\rm IR,\ 8-1000\ \mu m}$: After correcting for any torus contamination, the 8-1000 μm luminosity is calculated integrating the cold dust emission (starburst component emission). This infrared luminosity is used to estimate the $\rm SFR_{FIR}$ as explained in detail in §2.4.5.

2.4.5 Host galaxy properties

AGNfitter estimates galaxy properties such as stellar masses and star formation rates (SFR) and calculates the total posterior PDFs for these parameters. As before, the median values and uncertainties (16th and 84th percentiles) are given as representative values. The total stellar masses are computed from the masses of the single stellar population (SSP) that determine each galaxy template. The normalization of the templates give us a constraint about the number of SSPs and in turn the total stellar mass producing the galactic optical emission.

AGNfitter makes two independent SFR diagnoses both in the optical/UV and the far-infrared (FIR). In the optical regime, the normalization log parameter for the galaxy, *GA*,

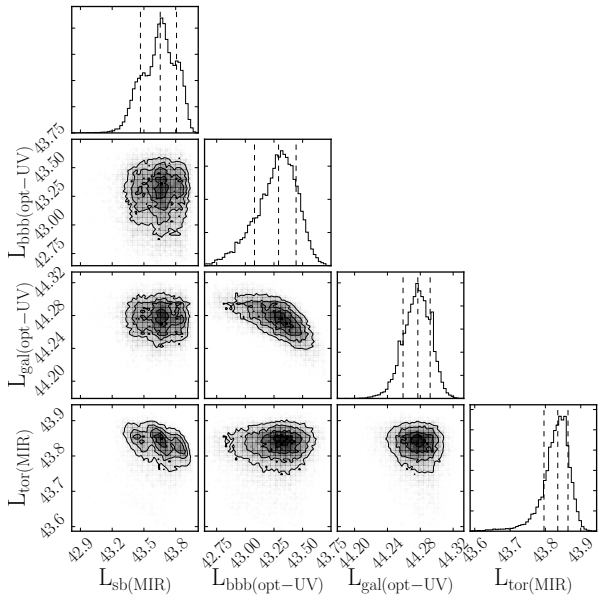

Figure 2.5: PDF triangle of the synthetic Type2 AGN shown in Figure 2.3: 1- and 2 dimensional PDFs of the default AGNfitter output on integrated luminosities is presented. The outer part of the triangle shows the 1-dimensional PDFs for each parameter as histograms. The lines indicate the medium and 1 σ uncertainties. The inner part of the triangle shows the 2-dimensional PDFs for pairs of parameters as contours. The different contours shades represent the 0.5, 1, 1.5 and 2 σ. The 2D relative posterior of the integrated luminosities $L_{\mathrm{bbb,\ 0.1-1\ \mu m}}$ and $L_{\mathrm{gal,\ 0.1-1\ \mu m}}$ show slightly twisted banana shaped contours, revealing that the estimation of the two parameters are degenerate.

permits to scale the emission of the generic galaxy template to the total emission needed for the fit. With the inferred total stellar mass and taking into account the age and the timescale of star formation history of the stellar populations (τ), we can calculate the star formation rates according to:

$$\left(\frac{\mathrm{SFR_{opt/UV}}}{M_{\odot} yr^{-1}}\right) = 10^{\mathrm{GA}} \times \left(\frac{M_{*\mathrm{sp}}}{M_{\odot}}\right) \times \left(\frac{\exp(-age/\tau)}{\tau\ yr^{-1}}\right), \tag{2.9}$$

where $M_{*\mathrm{sp}}$ is the mass of the stellar population.

The total FIR emission provides a different measurement of the SFR since it proves the emission of star forming regions reprocessed by dust grains in their surroundings. This estimation is of special relevance at redshifts $1 \leq z \leq 3$, where the highest star-formation rate galaxies appear to be dominated by dusty starbursts with high infrared luminosities (Chary & Elbaz (2001), Bouwens et al. (2009)). In order to derive the SFR from the starburst model component that dominates the FIR, we use the calibration derived in Murphy et al. (2011) for the total infrared wavelength range (8-1000 μm),

$$\left(\frac{\mathrm{SFR_{IR}}}{M_{\odot} yr^{-1}}\right) = 3.88 \times 10^{-44} \left(\frac{\mathrm{L_{IR}}}{\mathrm{erg\ s^{-1}}}\right). \tag{2.10}$$

Here, L_{IR} is the luminosity integrated over the starburst template in the wavelength range noted above, after a proper substraction of the AGN torus contribution from the total IR luminosity.

AGNfitter does not include the assumption of energy balance between the direct stellar emission in the optical and the reprocessed emission by cold and warm dust in the IR. This is chosen consciously in order to prevent mixing-up possible data uncertainties of the optical and the FIR. Both components are thus computed independently and this allows to test the power of each wavelength regime in tracing the SFR. A good agreement between both diagnoses is expected, although the far-infrared SFR tracer is highly dependent on the availability of good FIR data. In the cases where the data set does not contain enough FIR detections the MIR

emission is associated entirely to the torus component. In this way, the starburst emission, and consequently the SFR_{FIR}, are highly underestimated showing no agreement with the optical tracer.

2.4.6 Spectral energy distributions

The probabilistic approach of AGNfitter can be better visualized through the plotting of several different SED realizations, constructed from values randomly picked from the full posterior PDFs of the parameters. In the right panels of Figures 2.2 and 2.3, a representative number of SED realizations are shown simultaneously to exemplify the dynamic range of individual template models and total SEDs contained in the probability distributions. The number of displayed realizations is 8 by default but can be freely chosen by the user. Each realization comprises a set of five lines of different colors; one red line that represents the total SED as the linear combination of the physical components, and four lines of different colors, which correspond to the different physical components, following the color coding of Figure 2.1. Through the variety of SED shapes among single components it is easy to recognize which components are described by parameters with larger uncertainties. This is clear from the output-SED fitted for the mock Type2 AGN in Figure 2.3. There the BBB SED appears to be subject to large uncertainties due to a degeneracy among parameters determining the BBB amplitude (BB) and shape (altered by extinction parameter $E(B-V)_{bbb}$) and the galaxy normalization parameter. Similarly, the parameters determining the starburst template and torus appear to be slightly degenerate producing a large dynamic range of SED shapes for these components. The degeneracy among these parameters was discussed previously in the context of Figure 2.5, where the 2D-PDFs of the parameters for the same source were introduced. The visualization of different SED shapes from PDF realizations stresses the relevance of a careful consideration of the parameter uncertainties with the aim of a proper physical interpretation of the SED decomposition.

2.5 A test sample: XMM–COSMOS

AGNfitter is a multi-purpose SED fitting tool. It can be applied to different kinds of sources such as quiescent or starburst galaxies, as well as AGN/quasars, given a source redshift and photometric data. In the rest of this paper, we test the performances of AGNfitter by applying it to both obscured and unobscured X-ray selected AGN from the XMM–COSMOS survey, taking advantage of the unique multiwavelength coverage of the COSMOS field (Scoville et al. 2007).

The XMM-COSMOS catalog comprises 1822 point-like X-ray sources detected by XMM-*Newton* over an area of $\sim 2\,\mathrm{deg}^2$ for a total of ~ 1.5 Ms at a fairly homogeneous depth of ~ 50 ks (Hasinger et al. 2007, Cappelluti et al. 2009). All the details about the catalog are reported in Brusa et al. (2010). We consider in this analysis 1577 X–ray selected sources for which a reliable optical counterpart can be associated (see discussion in Brusa et al. 2010, Table 1) and we restrict our sample to sources in the catalog with secure spectroscopic redshifts. [3].

[3]The multi–wavelength XMM–COSMOS catalog can be retrieved from: http://www.mpe.mpg.de/XMMCosmos/xmm53 _release/, version 1st November 2011. This is an updated release of the catalog already published by Brusa et al. (2010).

2.5.1 Type1 and Type2 AGN samples

For the Type-1 AGN sample we have selected 1375 X–ray sources detected in the [0.5-2] keV band at a flux larger than 5×10^{-16} erg s−1 cm^{-2} (see Brusa et al. 2010). In this study we consider 426 objects from this sample that are spectroscopically classified as broad-line AGN on the basis of broad emission lines (FWHM > 2000 km s^{-1}) in their optical spectra (see Lilly et al. 2007; Trump et al. 2009). The origin of spectroscopic redshifts for the 426 sources is as follows: 118 objects from the SDSS archive (Adelman-McCarthy & et al. 2005; Kauffmann et al. 2003), 55 from MMT observations (Prescott et al. 2006), 66 from the IMACS observation campaign (Trump et al. 2007), 130 from the zCOSMOS bright 20k sample, 49 from the zCOSMOS faint catalog (see Lilly et al. 2007), and 8 from individual Keck runs (Brusa et al. 2010). For a detailed description of the sample properties see Elvis et al. (2012) and Hao et al. (2012).

To select an obscured AGN sample we have instead considered [2-10] keV detected objects in the XMM–COSMOS catalog having fluxes larger than 3×10^{-15} erg s^{-1} cm^{-2} (971 sources). From this sample we selected 288 AGN with spectroscopic redshift and optical spectra lacking broad emission lines (i.e. FWHM<2000 km s^{-1}): 259 are objects with either spectrally unresolved, high-ionization emission lines, exhibiting line ratios indicating AGN activity, or not detected high-ionization lines, where the observed spectral range does not allow to construct line diagnostics (Brusa et al. 2010). Not all AGN selected via this criterion show emission lines, e.g. 29 are classified absorption-line galaxies, i.e., sources consistent with a typical galaxy spectrum showing only absorption lines. Further details on the obscured AGN sample and on their properties are given by Lusso et al. (2012)

Altogether, the sample used for testing the capabilities of AGNfitter consists on 714 X–ray selected active galaxies optically classified into 426 Type1 and 288 Type2 AGN. Due to Malmquist bias and owing to the different selection criteria, the redshift distributions of the two population are considerably different, so that Type1 AGN cover a redshift range between $0.10 < z < 4.26$ ($\langle z_{T1} \rangle = 1.64$) while Type2s present redshifts in the range $0.05 < z < 3.52$ ($\langle z_{T2} \rangle = 0.85$).

2.5.2 Multi-wavelength coverage

The catalog includes multi-wavelength data from far-infrared to hard X-rays: *Herschel* data at 160 μm and 100 μm (Lutz et al. 2011), 70 μm and 24 μm MIPS GO3 data (Le Floc'h et al. 2009), IRAC flux densities (Ilbert et al. 2010), near-infrared J UKIRT (Capak et al. 2008), H-band (McCracken et al. 2010), CFHT/K-band data (McCracken et al. 2008), optical multiband photometry (SDSS, Subaru, Capak et al. 2007), and near- and far-ultraviolet bands with GALEX (Zamojski et al. 2007). The observations in the optical-UV and near-infrared bands are not simultaneous, as they span a time interval of about 5 years: 2001 (SDSS), 2004 (Subaru and CFHT) and 2006 (IRAC). In order to reduce possible variability effects, we have selected the bands closest in time to the IRAC observations (i.e., we excluded SDSS data, that in any case are less deep than other data available in similar bands).

Galactic reddening has been taken into account: we used the selective attenuation of the stellar continuum $k(\lambda)$ taken from Table 11 of Capak et al. (2007). Galactic extinction is estimated from Schlegel et al. (1998) for each object.

2.5.3 Treatment of upper limits

The COSMOS photometric catalogs do not provide forced photometry at the location of a source in the bands for which the object flux lies below the formal detection limit. Instead,

only upper limits are reported. These upper limits can nevertheless be highly informative, and place important constraints on model parameters, but we must consider how to implement these upper limits into our Gaussian likelihood. The correct approach would obviously be to perform forced photometry in all bands where a formal detection is not provided (Lang et al. 2014), which would give us a measurement and an error, with a large error reflecting the fact that the measurement (a marginal or non-detection) is very noisy. However, adding forced photometry to the entire XMM–COSMOS AGN sample is beyond the scope of the present work, hence we adopt the following crude approximation which nevertheless allows us to incorporate the information provided by the COSMOS upper limits. For non-detections, where the COSMOS catalog reports 5σ flux upper limits (F_+), AGNfitter creates a fictitious data point at a flux level of $0.5F_+$, and a fictitious symmetric error bar of $\pm(0.5F_+)$. In this way, upper limits can be trivially incorporated into our Gaussian likelihood in equation 4. Because our "upper limit" region spans from zero to F_+, this approach allows our MCMC sampling to accept all models with fluxes lying between zero and the upper limit ones. The inclusion of upper/lower limits in this fashion is necessary, since the information they provide can be very helpful for constraining the likelihood of some models.

2.6 Results and discussion on the test sample

2.6.1 Spectral energy distributions for Type1 and Type2 AGN

In this section we discuss general properties within the Type1 and Type2 AGN populations from an SED perspective. In Figure 2.6 we present some examples of SED fitting for Type1 AGN having low levels of extinction in the optical-UV ($E(B-V)_{bbb} < 0.2$). To visualize the dynamic range of the parameter values included in the PDF, we randomly pick eight different realizations from the posterior PDFs of each corresponding component SEDs. Since the AGN sample we considered in our analysis is selected in the X-rays, it is less prone to be biased in the optical. This gives us the opportunity to test AGNfitter over a wider variety of AGN/galaxy contributions than optically selected ones.

XID=21 and 5257 are good examples of how an AGN SED looks like in the case of both low-reddening and low-host galaxy contamination. Overall, 58% (248/426) of the total Type1 AGN sample have $E(B-V)_{bbb} \lesssim 0.2$. The BBB and the torus properties for these objects are nicely constrained and a clear dip at 1μm is visible, marking the division between hot-dust and accretion disc emission, consistent with what it is typically found in optically selected AGN samples (Elvis et al. 1994; Richards et al. 2006a; Shang et al. 2011). On the other hand, for these sources the fits to the the host galaxy and cold-dust components are not very informative. For the former this is because the AGN significantly outshines its host, whereas the latter is simply due to a lack of FIR detections.

There are also cases for which, although the BBB emission is significant ($L_{bbb,dered} > 10^{45}$ erg s^{-1}), the galaxy contribution at $\sim 1\mu$m is not completely negligible, making the overall shape of the AGN rather flat over several decades in frequency (see XID=21, 52, and 5081 as examples). As the BBB luminosity of the source decreases ($L_{bbb,dered} \simeq 10^{44-45}$ erg s^{-1}), even for cases with low BBB reddening, some sources require a significant galaxy contribution at $\sim 1\mu$m (e.g. XID=13, 53283, and 54513). About 75% of the sample have a contribution of the host galaxy of about 50% or more at 1μm. The lack of a 1μm inflection point in the SED between the UV and near-IR bumps (i.e. a conspicuous host galaxy contribution) is a common feature of X–ray selected AGN samples, since these usually contain fainter AGN for which the contrast to galaxy emission is lower (Elvis et al. 2012; Hao et al. 2014).

Figure 2.7 presents some examples of Type1s with significant amount of reddening in the

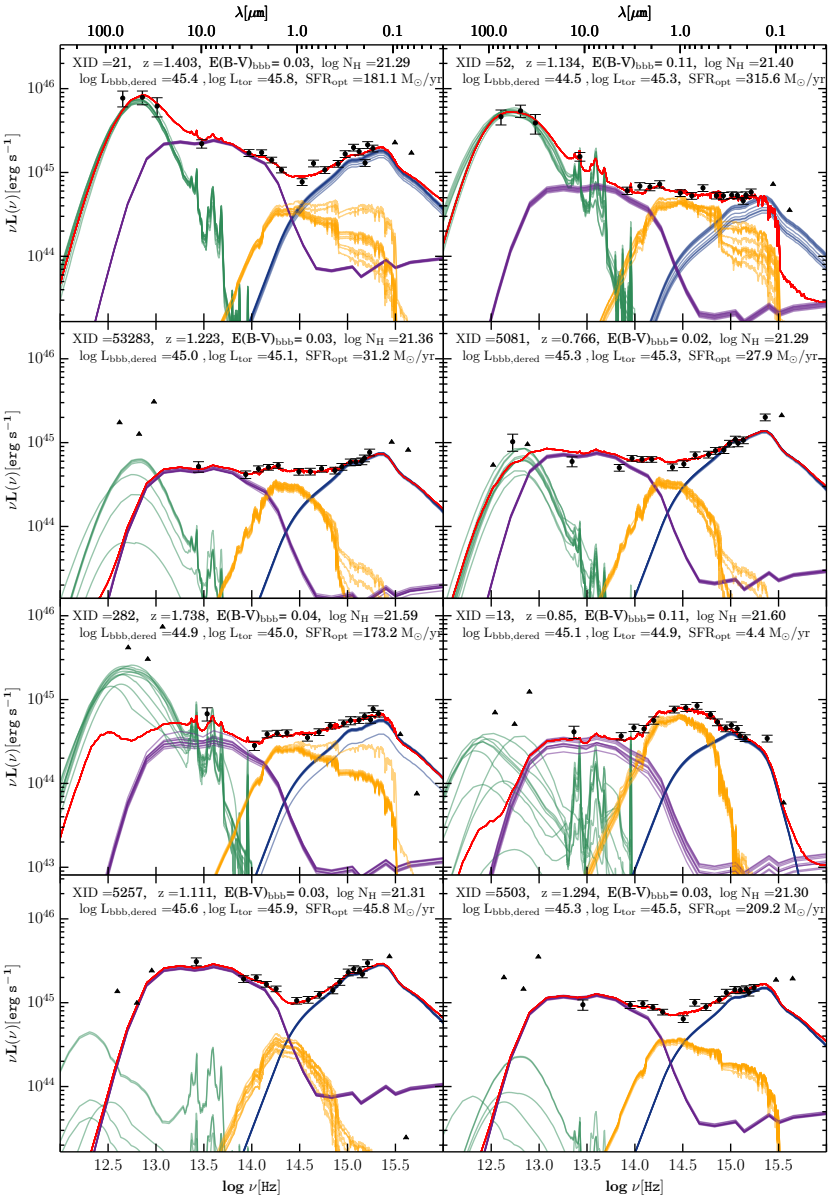

Figure 2.6: Example SEDs for Type 1 AGNs: Photometric detections are plotted against rest-frame wavelengths/frequencies as circular markers with error bars, while non-detections are represented as triangles. SED shapes of the physical components are presented as solid lines with colours assigned similarly to Figure 2.1, while the linear combination of these, the 'total SED', is depicted as a red line. We pick 8 different realizations from the parameter posterior probability distributions and over-plot these SEDs in order to visualize the effect of the parameters' uncertainties on the SEDS.

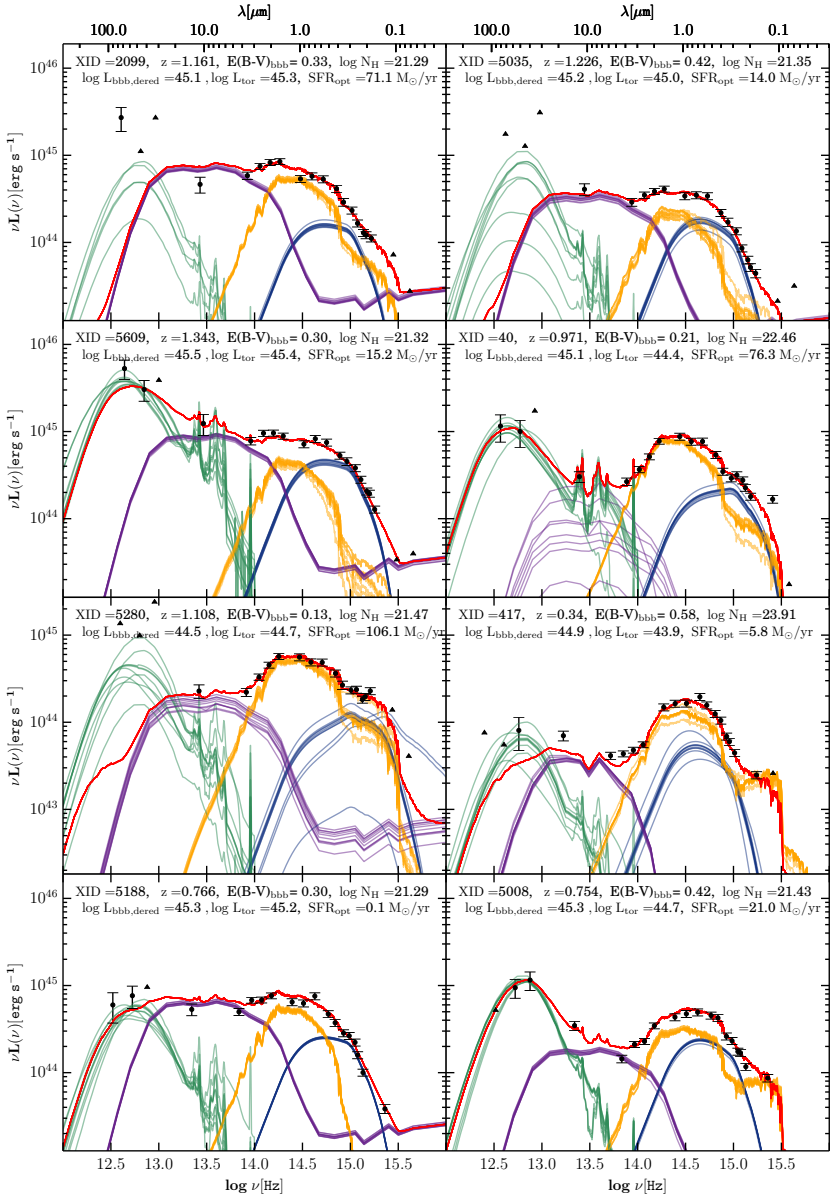

Figure 2.7: Example SEDs for reddened Type 1 AGNs: Photometric detections are plotted against rest-frame wavelengths/frequencies as circular markers with error bars, while non-detections are represented as triangles. SED shapes of the physical components are presented as solid lines with colours assigned similarly to Figure 2.1, while the linear combination of these, the 'total SED', is depicted as a red line. We pick 8 different realizations from the parameter posterior probability distributions and over-plot these SEDs in order to visualize the effect of the parameters' uncertainties on the SEDS.

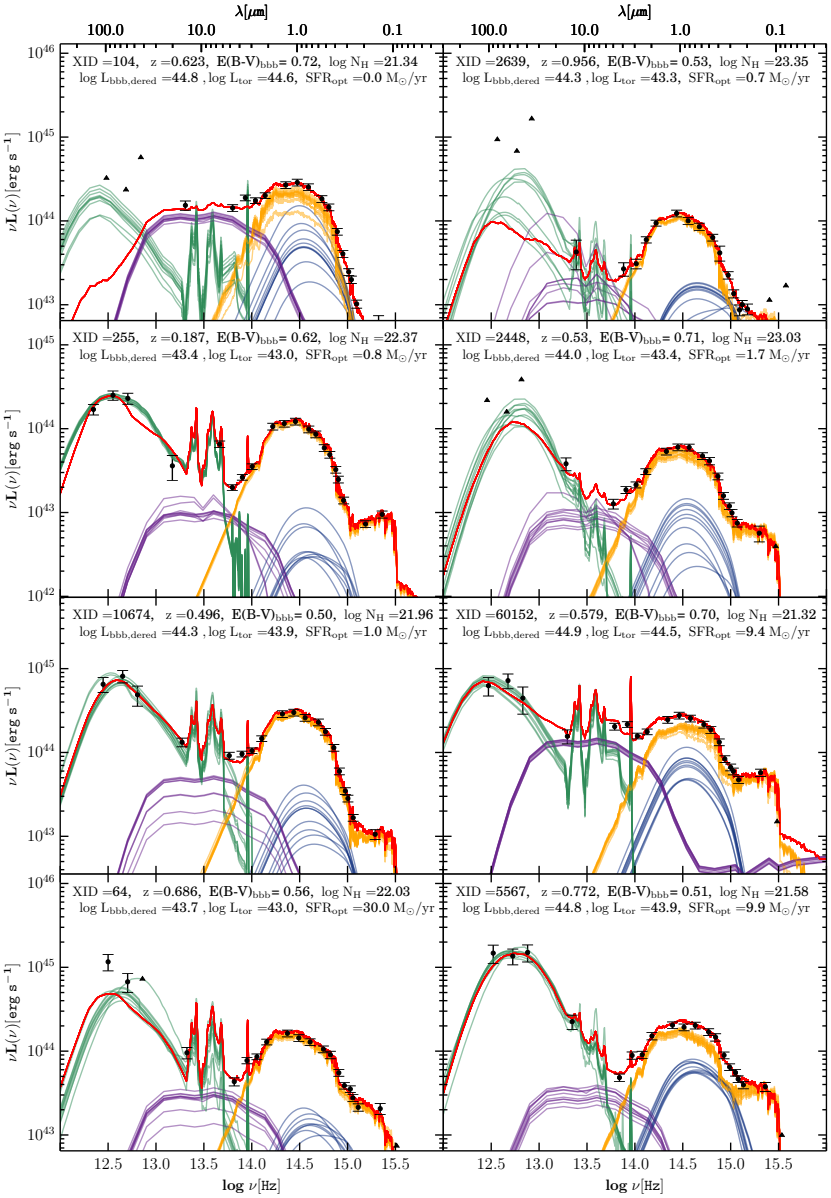

Figure 2.8: Example SEDs for Type 2 AGNs: Photometric detections are plotted against rest-frame wavelengths/frequencies as circular markers with error bars, while non-detections are represented as triangles. SED shapes of the physical components are presented as solid lines with colours assigned similarly to Figure 2.1, while the linear combination of these, the 'total SED', is depicted as a red line. We pick 8 different realizations from the parameter posterior probability distributions and over-plot these SEDs in order to visualize the effect of the parameters' uncertainties on the SEDS.

optical-UV ($E(B-V)_{bbb} \gtrsim 0.2$; about 42% of the Type1 AGN sample). The SEDs of such sources (e.g. XID=2099, 5035, 5609, and 40) are characterised by a sharp decline of the BBB in the optical-UV ($\lambda \sim 0.5 - 0.2\mu$m), and they can be considered AGN of intermediate-type (∼1.5 to 1.9). Objects with appreciable reddening still show degeneracy between BBB and the host-galaxy, despite our implementation of a prior on the maximum galaxy luminosity allowed at a given redshift. The BBB of a moderately reddened Type 1 AGN can also be equivalently modelled with a bright galaxy having very young stellar ages and a BBB with high reddening values (e.g. see XID= 417, 5280 in Figure 2.7 as examples), and as expected this degeneracy is even more pronounced in the case of low-luminosity AGN ($L_{bol} \sim 10^{44}$ erg s^{-1}). To break this degeneracy, an independent measurement of the host galaxy emission is needed, although it is not trivial to estimate for unobscured AGNs. One possibility is either to increase the threshold defining the characteristic galaxy luminosity (as discussed in § 2.3.5), and/or to include spectral information. For example, high H α/H β ratio ($\gg 3$) indicates high reddening.

Regarding mid-IR properties , Type1s are preferentially fitted with torus templates corresponding to an obscuring media of considerably low hydrogen column densities ($\log N_H < 22$). A quantitative study of the obscuration properties of this sub-sample is given in §2.6.3.

Figure 2.8 shows eight examples of SEDs for spectroscopically classified Type2s. Type2 AGN SEDs are dominated by the host galaxy emission at 0.5–2μm, while the BBB component is obviously more difficult to constrain, spanning a wider dynamic range than in the Type1 cases. Type2s are also characterised by high BBB reddening values (91% have $E(B-V)_{bbb} \gtrsim 0.2$), as well as large column densities of the torus component. Obscuration properties will be discussed in detail in § 2.6.3. Overall, the optical-UV portion of the Type-2 SEDs is very well fitted by stellar emission, with negligible contribution of the BBB. We also point out that the near-infrared emission at 10-20μm might be contaminated by emission features due to the stochastic heating of polycyclic aromatic hydrocarbon (PAH) molecules or carbon grains (e.g. Flagey et al. 2006). These features are associated with massive star-forming regions at much lower dust temperature (T<100 K). PAHs can be non negligible in obscured AGN and give rise to possible degeneracies with the torus emission produced by dust at pc scale. Such degeneracies may be solved by including priors on the cold-dust/torus emission which take into account the near-IR spectral information if available (e.g. line ratios, silicate absorption feature at 9.7 μm).

It is reasonable to ask whether the physical properties inferred by AGNfitter allow us to robustly distinguish between unobscured and obscured AGN. In the following discussion, we will use the obscuration properties inferred by AGNfitter to re-classify the total sample into Type1s and Type2s and we will compare our classification to the spectroscopic one available in XMM–COSMOS.

2.6.2 Physical parameters

Figure 2.9 present the output of AGNfitter on physical parameters for the total XMM–COSMOS AGN sample. As shown here, AGNfitter delivers vast information about integrated AGN luminosities, properties of the host galaxies and obscuration parameters. The large number of inferred properties can motivate a variety of science-cases related to AGN.

Figure 2.9 shows the parameter PDFs for the total Type1 (blue histograms) and Type2 AGN populations (orange histograms). These histograms were constructed sampling 500 random draws from each source's posterior PDF. Distinct from previous work, our treatment thus enables a proper inclusion of the parameter uncertainties in the histograms, allowing a fully probabilistic study of the global properties of the two populations under the consideration, and other inference effects which may shape the observed parameter PDFs.

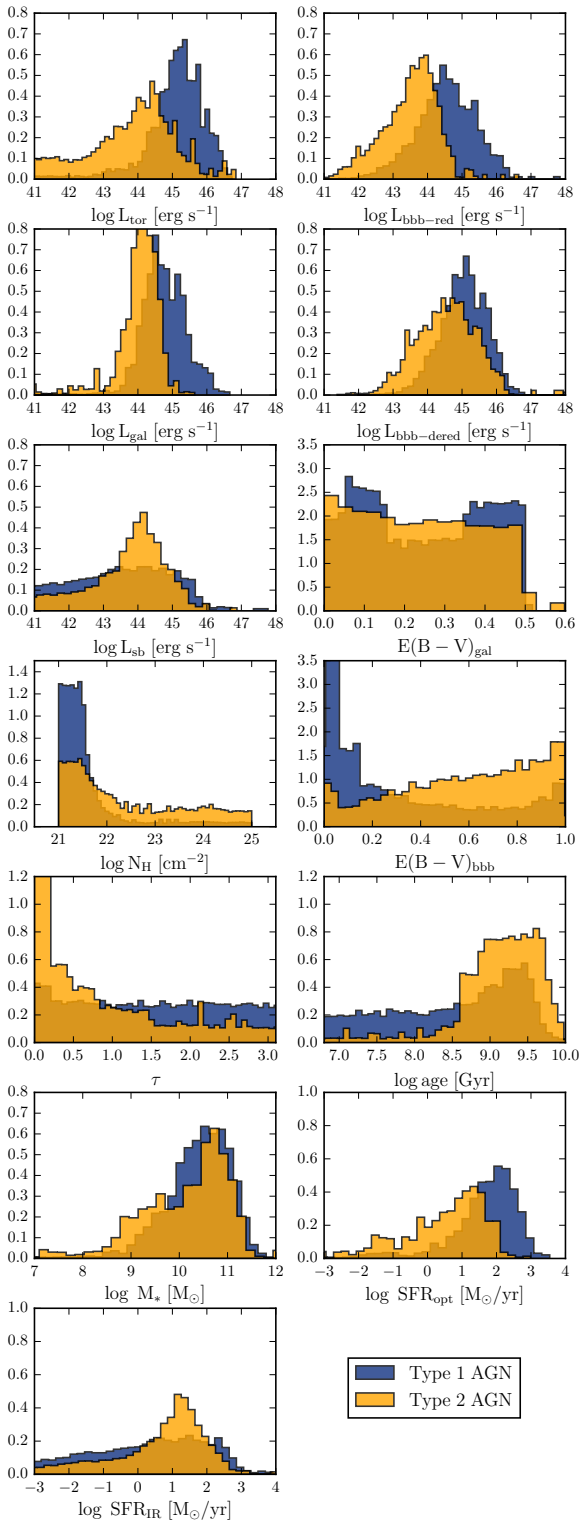

Figure 2.9: Distribution of the output parameters for the whole Type1 (blue histrogram) and Type 2 (orange histogram) AGN population. These histograms were constructed sampling 500 random draws from each source's PDFs of each parameter.

The upper four histograms of Figure 2.9 show the integrated luminosity distributions of Type1s and Type2s for $\log L_{tor}$, $\log L_{bbb-dered}$, $\log L_{gal}$, and $\log L_{bbb-red}$. On average, Type1s appear to be more luminous than Type2s in all the four parameters, but this is clearly a selection effect as the average redshifts probed by these two samples are different, i.e. Type1s are on average observed at higher redshift than Type2s (see §2.5). For instance, the $\log L_{tor}$ median values for Type1 AGN are on average over an order of magnitude higher ($45.20^{+0.61}_{-0.75}$) than those for Type2s ($44.01^{+0.98}_{-0.92}$).

The distribution of $L_{bbb-red}$ for Type1 AGN has a median value of $\log L_{bbb-red} = 44.55^{+0.83}_{-0.83}$ (the quoted uncertainties represent the 16th and the 84th percentiles of the distribution), while the median value for Type2s is $\log L_{bbb-red} = 43.59^{+0.62}_{-0.57}$, with a long tail to low BBB luminosities. Once we correct for extinction, the two $\log L_{bbb-dered}$ distributions nearly overlap within the uncertainties centered on similar median luminosity ranges: $45.08^{+0.65}_{-0.68}$ and $44.56^{+0.86}_{-0.61}$ for Type1s and Type2s, respectively, consistent with previous analysis on X–ray selected AGN samples (Lusso et al. 2011, 2012; Bongiorno et al. 2012; Lusso et al. 2013). 58% of the Type1 AGN appear to have relatively low levels of extinction ($E(B-V)_{bbb} < 0.2$), while the majority of Type2s exhibit significant reddening (91% with $E(B-V)_{bbb} \geq 0.2$), meaning a more appreciable reddening correction for the latter with respect to the Type1s. As a result, the shift of the $\log L_{bbb-dered}$ distribution for Type2s to higher values is more pronounced than for Type1s. AGN obscuration properties related to the hydrogen column density parameter N_H will be further discussed in § 2.6.3.

On the other hand, the starburst luminosities ($\log L_{sb,1-40\ \mu m}$) show a rather flat and uninformative distribution for Type1 AGN with respect to Type2s. A similar result is obtained for the FIR star-formation rates (SFR_{IR}) (which are derived from the total infrared emission $L_{IR,\ 8-1000\ \mu m}$). This is mainly due to the higher fraction of Herschel non-detections in the Type1 AGN with respect to the obscured AGN population. Only ∼10% of Type1 AGN are detected at both 100 and 160 μm, while Type2s have a detection fraction about 3 times higher (whereas at 70 μm, ∼ 8% and 15% of Type1 and Type2 are detected respectively). We find that the median L_{sb} luminosities and star-formation rates for Type2 AGN are $\log\ L_{sb} = 43.80^{+0.85}_{-1.14}$ and $\log\ SFR_{IR} = 0.95^{+0.82}_{-1.12}$, in agreement with previous analysis (Lusso et al. 2011; Bongiorno et al. 2012). We conclude that at least one detection in FIR bands is essential for any analysis of the cold dust properties of the galaxy. Such a study will be presented for a sample of optically selected AGN and quiescent galaxies in a forthcoming paper (Calistro Rivera et al. in preparation).

Previous studies found X–ray selected AGN to reside preferentially in massive ($M_* > 10^{10} M_\odot$) bulge-dominated galaxies with red colours (e.g. Lusso et al. 2011; Bongiorno et al. 2012, but see also Silverman et al. (2009); Xue et al. (2010)). On average, stellar masses for Type1 AGN appear to be slightly larger than that of Type2s, although their difference is not statistically significant within their uncertainties ($\log M_* = 10.46^{+0.56}_{-0.73}$ and $\log M_* = 10.29^{+0.63}_{-0.82}$ for Type1s and Type2s, respectively). Due to their galaxy dominated SED shapes, Type2s have really well constrained host-galaxy physical parameters, showing relatively older stellar populations ($age = 1.51^{+2.69}_{-0.80}$ Gyr) with respect to the Type1s ($age = 0.27^{+2.02}_{-0.264}$ Gyr), in agreement with earlier works (Lusso et al. 2011; Bongiorno et al. 2012). Type1s have instead a much wider distribution of both τ and ages, which means that recovering the host-galaxy properties for unobscured AGN is a challenging task, subject to considerably larger uncertainties than for Type2s. In general, stellar masses are robustly constrained despite of the presence of an AGN, since these are primarily determined by the emission at around rest-frame 1μm, where the contrast between the BBB and galaxy is usually minimized. This is however not the case for the SFR parameter, since it is highly sensitive to the optical/UV SED, which is on its turn highly sensitive to AGN contribution, especially for Type1 AGN.

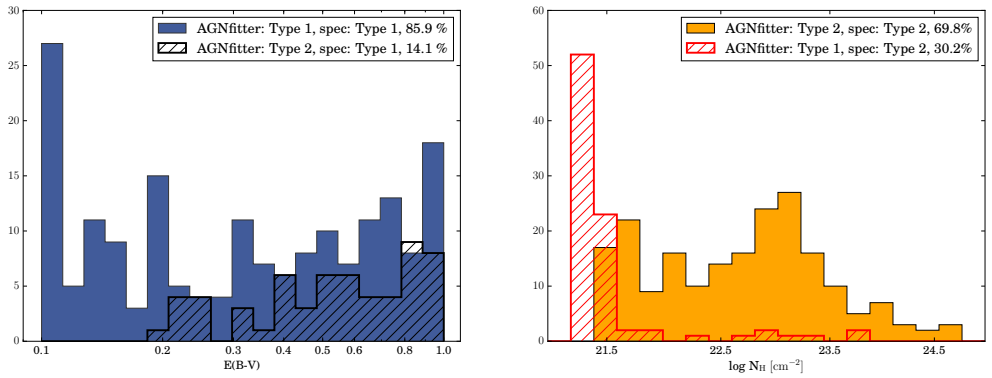

Figure 2.10: AGNfitter vs spectroscopic classification: the *left panel* shows the distribution of the Type1 sources for the reddening parameter $E(B-V)_{bbb}$. The filled blue distribution represents the spectroscopically classified Type1s that are also classified as such in AGNfitter, while the dashed black distribution represents the ones misclassified as Type2s. The *right panel* shows the distribution of the Type2 sources for the column density parameters $\log N_H$. The filled orange distribution represents the spectroscopically classified Type2s that are also classified as such in AGNfitter, while the dashed red distribution represent spectroscopic Type2s misclassified as Type1s by AGNfitter.

For completeness, we also reported in Figure 2.9 the distributions for the host-galaxy reddening $E(B-V)_{gal}$, and optical star formation rates (SFR_{opt}, corrected for extinction) for both AGN populations, although we note that the reliability of UV-based SFR indicators in galaxies has long been debated (e.g. Adelberger & Steidel 2000; Bell 2002).

All in all, due to the different redshift ranges covered by the two AGN populations, ($\langle z_{T2} \rangle \sim 0.85$, $\langle z_{T1} \rangle \sim 1.64$), one should consider the effect of the redshift while interpreting the results to avoid comparing sources that may be at different evolutionary stages. Nonetheless, our main aim here is to provide an overall view of the full range of the physical parameters estimated by AGNfitter for the AGN population as a whole.

2.6.3 AGN obscuration and classification

The parameters directly related to the obscuration properties of the nuclear emission are the dust reddening parameter $E(B-V)_{bbb}$ and the column density N_H. The parameter $E(B-V)_{bbb}$ quantifies the absorption and reprocessing of the direct AGN emission by gas and dust along the line of sight at host-galaxy scales, while the column density parameter ($\log N_H$) describes the absorbing dust distributed mainly at nuclear scales.

We compare AGNfitter results on these parameters with those yielded by the non-Bayesian SED fitting code presented in Lusso et al. (2013) for the Type1 population. While they find a median dust reddening value of $E(B-V)_{bbb} \leq 0.03$), AGNfitter finds a median value of $E(B-V)_{bbb} = 0.13^{+0.58}_{-0.11}$ (see Figure 2.9). The deviation from the literature results can be explained through the difference between our estimated median values from the PDFs and the maximum likelihood ones (best-fit) usually adopted in the literature.

This difference is especially relevant in the cases where the parameter $E(B-V)_{bbb}$ has an almost flat posterior PDF (as is the case for 36% of the Type1 AGN, which have a total error in $E(B-V)_{bbb}$ larger than 0.2). For this kind of Type 1 AGN, the maximum likelihood estimate of the reddening parameter is not precise and the flat and broad PDF push the median value to

larger reddening values, which also results in large uncertainties on this parameter (see Assef et al. 2010 for similar conclusions).

In contrast to the Type1s, no more than 9% of the Type2 sub-sample present low reddening values of $E(B–V)_{bbb} \leq 0.1$. The large majority of Type2 are highly reddened sources with a population median value of $E(B–V)_{bbb} = 0.64^{+0.28}_{-0.25}$.

A similar behaviour can be observed in the results for the column density parameter, $\log N_H$. As can be seen in Figure 2.9, Type1 AGNs clearly prefer low column densities with ~ 86 % having $\log N_H < 22$ as expected from their unobscured emission lines (population median value $N_H = 21.39^{+0.51}_{-0.26}$) . Type2 AGNs on the contrary, are more spread along large regimes of low and high column density, with only ~ 45 % having $\log N_H < 22$ (population median value $N_H = 22.02^{+1.95}_{-0.58}$). These column density values result from the different shapes of the torus SEDs, where higher column density is characterised by less near-IR emission of shorter wavelength, probably due to self-absorption of this energetic dust emission by the dust at lower temperatures distributed at larger scales (e.g. Figure 2.1). Overall, AGNfitter is able to recover general obscuration properties of both AGN classes.

The slight bimodality in the distributions for these two independent obscuration parameters provides the opportunity to develop a classification strategy. A multiwavelength classification through these AGNfitter parameters provides the clear advantage of being sensitive to photometric measurements over a wide wavelength range (mid-IR to opt-UV), in contrast to a spectral classification, which covers only a few thousand Angstroms in the rest-frame. Moreover, while spectroscopy can be rather expensive and is not always available for all sources, our method can be easily applied to complete multi-wavelength datasets.

We define the classification of the two AGN populations to be the following:

Type1 AGN:

$$N_H < 21.5 \cup 0 < E(B-V)_{bbb} < 0.2$$

Type2 AGN:

$$N_H > 21.5 \cap E(B-V)_{bbb} > 0.2$$

Although this is a hybrid sample because of the different selection effects employed, it nevertheless provides useful estimates for the true completeness and efficiency of classification for more uniformly selected X-ray AGN samples. The results of our classification scheme are presented in Fig. 2.10. As can be seen in the left panel, the majority of the broad emission line AGNs spectroscopically classified as Type1s are also classified as Type1s by the AGNfitter obscuration parameters, proving a completeness of (366/426, $\sim$ 86%). For the case of Type2s in the right panel of Fig. 2.10, our classification method is complete in $\sim$ 70% (201/288). A small fraction of the spectroscopically classified Type1s are misclassified as Type2s by AGNfitter's method (89/455), showing to be efficient at $\sim$80% for Type1 AGN. The false-positive ratio is slightly larger for Type2s, being 60/261 of spectroscopically classified Type2s missclassified as Type1 AGN by our method, proving an efficiency of $\sim$77% for Type2 sources.

The cases of disagreement with the spectroscopic approach does not necessarily imply that the SED fitting classification is incorrect. On the contrary, a multiwavelength approach as AGNfitter can be more sensitive to the global properties of the sources for such a classification, since it analyses the obscuration level in different independent components of the SED.

A similar approach has been used by Assef et al. (2013) based on a non-Bayesian SED fitting code, where they adopt E(B -V) = 0.15 as the dividing line for their classification. They choose this classification using an estimate from the standard X-ray boundary of a gas column

density of $N_H = 10^{22} cm^{-2}$ (Ueda et al. 2003) and the median value of the ratio $E(B-V)/N_H = 1.5 \times 10^{-23} cm^2 mag$ observed for the sample presented in Maiolino et al. (2001). Although a direct completeness comparison to the method of Assef et al. (2013) is not possible, since they do not test their method on spectroscopic classification, we calculate the completeness of their classification strategy applied to the fitting results of our sample. Following Assef et al. (2013) and using E(B -V) = 0.15 as the dividing line for the classification, we obtain a completeness ratio of 54% and 91% and an efficiency of 90% and 57% for Type1 AGN and Type2 AGN respectively. In general, our method present slightly better completeness and efficiency ratios, recovering a significantly larger fraction of Type1 sources, while slightly compromising on the completeness of Type2s. As this disagreement is likely to arise from the different SED-fitting approaches used to infer the obscuration parameters, a direct comparison of their classification strategy to spectroscopic classified samples would be needed.

2.7 Summary and Conclusions

We introduced AGNfitter: a fully Bayesian statistical tool for fitting and decomposing SEDs of active galaxies through MCMC sampling of the model parameters. The total active galaxy model in AGNfitter consists of the host galaxy emission, modelled as a combination of a stellar component and a starburst cold gas component and the nuclear AGN emission, modelled as a combination of an accretion disk (BBB) and a hot dust torus component. For both AGN and host galaxy models in the optical and UV, the effect of reddening along the line of sight is accounted for and corrected. Through informed sampling, the algorithm explores the parameter space that defines this model and computes the full PDFs of the parameters. AGNfitter calculates the median values with respective uncertainties of the following parameters:

- physical parameters: τ, age, $\log N_H$,
- reddening parameters: $E(B–V)_{bbb}$ and $E(B–V)_{gal}$,
- normalization variables: SB, BB, GA, TO

Multiple relevant properties for the characterization of the AGN and the host galaxy are also calculated. These are, for example, the integrated luminosities of the AGN components (e.g. L_{bol}, L_{bbb}, $L_{bbb-dered}$ and L_{tor}) and host galaxy properties (e.g. L_{gal}, L_{sb}, M_*, SFR_{opt}, and SFR_{FIR}).

The capability of AGNfitter in properly inferring these source properties was tested on mock active galaxies created as prototypical Type1 and Type2 SEDs. AGNfitter could accurately recover the input parameters of the synthetic SEDs and also provide insights into the degeneracies between emission components through the shapes of their PDFs.

The performance of the code for real data was tested on a sample of X-ray selected AGN from the XMM–COSMOS survey, which provides 15 band photometry from the UV to the far-IR for the construction of the SEDs. AGNfitter was applied to 714 sources (426 Type1 and 288 Type2 AGN), which were previously spectroscopically classified as Type1 and Type2 sources by their optical emission lines. The fitting-results include two independent model parameters, which are proxies for AGN obscuration. This allowed us to develop a classification strategy for unobscured (Type1) versus obscured (Type2) AGN, which shows a great agreement with the spectroscopic classification. The completeness fraction of our classification scheme is $\sim$ 86% and $\sim$ 70%, with an efficiency of $\sim$ 80% and $\sim$ 77%, for Type1 and Type2 AGNs respectively.

The complexity of AGN physics leaves many possibilities of improving the physical models used to approximate AGN emission. While they might be more detailed and accurate models for the different AGN components, these imply the treatment of larger parameter spaces with an unavoidable increase of degeneracies among the parameters. In those cases, the use of a Bayesian methodology as the one of AGNfitter is even more crucial.

The efficiency and code structure of AGNfitter allows new models to be easily integrated to the existing libraries. One significant improvement would be to implement a more flexible BBB model, which can be based on a physically motivated accretion disc model, possibly dependent on black hole mass and disc accretion rate (e.g. Slone & Netzer 2012), instead of a single empirical template. A further possible change could be the implementation of a more complex prior on the galaxy models to reflect the information from their total luminosity function. An interesting addition would be to allow the user to explore the effect on the galaxy/AGN parameters if an energy balance between the cold-dust and optical-UV star-formation is considered (e.g. da Cunha et al. 2008). Moreover, the implementation of a model of the IGM absorption such that rest-frame UV wavelengths at $\lambda < 1250$Å can be included in the fitting procedure, would be an additional improvement of our model.

AGNfitter's multi-wavelength approach allows the simultaneous study of multiple physical processes. This versatility makes of AGNfitter a flexible tool to address several physical questions related to AGN and galaxies. The AGNfitter python code is publicily available at `https://github.com/GabrielaCR/AGNfitter`.

Acknowledgements

The authors thank the anonymous referee for a careful reading and useful comments which have improved this manuscript. Joseph F. Hennawi acknowledges generous support from the Alexander von Humboldt foundation in the context of the Sofja Kovalevskaja Award. The Humboldt foundation is funded by the German Federal Ministry for Education and Research. Gabriela Calistro Rivera gratefully acknowledges support from the European Research Council under the European Union's Seventh Framework Programme (FP/2007- 2013)/ERC Advanced Grant NEWCLUSTERS-321271. We thank the members of the ENIGMA group [4] at the Max Planck Institute for Astronomy (MPIA) for insightful suggestions and discussions. We thank Daniel Foreman Mackey for his support on the implementation of the code Emcee as the MCMC core of AGNfitter. We thank Neil H.M. Crighton, Jose Onorbe, Alberto Rorai, Kenneth Duncan, and Marco Velliscig for important contributions in the scripting of the algorithm in Python. We thank Micol Bolzonella and Elena Zucca for useful comments and suggestions on the implementation of the prior on the galaxy luminosity function. We thank Huub Röttgering for his support during the final phase of the project.

Bibliography

Acquaviva, V., Gawiser, E., & Guaita, L. 2011, ApJ, 737, 47

Adelberger, K. L., & Steidel, C. C. 2000, ApJ, 544, 218

Adelman-McCarthy, J. K., & et al. 2005, VizieR Online Data Catalog, 2267, 0

Antonucci, R. 1993, ARA&A, 31, 473

[4] http://www.mpia-hd.mpg.de/ENIGMA/

Assef, R. J., Kochanek, C. S., Brodwin, M., et al. 2010, ApJ, 713, 970

Assef, R. J., Stern, D., Kochanek, C. S., et al. 2013, ApJ, 772, 26

Bell, E. F. 2002, ApJ, 577, 150

Berta, S., Lutz, D., Santini, P., et al. 2013, A&A, 551, A100

Bongiorno, A., Merloni, A., Brusa, M., et al. 2012, MNRAS, 427, 3103

Bouwens, R. J., Illingworth, G. D., Franx, M., et al. 2009, ApJ, 705, 936

Brusa, M., Civano, F., Comastri, A., et al. 2010, ApJ, 716, 348

Bruzual, G., & Charlot, S. 2003, MNRAS, 344, 1000

Calzetti, D., Armus, L., Bohlin, R. C., et al. 2000, ApJ, 533, 682

Capak, P., Aussel, H., Ajiki, M., et al. 2007, ApJS, 172, 99

—. 2008, VizieR Online Data Catalog, 2284

Cappelluti, N., Brusa, M., Hasinger, G., et al. 2009, A&A, 497, 635

Chary, R., & Elbaz, D. 2001, ApJ, 556, 562

Ciesla, L., Charmandaris, V., Georgakakis, A., et al. 2015, A&A, 576, A10

da Cunha, E., Charlot, S., & Elbaz, D. 2008, MNRAS, 388, 1595

Dale, D. A., & Helou, G. 2002, ApJ, 576, 159

Dale, D. A., Helou, G., Contursi, A., Silbermann, N. A., & Kolhatkar, S. 2001, ApJ, 549, 215

Donley, J. L., Koekemoer, A. M., Brusa, M., et al. 2012, ApJ, 748, 142

Elvis, M., Wilkes, B. J., McDowell, J. C., et al. 1994, ApJS, 95, 1

Elvis, M., Hao, H., Civano, F., et al. 2012, ApJ, 759, 6

Flagey, N., Boulanger, F., Verstraete, L., et al. 2006, in Astronomical Society of the Pacific Conference Series, Vol. 357, Astronomical Society of the Pacific Conference Series, ed. L. Armus & W. T. Reach, 85

Foreman-Mackey, D., Hogg, D. W., Lang, D., & Goodman, J. 2013, PASP, 125, 306

Gelman, A., & Rubin, D. B. 1992, Statist. Sci., 7, 457

Han, Y., & Han, Z. 2012, ApJ, 749, 123

Hao, H., Elvis, M., Civano, F., et al. 2012, ArXiv e-prints, arXiv:1210.3033

—. 2014, MNRAS, 438, 1288

Hasinger, G., Cappelluti, N., Brunner, H., et al. 2007, ApJS, 172, 29

Hastings, W. K. 1970, Biometrika, 57, 97

Hatziminaoglou, E., Fritz, J., Franceschini, A., et al. 2008, MNRAS, 386, 1252

Hernán-Caballero, A., Alonso-Herrero, A., Hatziminaoglou, E., et al. 2015, ApJ, 803, 109

Hopkins, P. F., Hernquist, L., Cox, T. J., et al. 2006, ApJS, 163, 1

Hopkins, P. F., Strauss, M. A., Hall, P. B., et al. 2004, AJ, 128, 1112

Ilbert, O., Salvato, M., Le Floc'h, E., et al. 2010, ApJ, 709, 644

Inoue, A. K., Shimizu, I., Iwata, I., & Tanaka, M. 2014, MNRAS, 442, 1805

Iovino, A., Cucciati, O., Scodeggio, M., et al. 2010, A&A, 509, A40

Johnson, S. P., Wilson, G. W., Tang, Y., & Scott, K. S. 2013, MNRAS, 436, 2535

Juneau, S., Dickinson, M., Bournaud, F., et al. 2013, ApJ, 764, 176

Kauffmann, G., Heckman, T. M., Tremonti, C., et al. 2003, MNRAS, 346, 1055

Komatsu, E., Dunkley, J., Nolta, M. R., et al. 2009, ApJS, 180, 330

Kovač, K., Lilly, S. J., Cucciati, O., et al. 2010, ApJ, 708, 505

Krawczyk, C. M., Richards, G. T., Mehta, S. S., et al. 2013, ApJS, 206, 4

Lacy, M., Storrie-Lombardi, L. J., Sajina, A., et al. 2004, ApJS, 154, 166

Lang, D., Hogg, D. W., & Schlegel, D. J. 2014, ArXiv e-prints, arXiv:1410.7397

Le Floc'h, E., Aussel, H., Ilbert, O., et al. 2009, ApJ, 703, 222

Lewis, A., & Bridle, S. 2002, Phys. Rev. D, 66, 103511

Lilly, S. J., Le Fèvre, O., Renzini, A., et al. 2007, ApJS, 172, 70

Lusso, E., Worseck, G., Hennawi, J. F., et al. 2015, MNRAS, 449, 4204

Lusso, E., Comastri, A., Vignali, C., et al. 2011, A&A, 534, A110

Lusso, E., Comastri, A., Simmons, B. D., et al. 2012, MNRAS, 425, 623

Lusso, E., Hennawi, J. F., Comastri, A., et al. 2013, ApJ, 777, 86

Lutz, D., Poglitsch, A., Altieri, B., et al. 2011, A&A, 532, A90

Madau, P. 1995, ApJ, 441, 18

Magorrian, J., Tremaine, S., Richstone, D., et al. 1998, AJ, 115, 2285

Maiolino, R., Marconi, A., Salvati, M., et al. 2001, A&A, 365, 28

Marconi, A., & Hunt, L. K. 2003, ApJ, 589, L21

Marconi, A., Risaliti, G., Gilli, R., et al. 2004, MNRAS, 351, 169

Mary Kathryn Cowles, B. P. C. 1996, Journal of the American Statistical Association, 91, 883

McCracken, H. J., Radovich, M., Iovino, A., et al. 2008, VizieR Online Data Catalog, 2286

McCracken, H. J., Capak, P., Salvato, M., et al. 2010, ApJ, 708, 202

Meiksin, A. 2006, MNRAS, 365, 807

Merloni, A., Bongiorno, A., Brusa, M., et al. 2014, MNRAS, 437, 3550

Metropolis, N., Rosenbluth, A. W., Rosenbluth, M. N., Teller, A. H., & Teller, E. 1953, The Journal of Chemical Physics, 21, 1087

Moller, P., & Jakobsen, P. 1990, A&A, 228, 299

Murphy, E. J., Condon, J. J., Schinnerer, E., et al. 2011, ApJ, 737, 67

Pirzkal, N., Rothberg, B., Nilsson, K. K., et al. 2012, ApJ, 748, 122

Planck Collaboration, Ade, P. A. R., Aghanim, N., et al. 2014, A&A, 571, A16

Prescott, M. K. M., Impey, C. D., Cool, R. J., & Scoville, N. Z. 2006, ApJ, 644, 100

Prevot, M. L., Lequeux, J., Prevot, L., Maurice, E., & Rocca-Volmerange, B. 1984, A&A, 132, 389

Prochaska, J. X., Madau, P., O'Meara, J. M., & Fumagalli, M. 2014, MNRAS, 438, 476

Richards, G. T., Lacy, M., Storrie-Lombardi, L. J., et al. 2006a, ApJS, 166, 470

Richards, G. T., Strauss, M. A., Fan, X., et al. 2006b, AJ, 131, 2766

Richstone, D. O., & Schmidt, M. 1980, ApJ, 235, 361

Sajina, A., Scott, D., Dennefeld, M., et al. 2006, MNRAS, 369, 939

Salvato, M., Hasinger, G., Ilbert, O., et al. 2009, ApJ, 690, 1250

Sanders, D. B., Phinney, E. S., Neugebauer, G., Soifer, B. T., & Matthews, K. 1989, ApJ, 347, 29

Schlegel, D. J., Finkbeiner, D. P., & Davis, M. 1998, ApJ, 500, 525

Scott, J. E., Kriss, G. A., Brotherton, M., et al. 2004, ApJ, 615, 135

Scoville, N., Aussel, H., Brusa, M., et al. 2007, ApJS, 172, 1

Serra, P., Amblard, A., Temi, P., et al. 2011, ApJ, 740, 22

Shang, Z., Brotherton, M. S., Wills, B. J., et al. 2011, ApJS, 196, 2

Shull, J. M., Stevans, M., & Danforth, C. W. 2012, ApJ, 752, 162

Silva, L., Granato, G. L., Bressan, A., & Danese, L. 1998, ApJ, 509, 103

Silva, L., Maiolino, R., & Granato, G. L. 2004, MNRAS, 355, 973

Silverman, J. D., Lamareille, F., Maier, C., et al. 2009, ApJ, 696, 396

Slone, O., & Netzer, H. 2012, MNRAS, 426, 656

Soifer, B. T., Boehmer, L., Neugebauer, G., & Sanders, D. B. 1989, AJ, 98, 766

Springel, V., Di Matteo, T., & Hernquist, L. 2005, MNRAS, 361, 776

Stern, D., Eisenhardt, P., Gorjian, V., et al. 2005, ApJ, 631, 163

Stevans, M. L., Shull, J. M., Danforth, C. W., & Tilton, E. M. 2014, ApJ, 794, 75

Stickel, M., Lemke, D., Klaas, U., et al. 2000, A&A, 359, 865

Telfer, R. C., Zheng, W., Kriss, G. A., & Davidsen, A. F. 2002, ApJ, 565, 773

Tilton, E. M., Stevans, M. L., Shull, J. M., & Danforth, C. W. 2016, ApJ, 817, 56

Trump, J. R., Impey, C. D., Gabor, J. M., et al. 2007, in Astronomical Society of the Pacific Conference Series, Vol. 373, The Central Engine of Active Galactic Nuclei, ed. L. C. Ho & J.-W. Wang, 726

Trump, J. R., Impey, C. D., Elvis, M., et al. 2009, ApJ, 696, 1195

Ueda, Y., Akiyama, M., Ohta, K., & Miyaji, T. 2003, ApJ, 598, 886

Urry, C. M., & Padovani, P. 1995, PASP, 107, 803

VanderPlas, J. 2014, ArXiv e-prints, arXiv:1411.5018

Worseck, G., & Prochaska, J. X. 2011, ApJ, 728, 23

Xue, Y. Q., Brandt, W. N., Luo, B., et al. 2010, ApJ, 720, 368

Zamojski, M. A., Schiminovich, D., Rich, R. M., et al. 2007, ApJS, 172, 468

Zheng, W., Kriss, G. A., Telfer, R. C., Grimes, J. P., & Davidsen, A. F. 1997, ApJ, 475, 469

3

The Wavelength Frontier: The low-frequency radio window on star forming galaxies and AGN

We present a study of the low-frequency radio properties of star forming (SF) galaxies and active galactic nuclei (AGN) up to redshift $z = 2.5$. The new spectral window probed by the Low Frequency Array (LOFAR) allows us to reconstruct the radio continuum emission from 150 MHz to 1.4 GHz to an unprecedented depth for a radio-selected sample of 1542 galaxies in ~ 7 deg^2 of the LOFAR Boötes field. Using the extensive multi-wavelength dataset available in Boötes and detailed modelling of the FIR to UV spectral energy distribution (SED), we are able to separate the star-formation (N=758) and the AGN (N=784) dominated populations. We study the shape of the radio SEDs and their evolution across cosmic time and find significant differences in the spectral curvature between the SF galaxy and AGN populations. While the radio spectra of SF galaxies exhibit a weak but statistically significant flattening, AGN SEDs show a clear trend to become steeper towards lower frequencies. No evolution of the spectral curvature as a function of redshift is found for SF galaxies or AGN. We investigate the redshift evolution of the infrared-radio correlation (IRC) for SF galaxies and find that the ratio of total infrared to 1.4 GHz radio luminosities decreases with increasing redshift: $q_{1.4\ \mathrm{GHz}} = (2.45 \pm 0.04) \times (1 + z)^{-0.15\pm0.03}$. Similarly, $q_{150\ \mathrm{MHz}}$ shows a redshift evolution following $q_{150\ \mathrm{GHz}} = (1.72 \pm 0.04) \times (1 + z)^{-0.22\pm0.05}$. Calibration of the 150 MHz radio luminosity as a star formation rate tracer suggests that a single power-law extrapolation from $q_{1.4\ \mathrm{GHz}}$ is not an accurate approximation at all redshifts.

G. Calistro Rivera, W. L. Williams, M. J. Hardcastle, K. Duncan, H. J. A. Röttgering et al.
MNRAS, **Volume 469**, Issue 3, p.3468-3488 (2017)

3.1 Introduction

Radio selected samples of galaxies primarily consist of two populations: star-forming galaxies (hereafter SF galaxies) and active galactic nuclei (AGN). As both star formation activity and black-hole growth in AGN are processes closely related to the overall mass growth of galaxies (Shapley 2011; Best & Heckman 2012), radio-emitting galaxies therefore represent a unique laboratory for investigating the epoch of peak galaxy assembly, $1 < z < 3$. While studies of these galaxies from the far-infrared (FIR) to the ultraviolet (UV) have contributed greatly to our understanding of galaxy evolution, statistically significant samples of radio-selected galaxies across cosmic time have only recently become available for exploration thanks to a new generation of radio facilities. At low radio frequencies the unprecedented sensitivity and resolution of the Low Frequency Array (LOFAR, van Haarlem et al. 2013) opens a new window for galaxy evolution studies.

Low frequency radio emission in SF galaxies and AGN have different physical origins, although both are thought to be dominated by synchrotron emission. In SF galaxies the synchrotron emission is powered by high-energy electrons and positrons (cosmic rays, CRs), accelerated in supernova remnants (SNRs), that emit when interacting with the diffuse magnetic field of the galaxy (Condon 1992). Due to the short lifetime of the massive stars producing Type II and Type Ib supernovae, the synchrotron emission in SF galaxies is closely related to recent star formation, so that its emission (e.g. at 1.4 GHz) is widely used as a star formation tracer (Condon 1992; Bell 2003; Schmitt et al. 2006; Murphy et al. 2011).

In radio-selected AGN, the synchrotron radiation is ultimately powered by the central accreting black hole. However, the observed emission is believed to be emitted from regions which differ depending on the nature of the AGN (see Smolcic 2016, for a review of AGN radio classifications). Fundamental physical differences have been seen between radio AGN classified as high-excitation and low-excitation radio galaxies (HERGs and LERGs, Hardcastle et al. 2007; Best & Heckman 2012), where HERGs appear to be the dominant population at high radio luminosities ($L_{1.4\mathrm{GHz}} > 10^{26}\,\mathrm{W\,Hz^{-1}}$), while LERGs appear to dominate below this limit. Most HERGs are observed to consist of three large-scale structures: jets, hotspots and lobes (consistent with Fanaroff & Riley (1974) class II, FRII galaxies). High-energy CRs first emit while being accelerated in the relativistic *jet*, which transports them from the central AGN to shock regions called *hotspots* (e.g. Meisenheimer et al. 1989). Finally, the CRs expand away from the hotspot center, forming the large *lobes* of synchrotron emission (e.g. Krause et al. 2012).

The synchrotron emission in all of these processes is commonly described by a power-law function $S(\nu) \propto \nu^{\alpha}$, where $S(\nu)$ is the radio flux density at a given frequency, ν, and α the corresponding power-law slope. Nevertheless, there are processes which can alter the shape of the spectra. While in SF galaxies the synchrotron emission is typically observed to follow a slope of $\alpha \sim -0.7$ (e.g. Gioia et al. 1982; Condon 1992; Yun et al. 2001), intrinsic changes in the CR energy distributions or environmental and ISM processes (free-free absorption, ionization losses, and synchrotron self-absorption) can significantly alter the spectral shape of this emission (Lacki 2013, and references therein), intrinsic changes in the CR energy distributions or environmental and ISM process . In AGN, both spectral ageing (e.g. Harwood et al. 2015) and the relative brightness of the different components (e.g. core, jets, hotspots and lobes) play an important role in shaping the integrated radio SEDs of radio AGN (e.g. Hardcastle 2009).

Multi-frequency spectral studies of the integrated radio SED of AGN are not widespread in the literature (though there are a few exceptions, Laing & Peacock 1980; Ker et al. 2012; Singh et al. 2013; Kharb et al. 2016; Mahony et al. 2016). Recent literature has focused on morphological studies through spectral index maps (e.g. Harwood et al. 2015; Vardoulaki et al. 2015).

A luminosity dependence of the spectral shape of the integrated radio spectrum was studied e.g. by Laing & Peacock (1980), where they suggest radio AGN with $L_{1.4\,\mathrm{GHz}} < 10^{25}\,\mathrm{W\,Hz^{-1}}$ have spectra that steepen at low frequencies, while brighter AGN show the opposite trend. Similarly, Whittam et al. (2016) observed spectral flattening for radio-selected galaxies at the high-frequency end (15.7 GHz) and suggest this may be due to the cores of Fanaroff & Riley (1974) class I sources (FRI) becoming dominant at these high frequencies. Deep multi-frequency radio observations of representative samples of galaxies are needed to study the radio SED and understand the physical processes shaping it.

Observational studies of the spectral properties of radio SF galaxies have so far focused on the local universe as sensitivity usually prevents the detection of statistically significant samples of galaxies at higher redshifts. An exception to this is the radio spectral slope study presented by Ibar et al. (2009, 2010) for a sample of submillimetre galaxies (SMGs). They found no redshift evolution of the spectral indices for SMGs, although due to the sparse coverage of the radio SED they could not rule out the presence of curvature. For local SF galaxies, spectral flattening towards low radio frequencies has been observed ($\nu < 1\,\mathrm{GHz}$), with thermal absorption or intrinsic synchrotron curvature as plausible explanations for this (Israel & Mahoney 1990; Clemens et al. 2010; Marvil et al. 2015). Theoretical models explaining an alternative picture to the simple power-law shape which includes spectral curvature have also been developed (e.g. Lacki 2013).

In SF galaxies the radio emission is typically calibrated to trace star formation based on a tight empirical correlation with the IR radiation (IR-radio correlation (IRC), de Jong et al. 1985; Helou et al. 1985). In the local universe the IRC has been observed to be roughly linear across more than three orders of magnitude in FIR-luminosity ($10^9 < L_{\mathrm{IR},(8-1000\mu m)}[\mathrm{L}_\odot] < 10^{12.5}$) (Yun et al. 2001; Magnelli et al. 2015), for different galaxy classes (from dwarf to ultra-luminous IR galaxies, ULIRGs), and in star-forming regions within galaxies (e.g. Dumas et al. 2011; Tabatabaei et al. 2013). The basic understanding of the IRC relies on both the cold dust IR emission and the radio emission being tracers of recent star formation (e.g. calorimeter model and conspiracy model, Voelk 1989; Lacki et al. 2010, respectively). The possibility of a redshift evolution of the IRC has motivated an extensive debate from the observational point of view: while several studies claim the existence of significant redshift evolution(Seymour et al. 2008; Ivison et al. 2010a; Magnelli et al. 2015; Delhaize et al. 2017), a few studies suggest that such an evolution is a product of selection biases (e.g. Appleton et al. 2004; Ibar et al. 2008; Jarvis et al. 2010; Sargent et al. 2010; Bourne et al. 2011) or a dust temperature dependence (e.g. Smith et al. 2014). In theoretical studies different trends as a function of redshift have also been discussed (e.g. Schober et al. 2016; Schleicher & Beck 2013; Lacki et al. 2010).

In this work we take advantage of the unique sensitivity and resolution of LOFAR (van Haarlem et al. 2013; Röttgering et al. 2011), combining deep 150 MHz radio observations (Williams et al. 2016) and the wealth of ancillary data available in the Boötes field to address some of the key outstanding questions regarding the radio emission of galaxies, namely, what are the star formation and AGN contributions to the radio continuum at low frequencies?; does the low-frequency radio emission of SF galaxies exhibit a correlation with the IR luminosity as tight as that observed at 1.4 GHz?; and if so, how does the IRC evolve with redshift at both 1.4 GHz and 150 MHz? Answering these questions is crucial to test the reliability of photometric-redshift estimations based on the radio–IR SEDs (e.g. Yun & Carilli 2002; da Cunha et al. 2015). Finally, this study will allow us to investigate the low-frequency radio emission as a SFR tracer of galaxy populations at higher redshifts.

This paper is structured as follows. In section 4.2 we present the multi-frequency radio and FIR to UV data used for this study, while section 3.3 describes the selection strategy for

our sample. In section 3.4 we discuss the SED analysis and classification into SF galaxies and AGN populations. The analysis of the spectral slope and curvature for the two populations is described in section 3.5. Next, the IRC in our data is investigated in section 3.6 and section 3.7 discusses the low frequency radio emission as a SFR diagnostic. Finally, section 3.8 summarizes our findings. Throughout the paper we adopt a concordance flat Λ-CDM cosmology with $H_0 = 70\,\mathrm{km\,s^{-1}\,Mpc^{-1}}$, $\Omega_\mathrm{m} = 0.3$, and $\Omega_\Lambda = 0.7$ (Komatsu et al. 2009; Planck Collaboration et al. 2014) and all quoted magnitudes assume the AB system (Oke & Gunn 1983) unless otherwise specified.

3.2 Survey data

The National Optical Astronomy Observatory (NOAO) Deep Wide-field survey (NDWFS; Jannuzi & Dey 1999) targeted the sky seen towards the constellation of Boötes as one of its deep extragalactic fields. Originally the NDWFS covered 9 $\mathrm{deg^2}$ in the optical and near-infrared B_W, R, I and K bands. Since then, the Boötes Field has been surveyed across the electromagnetic spectrum, including deep X-ray (Murray et al. 2005), mid-infrared (Jannuzi et al. 2010) and far-infrared (Oliver et al. 2012) photometric observations as well as extensive spectroscopic surveys (e.g. Kochanek et al. 2012). The field therefore represents one of the richest multi-wavelength datasets among the wide deep extragalactic surveys and is complementary to the deep radio observations provided by LOFAR.

3.2.1 LOFAR 150 MHz

The first source catalogue used for our sample selection is based on 150 MHz radio observations of the Boötes field (Williams et al. 2016) taken with the LOFAR High Band Antennae (HBA). The calibration and imaging were achieved with the 'Facet' calibration scheme presented by van Weeren et al. (2016), which corrects for direction dependent effects (DDEs) caused by the ionosphere and imperfect knowledge of LOFAR station beam shapes. The resulting image, as presented by Williams et al. (2016), covers 19 $\mathrm{deg^2}$ with an rms noise of $\sigma_\mathrm{rms} \sim 120 - 150\ \mu\mathrm{Jy\ beam^{-1}}$ in the central region of the field and a resolution of 5.6×7.4 arcsec. These values represent up to more than one order of magnitude improvement compared to the images existing at this wavelength (Intema et al. 2011; Williams et al. 2013). The source extraction for the catalogue was done using the Python Blob Detection and Source Measurement software, (PyBDSM: Mohan & Rafferty 2015), which performs Gaussian fitting to decompose radio interferometry images, grouping the Gaussians together into individual sources where appropriate. The LOFAR 150 MHz radio source catalogue contains 6276 sources detected with a peak flux density threshold of $5\sigma_\mathrm{rms}$ within the coverage region shown in Fig. 3.1. The LOFAR 150 MHz luminosity distributions for our total sample classified into SF galaxies and AGN are shown in the lower panel of Figure 3.2.

3.2.2 Radio photometry for the Boötes field

The construction of radio SEDs for the sources in the Boötes field is one of the main aims of this paper. Conveniently, the Boötes field has been covered by several previous radio surveys. Among these, the high sensitivity and the resolution of the VLA-P Survey at 325 MHz, GMRT observations at 608 MHz and the deep WSRT catalogue at 1.4 GHz, make them the best data sets to complement the LOFAR data in our study.

The VLA-P catalogue (Coppejans et al. 2015) used in this investigation, was drawn from a 324.5 MHz image of a radius of 2.05° in the NOAO Boötes field using Karl G. Jansky

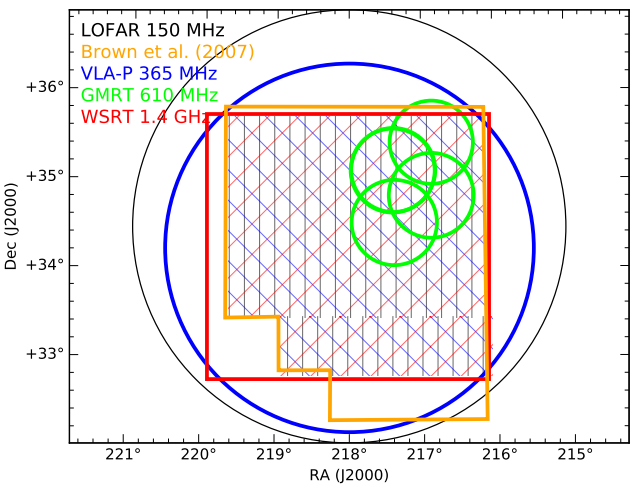

Figure 3.1: Spatial coverage of the optical and radio photometry including the I-band selected photometry presented by Brown et al. (2007) and the four deep catalogues at 150, 325, 610, 1400 MHz, available for the Boötes field. The dashed area is the area chosen for our study.

Very Large Array (VLA) P-band observations. The image covered a single pointing and has a resolution of 5.6×5.1 arcsec with a central noise of 0.2 mJy beam^{-1} increasing to 0.8 mJy beam^{-1} at the edge of the image. The source extraction for the catalogue was done using the PyBDSM software, (PyBDSM: Mohan & Rafferty 2015). The source detection threshold for the construction of the catalogue for this study is 3 $\sigma_{\rm rms}$. This is a reliable detection limit since our study includes only sources from the catalogue which have LOFAR detected counterparts. As discussed by Coppejans et al. (2015), the VLA-P catalogue was matched to WENSS (Rengelink et al. 1997) to check the absolute flux density scale and the primary beam correction.

The GMRT image at 608 MHz is a mosaic constructed from four pointings covering 1.95 deg^2 of the Boötes field (project code 28_064). The mosaic has a resolution of 5×5 arcsec and a noise level of $\sigma_{\rm rms} \sim 40 - 70\ \mu$Jy beam^{-1}. Primary flux density calibration was done with 3C286 using the wideband low-frequency flux density standard of Scaife & Heald (2012). The source extraction for the catalogue was also performed using the PyBDSM software, (PyBDSM: Mohan & Rafferty 2015).

The 1.4 GHz data (de Vries et al. 2002) are drawn from the deep (16×12 hr) Westerbork Synthesis Radio Telescope (WSRT) observations of the approximately 6.68 deg^2 Boötes Deep Field. The image covers 42 discrete pointings and has a limiting sensitivity of $\sigma_{\rm rms} \sim 28\,\mu$Jy beam^{-1} and a resolution of 13×27 arcsec. The source extraction in the public catalogue was done using automated routines described in detail by Rengelink et al. (1997), which consist basically of Gaussian fitting to islands of detected brightness in the radio map. The source detection threshold for the inclusion of the flux densities in the catalogue is 5 times the local rms, resulting in the full catalogue containing 3172 sources. Since the Boötes field has been covered by previous radio surveys at this wavelength such as the NRAO VLA Sky Survey (NVSS; Condon et al. 1998) and the Faint Images of The Radio Sky at 20 cm Survey (FIRST; Becker et al. 1995), these data were used to calibrate the survey flux densities and positions.

Assuming a spectral index of ∼-0.7, the LOFAR measurements offer sensitivity values comparable to the 1.4 GHz WSRT map presented by de Vries et al. (2002) (rms: 28 μJy beam^{-1}) and resolution values comparable to the 365 MHz VLA-P map published by Coppejans et al. (2015) (5.6 × 5.1 arcsec), which are the best radio data available at the respective frequencies to date.

Table 3.1: Multiwavelength coverage of the LOFAR+I-band selected sample in the Boötes field. The column of 'Detections' specifies which fraction of the final sample has counterparts in the respective bands.

	Band	$\nu[Hz], \lambda[m]$	Detections [%]
Selection	LOFAR	150 MHz	100%
	I	806 nm	100%
UV	NUV	300 nm	93%
	u	365 nm	99%
optical	B_W	445 nm	100%
	R	658 nm	100%
NIR	z	900 nm	99%
	Y	1020 nm	99%
	J	1222 nm	100%
	H	1630 nm	100%
	K	2190 nm	100%
MIR	IRAC1	3.6 μm	100%
	IRAC2	4.5 μm	100%
	IRAC3	5.8 μm	100%
	IRAC4	8.0 μm	100%
	MIPS24	24.0 μm	100%
FIR	SPIRE	250 μm	83%
	SPIRE	350μm	79%
	SPIRE	500 μm	67%
RADIO	WSRT	1.4 GHz	67% (88%[a])[b]
	GMRT	610 MHz	23% [c]
	VLA-P	325 MHz	63% (88% [a]) [b]

[a] After the flux cut applied for the curvature analysis (section 3.5.2)
[b] Forced photometry included for non-detections
[c] Due to spatial partial coverage, see Fig. 3.1

3.2.3 Optical and Infrared Photometry

The second source-catalogue used for our sample selection is the combined I-band-selected psf-matched photometry catalogue presented by Brown et al. (2007). The photometric bands included in the catalogue are presented in Table 3.1 covering a wide range of wavelengths, spanning from 0.15 to 24 μm.

This catalogue includes the original NDWFS observations in the optical and near- infrared; B_W, R, I and K bands. With an absolute positional uncertainty of < 0.1 arcsec, the I-band images reach depths of 24.9 AB magnitude ($5\sigma_{\rm rms}$ within 2 arcsec diameter aperture).

Mid-infrared (MIR) counterparts are drawn from the *Spitzer* Deep Wide-field Survey (SDWFS; Ashby et al. 2009), using the InfraRed Array Camera (IRAC) instrument on the *Spitzer* Space Telescope, providing images at 3.6, 4.5, 5.8, and 8.0 μm. Infrared 24 μm photometry from *Spitzer* was provided by the Multiband Imaging Photometer (MIPS) AGN and Galaxy Evolution Survey (MAGES; Jannuzi et al. (2010)), while deep J, H, K_s photometry was drawn from the NOAO Extremely Wide-field Infrared Imager (NEWFIRM; Autry et al. 2003) survey. A fraction of the total Boötes field is covered by the z-Boötes survey (Cool 2007), providing photometry in the z-band for 7.62 deg^2 of the field, with some gaps in the coverage due to the 10 arcmin gaps in the instrument CCDs. Y and $U_{\rm spec}$ bands photometry is provided using images from the Large Binocular Camera (LBC) mounted on the Large Binocular Telescope (LBT). Finally, NUV photometry (1800-2750 Å) has been included from the GALEX/GR6 surveys (Martin et al. 2003; Bianchi et al. 2014).

As described in detail by Brown et al. (2007), this psf-matched catalogue wass constructed by regridding and smoothing the individual survey images corresponding to the u-, B_w-,R-, I-, z-, Y-, J-, H- and K-bands to a common scale so that the sources' point spread functions (PSF) are Moffat profiles. Fluxes are extracted from these images for all the sources with I-band detections using SExtractor (Bertin & Arnouts 1996), while for the remaining bands (IRAC and MIPS bands) aperture fluxes were extracted. Regions surrounding very extended galaxies and saturated stars were excluded.

In total, the combined catalogue provides photometry for $\sim$ 830k sources, including galaxies and AGN with I-band magnitudes $I < 24$.

3.2.4 Far-infrared Photometry: HerMes DR3

Far-infrared photometry is a key ingredient for this study, as it allows us to constrain total infrared luminosities and trace SFRs of the sources. To increase the infrared spectral coverage of the final sample, we added SPIRE data at 250, 350 and 500 μm from the *Herschel* Multi-tiered Extragalactic Survey (HerMes; Oliver et al. 2012). One of the greatest challenges in measuring fluxes at such long wavelength is the high confusion noise, a result of the large SPIRE beam sizes. Since one effect of confusion is that it increases the positional uncertainty of sources (e.g., Hogg 2001), cross-identification with other wavelengths becomes very challenging. To deal with this issue, we use the third data release (DR3) cross-identification catalogues, which are selected with positional priors at 24 μm and obtained with the technique described by Roseboom et al. (2010). This technique consists basically of performing cross-identifications in map-space so as to minimise source blending effects by using a combination of linear inversion and model selection techniques. In this way they produce reliable cross-identification catalogues based on Spitzer MIPS 24 μm source positions, giving significantly greater accuracy in the flux density compared to other traditional source recovery methods and so recovering a much larger fraction of faint SPIRE sources.

The FIR photometry was included in the multi-wavelength data by cross-correlating the source selection catalogue described above with the *Hermes* DR3 catalogue, using the task

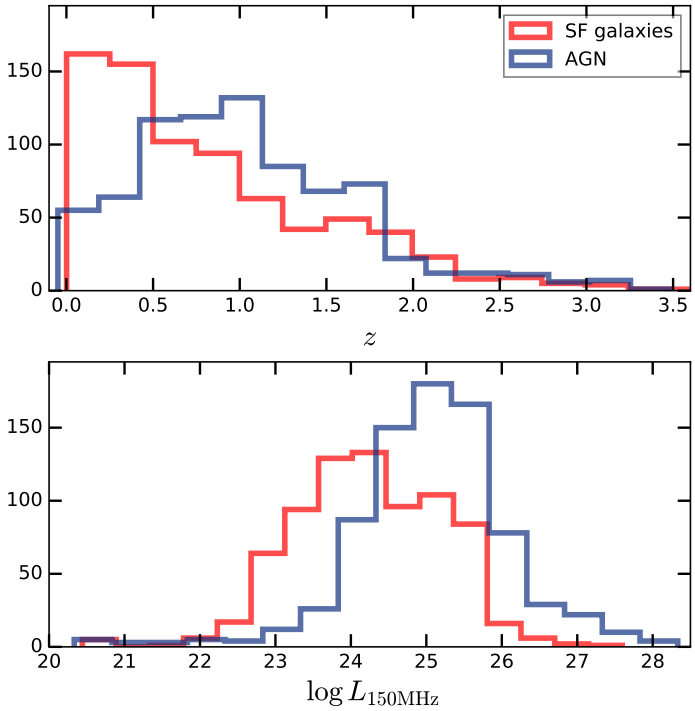

Figure 3.2: Redshift and LOFAR 150 MHz luminosity distributions for the SF galaxies (red) and AGN (blue) populations. The classification of the total sample into SF galaxies and AGN is explained in detail in section 3.4.2.

TSKYMATCH2 from the STILTS software package (TOPCAT implementation, Taylor 2006). Using the optical position of the sources in the Brown et al. (2007) catalogue, TSKYMATCH2 returned the SPIRE fluxes associated to all sources with MIPS 24 μm to optical separations of $r_{24-opt} < 3$ arcsec (less than half the FWHM of the MIPS 24 μm beam).

The percentage of sources with counterparts at different wavelengths are listed in Table 3.1.

3.2.5 Redshifts

The spectroscopic AGN and Galaxy Evolution Survey (AGES) has covered 7.7 deg^2 of the Boötes Field providing spectroscopic redshifts for 23 745 galaxies and AGN. However, given that the majority of sources at $z > 1$ in the AGES catalogue are QSOs, it is crucial to estimate robust photometric redshifts, as this study focuses on both AGN and star forming galaxies. Spectroscopic redshifts are available for around 45 and 35 per cent of our total selection of SF galaxies and AGN respectively (the selection and classification is described in sections 3.3 and 3.4) . Photometric redshifts are estimated as described below for the remaining fraction of the sources.

Photometric redshifts are provided by the optimised catalogue described by Duncan et al. (in prep.), produced using the Boötes photometry of Brown et al. (2007), presented above. The innovative method used for this redshift catalogue consists of combining three different z_{phot}-estimation methods, by using the EAZY photometric redshift software (Brammer et al. 2008) customized with three different template sets: one set of stellar only templates (EAZY default library; Brammer et al. 2008) and two sets including AGN and QSO contributions (SWIRE; Polletta et al. 2007) and (Atlas of Galaxy SEDs; Brown et al. 2014). This methodology has been motivated by the fact that comparisons of z_{phot}-estimation techniques have shown that

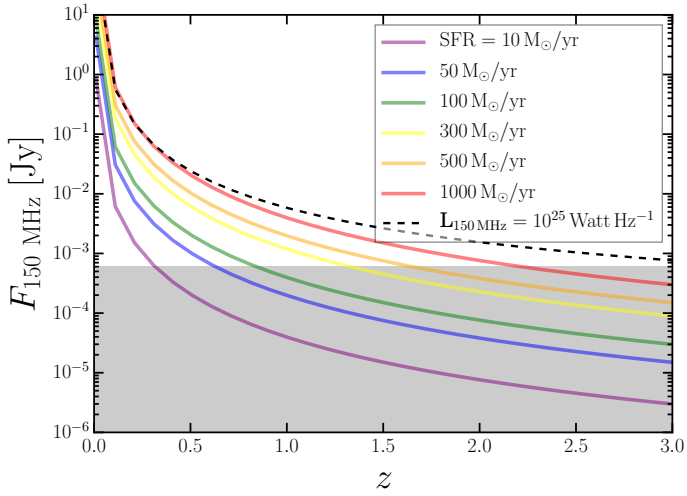

Figure 3.3: Test for completeness of the LOFAR selection. The solid lines depict the redshift evolution of the expected radio fluxes for different SF galaxies and are colour-coded by SFR. The 150 MHz luminosities where calculated based on the IR-radio correlation, assuming $q_{1.4\,\mathrm{GHz}} = 2.3$ and a spectral index of $\alpha = -0.7$ for the extrapolation from 1.4 GHz to 150 MHz. The dashed line corresponds to the 150 MHz flux evolution as a function of redshift for AGN of $\mathrm{L}_{150\mathrm{MHz}} > 10^{25}\mathrm{W\,Hz^{-1}}$. The grey shaded area displays the flux limit implied in our radio selection, which correspond to 5 σ_{rms}.

for a suite of multiple z-estimates, the ensemble average estimates offer significant statistical improvements in redshift accuracy compared to the estimates of any single set of predictions (Dahlen et al. 2013; Carrasco Kind & Brunner 2014). These three individual z_{phot} estimates were then combined using a Hierarchical Bayesian combination method (Dahlen et al. 2013), as an alternative to a straight addition of the probability distributions of the three z_{phot} estimates. The main advantage of this method is that it determines the consensus probability $P_{z_{\mathrm{phot}}}$ for each object, given the possibility that the individual measured probability distributions may be wrong. These results were also optimised using zero-point offsets calculated from the spectroscopic redshift sample. The redshift distributions for the total sample classified into SF galaxies and AGN are shown in the upper panel of Figure 3.2.

3.3 Sample Selection

The selection strategy for the sample of galaxies and AGN in the Boötes Field involved several steps. First, sources detected both in LOFAR 150 MHz and I-band were selected to build the primary source catalogue, which is additionally complemented by multi-wavelength ancillary data. Second, we constrained this catalogue to sources with positions within the region of overlap among the 150 MHz, 325 MHz and 1.4 GHz radio maps (see Section 3.2.2 and Fig. 3.1). Finally, we classified these sources into SF galaxies and AGN-dominated sources using the AGNFITTER algorithm (Calistro Rivera et al. 2016) and restrict the posterior analysis on the sub-samples separately.

3.3.1 LOFAR + I-band selection

The identification of optical counterparts to the LOFAR detections from the Brown et al. (2007) catalogue is described in detail by Williams et al., in prep. We use the likelihood ratio (LR) method (Richter 1975) to quantify the probability of an I-band detected galaxy being the true counterpart of the radio emission observed in the LOFAR map. The fully developed method used is described by Tasse et al. (2008). From the 3317 LOFAR-detected sources, which lie within the 9 deg^2 boundary of the Brown et al. (2007) catalogue, 2326 (70 per cent) are found to have unique optical counterparts.

Fig. 3.3 shows the implications of our radio selection for the nature of our sample. Lines correspond to the expected radio fluxes at 150 MHz, based on the IR-radio correlation, assuming $q_{1.4\,\mathrm{GHz}} = 2.3$ and a spectral index of $\alpha = -0.7$ for the extrapolation from 1.4 GHz to 150 MHz. We choose to use a value of $q_{1.4\,\mathrm{GHz}} = 2.3$ based on the observed median value of $q_{1.4}$ found for our sample (see Fig. 3.13). The flux cut from our radio selection is represented by the grey shaded area. Due to our selection, at $z < 1.3$ our sample appears to be complete for SF galaxies of $SFR > 300$ M$_\odot$/yr (yellow line). At redshifts $1.5 < z < 2.3$ only galaxies with $SFR > 1000$ $M_\odot$/yr are represented in a complete way according to the LOFAR selection. We expect to be complete for AGN of $\mathrm{L_{150MHz}} > 10^{25}\mathrm{W\,Hz^{-1}}$ at all redshifts. We thus conclude that at redshifts $z > 1.5$ our sample is limited to highly SF galaxies (starbursts) and radio-selected AGN.

3.3.2 Selection for radio SED construction

The radio SEDs constructed from the data described in Section 3.2.2 are built up mostly with three data points: LOFAR 150 MHz, VLA-P 365 MHz and WSRT 1400 MHz (Fig. 3.1), complemented with a partial coverage of GMRT observations at 610 MHz. From the 2326 LOFAR sources with optical counterparts, 1955 sources lie within the region of overlap among the 150 MHz, 325 MHz and 1.4 GHz radio maps required for our study. To study the shape of the radio continuum we need reliable spectral index measurements along the total frequency coverage. As spectral index measurements are prone to be easily affected by systematic offsets between different bands, special care should be exercised in having an homogeneous flux scales and in dealing with non-detections. We dedicate this section to this purpose, review all systematics intrinsic to each data set and corroborate the homogeneity of the flux scaling.

Flux scales

The combination or comparison of radio maps at different frequencies requires them to undergo a standard calibration scaling. For this study we adjust the fluxes of the four different bands to the scale that is most accurate at low radio frequencies, that of Scaife & Heald (2012). Since the main uncertainties of using a standard calibration scale are at frequencies lower that 1 GHz we focus our investigation on the LOFAR and VLA-P data sets. However, we note that the scaling of the high-frequency range covered by the GMRT and WSRT datasets was verified to also be consistent with the scale by Scaife & Heald (2012).

To investigate the reliability of LOFAR fluxes at 150 MHz, Williams et al. (2016) have compared high signal-to-noise sources to three other data sets with known calibrations in the Boötes Field: NVSS (at 1.4 GHz), WENSS (Rengelink et al. 1997) (at 365 MHz) and VLSSr (Lane et al. 2014) (at 74 MHz), where the WENSS fluxes had been scaled a priori by a factor of 0.9 to be consistent with the Scaife & Heald (2012) scale. The inference of the correction factor for the LOFAR fluxes consists of calculating the spectral indices between the lower (74 MHz) and higher (325, 1400 MHz) frequencies and predicting the LOFAR flux density

at the central frequency (150 MHz). The mean flux density ratio between the predicted and uncorrected LOFAR flux was found to be 1.01 ± 0.1. Finally, as described by Williams et al. (2016), this factor was used to adjust the LOFAR flux densities to the Scaife & Heald (2012) flux scale.

The reliability of the VLA-P flux-scale was tested using two independent approaches which yielded consistent results. First, we investigated the calibrator source (3C216) that lies in the Boötes field. We calculated the ratio the 325 MHz flux measured during the calibration of the map (which assumes the flux scale of Perley&Butler 2010) and the 325 MHz flux predicted by Scaife & Heald (2012). A correction factor of 0.91 was needed to adjust the calibrated fluxes to the standard scale of Scaife & Heald (2012). In a second approach, we compared high signal-to-noise VLA-P sources with their counterpart fluxes from the WSRT, GMRT and the LOFAR catalogues. The spectral indices between the lower (150 MHz) and higher frequencies (610 MHz, 1.4 GHz) were calculated and we could predict the VLA-P flux density at the central frequency (325 MHz). The mean flux density ratio between the predicted and uncorrected VLA-P flux was 0.91 ± 0.02, in agreement with the data-independent method presented above.

Non-detections

Although the sensitivity of the LOFAR image is equivalent to the WSRT sensitivity under the assumption of a spectral index of $\alpha \sim 0.7$, 33 per cent of the LOFAR selected sources are not detected in WSRT. This issue is also relevant for the VLA-P data, which are less sensitive ($\sigma_{\rm rms} \sim 0.2$ mJy beam^{-1}) than the equivalent LOFAR image at this frequency for the same assumed α ($\sigma_{\rm rms} \sim 0.074$ mJy beam^{-1}). We find that 37 per cent of the LOFAR selected sources are not detected in VLA-P.

To estimate the fluxes of the sources undetected in WSRT and VLA-P we use forced photometry technique. This process consists of extracting aperture fluxes from the radio maps at the location of known LOFAR selected sources. To calibrate this process we first applied the forced photometry on catalogued sources. We found that aperture fluxes were sensitive to artifacts of the imaging process (e.g. negative fluxes) and to reduce this effect, we used apertures smaller than the WSRT and VLA-P beam sizes. Finally, we used our results on catalogued sources to derive a correction factor, which was applied on the undetected sources. The flux uncertainties on the forced photometry were calculated by repeating the same flux extraction process as above using the corresponding rms-maps.

Although the aperture fluxes have been determined to be reliable, the results on radio continuum that are based on forced photometry (see Section 3.5), are carefully differentiated from those of SEDs fully sampled with detected sources, using forced photometry fluxes just as upper limits. Moreover, for more specific tests in the following sections we apply conservative flux cuts to minimize the fraction of non-detections in our data.

3.4 Analysis of AGN and SF galaxies with SED-fitting

The FIR to UV SEDs of the sources in our sample were decomposed into different physical contributions through fitting the multi-wavelength photometry using the SED-fitting algorithm AGNFITTER. Some examples of the fitting output are included in Appendix 3.19. An advantage of using AGNFITTER is that it is based on a Markov Chain Monte Carlo (MCMC) technique and infers the probability density functions (PDFs) of the physical parameters. This way it provides a robust calculation of their uncertainties and improving the recognition of correlations and degeneracies among them.

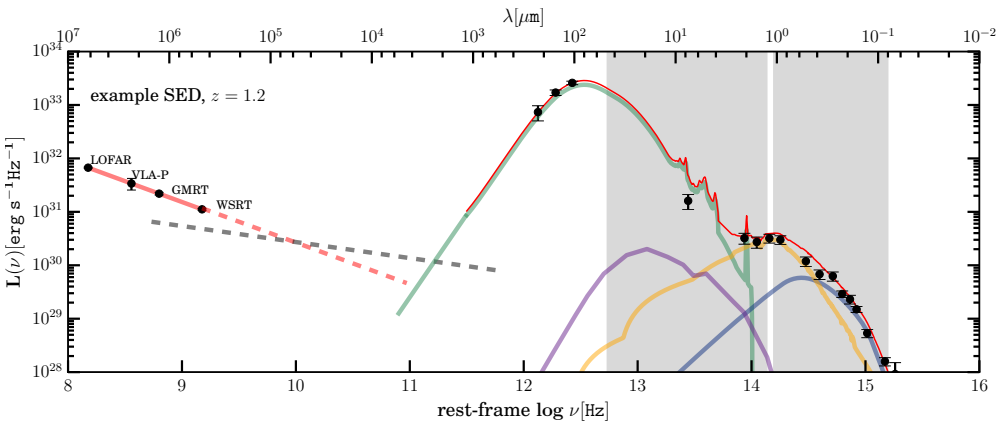

Figure 3.4: Example SED of dusty SF galaxy from our sample at z=1.2. The multi-wavelength coverage of our total sample is shown here, from the low-frequency radio till the UV regime. The radio data points represent the radio SED covered in this study: 150, 325, 610 MHz and 1.4 GHz. The FIR-UV photometry is decomposed into physical components of the host galaxy and the AGN using the code AGNFITTER. The integrated luminosities used in our classification scheme were computed by integrating the SED within the areas represented here as the grey-shaded rectangles. The left rectangle covers the integration limits for the main IR components: the galactic cold dust emission (green line) and the hot dust emission from the AGN torus (purple line). The right rectangle is the integration area for the optical main components: the stellar emission (orange line) and the accretion disk emission (blue line).The thin red line represents the total fitted SED. The dashed red and grey lines correspond to the synchroton and thermal contributions to the radio emission, respectively.

The total active galaxy model in AGNFITTER consists of the superposition of the host galaxy emission and the nuclear AGN emission. The host galaxy emission is modelled as a combination of a stellar component and the reprocessed emission of cold/warm dust in starburst regions. At nuclear scales, the AGN emission is modelled as a combination of an accretion disk component (Big Blue Bump, BBB) and a hot dust 'torus' component.

A large set of relevant physical parameters for the galaxy (SFR, M_*) and AGN (N_H-torus, L_{bol}) are calculated, some of which are detailed below. However, for full details we refer the reader to Calistro Rivera et al. (2016). From the 1955 LOFAR-I-band selected sources within the region of overlap between the multi-frequency radio data (section 3.3.2), 1542 ($\sim$ 79 per cent) can be classified as 758 SF galaxies and 784 AGN.

3.4.1 Stellar masses and star-formation rates

Stellar masses and SFRs (SFR_{opt}) were estimated by fitting the observed data to Bruzual & Charlot (2003) templates, assuming a Chabrier (2003) initial mass function (IMF) and an exponentially declining star formation history modulated by the time scale parameter τ. The distribution of stellar masses derived for our sample has a median value of $3.01^{+5.01}_{-2.50} \times 10^{10} M_\odot$, where the error bars correspond to the scatter given by the 16th and 84th percentiles. The templates were corrected for dust absorption assuming the Calzetti et al. (1994) reddening law. Additional SFRs from the IR-emission were calculated using integrated infrared luminosities of cold dust templates (SFR_{IR}) (Dale & Helou 2002; Chary & Elbaz 2001). To derive the SFRs from the fitted cold dust emission we use the calibrations presented by Murphy et al. (2011), which are an updated version from those by Kennicutt (1998). These estimates are described in detail in Calistro Rivera et al. (2016).

3.4.2 Classification into AGN and SF galaxies

The classification strategy consisted of comparing the disentangled contributions of the AGN and the host galaxy in both the optical-UV and the infrared regimes. It is important to note that this classification may still be contaminated by low excitation radio AGN (LERGs), which lack AGN signatures in their non-radio SED. In section 3.4.3 we will describe how we corrected for these potential mis-classifications.

In the optical-UV, the AGN contribution arises from the BBB luminosity L_{BB}, which is then compared to the galaxy stellar emission L_{GA}, integrating both inside the same frequency range $0.1 < \lambda < 10\,\mu$m. In the MIR, the AGN luminosity contribution is produced mainly by the torus L_{TO} and is compared to the cold dust emission in starburst regions of the host galaxy L_{SB}, as well integrating both components within the same frequency range $1 < \lambda < 40\,\mu$m. A representation of the SED decomposition and the integration ranges is shown in Fig. 3.4.

As presented in Fig. 3.5, in order to classify the total sample into SF galaxies and AGN we define the following scheme:

If the ratio of AGN torus to galaxy cold dust luminosities is smaller than one ($\log(L_{TO}/L_{SB}) < 0$), we consider the source's emission in the IR is dominated by star formation and we classify it as a SF-galaxy. The optical/UV contributions do not change the classification significantly, since the results for the 94 per cent of the sample which satisfy $\log(L_{TO}/L_{SB}) < 0$, also satisfy $\log(L_{BB}/L_{GA}) < 0$. In the cases with $\log(L_{BB}/L_{GA}) > 0$ (only around 6 per cent of the sample), the direct emission of the AGN accretion disk appears to dominate over the stellar emission. However, since their FIR emission is dominated by the dust component in star-forming regions, these sources may represent the fraction of highly obscured star forming galaxies (e.g. Casey et al. 2014) and are thus classified as star-forming galaxies.

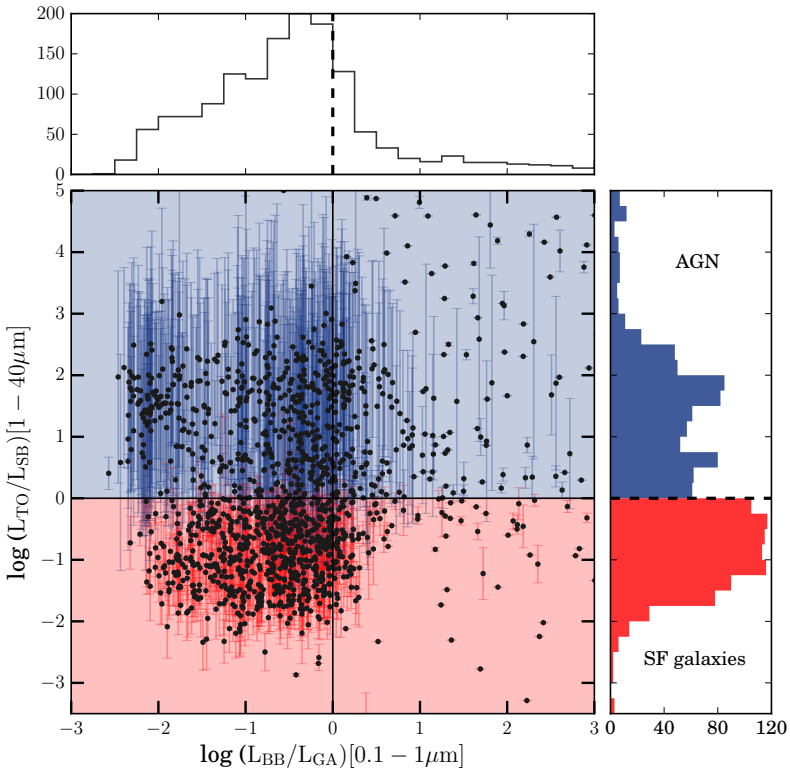

Figure 3.5: Classification into AGN and SF galaxies using ratios of integrated luminosities of galactic versus AGN components. Integrated luminosities were computed from component templates fitted with AGNFITTER. The red-shaded area shows the region populated by sources which are considered SF galaxies, while the blue-shaded areas are populated by sources classified as AGN. The data points are shown in black and their error bars are shown in red or blue, depending if their classified as SF galaxies or AGN, respectively.

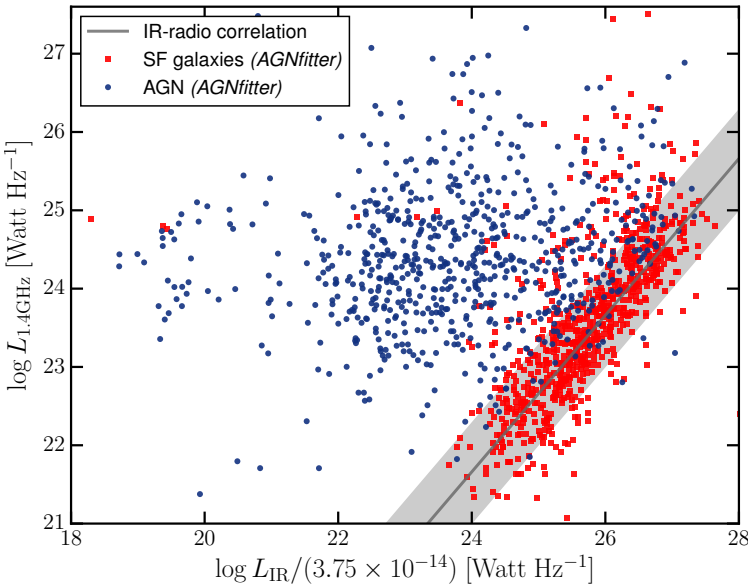

Figure 3.6: Comparison of the radio-independent classification by AGNFITTER to the IR-radio correlation. IR luminosities L_{IR} are inferred as the luminosities of the cold dust emission component in the sources' SEDs integrated within the range 8-1000 μm, while radio luminosities are k-corrected observations at 1.4 GHz, assuming a spectral index of $\alpha = -0.7$. The solid line represents the canonical value of the correlation $q = 2.3$, while the shaded area show a scatter of $\sigma = 0.5$. The red and blue data points represent the values for galaxies classified as SF galaxies and AGN respectively.

If the ratio of AGN torus to galaxy cold dust luminosities is greater than one ($\log(L_{TO}/L_{SB}) > 0$) the source is considered an AGN according to our scheme. In the optical, the classification as AGN is less stringent and the source may host an AGN both in the case were $\log(L_{BB}/L_{GA}) > 0$, where the accretion disk direct emission dominates the optical and if $\log(L_{BB}/L_{GA}) < 0$, where the source may present obscuration at nuclear scales and is considered an obscured AGN.

To test this classification, we take advantage of the availability of the radio data and use the infrared-radio correlation (IRC; e.g. Yun et al. 2001), which is a property observed almost exclusively by SF galaxies and radio-quiet AGN. Fig. 3.6 shows an excellent agreement between the radio independent classification method based on SED-fitting compared to the IRC results. This illustrates the capability of our method in classifying the sources into AGN and galaxies. Prior to our correction for contamination by LERGs our samples consists of 810 SF galaxies and 732 AGN, both populating the redshift range from 0.05 to 2.5.

3.4.3 Contamination by Low Excitation Radio Galaxies

A consequence of classifying AGN and galaxies based on their SEDs from the FIR-UV is that the population of LERGs are prone to be misclassified as galaxies, due to the lack of AGN signature in their non-radio SED. This mis-classification can be partially corrected by the assumption that LERGs would populate the area in the IRC typically covered by AGN, despite being classified as SF galaxies. In Fig. 3.6 LERG candidates are the red data points which are outliers from the IRC area ($q \sim 2.3 \pm 0.5$, as estimated below in section 3.6).

We applied a conservative correction for LERGs contamination and reclassified the LERG candidates into the AGN class by choosing the values below the 2.5 sigma region of the IRC value to be the division line ($q = 2.3 - 2.5\sigma = 0.8$, as observed for our sample). This correction finds a total of 52 LERGs in our sample, which represents around 7 per cent of the total AGN population in our data. To test our correction we investigate other properties of the 52 sources identified as LERGs. We find that although LERGs have IR luminosities dominated by SF processes by definition $\log(L_{TO}/L_{SB}) < 0$, the dominance is clearly weak ($\log(L_{TO}/L_{SB}) \sim -0.50 \pm 0.51$) compared to the values for SF galaxies ($\log(L_{TO}/L_{SB}) \sim -1.08 \pm 1.04$, were the errorbars represent the scatter given by the 14th and 86th percentiles). Since these sources present a tendency towards the values of the HERGs classified as AGN ($\sim 1.4 \pm 1.2$), these results support the reliability of our correction. For a detailed discussion of the properties of mass-selected LERGs and HERGs populations within Boötes see Williams et al. (in prep).

We note that this correction applies for sources where AGN and star-formation activity are mutually exclusive processes, but this is not generally expected since AGN activity may occur in strongly star-forming galaxies (Stevens et al. 2003; Rees et al. 2016). Moreover, since the IRC is a central topic of this work, the classification of our sources needs to be as independent of it as possible to avoid biases in the results. Through the chosen limits, we consider our correction is conservative enough for our purposes.

Our final sample consists of 758 SF galaxies and 784 AGN, which are well covered in the redshift range $z = [0.05, 1.7]$, while the redshift range $z = [1.7, 2.5]$ is slightly affected by incompleteness due to the flux limit of the data.

3.4.4 Comparison of the classification strategy with literature values

A classification based solely on the SED-fitting output yields that the relative source fractions of SF galaxies and AGN is 49 and 51 per cent respectively, given our LOFAR-I-band selected sample. A direct comparison to other observational and theoretical studies on this fraction is a complex task, since it is highly dependent on the sensitivity of the surveys (e.g. Jarvis &

Rawlings 2004; Appleton et al. 2004; Ibar et al. 2008; Simpson et al. 2012). For instance, a similar LOFAR-selected sample presented by Hardcastle et al. (2016) shows a number density split of SF galaxies to AGN of approximately 30/70. The lower SF galaxies fraction found can be explained due to the shallower radio data used in that study but also due to their different selection criteria (based on the FIR-radio correlation only). However, by using their selection criteria in our sample we still recover our original fraction of ∼50/50. Similarly, a study of radio sources selected at 3 GHz in the COSMOS field (Delvecchio et al. 2017) finds a SF galaxies/AGN ratio of ∼ 60/40 based on an equivalent SED-fitting classification.

Investigations of the SF galaxy fraction in 1.4 GHz radio surveys (e.g. Seymour et al. 2008; Bonzini et al. 2013; Smolčić et al. 2008) have found that while SF galaxies show predominance at low flux densities, the AGN population start dominating at 100 μJy. Assuming a spectral index value of ~ -0.7 this turning point corresponds to $\sim 600\,\mu$Jy at 150 MHz, which is close to the detection limit of our sources. Based on these assumptions, the observed 49/51 ratio in our study is thus in agreement with the ratio expected for the flux regime around the dominance turning point.

3.5 The radio SEDs of SF galaxies and AGN

We characterize the radio SED for galaxies and AGN by calculating the distributions of different spectral indices, which we define as:

$$\alpha_{\nu_1}^{\nu_2} = \frac{\log(S_{\nu_1}/S_{\nu_2})}{\log(\nu_2/\nu_1)}, \tag{3.1}$$

For the total sample we calculate the most general spectral index α_{150}^{1400} using only the two extreme points of the total frequency range studied, from 150 MHz to 1.4 GHz.

More detailed spectral properties such as curvature are studied by calculating adjacent frequency pairs, α_{325}^{1400} and α_{150}^{325} in Section 3.5.2. To reliably measure spectral indices over narrow frequency ranges requires higher signal to noise data. We therefore use a subsample with LOFAR fluxes above 2 mJy in order to minimize the effect of non-detections on these results. Finally, the spectral study is refined for a fraction of the total sample which has GMRT spatial coverage at 610 MHz in Section 3.5.3. For this sub-sample (25 per cent of the total) the distributions of three different spectral indices are calculated for adjacent frequency pairs α_{610}^{1400}, α_{325}^{610} and α_{150}^{325}.

3.5.1 Spectral index α_{150}^{1400} – all sources

The distribution of the spectral index α_{150}^{1400} in Fig. 3.7 includes the complete LOFAR-I-band selected sample. Note that we use forced photometry in the cases of non-detections in 325 MHz or 1.4 GHz. We obtain the median and scatter values for the distributions of SF galaxies and AGN: $\alpha_{150}^{1400} = -0.78^{+0.24}_{-0.24}$ and $\alpha_{150}^{1400} = -0.73^{+0.33}_{-0.30}$ respectively, derived according to the 16th, 50th and 84th percentiles of the total samples.

For a proper interpretation of the width of the distribution, whether it corresponds to measurement errors or intrinsic spread of the spectral index distribution, we fit a Gaussian distribution to the total samples. Using an MCMC algorithm (emcee: Foreman-Mackey et al. 2013) we infer the parameters μ and σ (mean value and intrinsic spread) that characterise the intrinsic distribution of the parameters, independently of the measurement errors. In order to avoid that extreme outliers have a strong effect on the fit we restrict the fit on 99.7 percent of the population distributed around the median value. We choose this very conservative cut in

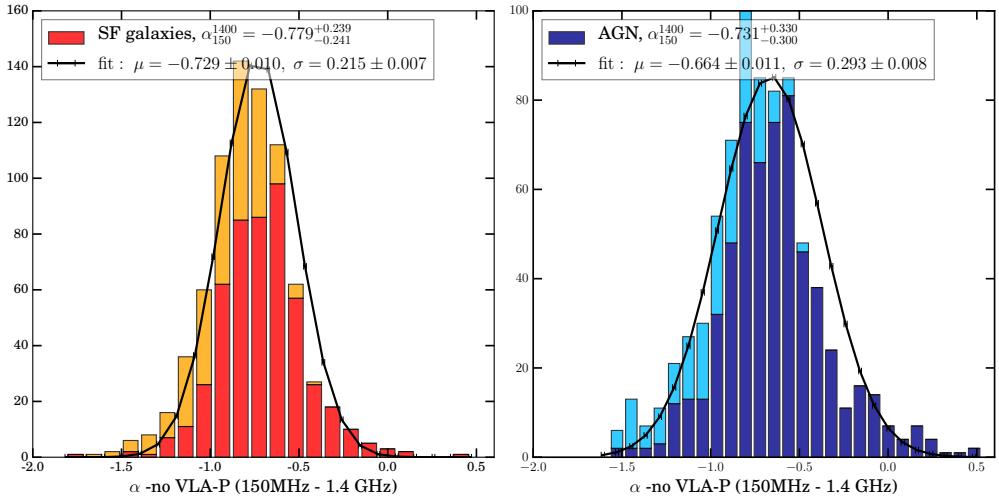

Figure 3.7: Spectral index α_{150}^{1400} for SF galaxies (*upper panel*) and AGN-dominated galaxies (*lower panel*). Values corresponding to the 16th, 50th and 84th percentiles are calculated for the total sample. Detected and undetected sources in 1.4 GHz are depicted in red and orange respectively for SF galaxies, and dark blue and sky blue for AGN. The *solid line* displays the fitted Gaussian with mean μ and intrinsic scatter σ.

order not to alter the shape of the distributions, which are characterised by longer tails than a normal distribution. The logarithm of the likelihood function obtained through the fitting of these parameters, assuming the measurement errors are Gaussian, is given by

$$ln\,\mathcal{L} = C - \frac{1}{2}\sum\left(ln(\sigma^2 + e_i^2) + \frac{(x_i - \mu)^2}{\sigma^2 + e_i^2}\right), \tag{3.2}$$

where σ (spread of the intrinsic distribution) and e_i (measurement errors) are coupled. Strictly speaking, the distribution described by Eq. 3.2 is not a Gaussian, but a weighted sum of Gaussians with varying widths. To visualize the shape of the intrinsic distribution, Gaussian distributions with the μ and intrinsic σ inferred above are over-plotted on the histograms of Fig. 3.7.[1]

The distribution of the SF galaxy sample is best fitted with a mean value $\mu = -0.729 \pm 0.010$ and intrinsic scatter of $\sigma = 0.215 \pm 0.007$, while the spectral index distribution for AGN presents $\mu = -0.664 \pm 0.0112$ and $\sigma = 0.294 \pm 0.008$. Although the median values of the SF-galaxy population are slightly higher than the AGN population, and the fitted mean values show a similar trend, both populations are consistent within the error bars. To test the difference between both distributions for significance we used the non-parametric two-sample Kolmogorov-Smirnov (KS) test and found that the distributions are statistically different at a confidence level greater than 99.9 per cent for all sources and even greater when considering only detections. In conclusion we find that using the total spectral index α_{150}^{1400} to characterize the radio SEDs of galaxies, a statistically significant difference between

[1]The slight apparent mismatch between the fit and the data (especially for the AGN sample) is explained by the presence of the small bulk of outlier sources at the high frequency tail of the spectral index distribution, by undetected sources (orange / sky blue bars) being weighted less than detections (red /dark blue bars) due to their larger errors (following Eq. 3.2) and by the fact that a Gaussian fit is only an approximate description of the distribution.

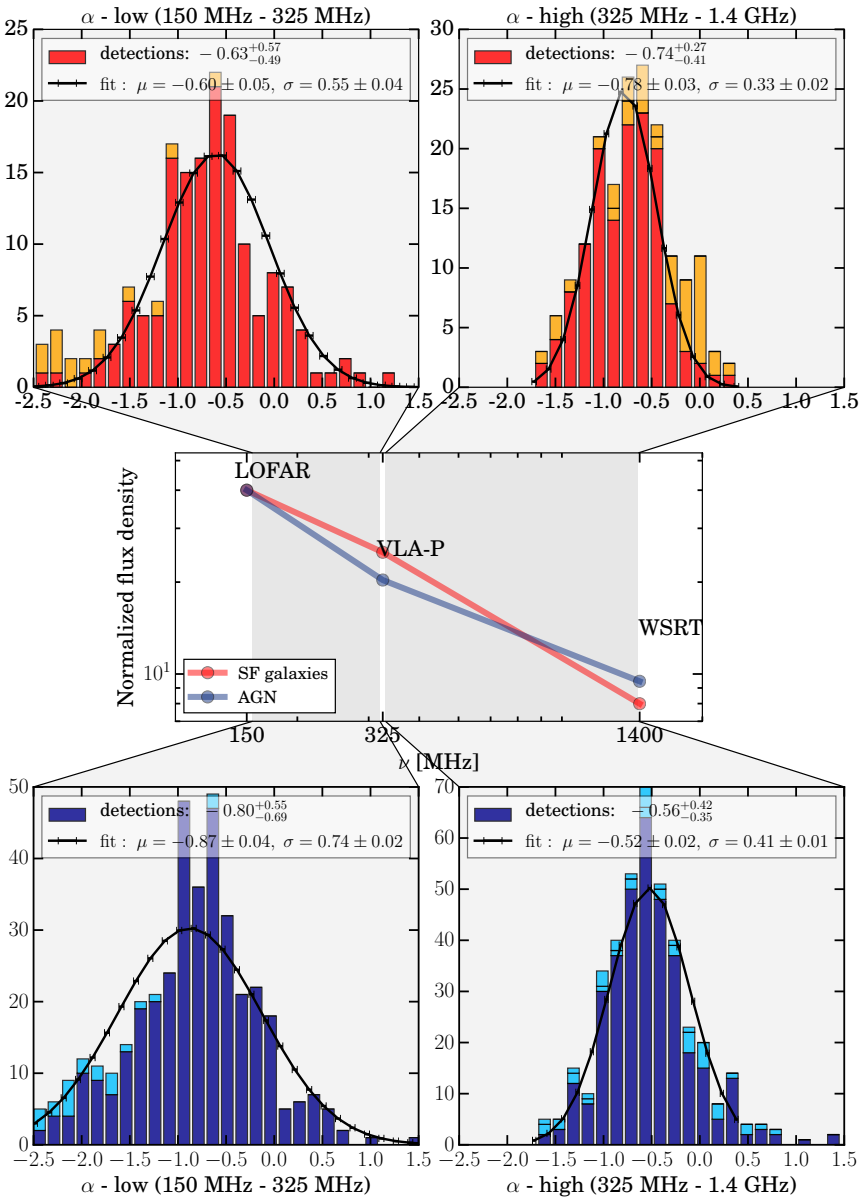

Figure 3.8: Spectral indices α_{325}^{1400} and α_{150}^{325} for SF galaxies (*upper panel*) and AGN-dominated galaxies (*lower panel*). Detected and undetected sources in 1.4 GHz are depicted in red and orange respectively for SF galaxies, and dark blue and sky blue for AGN. Median and scatter values corresponding to the 16th, 50th and 84th percentiles are calculated for all detected sources in VLA-P and WSRT ($\sim$ 90 per cent of the total). The *solid line* displays the fitted Gaussian with mean μ and intrinsic scatter σ. A schematic representation of the observed curvature is also shown in the central panel for SF galaxies (red line) and AGN (blue line).

starburst-dominated and the AGN-dominated sample is found, where the total sample of SF galaxies show a slightly steeper spectra than AGN with a difference in their median values of $\delta\alpha_{150}^{1400} = -0.048 \pm 0.011$. The resulting values agree with previous calculations of the low-frequency spectral slope in the literature (starbursts: Condon 1992; Ibar et al. 2008; Ivison et al. 2010a; Marvil et al. 2015), (AGN: Singh et al. 2013).

3.5.2 Spectral indices α_{150}^{325} and α_{325}^{1400}

Higher order spectral properties such as curvature and higher order features can be studied by adding the central P-band observations at 325 MHz to the data set.

Biased curvature observations due to non-detections

Before including the central data point, we need to model our expectations according to the characteristics of the available data. Following the distribution of α_{150}^{1400} presented above, a single slope spectrum around -0.73 and -0.67 for galaxies and AGN would imply observing similar values for the spectral indices α_{325}^{1400} and α_{150}^{325}, when adding the central data point at 325 MHz. However, measurement uncertainties can easily alter these observations and produce biased conclusions on curvature. An important bias is the detection level of the central band, which can severely compromise the interpretation of steep spectra undetected in this band, shifting the median to flatter spectra towards lower frequencies. We simulated the behaviour of our sample of LOFAR selected sources assuming that their spectral indices follow the ones observed in the histograms of Fig. 3.7, and proceed to mimic similar systematics to those of our sample to investigate the expected values after the addition of the 325 MHz data point. The distributions resulting from the simulations show a clear offset in these values compared to the initial distribution; demonstrating the biasing effect of using upper limits or excluding undetected sources without a proper treatment.

We would like to point out that this is important for the interpretation of results on radio continuum studies constructed from data of diverse sensitivity similar to ours (see e.g.: Marvil et al. 2015; Clemens et al. 2010). To overcome these biases we proceed with a cut in LOFAR fluxes and select sources above 2 mJy, reducing the percentage of undetected sources in VLA-P from 41 per cent to 14 per cent for SF galaxies and 27 per cent to 10 per cent for AGN, leaving us still with a large enough sample for a statistical study with 189 SF galaxies and 421 AGN.

Results on flux-selected sources with $S_{150} > 2.0$ mJy

Histograms of the low and high frequency spectral indices for SF galaxies and AGN are presented in Fig. 3.8. We quote the median values and scatter based on the 16th and 84th percentiles of the distributions and fit a Gaussian to the distribution of sources with VLA-P detections (red and dark blue areas for galaxies and AGN respectively).

The upper panel of Fig. 3.8 shows the median and scatter values of the spectral index distributions for SF galaxies: $\alpha_{150}^{325} = -0.63_{-0.49}^{+0.57}$ and $\alpha_{325}^{1400} = -0.74_{-0.41}^{+0.27}$. A simple comparison of the median values of the two different spectral index distributions (similarly, using mean values from the fitted Gaussian curves) shows in general a slight flattening towards lower frequencies. Using the non-parametric two-sample KS-test, we find that the difference between the low- and high frequency distributions of SF galaxies is highly significant at a level greater than 99.99 per cent (p-value$< 10^{-11}$). Our statistical study thus concludes that the spectral continuum for our SF galaxy sample is consistent with a curved spectrum, showing a slight flattening towards lower frequencies.

Similarly, the lower panels of Fig. 3.8 present the median and scatter values for the population of AGN: $\alpha_{150}^{325} = -0.80^{+0.55}_{-0.69}$ and $\alpha_{325}^{1400} = -0.56^{+0.42}_{-0.35}$. In contrast to the SF galaxies population, the medians of the distributions and fitted mean values in the lower panels of Fig. 3.8 show a steepening towards lower frequencies with a difference in the mean values of the Gaussian fits of $\Delta\alpha \sim -0.35 \pm 0.05$. Also here, we test this observation for statistical significance using the two-sample KS-test. We find that the sample of galaxies hosting AGN present curvature in their radio SED with a confidence level greater than 99.99 per cent (p-value$< 10^{-11}$). Our study thus concludes that radio SEDs of AGN in our sample show a statistically significant steepening in their radio continuum going to lower frequencies.

These results will be discussed in a physical context in section 3.5.6. We would like to remark that the significant differences found between the spectral curvature of SF galaxies and AGN in Fig. 3.8 confirm that the observed curvature is a real spectral feature and not due to calibration issues in our sample.

3.5.3 Spectral indices α_{150}^{325}, α_{325}^{610} and α_{610}^{1400}

We take advantage of the partial availability of GMRT data at 610 MHz and construct low-frequency radio SEDs with four data points for the fraction of sources that lie inside the GMRT coverage (green region in Fig. 3.1). The GMRT subsample constitutes 24 per cent of the total sample of LOFAR-I-band selected sources with LOFAR fluxes $S_{150} > 2$ mJy, which implies a total of 198 sources. Only 11 per cent have VLA-P non-detections and are replaced by forced-photometry. Taking into account detected sources this sub-sample consists of 41 SF galaxies and 101 AGN.

As expected from a solely spatial cut, the spectral index distributions present similar median values to the total field, with general spectral indices for SF galaxies of $\alpha_{150}^{1400} = -0.80 \pm 0.27$, and for AGN of $\alpha_{150}^{1400} = -0.70 \pm 0.31$. Adding one more data point to the radio SEDs, we calculate the three spectral indices α_{150}^{325}, α_{325}^{610} and α_{610}^{1400} following Eq. 3.1. Constructing the total SED, as sketched in the central panel of Fig. 3.9, we are able to recover spectral index ratios which suggest a consistent behaviour (within the larger statistical errors) with our previous finding in Fig. 3.8.

The upper and lower panels of Fig. 3.9 show three spectral index distributions for low, medium and high frequency pairs for both SF galaxies and AGN, respectively. While the distributions' median values for SF galaxies ($\alpha_{610}^{1400} = -0.82, \alpha_{325}^{610} = -0.89$ and $\alpha_{150}^{325} = -0.65$) suggest a slight tendency to have flatter spectra towards low frequencies, the distributions' medians for AGN ($\alpha_{610}^{1400} = -0.59, \alpha_{325}^{610} = -0.63$ and $\alpha_{150}^{325} = -0.67$) are consistent with a steepening of the continuum going towards lower frequencies. A quick examination to these characteristic values suggest these results are similar to the results of section 3.5.2, finding curvature as sketched in the middle panel of Fig. 3.8.

To test this systematic curvature for statistical significance, a KS-test on the difference of the spectral index distributions was performed. Comparing all three spectral index distributions at adjacent frequency pairs we find that the curvature is not statistically significant, since the KS-test could not reject the null-hypothesis due to the small statistics of the sub-sample with GMRT coverage (40 SF galaxies and 102 AGN). However, a KS-test on the distributions of the spectral indices at the extremes of the frequency coverage, α_{610}^{1400} and α_{150}^{325}, shows that a difference between these distributions is statistical significant for the AGN population at a level of 98 per cent, consistent with curvature and confirming the results of the previous section. For the SF-galaxy population this is not the case. This may be due to the small sample used for the study in this section (40 sources), which weakens the statistics.

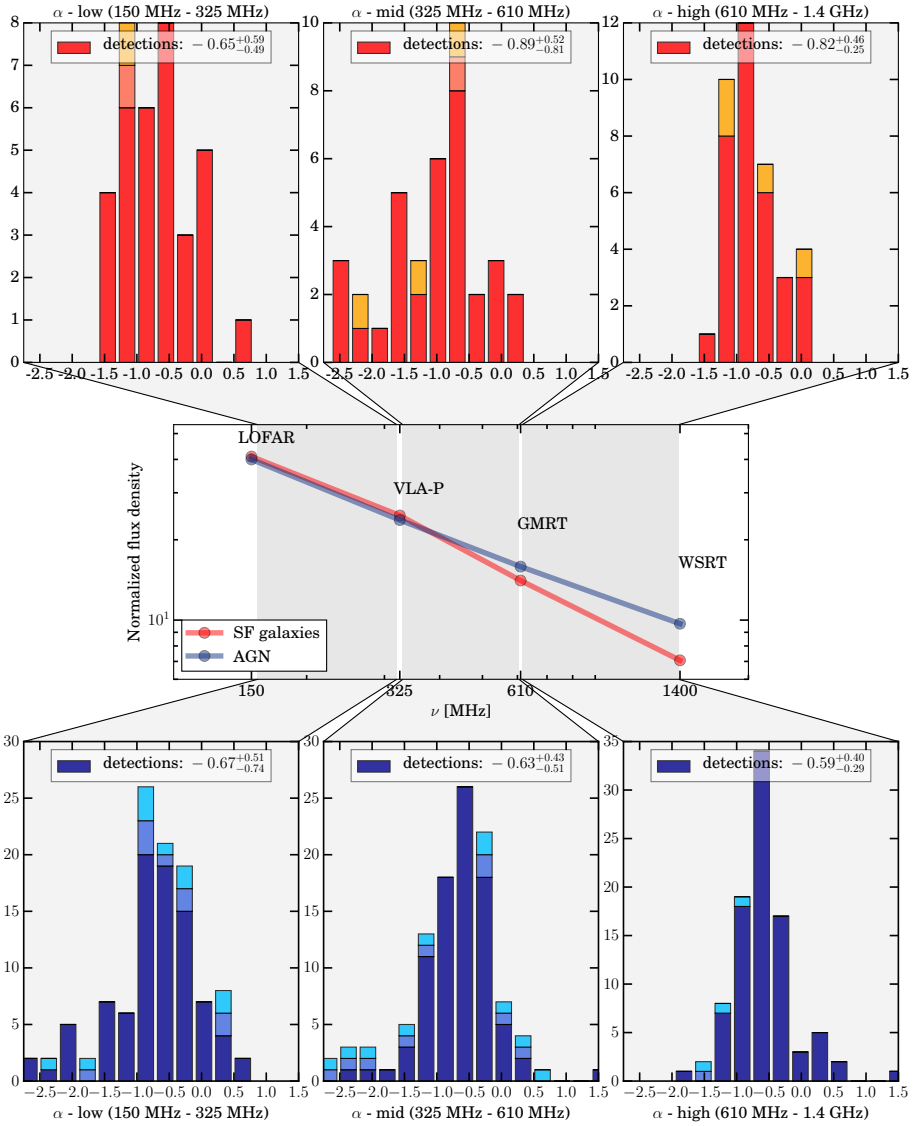

Figure 3.9: Spectral indices α_{610}^{1400},α_{325}^{610} and α_{150}^{325} for SF galaxies (*upper panel*) and AGN-dominated galaxies (*lower panel*). These distributions corresponds to the fraction of our sample with GMRT coverage (see Fig. 3.1), which makes up ∼ 25 per cent of the total sample. Detected and undetected sources in 1.4 GHz are depicted in red and orange respectively for SF galaxies, and dark blue and sky blue for AGN. Values corresponding to the 16th, 50th and 84th percentiles are calculated for all detected sources in VLA-P and WSRT (∼ 95 per cent of the total). A schematic representation of the observed curvature is also shown in the central panel for SF galaxies (red line) and AGN (blue line).

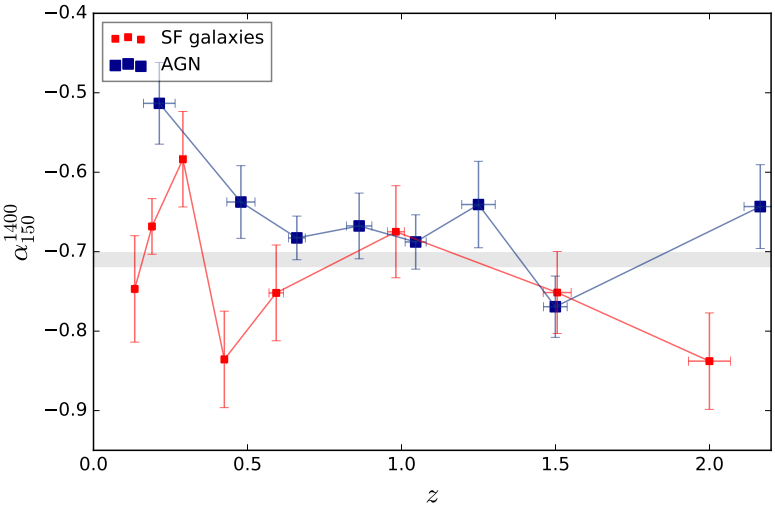

Figure 3.10: Evolution of spectral index α_{150}^{1400} as a function of redshift for SF galaxies (red) and AGN (blue). The data points are the mean values of α_{150}^{1400}, grouped in bins of equal density. The error bars represent bootstrap errors.

3.5.4 Redshift evolution of the spectral curvature

In Figs. 3.10 and 3.11 we study the redshift evolution of the total spectral index α_{150}^{1400} and the curvature parameter $\alpha_{150}^{325} - \alpha_{325}^{1400}$, respectively. For this study we use the samples with detections in both VLAP and WSRT (∼90 per cent of the sample with $S_{150} > 2.0$ mJy), which correspond to the characteristic values estimated from the distributions in Fig. 3.8.

Investigating the change in total slope as a function of redshift is important to validate the approximation of a single power law as the k-correction for radio luminosities. This assumption holds as long as the SED slope remains constant at the rest-frame frequencies for low redshift (150 MHz-1.4 GHz at $z \sim 0$) and high redshift (450 MHz-4.2 GHz at $z = 2$) sources. Fig. 3.10 shows that evolution of the slope as a function of redshift cannot be clearly recognized for either populations but shows a large scatter around the canonical value of $\alpha_{150}^{1400} = -0.7$. Specifically for AGN, some data points in Fig. 3.10 may suggest an unclear trend as a function of redshift. However, using a linear fitting to the data points we find a redshift evolution very close to 0 (slope= -0.05 ± 0.03). We also tested the robustness of this finding using different binning schemes and the result remains consistent. This result is expected since the rest-frame frequency range covered by our sample should be completely dominated by synchrotron emission and the strong flattening from thermal emission should not be visible below frequencies around 10 GHz (e.g. Gioia et al. 1982).

A non-evolving mean spectral slope disfavours a scenario where the synchrotron spectral shape would be significantly affected by large scale properties of the galaxy that present a strong redshift evolution, such as integrated luminosities or SFRs. On the contrary, the absence of such an evolution suggests that the synchrotron emission would be determined by other rather local properties affecting the CR injection mechanisms that are not coupled to an evolution in redshift. Examples of such processes are CR acceleration mechanisms and energy losses confined to sub-kpc structure around individual supernova remnants, galactic magnetic fields, and the immediate surrounding interstellar medium. We suspect these local properties establish the shape of the radio SED, while differences in global properties may

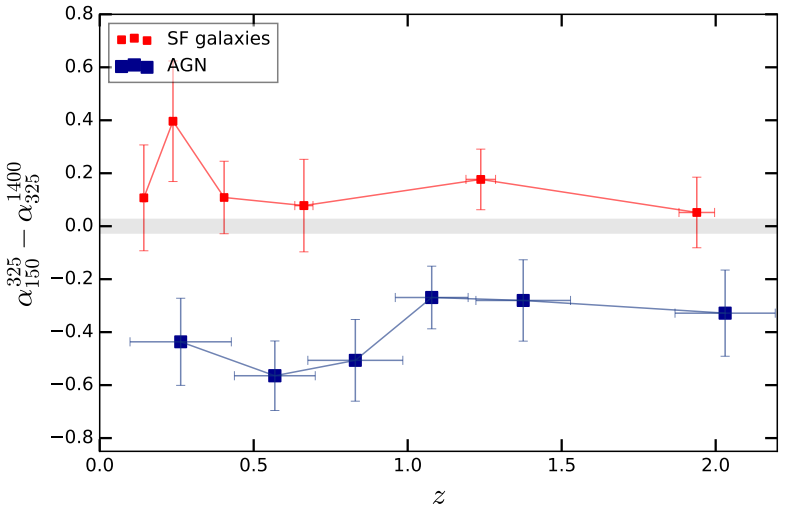

Figure 3.11: Evolution of the spectral curvature parameter ($\alpha_{150}^{325} - \alpha_{325}^{1400}$) as a function of redshift for SF galaxies (red) and AGN (blue). The data points are the mean values of the curvature parameter, binned in groups of equal density in redshift. The error bars represent bootstrap errors.

primarily affect the normalisation of the spectrum. This result is consistent with the findings of Magnelli et al. (2015) and Ivison et al. (2010b), who found no significant evolution of the spectral index $\alpha_{610\mathrm{MHz}}^{1.4\mathrm{GHz}}$ with redshift across $0 < z < 3$ for SF galaxies.

Fig. 3.11 shows the redshift evolution of the spectral curvature, parametrized as the difference between spectral indices α_{150}^{325} and α_{325}^{1400}, binned in six different redshift bins of equal sample sizes. The most remarkable observation is that a contrast between the curvature of both populations is clearly present at all redshifts. While SF galaxies show continuously positive values of $\alpha_{150}^{325} - \alpha_{325}^{1400}$, AGN present negative values, consistent with Figs. 3.8 and 3.9.

We find no clear evolution of the curvature with redshift for both SF galaxies and AGN populations, as shown in Fig. 3.11. We quantify this by fitting straight lines of different slopes for both binned populations. We find that the slope for the SF galaxies population is consistent with zero (-0.055 ± 0.103), while the slope for AGN is found to be 0.147 ± 0.096. We test these results for significance by calculating the coefficient of determination statistics R^2, which describes the proportion of the variance in the curvature parameter that is predictable from the redshift evolution given by the fit. From the results of the coefficient of determination we find that the fits for the SF galaxies and AGN populations account for less than 13 and 40 per cent of the scatter respectively. Given the very small slope values, the relatively large errors and the low values of R^2, we conclude that we find no significant redshift evolution of the spectral curvature.

Finally, we explore the redshift dependence of the total sample if undetected sources were also included. Although non-detections produce no significant differences to the total characterization of the curvature due to their low fraction (10 percent), we find that they imprint a weak redshift dependence on the results. This effect occurs since luminosities of undetected fluxes are calculated as the product of a narrow distribution of fluxes close to the noise limit and the squared luminosity distance which imprints a strong redshift dependence. This observation is especially important for samples of large non-detection fractions, as we will discuss

in section 3.6.

3.5.5 Spectral curvature dependence on other properties

To investigate the origin of the spectral curvature for galaxies and AGN, we studied its dependence on the different physical properties inferred by SED-fitting. For the SF galaxy sample, no dependence on IR luminosity was found and consequently on SFR_{IR}. Similarly we investigated the evolution of spectral curvature as a function of specific star formation rate sSFR, estimated by the SED fitting routine, and found no significant dependence.

For the AGN sample, a significant evolution was found as a function of the integrated luminosity of the torus component L_{TO}, which represents a proxy for the total AGN power. As shown in Fig. 3.12, this suggests that more powerful AGN seem to present weaker curvature, i.e. flatter spectra. We quantify this by fitting straight lines of different slopes to the z-evolution of the binned AGN population presented in Fig. 3.12. We estimate the slope to be 0.168 ± 0.019, where the fit accounts for 93 per cent of the scatter according to the coefficient of determination of this fit. Since the spectral curvature of AGN does not present a redshift dependence as significant as this luminosity dependence (Fig. 3.11), our results suggest that AGN-luminosity is the driver of this spectral curvature trend. We discuss these observations in section 3.5.6.

3.5.6 Comparison with previous spectral index studies

In this section radio SEDs from 150 MHz to 1.4 GHz have been constructed for the total population of LOFAR-selected sources with fluxes above 2 mJy. Our results suggest the presence of oppositely directed curvature in the radio continuum of star-forming compared to AGN-dominated galaxies. While SF galaxies present a slight flattening towards lower frequencies suggesting positive curvature, AGN radio SEDs reveal a systematic steepening towards lower frequencies, implying negative curvature. Moreover, no redshift evolution of the spectral curvature was found for both the SF galaxy and AGN populations. Comparing our results to previous findings in the literature is not a trivial task due to the unparalleled depth of our observations, particularly at low frequencies, which allows us to study the radio SED properties of sources to higher redshifts and lower luminosities than previous studies.

SF galaxies

Several studies of the radio SEDs of nearby SF galaxies agree with our results that positive curvature is not an unusual spectral property at low frequencies (e.g. Marvil et al. 2015; Murphy et al. 2013; Williams & Bower 2010; Clemens et al. 2010; Condon 1992; Israel & Mahoney 1990), although few differences are to be noted. For instance, the average spectrum of Marvil et al. (2015) nearby sources is curved following a change of $\Delta\alpha = 0.2$ per logarithmic frequency decade towards lower frequencies, which is a stronger flattening than that found in this study ($\Delta\alpha = 0.1$). One possible explanation is that Marvil et al. (2015) include a large fraction of non detections at the central wavelengths (> 60 per cent for two of the four frequencies sampled), which is an important source of biased curvature if the results of our simulation in Section 3.5.2 applies here as well. Similarly, Clemens et al. (2010) studied 20 nearby LIRGS and ULIRGS from 244 to 8.4 GHz, finding complex curvature in their source as well as claiming not only flattening but a strong turn over at around 1 GHz, which when extrapolated towards lower frequencies, implies a positive spectral index at frequencies < 1 GHz. With the availability of LOFAR data at 150 MHz we can confirm this is not the case

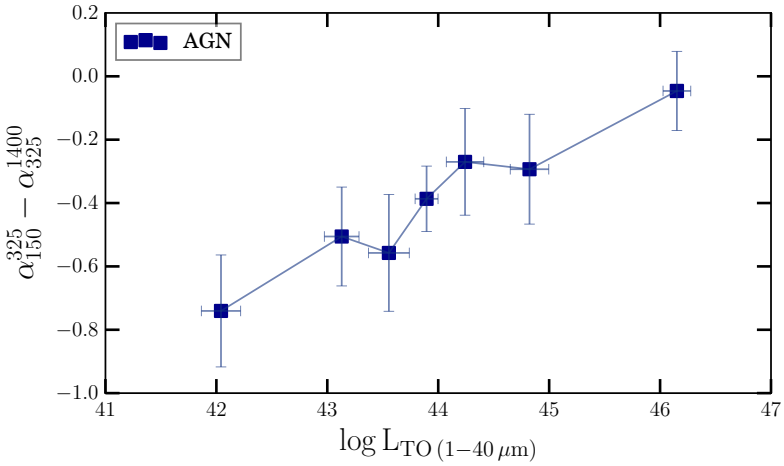

Figure 3.12: Curvature observed in AGN plotted against the torus luminosity L_{TO}, integrated in the wavelength range 1-40 μm. The data points are the mean values of the curvature parameter, binned in groups of equal density in L_{TO}. The error bars represent bootstrap errors.

for most of the SF galaxies present in our field but the curvature is rather small, presenting a slightly flatter slope but still of negative sign.

Spectral flattening in SF galaxies hints towards physical conditions which, integrated over the total galaxy, appear to be a common property in our SF galaxies sample and are expected to remain constant at all redshifts. These conditions can be intrinsic to the production of the cosmic ray electrons (CRE) responsible for the synchrotron emission component (Basu et al. 2012) or environmental, connected to the extreme interstellar medium (ISM) in star-forming regions into which the CREs are injected (Lacki 2013). Consistent with the second hypothesis, Murphy et al. (2013) find increasing flattening of radio spectral index of galaxies with increasing specific star formation rate (sSFR). We find such a dependence neither for sSFR nor for SFR. Similarly, Basu et al. (2015) find that the flattening of the spectral index of nearby SF galaxies is unlikely to be caused by thermal free-free absorption but instead suggest a dependence on gas surface density. Due to the lack of gas surface density tracers in our sample, we can not test for this.

AGN

Other attempts have been made in the construction of radio SED for radio AGN, but these have been limited to small samples and/or single spectral index studies (e.g. Laing & Peacock 1980; Singh et al. 2013; Mauch et al. 2013; Kharb et al. 2016; Hardcastle et al. 2016). Understanding the physical processes which drive integrated radio spectra of AGN is not an easy task due to the multiple physical conditions contributing to its total emission, as multi-component structures and orientation effects, and hence studies have focused on spectral index maps (α maps) of spatially resolved sources (Vardoulaki et al. 2015; Harwood et al. 2015). For instance, in the case of FRI and FRII sources, the spectral shape can be dramatically different between jet, lobes to hot spots due to spectral ageing (Harwood et al. 2015). While hot-spots are sources of constant CRE supply and present flat spectral indices (Laing & Peacock 1980), lobes consist of earlier-ejected material which has lost energy, producing considerably steeper radio spectral indices. The overall spectrum thus depends on the history and environment of

the radio source.

An important question to understand the integrated radio spectra is which of the physical components dominate the total emission, at different frequency ranges, and across different orders of magnitude in luminosity? A basic consensus among the observations is that radio AGN present generally flatter spectra in the GHz regime than SF galaxies (Murphy et al. 2013), similar to our finding in Section 3.5 and, mainly for sources at $z > 0.7$ and frequencies $\nu > 325$ MHz, in Fig. 3.8. As hot-spots can be the dominant source in total flux density in luminous sources (Jenkins & McEllin 1977), this could suggest that these frequencies are dominated by hotspot emission. Consistent with our observation in Fig. 3.12, Laing & Peacock (1980) finds a luminosity dependence of the integrated spectral shapes for a sample of radio sources selected at 178 and 2700 MHz, arguing that more powerful sources have flatter spectra than weaker sources, while weaker sources have spectra which steepen at low frequencies (but see also Rees et al. 2016, for different results). While their study is limited to a much smaller sample and luminosity range due to their shallower data, we are able to confirm the luminosity dependence, ruling out a redshift dependence. The steepening at low frequencies observed for our weaker AGN sources could be explained by steep-spectrum components dominating in this frequency regime, while flat-spectrum components become relatively more important at higher frequencies, causing the spectral index to flatten. These observations are in good agreement with the results presented by Whittam et al. (2016). They report spectral flattening for radio-selected galaxies at the high-frequency end (15.7 GHz) and suggest this may be due to the cores of Fanaroff & Riley (1974) class I sources (FRI) becoming dominant at these high frequencies.

However, considering high flux uncertainties is especially relevant for AGN due to the different combinations of resolution and source extraction methods used, as they are extended sources. In contrast, this is not a relevant issue for SF galaxies, which are mostly compact sources. These uncertainties might weaken the strength of our conclusions on AGN and better radio data and larger samples are needed to confirm this finding.

3.6 The infrared-radio correlation (IRC)

A remarkable property intrinsic to the radio SED of SF galaxies is the tight correlation with infrared luminosity, which has been observed at a few radio bands across five orders of magnitude in luminosity (Yun et al. 2001). In this section we will characterize the IRC for the 1.4 GHz and the LOFAR data at 150 MHz and investigate its evolution with redshift for our sample. For this study we include all detected and undetected sources in both the 1.4 GHz WSRT and the *Herschel*-SPIRE data. As explained in detail in section 3.3.2, undetected fluxes are estimated using forced photometry measurements on the positions of LOFAR-detected sources. In this section we discard AGN and consider only sources selected as SF galaxies from the total LOFAR-I-band sample, which comprises ~810 galaxies.

The IRC is parametrized by the widely used value $q_{\rm irc}$, which is defined as the ratio

$$q_{irc} = \log\left(\frac{L_{\rm IR}/(3.75\times10^{12}\ {\rm Hz})}{L_{\rm radio}}\right), \tag{3.3}$$

where $L_{\rm IR}$ is the total rest-frame infrared luminosity (in erg s^{-1}) of the cold dust SED template integrated along the rest-frame frequency range $8-1000\,\mu$m (equivalent to Helou et al. 1985; Bell 2003; Ivison et al. 2010a; Sargent et al. 2010; Bourne et al. 2011; Murphy et al. 2011). $L_{\rm radio}$ is the luminosity at the radio frequency to be studied, in this case 1.4 GHz or 150 MHz in erg s^{-1} Hz^{-1}. The factor 3.75×10^{12} Hz is the frequency corresponding to 80 μm, used in the definition to make q_{irc} a dimensionless quantity.

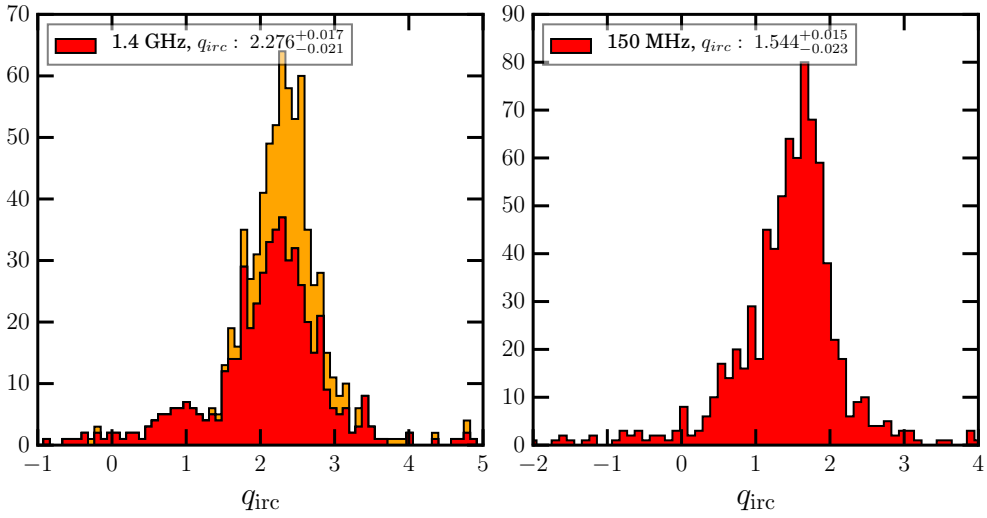

Figure 3.13: Histograms representing the distributions of q_{irc} for the subsample of SF galaxies only. The q_{irc} values are calculated using radio luminosities at 1.4 GHz (*upper panel*) and at 150 MHz (*lower panel*). Red bars represent detections at the corresponding radio frequencies, while orange bars represent forced-photometry values at 1.4 GHz. We quote the median values of q_{irc} in the legends, where the error bars represent the error on the median. Note that the small number of outlier galaxies with low q_{irc} values in both panels (misclassified by our IR-based method) were carefully excluded for the redshift-evolution study in Fig. 3.14.

Radio rest-frame luminosities are computed using k-corrections inferred assuming $S_\nu \propto \nu^\alpha$, where α is the mean value observed for the SF galaxies distribution $\alpha = -0.73$ (see Fig. 3.7). We use a fixed α value for this study, since the available data does not sample the radio SED curvature accurately enough for a useful k-correction.

In contrast to most previous studies, our unique infrared coverage and the large dust models library allow us to robustly compute the total infrared luminosities. This approach has several advantages over using bolometric corrections based on monochromatic luminosities and single models as discussed by Smith et al. (2014). Moreover our MCMC approach in SED fitting allows us to infer robust uncertainties for the luminosities and consequently for q_{irc}.

3.6.1 The IRC at 1.4 GHz and its redshift evolution

While 1.4 GHz luminosities of SF galaxies clearly follow the IRC (Fig. 3.6), in the upper panel of Fig. 3.13 $q_{1.4}$ is scattered in a distribution with a median value of $q_{1.4} = 2.28^{+0.017}_{-0.021}$, where the error bars represent the error on the median. Fig. 3.13 reveals a small number of outlier galaxies exhibiting a radio excess, which is the consequence of contamination as part of our IR-based classification. Note that these were carefully excluded for the redshift-evolution study in the next section. This $q_{1.4}$ distributions agrees well with the literature within the errors, although it is slightly lower than most of the local values observed for local SF galaxies (e.g. using FIR emission: $q_{1.4} = 2.34 \pm 0.26$ Yun et al. (2001), $q_{1.4} = 2.3$ Helou et al. (1985), using total IR emission as in our case: $q_{1.4} = 2.64 \pm 0.26$ Bell (2003)). In this section we investigate which parameter drives this offset and is able to explain the scatter observed.

In Fig. 3.14 we test the evolution of $q_{1.4}$ (1.4 GHz) as a function of redshift. To quantify a redshift evolution we fit the function: $q_{1.4} = C \times (1+z)^\gamma$, where C is a constant and γ the variable driving the evolution. We include only 86 per cent of sources, which lie within the 2σ region of the distribution in Fig. 3.13, so that the fit is not driven by outliers. To account for measurement uncertainties in both variables and intrinsic scatter, the linear regression to infer the parameters is based on the likelihood function

$$\mathcal{L} = \sum \left(\sigma_{\rm tot} + \frac{(q_{\rm obs} - (C \times (1+z)^\gamma))^2}{\sigma^2_{\rm tot}} \right), \tag{3.4}$$

where

$$\sigma_{\rm tot} = \sqrt{\sigma^2_{\rm int} + \Delta q^2_{obs}} \tag{3.5}$$

The fitting results for $q_{1.4}$ in Fig. 3.14 suggest an evolution with redshift given by

$$q_{1.4}(z) = (2.45 \pm 0.04) \times (1+z)^{-(0.15 \pm 0.03)} \tag{3.6}$$

with an intrinsic scatter of $\sigma_{\rm int} = 0.53$.

As expected, after the fit for redshift evolution the value $q_{1.4}$ at $z = 0$ is higher than the median value of the total sample by $\delta = 0.11$. To infer the proportion of the variance in the distribution of Fig. 3.13, which is explained by the z-evolution, we infer the coefficient of determination R^2, defined in this case as,

$$R^2 = \frac{\sum_i (q_{\rm obs-i} - q_{1.4}(z_i))^2}{\sum_i (q_{\rm obs-i} - \langle q_{\rm obs} \rangle)^2} \tag{3.7}$$

where $q_{\rm obs-i}$ are the observed q-values and $q_{1.4}(z)$ are values calculated following Eq. 3.6. We calculate that the redshift evolution accounts for ~ 6 per cent of the variance in the total distribution, while most of the intrinsic scatter is still not explicable.

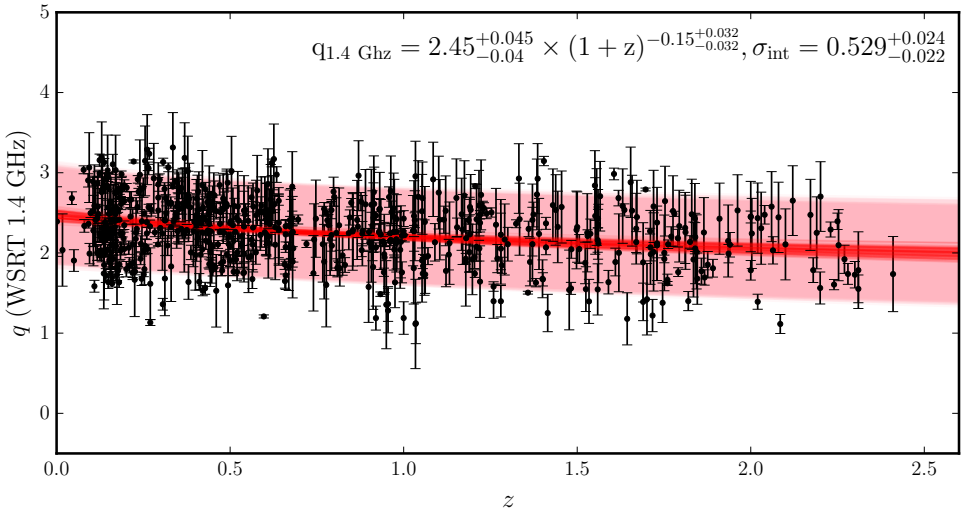

Figure 3.14: q-value for the IRC corresponding to radio luminosities at 1.4 GHz plotted against redshift. Black error bars depict the observed values within the 2σ region of the q-distribution in Fig. 3.13, while red lines correspond to the fitted q-values inferred by the equation in the legend, taking into account uncertainties on the parameters calculated through MCMC sampling. The pink shaded area correspond to the fitted intrinsic scatter of the correlation.

A dependence of the $q_{1.4} - z$ evolution on the $\alpha - z$ evolution around 1.4 GHz is unlikely, since this would imply a clear evolution of α_{tot} in Fig. 3.10, which is not observed. Moreover, since the spectral curvature discussed in our study is observed only at lower frequencies this should not affect the k-correction for the 1.4 GHz luminosities. To investigate whether this redshift dependency is rather a luminosity dependence of the $q_{1.4}$ we separated the total sample into luminosity bins of similar sample sizes and were able to confirm a redshift evolution inside most of the luminosity bins, discarding such a degeneracy (see plots in Appendix 3.A for details). Finally, we test whether the z-evolution of $q_{1.4}$ is related to a changing ratio of AGN and SF contribution to the IR emission ($L_{\mathrm{TO}}/L_{\mathrm{SB}}$). We find no correlation between these quantities indicating that the redshift evolution is not due to AGN contamination.

We discuss possible explanations to the offset observed between the mean $q_{1.4}$ of our sample ($q_{1.4} \sim 2.28 \pm 0.02$) and the local mean IRC found by (Bell 2003, $q_{1.4} \sim 2.64 \pm 0.26$)). An important factor to take into account in IRC studies is its sensitivity to selection biases (Sargent et al. 2010). A common selection bias in radio-selected samples arises from samples being incomplete at IR data for sources with faint radio fluxes (Ibar et al. 2008; Sargent et al. 2010). This might not affect our sample, since the FIR emission expected for the 150 MHz fluxes in our sample (based on the IRC) is considerably above the flux limit of the XID SPIRE fluxes (Roseboom et al. 2010). Non-detections comprise less than 17 per cent and are compensated using forced photometry. Moreover, as discussed above, no direct dependence of the z-evolution of $q_{1.4}$ on radio luminosity could be found (Appendix). We note that by using a radio-selected sample we might be losing the FIR-dominated sources which drop out at the radio at the high redshift end of our sample and could shift the distribution to lower $q_{1.4}$ values. However, Casey et al. (2012) remarked that the XID SPIRE fluxes are complete in relation to a pure SPIRE selected sample and that the fraction of sources that

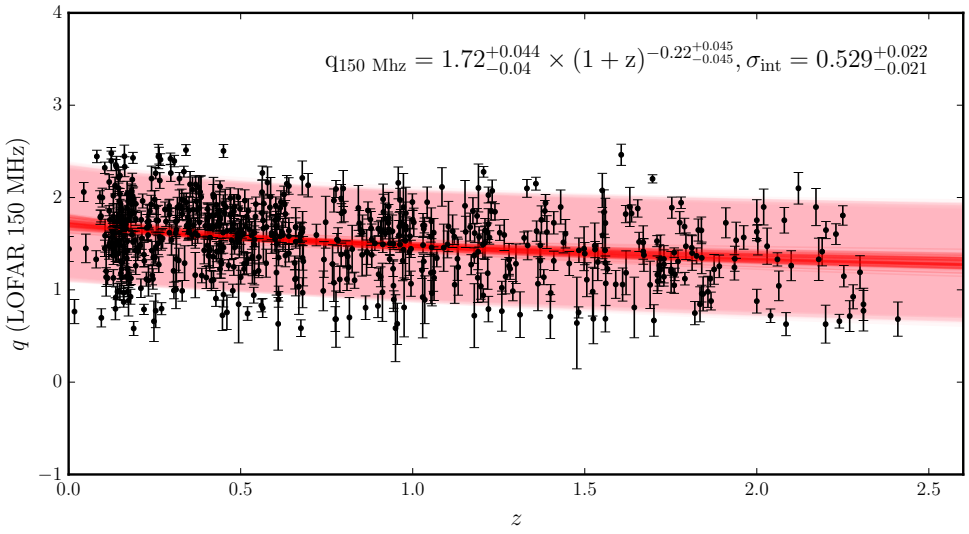

Figure 3.15: q-value for the IRC corresponding to radio luminosities at 150 MHz plotted against redshift. Black error bars depict the observed values within the 2σ region of the q-distribution in Fig. 3.13, while red lines correspond to the fitted q-values inferred by the equation in the legend, taking into account uncertainties on the parameters calculated through MCMC sampling. The pink shaded area correspond to the fitted intrinsic scatter of the correlation.

could drop out in the radio at $z < 2$ is negligible. Since > 90 per cent of the sources in our sample have redshifts $z < 2$, the possible bias against faint radio sources is not significant.

The mean $q_{1.4}$ value of our total distribution is lower ($\delta q_{1.4} \sim 0.36$) than the local mean IRC presented by Bell (2003). However, from the fitted redshift-evolution in Equation 3.6 the predicted $q_{1.4}$ value corresponding to the local universe would be $q_{1.4} \sim 2.45$ which is well within the error on the mean quoted by (Bell 2003, $q_{1.4} \sim 2.64 \pm 0.26$)). The tension between our observations and those by Bell (2003) is therefore reduced. The offset between the mean $q_{1.4}$ values can be primarily explained by the redshift evolution and the different redshift ranges probed in the two studies.

The picture of decreasing $q_{1.4}$ values as a function of redshift is being supported by a number of studies based on FIR and radio data sets of variate properties. Although some theoretical studies predict the opposite trend (Schober et al. 2016) and few observational studies claim to find no observable trend (Pannella et al. 2015), a long list of recent *Herschel*-FIR and *Spitzer*-IR based studies have observed a redshift evolution of $q_{1.4}$ (e.g., Ivison et al. 2010a; Bourne et al. 2011; Casey et al. 2012; Jarvis et al. 2010; Smith et al. 2014; Magnelli et al. 2015; Delhaize et al. 2017). However, some of these studies have chosen to favour a no-trend scenario due to the modest evolution compared to the large size of their measurement errors or other observed dependences. It is reassuring that our results are consistent with studies that take into account the treatment of biases due to selection as presented by Ivison et al. (2010a), which compare different selections to test their results and Magnelli et al. (2015), which is based on a mass-selected galaxy sample. They find an evolution that goes as $q_{1.4} \propto (1+z)^{-0.12}$ and $q_{1.4} \propto (1+z)^{-0.15}$ respectively. Similarly, Delhaize et al. (2017) find a redshift evolution of $q_{1.4} \propto (1+z)^{-0.19}$ using highly sensitive 3GHz VLA observations and *Herschel*-FIR data

and accounting for radio and IR non-detections through survival analysis.

3.6.2 The IRC at 150 MHz and its redshift evolution

One main focus of this study is to investigate for the first time the IRC for radio emission at low frequencies, which is crucial for LOFAR observations and relevant as well for future SKA data. Similarly to the previous section, we calculate the value of the IRC parameter for the 150 MHz data and present the distribution of q_{150} in the lower panel of Fig. 3.13. The distribution of q_{150} presents a median value and error on the median of $q_{150} = 1.544^{+0.015}_{-0.023}$.

It is customary to calculate the value of q_{irc} for different radio frequencies interpolated from the well calibrated value $q_{1.4}$ at 1.4 GHz (e.g., Yun et al. 2001; Murphy et al. 2011) and under the assumption of a single power law radio emission. Such a value would be calculated as

$$q_{150,exp} = q_{1.4} + \log\left(\frac{1400}{150}\right)^{\alpha} \tag{3.8}$$

Assuming a unique power law value from 1400 to 150 MHz of $\alpha = -0.73$, we obtain an expected q-value of $q_{150,exp} = 1.59$. This value is well in agreement with the distribution observed in the lower panel Fig. 3.13 ($q_{150,obs} = 1.54$) given the errors.

Also here we consider sources with q-values within the 2σ region of the distribution in Fig. 3.13 and investigate the evolution of q_{150} with redshift. We find the relation

$$q_{150}(z) = (1.72 \pm 0.04) \times (1+z)^{-(0.22\pm0.05)} \tag{3.9}$$

with an intrinsic scatter of $\sigma_{\rm int} = 0.53$. Proceeding with a similar analysis as for $q_{1.4}$, we calculate the R^2 values for this regression and obtain that the redshift evolution accounts for ~ 8.4 per cent of the variance in the total distribution, while most of the intrinsic scatter is still not accounted for.

One remarkable property of the redshift evolution of q_{150} is that its redshift dependence, $q_{150} \propto (1+z)^{-0.22\pm0.05}$, is slightly stronger ($\delta\gamma = 0.07$) than that observed for $q_{1.4}$, with $q_{1.4} \propto (1+z)^{-0.15\pm0.04}$. We explore the connection between the stronger redshift dependence of q_{150} and our results on the spectral curvature described in section 3.5.4.

In Fig. 3.11 we have shown that the spectral curvature is not a function of redshift when considering only the detected sources in 1.4 GHz (90 per cent of total). We added that the inclusion of the remaining fraction of undetected sources (10 per cent) would imprint a weak redshift dependence on the results (section 3.5.4). However, in that case we clarified that this finding produced no significant differences to the total characterization of the curvature. In contrast to section 3.5.4, for the present IRC study we use the total LOFAR-I-band selected sample for which 33 percent of sources have non-detections at 1.4 GHz (Table 3.1). These non-detections will have a stronger impact here than in the spectral curvature study.

We quantify this impact by investigating the redshift evolution of subsamples of 1.4 GHz detections and non-detections exclusively. For the subsample of detected sources we find an evolution of $q_{1.4} \propto (1+z)^{-0.22\pm0.04}$, which is a similar result to the one obtained from q_{150}. The study comprising exclusively sources undetected in 1.4 GHz returns an evolution of $q_{1.4} \propto (1+z)^{-0.07\pm0.04}$. From these results we conclude that the weaker redshift evolution of $q_{1.4}$ compared to q_{150} is an effect of non-detections in 1.4 GHz rather than a result of any evolution in the spectral curvature (see Fig. 3.11, which illustrates the lack of redshift evolution). We thus conclude that the redshift evolution in both IRC parameter distributions are consistent to a large extent. These observations suggest that the strength of the redshift dependence found for $q_{1.4}$ can be considered a lower limit and that a stronger evolution is possible.

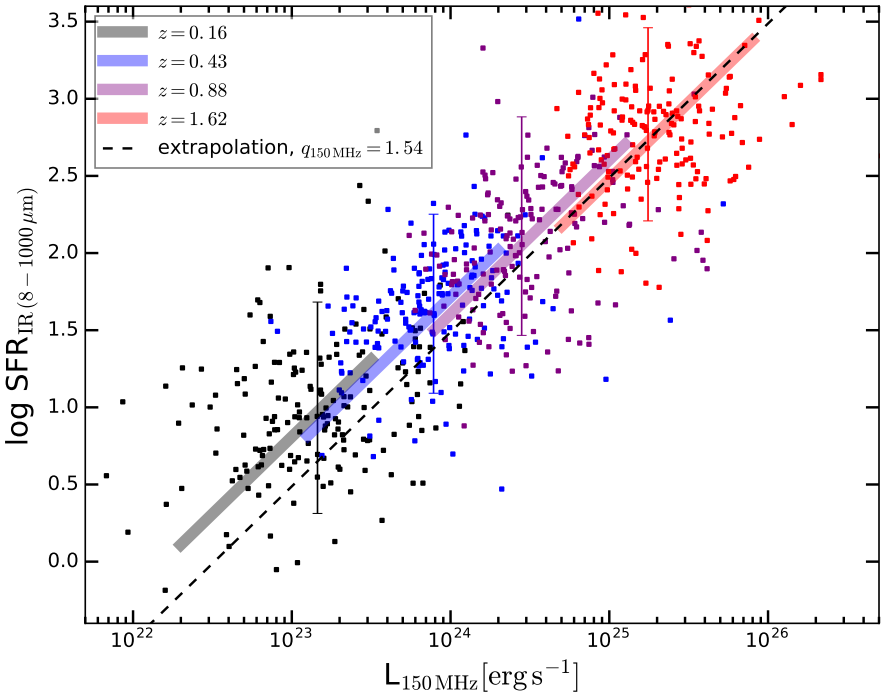

Figure 3.16: SFR inferred from the total infrared luminosity as a function of radio luminosity at 150 MHz. Scatter points are the observed median SFR values of all SF-sources, colour-coded by redshift bin. Redshifts were binned in groups of equal density, where median values of each bins are labeled in the legend. The transparent lines following the same colour-coding correspond to the calculated SFR values using Eq.3.11.The dotted line shows the SFR values, when a non-evolving q-value is assumed.

3.7 The low frequency radio luminosity as a SFR tracer

Calibrating non-thermal radio continuum emission as a SFR tracer is done mostly based on the IRC due to the reliability of the IR emission as an extinction-free SFR diagnostic (see also Brown et al. (in prep.) and Gürkan et al. (in prep.) for other studies on this at low redshifts). Since this is especially important for our sample due to the dusty environments observed in highly SF galaxies, we use the total IR data ($8 - 1000\,\mu$m, see section 3.4 for details) to compute the SFRs throughout the paper following:

$$\left(\frac{\mathrm{SFR_{IR}}}{\mathrm{M_\odot yr^{-1}}}\right) = 3.88 \times 10^{-44} \left(\frac{\mathrm{L_{IR}}}{\mathrm{erg\ s^{-1}}}\right). \tag{3.10}$$

as presented as well by Murphy et al. (2011) and Bell (2003). Combining Equations 3.10, 3.3 and 3.9 one can express the 150 MHz luminosity as a SFR as:

$$\left(\frac{\mathrm{SFR_{150\ MHz}(z)}}{M_\odot yr^{-1}}\right) = 1.455 \times 10^{-24} \times 10^{\mathrm{q_{150}(z)}} \times \left(\frac{\mathrm{L_{150}}}{\mathrm{erg\ s^{-1}}}\right), \tag{3.11}$$

where the factor $(1.455 \times 10^{-24} \times 10^{\mathrm{q_{150}(z)}})$ is equivalent to 2.450×10^{-24}, 2.289×10^{-24}, 2.149×10^{-24} and 1.965×10^{-24} for redshifts z around 0.1, 0.5, 1.0 and 2.0, respectively.

In Fig. 3.16 we show how the redshift evolution of the q_{150}-value suggests a more accurate SFR estimation compared to assuming a unique q_{150} value. We over-plot the observed median SFR_{IR} values of all SF-sources (scatter points) to the inferred SFR values using Eq.3.11 (transparent lines), both colour-coded by redshift bins. In contrast we plot the SFR values, as assuming a unique q_{150}-value at all redshifts as a dotted black line. As can be seen in Fig. 3.16, values derived from Eq.3.11 give a better description of the data.

3.8 Summary

In this paper we have investigated two properties of radio selected SF galaxies and AGN, namely their radio spectral energy distributions and the IR-radio correlation (IR), and how these evolve across the bulk of cosmic history. Our study is based on a radio and I-band selected sample from the Boötes field and comprises $\sim$ 1500 galaxies at redshifts of $0.05 < z < 2.5$. Taking advantage of the rich multi-wavelength coverage available for the Boötes field, we constructed panchromatic SEDs for our sample, incorporating UV/optical to far-infrared observations. The sources were then classified into star-formation and AGN-dominated galaxies using a multi-wavelength SED-fitting method (AGNFITTER code, Calistro Rivera et al. 2016).

We have characterized the statistical radio spectral index and spectral curvature properties for our total samples of SF galaxies and AGN using deep radio data across a wide range in radio frequency (150, 325, 610 MHz and 1.4 GHz). Additionally, intrinsic physical properties of the galaxy and AGN were investigated by calibrating spectral properties with parameters inferred from multi-wavelength SED-fitting. We arrive at the following conclusions:

- SF galaxies exhibit an average radio spectral slope of $\alpha_{150}^{1400} = -0.73$. In comparison, AGN were found to exhibit a flatter spectral slope, $\alpha_{150}^{1400} = -0.67$. Although the difference is small compared to the width of the observed α_{150}^{1400} distributions we find it to be statistically significant.

- Observations of radio SEDs indicate a difference in the curvature of the radio continuum for SF galaxies compared to AGN-dominated galaxies. SF galaxies exhibit a slightly curved radio spectrum which flattens at frequencies < 325 MHz. Conversely, AGN-dominated radio galaxies display a curved radio spectrum which shows a systematic steepening towards low frequencies below 1.4 GHz. In both cases we find these results to be significant based two-sample KS-tests.

- No evolution of the curvature with redshift is observed for both the SF galaxies and AGN samples.

- In SF galaxies we found no dependence of the curvature on star-formation rate or specific star-formation rate.

- A correlation between the radio spectral curvature and torus luminosity is observed for AGN, with low luminosity AGN exhibiting a higher degree of steepening than high luminosity sources.

In addition to studying the radio SEDs, the extensive mid- to far-IR data available for our sample allowed us to also study in detail the infrared radio correlation (IRC) for the star-forming galaxies:

- An evolution with redshift of the IRC for 1.4 GHz radio luminosities is observed, following $q_{1.4}(z) = 2.45 \pm 0.04 \times (1+z)^{-0.15\pm0.03}$, where $q_{1.4}$ is the ratio between the total infrared luminosity ($L_{IR}, 8-1000\,\mu m$) and the 1.4 GHz radio luminosity ($L_{1.4\,GHz}$). The

observed evolution accounts only for $\sim$ 6 per cent of the variance of the distribution. The large observed intrinsic scatter of $\sigma_{int} = 0.53$ is still predominantly unexplained. We discuss that the inclusion of radio non-detections in this sample may bias the result towards a weaker redshift dependence and thus conclude that this evolution can be considered a lower limit for the IRC at 1.4 GHz.

- Similarly, an evolution of the IRC with redshift for 150 MHz radio luminosities is found following $q_{150}(z) = 1.72 \pm 0.04 \times (1+z)^{-0.22\pm0.05}$. A comparison of the observed q_{150} values and those extrapolated from $q_{1.4}$, as a function of redshift, give similar results but with some scatter around $z \sim 1$.

- After converting $L_{\rm IR}$ to $\rm SFR_{IR}$ to calibrate the low frequency radio luminosity as a measure of SFR, we show that the observed IRC redshift evolution is potentially an important factor for the future use of radio-luminosity to estimate un-biased star-formation rates.

3.9 Acknowledgements

The authors thank the anonymous referee for the very careful reading of the manuscript and the many insightful comments and suggestions that improved the paper. We thank Jacqueline Hodge, Frank Israel and Michael Brown for useful discussions and suggestions. GCR, KJD and HJR acknowledge support from the European Research Council under the European Union's Seventh Framework Programme (FP/2007- 2013) /ERC Advanced Grant NEWCLUSTERS-321271. WLW and MJH acknowledge support from the UK Science and Technology Facilities Council [ST/M001008/1]. PNB is grateful for support from the UK STFC via grant ST/M001229/1. MJJ acknowledges support from UK Science and Technology Facilities Council and the South African SKA Project EKM acknowledges support from the Australian Research Council Centre of Excellence for All-sky Astrophysics (CAASTRO), through project number CE110001020. GJW Gratefully acknowledges support from The Leverhulme Trust. This research made use of ASTROPY, a community-developed core Python package for astronomy (Astropy Collaboration et al. 2013) hosted at `http://www.astropy.org/`.

Bibliography

Appleton, P. N., Fadda, D. T., Marleau, F. R., et al. 2004, ApJS, 154, 147

Ashby, M. L. N., Stern, D., Brodwin, M., et al. 2009, ApJ, 701, 428

Autry, R. G., Probst, R. G., Starr, B. M., et al. 2003, in Proc. SPIE, Vol. 4841, Instrument Design and Performance for Optical/Infrared Ground-based Telescopes, ed. M. Iye & A. F. M. Moorwood, 525–539

Basu, A., Beck, R., Schmidt, P., & Roy, S. 2015, MNRAS, 449, 3879

Basu, A., Roy, S., & Mitra, D. 2012, ApJ, 756, 141

Becker, R. H., White, R. L., & Helfand, D. J. 1995, ApJ, 450, 559

Bell, E. F. 2003, ApJ, 586, 794

Bertin, E., & Arnouts, S. 1996, A&AS, 117, 393

Best, P. N., & Heckman, T. M. 2012, MNRAS, 421, 1569

Bianchi, L., Conti, A., & Shiao, B. 2014, Advances in Space Research, 53, 900

Bonzini, M., Padovani, P., Mainieri, V., et al. 2013, MNRAS, 436, 3759

Bourne, N., Dunne, L., Ivison, R. J., et al. 2011, MNRAS, 410, 1155

Brammer, G. B., van Dokkum, P. G., & Coppi, P. 2008, ApJ, 686, 1503

Brown, M. J. I., Dey, A., Jannuzi, B. T., et al. 2007, ApJ, 654, 858

Brown, M. J. I., Moustakas, J., Smith, J.-D. T., et al. 2014, ApJS, 212, 18

Bruzual, G., & Charlot, S. 2003, MNRAS, 344, 1000

Calistro Rivera, G., Lusso, E., Hennawi, J. F., & Hogg, D. W. 2016, ApJ, 833, 98

Calzetti, D., Kinney, A. L., & Storchi-Bergmann, T. 1994, ApJ, 429, 582

Carrasco Kind, M., & Brunner, R. J. 2014, MNRAS, 442, 3380

Casey, C. M., Narayanan, D., & Cooray, A. 2014, Phys. Rep., 541, 45

Casey, C. M., Berta, S., Béthermin, M., et al. 2012, ApJ, 761, 140

Chabrier, G. 2003, PASP, 115, 763

Chary, R., & Elbaz, D. 2001, ApJ, 556, 562

Clemens, M. S., Scaife, A., Vega, O., & Bressan, A. 2010, MNRAS, 405, 887

Condon, J. J. 1992, ARA&A, 30, 575

Condon, J. J., Cotton, W. D., Greisen, E. W., et al. 1998, AJ, 115, 1693

Cool, R. J. 2007, ApJS, 169, 21

Coppejans, R., Cseh, D., Williams, W. L., van Velzen, S., & Falcke, H. 2015, MNRAS, 450, 1477

da Cunha, E., Walter, F., Smail, I. R., et al. 2015, ApJ, 806, 110

Dahlen, T., Mobasher, B., Faber, S. M., et al. 2013, The Astrophysical Journal, 775, 93

Dale, D. A., & Helou, G. 2002, ApJ, 576, 159

de Jong, T., Klein, U., Wielebinski, R., & Wunderlich, E. 1985, A&A, 147, L6

de Vries, W. H., Morganti, R., Röttgering, H. J. A., et al. 2002, AJ, 123, 1784

Delhaize, J., Smolcic, V., Delvecchio, I., et al. 2017, ArXiv e-prints, arXiv:1703.09723

Delvecchio, I., Smolcic, V., Zamorani, G., et al. 2017, ArXiv e-prints, arXiv:1703.09720

Dumas, G., Schinnerer, E., Tabatabaei, F. S., et al. 2011, AJ, 141, 41

Fanaroff, B. L., & Riley, J. M. 1974, MNRAS, 167, 31P

Foreman-Mackey, D., Hogg, D. W., Lang, D., & Goodman, J. 2013, PASP, 125, 306

Gioia, I. M., Gregorini, L., & Klein, U. 1982, A&A, 116, 164

Hardcastle, M. J. 2009, in Astronomical Society of the Pacific Conference Series, Vol. 407, The Low-Frequency Radio Universe, ed. D. J. Saikia, D. A. Green, Y. Gupta, & T. Venturi, 121

Hardcastle, M. J., Evans, D. A., & Croston, J. H. 2007, MNRAS, 376, 1849

Hardcastle, M. J., Gürkan, G., van Weeren, R. J., et al. 2016, ArXiv e-prints, arXiv:1606.09437

Harwood, J. J., Hardcastle, M. J., & Croston, J. H. 2015, MNRAS, 454, 3403

Helou, G., Soifer, B. T., & Rowan-Robinson, M. 1985, ApJ, 298, L7

Hogg, D. W. 2001, AJ, 121, 1207

Ibar, E., Ivison, R. J., Best, P. N., et al. 2010, MNRAS, 401, L53

Ibar, E., Ivison, R. J., Biggs, A. D., et al. 2009, MNRAS, 397, 281

Ibar, E., Cirasuolo, M., Ivison, R., et al. 2008, MNRAS, 386, 953

Intema, H. T., van Weeren, R. J., Röttgering, H. J. A., & Lal, D. V. 2011, A&A, 535, A38

Israel, F. P., & Mahoney, M. J. 1990, ApJ, 352, 30

Ivison, R. J., Magnelli, B., & Ibar, E. e. a. 2010a, A&A, 518, L31

Ivison, R. J., Alexander, D. M., Biggs, A. D., et al. 2010b, MNRAS, 402, 245

Jannuzi, B., Weiner, B., Block, M., et al. 2010, in Bulletin of the American Astronomical Society, Vol. 42, American Astronomical Society Meeting Abstracts #215, 513

Jannuzi, B. T., & Dey, A. 1999, in Astronomical Society of the Pacific Conference Series, Vol. 191, Photometric Redshifts and the Detection of High Redshift Galaxies, ed. R. Weymann, L. Storrie-Lombardi, M. Sawicki, & R. Brunner, 111

Jarvis, M. J., & Rawlings, S. 2004, New Astronomy Review, 48, 1173

Jarvis, M. J., Smith, D. J. B., Bonfield, D. G., et al. 2010, MNRAS, 409, 92

Jenkins, C. J., & McEllin, M. 1977, MNRAS, 180, 219

Kennicutt, Jr., R. C. 1998, ARA&A, 36, 189

Ker, L. M., Best, P. N., Rigby, E. E., Röttgering, H. J. A., & Gendre, M. A. 2012, MNRAS, 420, 2644

Kharb, P., Srivastava, S., Singh, V., et al. 2016, MNRAS, 459, 1310

Kochanek, C. S., Eisenstein, D. J., Cool, R. J., et al. 2012, ApJS, 200, 8

Komatsu, E., Dunkley, J., Nolta, M. R., et al. 2009, ApJS, 180, 330

Krause, M., Alexander, P., Riley, J., & Hopton, D. 2012, MNRAS, 427, 3196

Lacki, B. C. 2013, MNRAS, 431, 3003

Lacki, B. C., Thompson, T. A., & Quataert, E. 2010, ApJ, 717, 1

Laing, R. A., & Peacock, J. A. 1980, MNRAS, 190, 903

Lane, W. M., Cotton, W. D., van Velzen, S., et al. 2014, MNRAS, 440, 327

Magnelli, B., Ivison, R. J., Lutz, D., et al. 2015, A&A, 573, A45

Mahony, E. K., Morganti, R., Prandoni, I., et al. 2016, MNRAS, 463, 2997

Martin, C., Barlow, T., Barnhart, W., et al. 2003, in Proc. SPIE, Vol. 4854, Future EUV/UV and Visible Space Astrophysics Missions and Instrumentation., ed. J. C. Blades & O. H. W. Siegmund, 336–350

Marvil, J., Owen, F., & Eilek, J. 2015, AJ, 149, 32

Mauch, T., Klöckner, H.-R., Rawlings, S., et al. 2013, MNRAS, 435, 650

Meisenheimer, K., Roser, H.-J., Hiltner, P. R., et al. 1989, A&A, 219, 63

Mohan, N., & Rafferty, D. 2015, PyBDSM: Python Blob Detection and Source Measurement, Astrophysics Source Code Library, ascl:1502.007

Murphy, E. J., Stierwalt, S., Armus, L., Condon, J. J., & Evans, A. S. 2013, ApJ, 768, 2

Murphy, E. J., Condon, J. J., Schinnerer, E., et al. 2011, The Astrophysical Journal, 737, 67

Murray, S. S., Kenter, A., Forman, W. R., et al. 2005, ApJS, 161, 1

Oke, J. B., & Gunn, J. E. 1983, ApJ, 266, 713

Oliver, S. J., Bock, J., Altieri, B., et al. 2012, MNRAS, 424, 1614

Pannella, M., Elbaz, D., Daddi, E., et al. 2015, ApJ, 807, 141

Planck Collaboration, Ade, P. A. R., Aghanim, N., et al. 2014, A&A, 571, A16

Polletta, M., Tajer, M., Maraschi, L., et al. 2007, ApJ, 663, 81

Rees, G. A., Spitler, L. R., Norris, R. P., et al. 2016, MNRAS, 455, 2731

Rengelink, R. B., Tang, Y., de Bruyn, A. G., et al. 1997, A&AS, 124, doi:10.1051/aas:1997358

Richter, G. A. 1975, Astronomische Nachrichten, 296, 65

Roseboom, I. G., Oliver, S. J., Kunz, M., et al. 2010, MNRAS, 409, 48

Röttgering, H., Afonso, J., Barthel, P., et al. 2011, Journal of Astrophysics and Astronomy, 32, 557

Sargent, M. T., Schinnerer, E., Murphy, E., et al. 2010, ApJ, 714, L190

Scaife, A. M. M., & Heald, G. H. 2012, MNRAS, 423, L30

Schleicher, D. R. G., & Beck, R. 2013, A&A, 556, A142

Schmitt, H. R., Calzetti, D., Armus, L., et al. 2006, ApJS, 164, 52

Schober, J., Schleicher, D. R. G., & Klessen, R. S. 2016, ArXiv e-prints, arXiv:1603.02693

Seymour, N., Dwelly, T., Moss, D., et al. 2008, MNRAS, 386, 1695

Shapley, A. E. 2011, ARA&A, 49, 525

Simpson, C., Rawlings, S., Ivison, R., et al. 2012, Monthly Notices of the Royal Astronomical Society, 421, 3060

Singh, V., Shastri, P., Ishwara-Chandra, C. H., & Athreya, R. 2013, A&A, 554, A85

Smith, D. J. B., Jarvis, M. J., Hardcastle, M. J., et al. 2014, MNRAS, 445, 2232

Smolcic, V. 2016, ArXiv e-prints, arXiv:1603.05687

Smolčić, V., Schinnerer, E., Scodeggio, M., et al. 2008, ApJS, 177, 14

Stevens, J. A., Ivison, R. J., Dunlop, J. S., et al. 2003, Nature, 425, 264

Tabatabaei, F. S., Schinnerer, E., Murphy, E. J., et al. 2013, A&A, 552, A19

Tasse, C., Le Borgne, D., Röttgering, H., et al. 2008, A&A, 490, 879

Taylor, M. B. 2006, in , 666

van Haarlem, M. P., Wise, M. W., Gunst, A. W., et al. 2013, A&A, 556, A2

van Weeren, R. J., Williams, W. L., Hardcastle, M. J., et al. 2016, ApJS, 223, 2

Vardoulaki, E., Charmandaris, V., Murphy, E. J., et al. 2015, A&A, 574, A4

Voelk, H. J. 1989, A&A, 218, 67

Whittam, I. H., Riley, J. M., Green, D. A., et al. 2016, MNRAS, 457, 1496

Williams, P. K. G., & Bower, G. C. 2010, ApJ, 710, 1462

Williams, W. L., Intema, H. T., & Röttgering, H. J. A. 2013, A&A, 549, A55

Williams, W. L., van Weeren, R. J., Röttgering, H. J. A., et al. 2016, MNRAS, 460, 2385

Yun, M. S., & Carilli, C. L. 2002, ApJ, 568, 88

Yun, M. S., Reddy, N. A., & Condon, J. J. 2001, ApJ, 554, 803

3.A Luminosity vs redshift dependence of the IRC

Figures 3.17 and 3.18 show that the redshift evolution is found also within subsamples of similar luminosity, suggesting the trend observed in Figs. 3.14 and 3.15 is not the consequence of a dependence on luminosity.

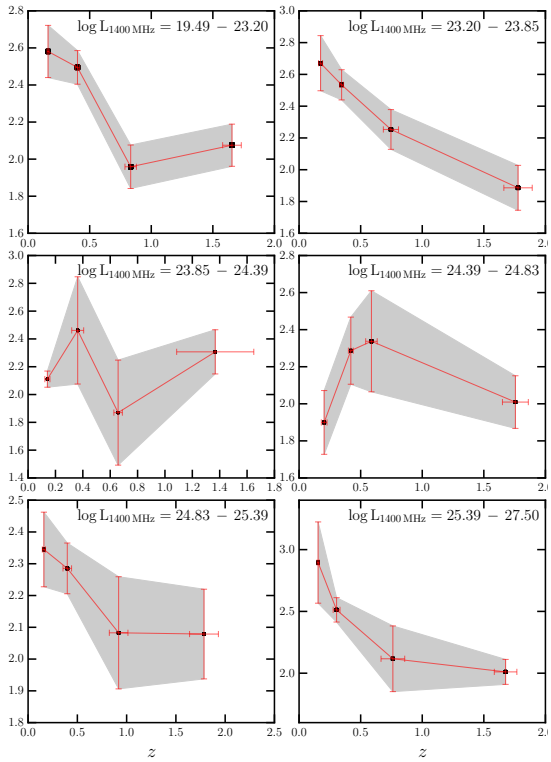

Figure 3.17: q-value for the IRC corresponding to the radio at 1.4 GHz plotted against redshift for different luminosity bins. Error bars correspond to bootstrap errors.

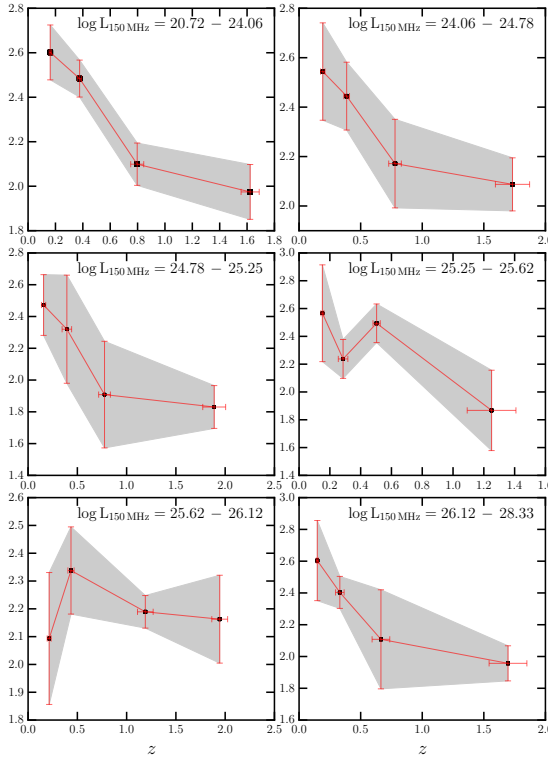

Figure 3.18: q-value for the IRC corresponding to the radio at 150 MHz plotted against redshift for different luminosity bins. Error bars correspond to bootstrap errors.

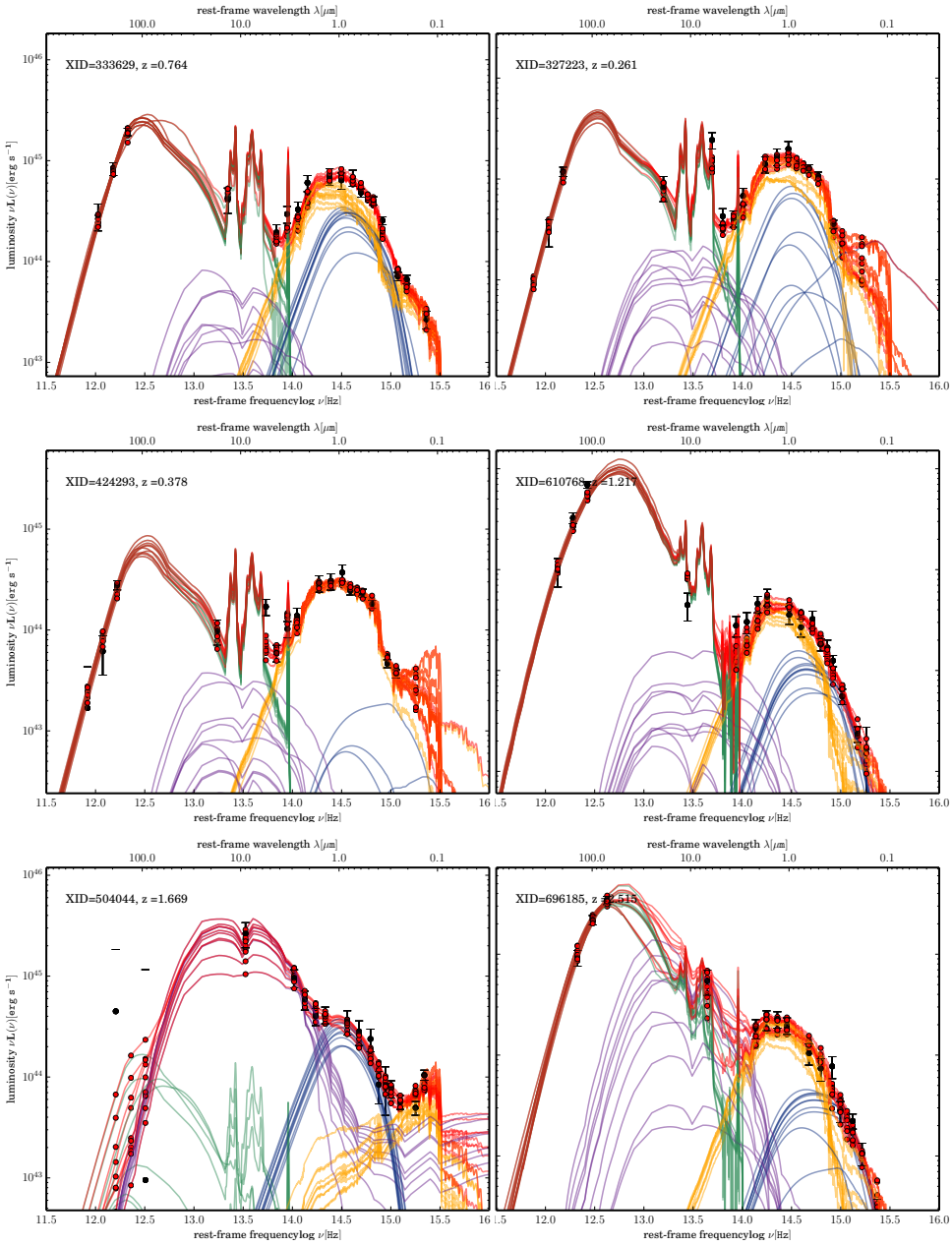

Figure 3.19: SED-fitting examples: Photometric data points for each source are plotted as black circular markers with error bars. We pick 8 different realizations from the parameters posterior probability distributions and over-plot them in order to visualize the effect of the parameters' uncertainties on the SEDS. The SED shapes of the physical components are presented as solid lines: the galactic cold dust emission (green), the hot dust emission from the AGN torus (purple), the stellar emission (orange) and the accretion disk emission (blue).The linear combination of these, the 'total SED', is depicted as a red line.

4

The Resolution Frontier I: Resolving the distributions of CO, dust continuum and stellar emission with ALMA and HST

We use ALMA observations of four sub-millimetre galaxies (SMGs) at $z \sim 2-3$ to investigate the spatially resolved properties of the inter-stellar medium (ISM) at scales of 1–5 kpc (0.1–0.6″). The velocity fields of our sources, traced by the ^{12}CO($J = 3-2$) emission, are consistent with disk rotation to first order, implying average dynamical masses of $\sim 3 \times 10^{11} M_{\odot}$within two half-light radii. Through a Bayesian approach we investigate the uncertainties inherent to dynamically constraining total gas masses. We explore the covariance between the stellar mass-to-light ratio and CO-to-H_2 conversion factor, α_{CO}, finding values of $\alpha_{CO} = 1.1^{+0.8}_{-0.7}$ for dark matter fractions of 15%. We show that the resolved spatial distribution of the gas and dust continuum can be uncorrelated to the stellar emission, challenging energy balance assumptions in global SED fitting. Through a stacking analysis of the resolved radial profiles of the CO(3-2), stellar and dust continuum emission in SMG samples, we find that the cool molecular gas emission in these sources (radii ∼5–14 kpc) is clearly more extended than the rest-frame ∼250 μm dust continuum by a factor > 2. We propose that assuming a constant dust-to-gas ratio, this apparent difference in sizes can be explained by temperature and optical-depth gradients alone. Our results suggest that caution must be exercised when extrapolating morphological properties of dust continuum observations to conclusions about the molecular gas phase of the ISM.

G. Calistro Rivera, J. A. Hodge, Ian Smail, A. M. Swinbank, A. Weiß et al.
ApJ, **Volume 863**, Issue 1, p. 56-72 (2018)

4.1 Introduction

The process of massive galaxy assembly in the Universe has been identified to peak between $1 < z < 3$, where the majority of the stars in the present-day galaxies formed (e.g., Madau & Dickinson 2014). This star formation (SF) is likely strongly connected to the gas content and its distribution in the interstellar medium (ISM) and the efficiency with which this gas is transformed into stars (e.g. Decarli et al. 2016; Scoville et al. 2017; Tacconi et al. 2017). Gas-rich, dusty galaxies, as submillimetre galaxies (SMGs; e.g., Blain et al. 2002) are effective laboratories to characterize this star-forming ISM due to their high molecular gas content (Bothwell et al. 2013) and their bright dust continuum emission ensured by their selection. Moreover, they appear to contribute around 20% of the total star-formation rate density at $z \sim 2-3$ (e.g., Swinbank et al. 2014) and are thus an important tracer of the star formation occurring in massive galaxies at this epoch.

The characterization of the star-forming ISM at these high redshifts is typically achieved through observations of the rotational transitions of carbon monoxide (CO) or through deep imaging of the Rayleigh-Jeans (RJ) tail of the dust continuum emission (for reviews see, Carilli & Walter 2013; Casey et al. 2014). However, calculations based on these ISM tracers involve a number of assumptions about the inferred gas properties. Although CO is the most strongly emitting molecule, it is only the second most abundant molecule in the galaxy ISM after molecular Hydrogen, H_2, and a conversion factor (α_{CO}) from the ground-state CO($J = 1-0$) luminosity to H_2 (e.g., Bolatto et al. 2013) is thus required to compute the total molecular content. As a result there have been numerous observational (e.g., Tacconi et al. 2008; Danielson et al. 2011; Genzel et al. 2012; Hodge et al. 2012; Bolatto et al. 2013; Bothwell et al. 2013; Accurso et al. 2017) and theoretical (e.g., Narayanan et al. 2011, 2012; Lagos et al. 2012) efforts to constrain α_{CO} in different galaxy populations, which represents a significant uncertainty in total gas mass estimations.

In the local universe, the range of α_{CO} values is observed to span a factor of ~5, and it has been shown to be a function of several galaxy properties such as gas density, temperature, and metallicity (Bolatto et al. 2013), which likely evolve with redshift.

Another approach to estimate galaxy gas masses is to use the dust continuum observations as a proxy for the ISM content at low and intermediate redshifts (e.g. Hildebrand 1983; Leroy et al. 2011; Magdis et al. 2011; Scoville et al. 2014). Recently, Scoville et al. (2016) combined molecular gas masses inferred from existing CO detections and dust continuum measurements in an attempt to calibrate an empirical scaling factor for using global measurements of the Rayleigh-Jeans dust continuum (probed in the sub-mm regime) to estimate the total ISM masses. Although they find that this calibration holds for measurements over three orders of magnitude in infrared luminosity and for different populations including SMGs, this is based on significant assumptions about the properties of the dust spectral energy distribution (SED) in addition to the uncertainties on the α_{CO} parameter assumed for the calibration. To test the validity of these assumptions, observational constraints on the physics of the high-redshift ISM are required.

Spatially unresolved high-redshift surveys of CO and dust continuum have begun to make progress on these tracers and their implications for the SF picture from a global perspective. Over 200 detections of CO line emission at high redshift have been reported ($z > 2$; Carilli & Walter 2013) from both individual sources (e.g., Genzel et al. 2012; Hodge et al. 2012; Strandet et al. 2017) and larger statistical surveys (Ivison et al. 2011; Bothwell et al. 2013; Sharon et al. 2016; Walter et al. 2016). In addition, multiple sub-mm continuum surveys have been conducted to characterize the dust emission and population properties of SMGs (Hodge et al. 2013b; Karim et al. 2013; Simpson et al. 2017). Statistical studies (e.g., Bothwell et al. 2013; Sharon et al. 2016) have shed light on the average level of excitation for SMGs, which

are observed to have large scatter at high excitation levels $J \geq 4$ (e.g., Narayanan & Krumholz 2014) but behave relatively homogeneously at $J \leq 3$ with excitation ratios of $r_{3-1} = 0.78 \pm 0.27$ (Sharon et al. 2016). Moreover, high-excitation CO transitions ($J \geq 4$) have been observed to underestimate the gas masses, since they appear to be biased to trace the most compact molecular emission only (e.g., Engel et al. 2010). Finally, using ISM mass estimates based on dust-continuum observations and assuming a constant dust/gas ratio (e.g., Leroy et al. 2011), Genzel et al. (2015), Scoville et al. (2017) and Tacconi et al. (2017) were able to investigate statistically the evolution of the unresolved star-forming ISM for SF galaxies across cosmic time.

At high resolution, significant progress with the characterization of the high-redshift ISM has been achieved through the observation of gravitationally lensed sources, as part of surveys conducted by the South Pole Telescope (*SPT*; e.g., Greve et al. 2012; Vieira et al. 2013; Spilker et al. 2016) and *Herschel* (e.g. Harris et al. 2012; Wardlow et al. 2013). Lensing observations, however, are prone to be affected by differential magnification when a detailed lensing model is not available (e.g., Serjeant 2012; Hezaveh et al. 2012). Moreover, caution must be exercised when interpreting intrinsic integrated properties of the CO emission in strongly lensed galaxies, since these can be biased against the less-magnified regions.

Only a handful of studies have characterized the ISM on sub-galactic scales in unlensed high-redshift galaxies (e.g., Tacconi et al. 2008; Engel et al. 2010; Hodge et al. 2012, 2013a; Aravena et al. 2014; Decarli et al. 2016; Tadaki et al. 2017b; Chen et al. 2017), and even fewer have studied the dust-continuum emission and gas observations on comparable scales. High-resolution imaging is crucial for characterizing the ISM in galaxies, since apart from providing a better morphological description of the gas or dust continuum emission, this information is key for estimating fundamental properties such as gas surface density. Moreover, through dynamical modeling of the velocity fields, one can derive dynamical mass estimates (de Blok & Walter 2014), which reflect the total mass of baryonic and non baryonic matter contained within the region traced by the observed line emission, and thus constraints the sum of stellar, gas, and dark matter masses. When complemented with stellar mass and dark matter fraction assumptions, dynamical mass estimates can constrain the total mass of the gas reservoirs (Tacconi et al. 2008; Hodge et al. 2012), and hence the α_{CO} parameter.

However, estimating the mass of the other components is also complex, for example the stellar mass of a galaxy is usually inferred via SED fitting, which is prone to induce strong degeneracies between parameters such as the star formation history, dust reddening, luminosity-weighted age of the stellar populations and mass-to-light ratio, especially for highly star-forming galaxies such as SMGs (e.g., Hainline et al. 2011; Simpson et al. 2014, 2017). The dark matter fraction represents a large source of uncertainty, as no independent measurement of its mass is possible. While recent spectroscopic surveys have claimed dark matter fractions around 10–30%, (Price et al. 2016; Wuyts et al. 2016; Genzel et al. 2017) revealing that star-forming galaxies at $z > 2$ appear to be heavily baryon dominated, these calculations involve making similar uncertain assumptions about the gas fractions. Shedding light on the impact of these uncertainties on the α_{CO} and gas mass estimations is thus imperative for an improved characterization of the high-redshift ISM.

The collecting area and sensitivity of the Atacama Large Millimeter Array (ALMA) is transforming our view of the star-forming ISM in distant galaxies. While high-resolution studies of the dust continuum emission in SMGs with ALMA have shown this material appear to be mostly distributed in compact regions (Simpson et al. 2015; Ikarashi et al. 2015; Tadaki et al. 2017a; Hodge et al. 2016), the extended sizes revealed by the few resolved CO detections of luminous sources (Riechers et al. 2010; Hodge et al. 2012; Emonts et al. 2016; Chen et al. 2017; Tadaki et al. 2017b; Dannerbauer et al. 2017; Ginolfi et al. 2017) challenge

Table 4.1: Description of the ALMA Cycle 2 Band 3 observations and native beam properties

	ALESS49.1	ALESS57.1	ALESS67.1	ALESS122.1
R.A. (J2000)	03:31:24.72	03:31:51.92	03:32:43.20	03:31:39.54
Dec. (J2000)	−27 : 50 : 47.1	−27 : 53 : 27.1	−27 : 55 : 14.3	−27 : 41 : 19.7
z (opt)	2.95	2.94	2.12	2.02
z (CO(3-2))	2.943 ± 0.001	2.943 ± 0.002	2.121 ± 0.004	2.024 ± 0.001
Natural weighted imaging				
Cleaning mask radius [″][1].	1.8	0.8	2.0	1.0
Synthesized beam FWHM [″]	0.69 × 0.63	0.67 × 0.60	0.56 × 0.48	0.45 × 0.35
Continuum RMS [μJy beam^{-1}]	17.6	19.5	18.2	16.3
Channel widths in final cubes [MHz]	15.6[2]	60.5	81.5	77.3
Channel widths in final cubes [km s^{-1}]	54[??]	200	213	196
Channel RMS [μJy beam^{-1}]	182[??]	148	113	131

4

general assumptions of co-spatial interwoven dust and gas generally assumed by models. Spatially resolved observations of CO and dust continuum emission for homogeneously selected samples and modelling their interplay, e.g. through radiative transfer approximations, may help characterize the distributions and physics of dust and gas in the high-redshift ISM.

Here, we present high-resolution imaging of the CO emission in four SMGs from the ALESS survey (Hodge et al. 2013b; Karim et al. 2013) at sub-arcsecond resolution. We address the following questions, which remain open in ISM studies at high redshift: How is the molecular gas distributed in relation to the dusty ISM and the stellar populations? What implications do these distributions have for the assumptions made for the dust spectral energy distributions and dust-to-gas ratios at high redshift? How reliable are gas mass estimations? What uncertainties do stellar mass estimates and dark matter fraction assumptions introduce into the total gas mass estimation? The paper is structured as follows: in Section 4.2 we describe the ALMA data reduction and the imaging of the CO(3-2) maps. In Section 4.3 we present the analysis of the kinematic properties of the CO(3-2) emission in our sources and present the implications of these to total gas estimates. In Section 4.4 we present a statistical analysis of the distributions of gas, dust continuum and stellar emission and discuss the physical implications of these findings. Throughout the paper we adopt a Λ-CDM cosmology, consistent with the values given by the Planck Collaboration et al. (2014), with $\Omega_\Lambda = 0.69$, $\Omega_m = 0.31$ and $H_0 = 67.7$ km s^{-1}Mpc^{-1}.

4.2 Observations and Imaging

4.2.1 Target selection ALMA observations

We present ALMA Cycle 2 observations of the CO emission from four SMGs, ALESS49.1, ALESS57.1, ALESS67.1 and ALESS122.1. These sources were selected from the ALESS survey (Hodge et al. 2013b; Karim et al. 2013): an ALMA Cycle 0 follow-up program of 126 sources detected in the single-dish LABOCA Extended *Chandra* Deep Field South (ECDFS) Submm Survey (LESS, Weiß et al. 2009). These four sources were selected as they are spectroscopically confirmed at redshifts $2.1 < z < 2.9$ as the result of an extensive spectroscopic follow-up campaign (Danielson et al. 2017). Three of the four sources in our sample were detected (ALESS57.1 and ALESS67.1) or marginally detected (ALESS122.1, through stacking) in the X-rays (Wang et al. 2013), using 4 Ms *Chandra* observations of the CDFS region (Xue et al. 2011) and 250 ks observations in the ECDFS (Lehmer et al. 2005). ALESS57.1 and ALESS122.1 are reported as AGN candidates (Wang et al. 2013; Danielson et al. 2017), while the origin of the X-ray emission in ALESS67.1 is most probably related to star formation.

ALMA observations were taken in Cycle 2 as part of the project 2013.1.00470.S (PI: Hodge), with a total integration time of ~2.5 hours in ALMA Band 3, covering the spectral range expected for the line emission of the CO(3-2) transition at these redshifts. The sources were observed on 2015 September 4, 6 and 20, using the 12-meter array and under good phase stability/weather conditions, with PWV at zenith ranging between 1.56–3.03 mm. The antenna configuration consisted of 33, 36 and 35 antennas, respectively, achieving synthesized beam sizes that range between 0.34 – 0.67″ major axis FWHM with largest angular scales (LAS) between 1.9–2.9″. The observations were calibrated based on Jupiter as the flux-calibrator, J0334-4008 as the band-pass calibrator, and J0334-401 as the phase calibrator.

New ALMA observations of ALESS49.1 (Wardlow et al. 2018) were taken during Cycle 4 on 2016 November 12, 16 and 20 as part of the project 2016.1.00754.S (PI: Wardlow). These observations were carried out using a total integration time of ~ 2700 s and using the longest baselines of ~ 650 m. With an angular resolution of 1.1″, these additional data increase the signal-to-noise ratio (SNR) of our high-resolution data. We concatenated both Cycle 2 and Cycle 4 datasets achieving a combination of high-resolution imaging, high SNR and at the same time reducing concerns whether we might have resolved out any significant flux from ALESS49.1, thanks to the short baselines covered. An analysis of the environment of ALESS49.1 is presented in Wardlow et al. (2018).

The ALMA data were calibrated following the ALMA pipeline and using the Common Astronomy Software Application package (CASA, McMullin et al. 2007). Manual flagging of a few corrupted time windows for ALESS57.1 was required after an inspection of the calibration output. The imaging process was carried out using CASA tasks (version 4.7.0). The uv-data were Fourier transformed and deconvolved from the point spread function using the CASA CLEAN algorithm. After resampling of the visibilities at different spectral resolutions to optimize the SNR, we produced the final data cubes averaging the visibilities to channel widths of 16, 61, 82 and 77 MHz for ALESS49.1, 57.1, 67.1, 122.1, respectively. At the native resolution, the rms values achieved for the final data cubes range from 0.11-0.18 mJy beam^{-1} (see Table 4.1).

Due to the high spatial resolution of the data, it is not trivial to estimate the masks on which to apply the CLEAN task. We adopted an iterative cleaning technique (e.g., Chen et al. 2017), in order to optimize the mask size estimation to include possible extended low surface brightness emission. Iterative cleaning consists of drawing concentric circular mask regions at increasing radii and applying the CLEAN task and line flux extraction within them. Plotting the resulting line fluxes against the corresponding circular region radii, a curve of growth is produced (see upper right panels of Fig. 4.1). The expected behaviour of the measured flux density in a curve of growth is to continuously increase as a function of radius, reaching a point of convergence at the maximum extent of the source. We used the masks inferred from the iterative cleaning method to extract the final line cubes. We explored the data for emission at different spatial scales and surface brightness, first at the native resolution using natural weighting, then using a Briggs weighting with a robustness parameter 0.5, to image the CO emission at lower SNR but slightly higher spatial resolution and finally, by tapering the visibilities to lower resolutions (1.5-2 × native beam size) to recover extended emission.

4.2.2 CO(3-2) line detections and continuum

We detect significant CO(3-2) line emission for the four sources in our sample even from the dirty data cubes, i.e. in the Fourier transformed visibilities prior to the beam deconvolution (cleaning process). The CO detections are coincident with the expected ALMA Cycle 0 positions, and at frequencies which confirm the previously reported spectroscopic redshifts (Table 4.1). We identify strong line detections for all the sources in the final line cubes constructed

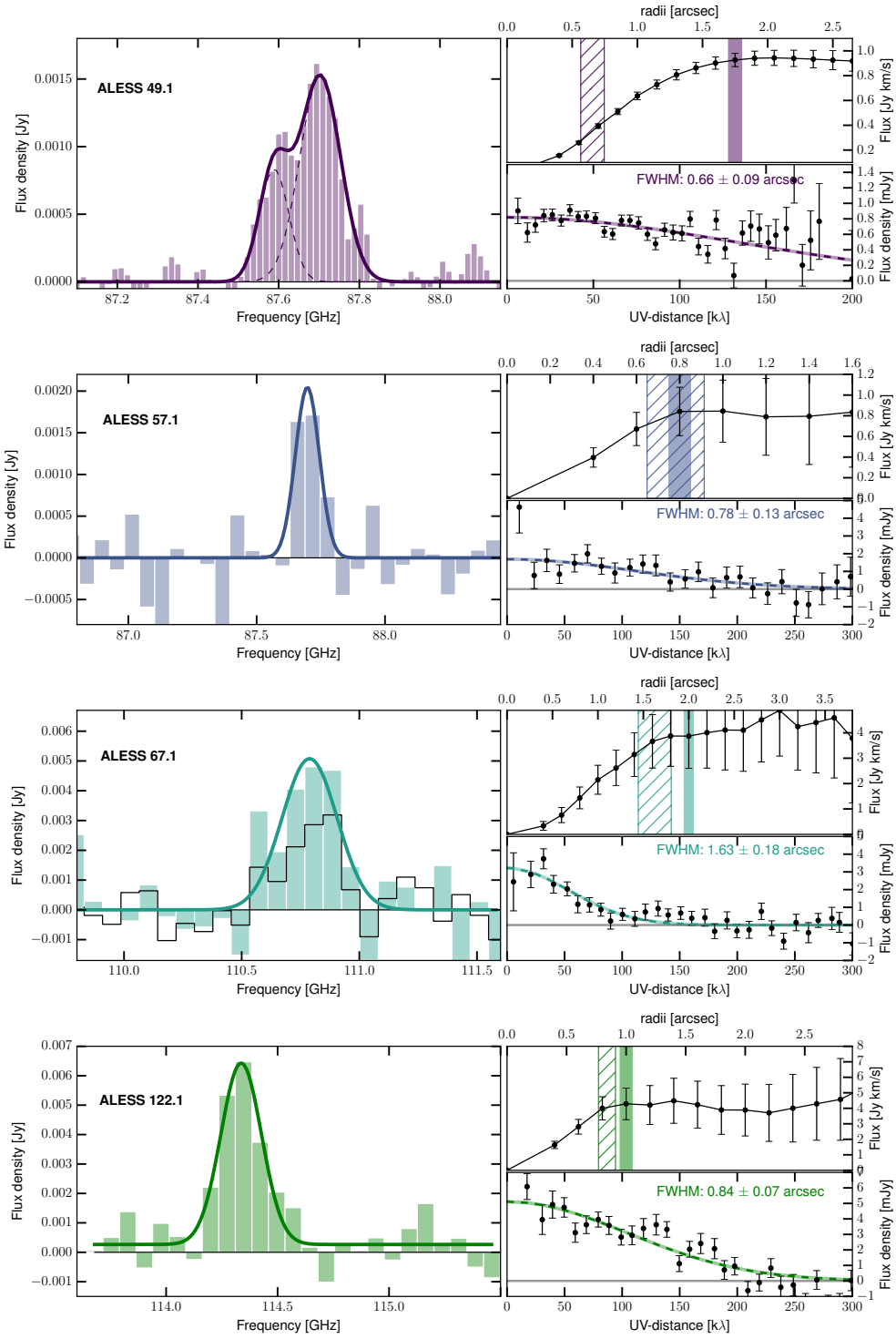

Figure 4.1: (Continued on the following page.)

Figure 4.1: **Analysis of the CO(3-2) data:** The *left panels* show the CO(3-2) spectra of our sources. The spectral resolution is ~54, 200, 213, and 116 km s^{-1}, for ALESS49.1, ALESS57.1, ALESS67.1 and ALESS122.1, respectively. Gaussian fits to the spectra are shown by the solid lines. For ALESS49.1 we fit a two-component Gaussian profile and show each component as dotted lines. For ALESS67.1, we additionally show the CO spectrum extracted exclusively from within a mask of ~ 1" around the centroid of the main component as a black line (see Section 4.2.2 for more details). The *right panels* show two methods used to calculate the cleaning masks and intrinsic source sizes, respectively. The first method (*top right*) is a curve-of-growth analysis, where the shaded area shows the radius at convergence. This method was used to determine the size of the area used for masking the cleaning process. The second method (*bottom right*) is the analysis of the visibilities (uv)-profiles, which reliably estimate intrinsic source sizes. A single Gaussian fit to the uv-data is shown by the line. The half-light radius $r_{1/2}$ from the uv-fitting method is a more robust estimate of the true size of the sources, since the curve-of-growth analysis is prone to be affected by correlated noise. We draw hashed areas to show the FWHM from the Gaussian fit (i.e., $2\times r_{1/2}$) on the top-right panel and see that in most cases, it roughly corresponds to the peak of the curve of growth.

by applying the circular cleaning masks described in Section 4.2.1. Fig. 4.1 show the data as well as Gaussian profile fits to the extracted spectra. The estimated CO(3-2) line parameters are summarized in Table 4.2. We next briefly describe some important features of the line emission of each source.

The CO spectrum of ALESS49.1 is clearly best described by a double-peaked profile and was thus fitted using an asymmetrical two-Gaussian model. The red and blue component line widths are 280 ± 40 km s^{-1}and 390 ± 30 km s^{-1}(FWHM), respectively, and are separated by 300 ± 20 km s^{-1}.

The CO spectrum of ALESS57.1 is marginally spectroscopically resolved. Nevertheless, the line width is appropriately approximated by a Gaussian fit and the resulting values are summarized in Table 4.2.

The CO line of ALESS67.1 shows a very large line width (FWHM~ 800 km s^{-1}) and appears asymmetric although the asymmetry is not statistically significant, due to the low SNR in this source. We postulate that the CO line of ALESS67.1 is produced by two sources of emission. This is supported by the velocity averaged image (Fig. 4.2), where two spatial components are recognizable independently in both CO (ALMA) and optical/near-infrared (*HST*) imaging: one main right component of around 1 arsec radius and a second extended emission in the east. We thus give preference to the description of this CO line as originating in two sources (possibly an early stage of a merger event) and focus on the emission extracted from the main component (1 arsec radius), which is shown as a black line overlaid on the total line emission in Figure 4.1.

The CO spectrum of ALESS122.1 is the brightest in our sample, and its line profile is well described by a single-Gaussian fit. Table 4.2 lists the CO(3-2) line properties and best-fit parameter values. A detailed description of the velocity field sampled by these CO lines will be provided in Section 4.3.2.

Continuum images were made for all the sources after excluding the channels contributing to the CO(3-2) line emission. Using natural weighting to achieve the highest sensitivity[3], we obtained images with $\sigma_{\rm rms} \sim 6, 20, 18, 12$ μJy beam^{-1}, as summarized in Table 4.1. The

[3]The rms for ALESS49.1 is achieved using the concatenated dataset which has a lower resolution ($\theta_{\rm beam}$ ~0.7″) than the Cycle 2 only (~0.6″), as discussed in Section 4.2. The 88 GHz continuum emission measured from the Cycle 4 low resolution data alone ($\theta_{\rm beam}$ ~1.5″) has a ~ 9σ detection

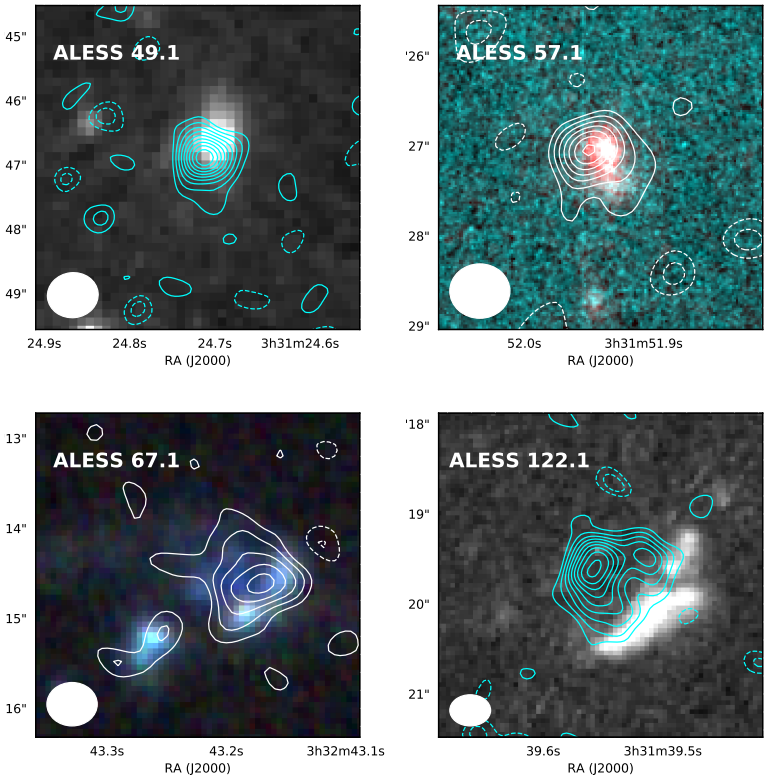

Figure 4.2: CO(3-2) velocity averaged contours overlaid on optical/near-IR cutouts from the available *HST*-WFC3 and/or ACS imaging. Resolutions of 0.4–0.6″ are achieved through natural weighting. The contours are obtained by averaging over the velocity range corresponding to the FWHM of the Gaussian fit to the CO spectrum. The contours in all maps show 2-10 $\sigma_{\rm rms}$ regions, where the $\sigma_{\rm rms}$ for the velocity averaged images is: (0.10 mJy beam^{-1}) for ALESS49.1, (0.15 mJy beam^{-1}) for ALESS57.1, (0.11 mJy beam^{-1}) for ALESS67.1 and (0.13 mJy beam^{-1}) for ALESS122.1. The beam sizes are shown in the lower-left corners of the images. The background map for ALESS49.1 represents the H_{160} imaging, the two-color map for ALESS57.1 uses the H_{160} and I_{814} fluxes, the background r-g-b map for ALESS67.1 represents $H_{160}, J_{125}, Y_{105}$ and the background map for ALESS122.1 shows the I_{814} imaging. The *HST* imaging has been corrected for astrometric offsets using *GAIA* data. We see that our observations strongly detect and resolve the CO emission of these sources on scales of 3–5 kpc, finding different morphologies in both CO and stellar emission.

continuum emission is detected in only two of the four sources in our data set: ALESS49.1 and ALESS122.1. In both cases, the naturally weighted dust continuum emission at 3mm (rest-frame ~850 μm) is detected at 4-σ significance at sub-arsecond resolution (Table 4.2).

To test for consistency with the Cycle 0 continuum observations at 870μm (Hodge et al. 2013b), we use an extrapolation following $S_\nu \propto \nu^{2+\beta}$, where S_ν is the measured flux density and β is the dust emissivity spectral index. Adopting $\beta = 1.5$ as a reasonable assumption for dusty galaxies (Swinbank et al. 2014; Casey et al. 2014), the values extrapolated from 870μm are consistent with our measured $S_{3\mathrm{mm}}$ peak flux densities and upper limits, which are listed in Table 4.2.

4.2.3 Source size estimation

High-resolution imaging reveals the detailed structure of the gas and dust continuum emission, which is key for placing constraints on the dynamical states of the sources. However, high-resolution interferometry is less sensitive to extended, low surface brightness emission, and thus care must be exercised in the estimation of the source sizes (e.g. Emonts et al. 2016; Dannerbauer et al. 2017; Ginolfi et al. 2017). Although the iterative cleaning method presented in Section 4.2.1 can provide a sense of the *total* source extent, it is prone to correlated noise effects and consequently may yield uncertain results. Moreover, iterative cleaning can only provide an (intrinsic) source size estimate when the extent of the source is greater than the synthesized beam. To determine the sizes independently of these possible beam-convolution effects intrinsic to the imaging process, we estimate the sizes directly from the uv-data (lower right panels of Figure 4.1).

We extract the uv-data corresponding to the frequencies within the FWHM of the line from the continuum-subtracted cube, centered at the CO(3-2) observed frequency. For each source, we then average the visibilities at different uv-distances and plot the resulting amplitudes against them, as shown in Fig. 4.1, where the data points correspond to the mean amplitude of the visibilities within each bin and the errors are the corresponding standard deviation of the mean. We fit a Gaussian profile to the data, taking into account the uncertainties, and measure the half-light radius of the source, which corresponds to the radius within which half of the light of the galaxy is contained. We report the estimated half-light radii $r_{1/2}$ in Table 4.2 and adopt these values for our analysis. The half-light radii of our sources range between 0.4–0.8″, which correspond to 2.6–6.9 kpc at the respective redshifts, implying total physical sizes (FWHM) of $\sim$ 10 kpc. In a study of the CO(3-2) emission of a similar sample of SMGs at $z \sim 2-3$, Tacconi et al. (2008) find sizes ranging between 2–12 kpc. More recent high-resolution molecular gas studies have reported similar sizes for low-J ($J \leq 3$) CO emission (e.g., Riechers et al. 2011; Ivison et al. 2011; Hodge et al. 2012). It is interesting to note that available high-J CO observations for some of these sources ($J = 6$; Engel et al. 2010) reveal that the physical extent of the emission may decrease for higher J-transitions.

Figure 4.2 shows the CO(3-2) emission overlaid on the stellar emission as traced by the WFC3/IR (bands $H_{160}, J_{125}, Y_{105}$) and/or ACS imaging ($I_{814}$) from *HST* (e.g., Chen et al. 2015). We note that the astrometry in the *HST*-images has been corrected based on the *GAIA* star positions, which are aligned to the Fifth Fundamental Catalogue (FK5) (Gaia Collaboration et al. 2016). With the exception of ALESS122.1, the CO gas overlaps with the stellar distributions, although they have slight offsets (0.1 − 0.3", 1–3 kpc offsets). The sizes of the gas and stellar distribution in these sources are also roughly similar. Specifically, the ratio of the *HST* H_{160} imaging (Chen et al. 2015) to CO half-light radii of these ALESS sources ranges between 1 and 1.5 (ALESS122.1 not included here as no H_{160} is available). We will compare the extent of the different components in a statistical study for SMG populations in Section 4.4.2. ALESS122.1 displays the striking feature that the gas and stellar emission are

Table 4.2: CO(3-2) line properties and estimated quantities.

	ALESS49.1	ALESS57.1	ALESS67.1	ALESS122.1
CO(3-2) $r_{1/2}$ [kpc]	2.6 ± 0.4	3.1 ± 0.5	6.9 ± 0.8	3.6 ± 0.3
$\mathrm{FWHM_{CO(3-2)}}$[km s^{-1}]	610 ± 30	360 ± 90	720 ± 160 (500 ± 110)[a]	600 ± 80
Dust continuum $S_{3\,\mathrm{mm}}$[μJy]	34 ± 6	54 ± 18	≤ 54[b]	≤ 60[b]
Inclination i[degrees][c]	80 ± 30	40 ± 50	50 ± 20	40 ± 20
Velocity integrated flux density $I_{\mathrm{CO(3-2)}}$ [Jy km s^{-1}]	0.89 ± 0.07	0.8 ± 0.2	3.9 ± 1.2 (1.8 ± 0.5)[a]	4.2 ± 0.8
Velocity integrated flux density $I_{\mathrm{CO(1-0)}}$ [Jy km s^{-1}]	–	–	0.44 ± 0.08 [d]	0.64 ± 0.07[d]
CO(3-2) line luminosity $L'_{\mathrm{CO(3-2)}}$ [10^{11} K km s^{-1} pc^2]	0.39 ± 0.03	0.4 ± 0.1	1.0 ± 0.3 (0.5 ± 0.1)[a]	1.0 ± 0.2
CO(1-0) line luminosity $L'_{\mathrm{CO(1-0)}}$ [10^{11} K km s^{-1} pc^2]	0.5 ± 0.2[e]	0.5 ± 0.2[e]	1.0 ± 0.2[d]	1.3 ± 0.2[d]
Molecular gas mass [10^{11}M$_\odot$($\alpha_{\mathrm{CO}} = 1.$)]	0.5 ± 0.2	0.5 ± 0.2	1.0 ± 0.2	1.3 ± 0.2
$M_{\mathrm{dyn}}(r \leq 2r_{1/2})$ [10^{11} M$_\odot$]	1.1 ± 0.2	1.1 ± 0.5	3.6 ± 1.6	5.3 ± 1.6
Stellar mass[f] [10^{11}M$_\odot$]	0.4 ± 0.1	0.8 ± 0.1	2.4 ± 2.1	0.8 ± 0.5
Infrared luminosities $L_{\mathrm{IR(3-2000\ \mu m)}}$[$\times 10^{12} L_\odot$][f]	6.8 ± 0.6	2.3 ± 2.2	5.0 ± 1.5	8.3 ± 2.5
SFR[f] [M$_\odot$ yr^{-1}]	700 ± 100	200 ± 200	400 ± 100	700 ± 200

[a] Values restricted to the main component of ALESS67.1 shown in Fig. 4.1. These values were used for the calculation of the dynamical masses using the disk approximation in Section 4.3.3.

[b] 3σ upper limits.

[c] Computed from axial ratios estimated with the CASA task IMFIT

[d] Measured by Huynh et al. (2017).

[e] Estimated using $r_{3/1} = 0.78 \pm 0.27$ (Sharon et al. 2016).

[f] As presented by da Cunha et al. (2015)

completely offset. We must point out, however, that the stellar emission in ALESS122.1 is exclusively represented by the ACS I_{814} band imaging (rest-frame 270 nm), in contrast to the other three sources which are covered by at least one WFC3/IR band. This particular case will be discussed in detail in Section 4.4.1.

Previous studies have shown that submillimeter continuum observations of similar galaxy populations reveal very compact rest-frame far-infrared-emitting regions, with median half-light radii of only $\sim$ 0.7–1.6 kpc (e.g., Simpson et al. 2015; Ikarashi et al. 2015; Hodge et al. 2016; Oteo et al. 2017). This is significantly more compact than the molecular gas emission in our sources. This difference in compactness is similarly observed between the dust continuum and radio emission of SMGs. Median radii of radio emitting regions originating from SMGs have been reported to be around 2.1 kpc in average (e.g., Chapman et al. 2004; Biggs & Ivison 2008; Miettinen et al. 2015, 2017; Thomson 2018). Motivated by these differences, we will explore in detail the relation between the radial profiles of the molecular gas, the dust continuum emission (at rest-frame 250μm) and stellar emission in Section 4.4.2.

4.3 Dynamical constraints to the total gas masses

4.3.1 Molecular gas masses

The masses of the CO(3-2) emitting gas in our sources can be estimated from the observed ^{12}CO(J=3-2) line luminosities $L'_{\rm CO}$. These were calculated following Solomon & Vanden Bout (2005) as $L'_{\rm CO} = 3.25\times10^7\ {\rm S_{CO}\Delta v}\ \nu_{\rm obs}^{-2}\ {\rm D_L^2}(1+{\rm z})^{-3}$ K km s^{-1}pc^2, where $S_{\rm CO}\Delta v$ is the velocity integrated flux, in Jy km s^{-1}; $\nu_{\rm obs}$ is the observed frequency, in GHz; and $D_{\rm L}$ is the luminosity distance in Mpc. The resulting values are listed in Table 4.2. Through an extrapolation from these CO masses we can calculate the total molecular content of the systems (dominated by H_2), by assuming a CO line luminosity to H_2 (+He) mass conversion factor, $\alpha_{\rm CO}$, and a brightness temperature ratio of CO(J=3-2) to CO(J=1-0). However, the combination of spatial and spectroscopic resolution of our data allows us to make an estimate of the total gas mass independently of the above mentioned assumptions, by estimating kinematic parameters (Section 4.3.2) and using further multiwavelength information to estimate the stellar mass contribution (Section 4.3.4). But to begin with we use the classical approach to estimate the molecular gas masses as a function of $\alpha_{\rm CO}$.

Using the measurements of ^{12}CO(J=1-0) by Huynh et al. (2017) for ALESS67.1 and ALESS122.1 (see Table 4.2), we calculate their brightness temperature ratio $r_{3/1} = L_{\rm CO(3-2)}/L_{\rm CO(1-0)}$, which yields $r_{3/1} = 1.01 \pm 0.36$ and $r_{3/1} = 0.77 \pm 0.19$, respectively. This is consistent with previous estimates for the SMG population (Ivison et al. 2011; Bothwell et al. 2013; Sharon et al. 2016). For ALESS49.1 and ALESS57.1 we estimate the ^{12}CO(1-0) emission using the excitation ratio for SMGs derived by Sharon et al. (2016), $r_{3/1} = 0.78 \pm 0.27$, yielding $L'_{\rm CO(1-0)} = (0.5 \pm 0.2)\times10^{11}$ K km s^{-1} pc^2, for both sources. The derived molecular gas masses as a function of $\alpha_{\rm CO}$ (equivalent to $\alpha_{\rm CO} = 1$) are reported in Table 4.2.

In order to investigate possible effects of the presence of an AGN on the molecular gas in our sample, we explore possible correlations between galaxy properties inferred from the CO measurements (listed in Table 4.2). We test for any bimodality in the distribution of properties such as the FWHM of the CO line, the gas-to-stellar mass fraction and star formation efficiency ($SFE = SFR/M_{\rm gas}$) corresponding to sources with and without an AGN (ALESS57.1 and ALESS122.1 are the AGN-host candidates in our sample, see Section 4.2.1). We find no clear bimodality correlated to the presence or absence of an AGN, although we note that this result is not conclusive given the very small size of our sample. However, we expect that the scales probed by our CO observations are not affected by AGN, since the CO transition

probed ($J = 3 - 2$) is not expected to be a tracer of AGN excitation (e.g., Sharon et al. 2016).

4.3.2 CO line kinematics

The morphological and kinematic properties of our resolved CO images allow us to explore the nature of these star-forming systems, whether these are in an early stage of a merger with a chaotic structure, or whether their velocity fields are described by an ordered rotating disk. It is important to note, however, that these scenarios are not mutually exclusive. Observing dynamics consistent with a rotating disk does not preclude the galaxy from being a merging system, as the gas is collisional and an ordered rotating disk can quickly reform after the final coalescence stage as has been shown observationally and theoretically (Robertson et al. 2006; Hopkins et al. 2009, 2013; Ueda et al. 2014).

While the few existing examples of CO detections at similar resolution suggest a mixture of mergers and disk-like motion (e.g., Tacconi et al. 2008; Engel et al. 2010; Hodge et al. 2012), recent high resolution continuum imaging of SMGs has shown that the dust continuum emission (at rest-frame 250 μm) is mostly described by compact disk profiles (e.g. Simpson et al. 2015; Hodge et al. 2016). Here we use our high-resolution CO observations to directly test the kinematics of these systems.

Position–velocity diagrams

To estimate the kinematic properties of our sources we first investigate their position–velocity (PV) diagrams. We apply the interactive PV Diagram Creation task from the CASA VIEWER to the data cubes of our sources with spectral resolution corresponding to channel widths of $\sim 100\,\mathrm{km\,s^{-1}}$. The lower panel of Figure 4.3 show the kinematical major axis chosen for the extraction of the PV diagrams overplotted as blue arrows on the velocity-averaged CO images. The upper panels show the resulting PV diagrams for the respective sources. We find velocity gradients in the PV diagrams of three of our four sources (with ALESS67.1 also showing some weak signs), suggesting that the bulk of emission in these sources is dominated by rotation.

The velocity gradients of ALESS49.1, ALESS57.1 show double peaks at each side of the galactic center, although the detailed velocity structure is ambiguous given the modest SNR. In ALESS49.1, the double-peaked spatial structure gives rise to the double-peaked line profile observed in Figure 4.1. Since both sources have the CO centered on a single optical nucleus (as seen from their high-resolution *HST* imaging), the velocity structure suggests the presence of a disk structure or a disk-shaped merger remnant, rather than an early stage merger.

The CO emission in ALESS67.1 and its velocity structure appears more chaotic, which is probably accentuated by the combination of extended emission and the lower SNR achieved in this source. A detailed analysis of the velocity structure of this individual source has been conducted in a complementary study by Chen et al. (2017). They presented *SINFONI* Hα observations of ALESS67.1, revealing that the extended CO emission (including the second component to the south-east) follows the bulk rotational motion of the rest-frame optical Hα emission line. Kinematic modelling of both lines concluded the bulk of the molecular gas in ALESS67.1 could be described as an on-going merger, although without being able to reject a rotating disk given the errors. It is still uncertain whether ALESS67.1 is a multi-component system in an early state of merging. This scenario has been discussed in Section 4.2.2 based on our CO and *HST* observations, and it has also been supported by the analysis of its kinematics based on ancillary data by Chen et al. (2017). For further dynamical mass calculations we will only consider the properties of the most luminous component of ALESS67.1 (Table 4.2), and assume that this component is well-described by a rotating disk.

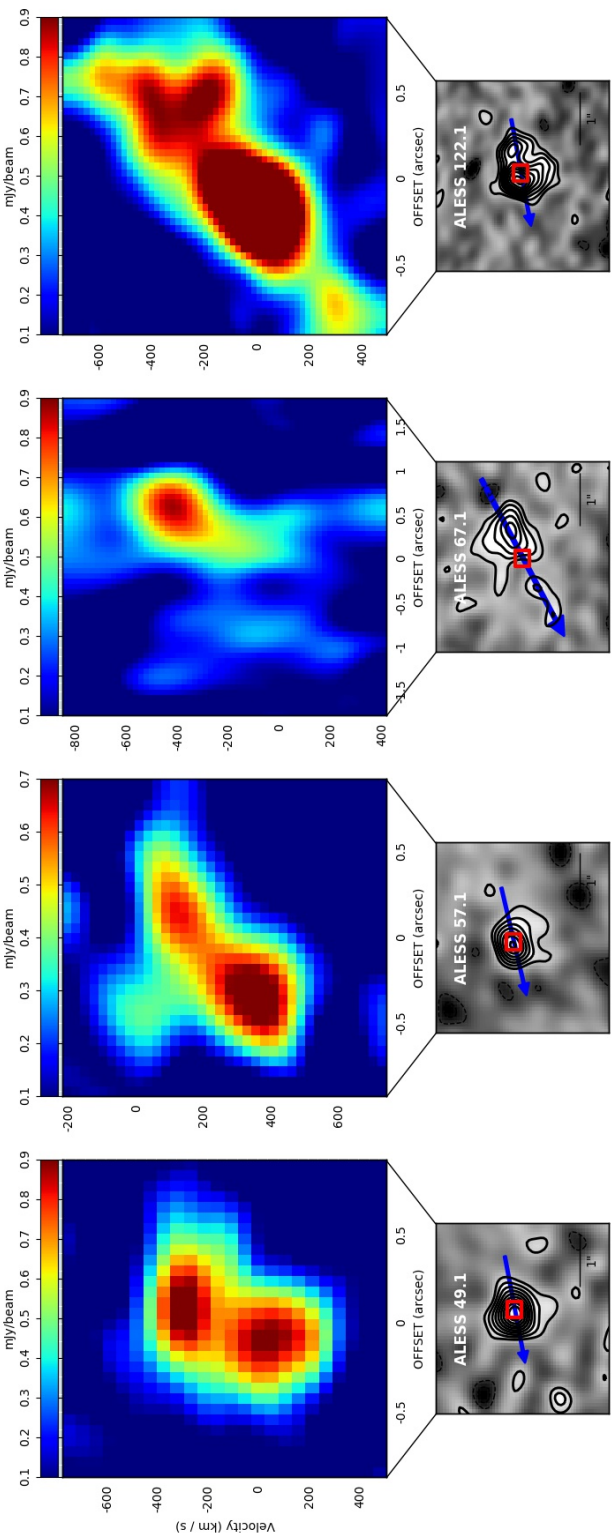

Figure 4.3: Position–velocity (PV) diagrams for the CO(3-2) emission in our sources. The *lower panels* show the velocity-averaged CO images of our sources. The arrows represent the kinematical major axis chosen for the extraction of the PV diagrams, the arrow head shows positive velocity offset, and the squares show the origin of the PV plot. The upper panels show the corresponding resulting PV diagrams for the respective sources. Velocity gradients from the south-west to north-east direction can be recognized in at least three sources (ALESS 67.1 may also have weak evidence), suggesting that the CO emitting material in these sources is supported by rotation with velocity gradients of ~300 km s^{-1} on spatial scales of ~ 0.2–0.7″.

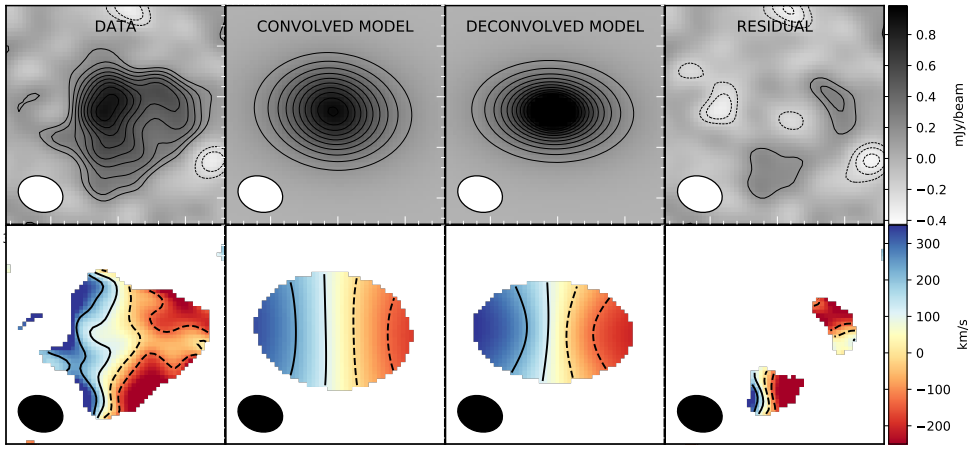

Figure 4.4: Modelling of the morphology and kinematics of ALESS122.1 with GALPAK3D. The top row shows the zeroth-moment maps (integrated intensity) of the observed, convolved model, deconvolved model and residual cubes. The contour lines in the top row show the 2-9 $\sigma_{\rm rms}$ levels, where $\sigma_{\rm rms}$ is the noise level of the zeroth-moment maps. The bottom row shows the first-moment maps (intensity-weighted velocity) of the corresponding cubes, showing only regions with fluxes $> 2\sigma_{\rm rms}$. The color scale represents the width of the CO line in km s^{-1}. The low-intensity levels of the residual maps show that the bulk of the emission can be described by disk rotation. This, however, does not preclude the galaxy from being a merger, as an ordered rotating disk can be quickly 'reformed' after the final coalescence stage in a few dynamical times (Robertson et al. 2006; Hopkins et al. 2013)

ALESS122.1 is the source with highest SNR in our sample and its velocity structure is consistent with disk rotation. Due to these reasons it was possible to analyse its velocity field quantitatively using a rotating disk model, as will be described in Section 4.3.2.

Although the velocity gradients may be consistent with large-scale disk rotation as a bulk motion, we emphasize that no conclusions can be drawn to exclude complex, disturbed gas motions on scales smaller than the resolution limit of our data. Based on this qualitative analysis of the PV-diagrams in Figure 4.3, we will adopt the scenario of a rotating disk for our sources for the computation of their dynamical masses. The velocity line width (and thus an estimate of the velocity dispersion) and other morphological properties will be adopted from the values listed in Table 4.2.

Kinematic Modelling

To quantitatively describe the kinematics of the molecular gas in our sources, we model the data using the modelling package GALPAK3D. GALPAK3D is a Bayesian parametric Markov Chain Monte Carlo fitter for three-dimensional (3D) galaxy data that attempts to disentangle the galaxy kinematics from resolution effects (Bouché et al. 2015). Starting from a set of uniform priors on the disk parameters (source center, radius, inclination, velocity dispersion, etc.), a 3D disk galaxy model is produced assuming an exponential radial flux profile. The fitting process consists then in comparing the observed data cube to mock data cubes modelled at each point of the parameter space. In each step the reduced χ^2_ν value is then minimized to

efficiently sample the probability density functions of the parameters. The reliability of the inferred kinematic parameters in GALPAK3D goes approximately as $\frac{\delta p}{p} \propto \frac{r_{1/2}}{r_{beam}} \times SB_{1/2,obs}$, i.e. the uncertainty in the inference of the parameter p is inversely proportional to the source size to resolution ratio ($\frac{r_{1/2}}{r_{beam}}$) and surface brightness of the source ($SB_{1/2,obs}$). Given the dependence of these uncertainties on the quality of the data and due to the SNR limits in most of our sources, we were able to apply this method only to the source with highest SNR and resolution, ALESS122.1. For the sources on which the dynamical modelling cannot be applied, we use the line profiles to draw estimates of kinematic properties such as rotational velocity (Section 4.3.3).

Figure 4.4 shows zeroth-moment (integrated intensity) and first-moment (intensity-weighted velocity) maps for ALESS122.1. The four images correspond to the moment maps of the observed data cube, the convolved model, deconvolved model and residual (model-substracted) cubes, where the latter three cubes are output products of GALPAK3D. We estimated the noise per pixel in the zeroth-moment map as $\sqrt{N} \times \sigma_{chan}$, where N is the number of channels used and σ_{chan} is the rms noise per channel. Using this value, for the computation of the first moment maps of the four cubes, we masked out all pixels with SNR<2. The bottom row of Figure 4.4 shows the first-moment maps (intensity-weighted velocity) of the corresponding cubes. The color scale has been chosen to represent the velocity width of CO line of the source.

The resulting 3D model cube shows a modest agreement with the data, with a reduced χ^2_ν of 1.87, which is calculated over the total area and frequency range covered by the observed and modelled data cubes, as represented in Figure 4.4. The slightly-high reduced χ^2_ν value can be explained by residual structure, which can be seen in the 0th and 1st moment maps of the residual cubes. The model parameters obtained for the source agree with comparable properties inferred directly from the line profile.

The bulk of the velocity field of ALESS122.1 is consistent with a rotation-dominated disk (mindful of the residual clumps), with an inclination of $i \sim 52°$, a maximum rotational velocity of $v_{\rm max} \sim 560\,{\rm km\,s^{-1}}$, and a velocity dispersion of $\sigma_v \sim 130\,{\rm km\,s^{-1}}$. The residual image in the right upper panel of Figure 4.4 reveals few residual clumps between 2-3 σ significance, consistent with being noise. We conclude that the bulk of the velocity field is to a first order consistent with disk rotation.

4.3.3 Dynamical Masses

The kinematic properties of a galaxy, obtained e.g. through modelling its velocity field, can provide a reliable estimation of the mass enclosed within the region covered by the emitting medium. At high redshift, this is a complicated task, since observations of molecular gas are frequently poorly spatially resolved and the morphology of the mass distributions are thus usually unknown. Based on the kinematic study above and the size estimates from our analysis, we calculate the dynamical masses assuming the bulk of the emission in our sources can be well described by a rotating disk. The total dynamical mass within a radius $r = 2r_{1/2}$ is then given by:

$$M_{\rm dyn}(r < 2r_{1/2}) = \frac{(v_{\rm max}/\sin(i))^2 \times 2r_{1/2}}{G}, \tag{4.1}$$

where $r_{1/2}$ is the half light radius estimated through *uv*-fitting measured in kpc, i is the inclination of the galaxy (4.2) and G the gravitational constant (e.g., Solomon & Vanden Bout 2005; Erb et al. 2006; de Blok & Walter 2014). In the cases where the velocity field cannot be modelled and $v_{\rm max}$ cannot be directly inferred, we can use the approximation that the velocity width is twice the maximum rotational velocity and thus we can replace $v_{\rm max} = 1/2 \times \Delta V_{\rm FWHM}$

in Equation 4.1. This is a good assumption for a flat rotation curve with a steep inner rise and a filled exponential disk as shown by de Blok & Walter (2014). For ALESS122.1 we use the parameter values for $v_{\rm max}$ resulting from the kinematic modelling in Section 4.3.2, although both estimates provide consistent results within errors.

A large uncertainty in the estimation of the dynamical masses is contributed by the inclination angle of the disk. In previous dynamical-mass studies, it has been customary to adopt a value of $< \sin^2(i) >= 2/3$ (corresponding to i=54.7 deg), which is the average value expected for a randomly oriented population of disk galaxies. However, given our high resolution data, we have enough information to use a simple assumption motivated by the early observation that the apparent axis ratio is closely related to the inclination angle for a disk. We use the relation $cos^2(i) = ((b/a)^2 - q_0^2)(1 - q_0^2)^{-1}$ (Hubble 1926), where (b/a) is the axis ratio and q_0 is the inherent thickness of the disk, assuming $q_0 = 0.1$ (Nedyalkov 1993) . Obtaining the deconvolved axis ratios using the CASA routine IMFIT, we compute the inclination angles for ALESS49.1, ALESS57.1, ALESS67.1 and ALESS122.1 to be $i \sim 80 \pm 30°, 40 \pm 50°, 50 \pm 20°$ and $40 \pm 20°$, respectively. For ALESS122.1, where a more complex analysis was possible in Section 4.3.2, we will adopt the inclination angle estimated through the kinematic modelling, $i \sim 52 \pm 2°$, which is in agreement with the axis-ratio approximation within the errors. Although this is an approximation and the uncertainties are large, this estimation is superior to assuming the single value of $< \sin^2(i) >= 2/3$ for all systems, since the inclination in individual sources may anti-correlate with line width. It is interesting to note the high inclination angle of ALESS49.1, which is also supported by the small CO size and double-peaked line profile. Although these profiles are not uncommon for rotating disks and have been found in at least 40% of SMGs (Tacconi et al. 2008; Bothwell et al. 2013), the asymmetry between the double-peaked profile suggests a non-uniform distribution of the gas in the 'disk', produced possibly by minor instabilities or an unresolved merger of two gas disks.

The resulting dynamical masses for our sample range from 1–5×10^{11}M$_\odot$(Table 4.2), as calculated within 2× the half-light radii of the sources $r_{1/2}$. These values are in general agreement with previous measurements of the dynamical masses of two of these sources based on other tracers (CO(J=1-0) and Hα, Huynh et al. 2017; Chen et al. 2017). [4] This range corresponds to masses at the high end of the average values found for other SMG samples by Ivison et al. (2010) (2.3×10^{11}M$_\odot$), Tacconi et al. (2008) (1.3×10^{11}M$_\odot$), Engel et al. (2010) ($\sim 1.9 \times 10^{11}$M$_\odot$) and slightly below the values found for some extreme sources such as GN20 ($5.4 \pm 2.4 \times 10^{11}M_\odot$, Hodge et al. 2012) and SMMJ131201 ($9.5 \pm 2.4 \times 10^{11}M_\odot$, Engel et al. 2010). The uncertainties in these values are propagated from all parameters used in their calculation, including the inclination angles i (Table 4.2).

4.3.4 Implications on α_{CO} and M_*/L estimates

The dynamical mass estimates discussed in Section 4.3.3 can be related to the various mass components in galaxies following:

$$M_{dyn}(r \leq 2r_{1/2}) = M_{\rm baryons}(r \leq 2r_{1/2}) + M_{\rm DM}(r \leq 2r_{1/2}), \tag{4.2}$$

[4] In a study of the CO(1-0) emission, Huynh et al. (2017) found equivalent dynamical masses of $M_{\rm dyn} \sin i^2 = (2.1 \pm 1.1)$ and $(3.2 \pm 0.9) \times 10^{11} M_\odot$ for ALESS122.1 and ALESS67.1, respectively. Although discrepancies were expected given that they used optical instead of CO extensions due to the low resolution of their CO data and assumed an inclination angle of $\sin^2(i) = 2/3$, their result is consistent with ours given the errors. Similarly, a dynamical study of the $H\alpha$ emission in ALESS67.1 presented by Chen et al. (2017) estimated a dynamical gas mass of $M_{\rm dyn} = (2.2 \pm 0.6) \times 10^{11} M_\odot$ for ALESS67.1. Although this estimation resulted from the analysis of the total source, while our calculation used only the main component of the source, the values estimated agree with our calculations within the errors.

where $M_{\rm baryons} = M_{\rm gas} + M_*$ and $M_{\rm DM}$ is the dark matter contribution. Thus, given assumptions on the dark matter (DM) content and stellar masses, the dynamical mass estimates can be used as an independent method to constrain the total gas masses in galaxies. Before we proceed to constrain the gas masses using this method, we summarize the unknown parameters intrinsic to this calculation. We note that given the scarcity of CO($J \leq 3$) gas data at high resolution, most of the existing literature on molecular gas in high-redshift galaxies usually assume fixed values for unknown parameters, estimating gas masses which are thus sensitive to these assumptions and lacking information on the inherent systematic uncertainties.

To begin with, the H_2 molecules that comprise the bulk of the molecular gas reservoir in galaxies are not directly observable. Measurements of molecular gas thus rely on CO observations, via a conversion from the ground-state CO(1-0) luminosity which is parametrized with the factor $\alpha_{\rm CO}$. Indeed, high-redshift measurements are providing increasing evidence that the $\alpha_{\rm CO}$ values in the early universe can be lower than in solar-metallicity galactic disks ($\alpha_{\rm CO} \sim 0.8$–1.0, e.g., Tacconi et al. 2008; Hodge et al. 2012; Bothwell et al. 2013).

In addition to the uncertainties in the total gas mass estimation, stellar mass estimates are typically obtained via SED-fitting, which relies on assumptions regarding the star formation history (SFH) of the stellar populations and dust attenuation, which can be uncertain especially for starburst systems (such as SMGs). In particular, it has been increasingly observed that SED fitting of starburst systems suffers from a degeneracy between the SFH, the mass-to-light ratio ($M_*/L_{\rm H}$) and the age of the galaxy (Hainline et al. 2011; Michałowski et al. 2012; Simpson et al. 2014). This degeneracy means that in a galaxy with an instantaneous-burst SFH the total stellar mass would be contained almost exclusively within young luminous stellar populations, resulting in a low ($M_*/L_{\rm H}$) ~ 0.05. Conversely, in a galaxy of intermediate age with a constant SFH, most of the stellar mass would be distributed in old faint populations whose emission is outshone by the luminous newly born stars, implying a higher mass-to-light ratio ($M_*/L_{\rm H} \sim 0.3$). As shown by recent resolved SED-fiting studies (Sorba & Sawicki 2018), this effect could underestimate total stellar masses by factors of up to 5, especially in sources of high specific star-formation rates such as SMGs.

Rather than adopting a single (M_*/L_H) or $\alpha_{\rm CO}$, we can instead parametrize the baryonic mass as:

$$M_{\rm baryons} = L_H \times M_*/L_H + \alpha_{\rm CO} \times L_{\rm CO}, \tag{4.3}$$

where L_H is the rest-frame H-band luminosity corrected for dust obscuration (here estimated by da Cunha et al. 2015) and $L_{\rm CO}$ is the CO(J=1-0) luminosity estimated in this work.

Finally, the dynamical mass of a galaxy also includes the mass of the non-baryonic dark-matter (DM) component, which is a source of uncertainty, as no independent measurement of this mass fraction is available for our SMGs. Unlike observations in local disk galaxies, which have reported dark matter fractions ($f_{\rm DM}$) of $\sim 50\%$ (e.g., Courteau & Dutton 2015), it has been claimed by recent spectroscopic surveys (e.g., Price et al. 2016; Wuyts et al. 2016; Genzel et al. 2017) that more compact star-forming disk galaxies at $z > 2$ appear to be heavily baryon dominated with $f_{\rm DM}$ ~10–20%, although these calculations involve the same unknown factors as are used for the gas fractions. In contrast, recent simulations (e.g. Lovell et al. 2018) have reported that the dark matter fractions in disc-like galaxies could range up to 65% for galaxies with stellar masses similar to SMGs ($\sim 10^{11} {\rm M}_\odot$). Combining equations 4.2 and 4.3, the total mass can be expressed as:

$$M_{\rm dyn} = \frac{L_H \times (M_*/L_H) + L_{\rm CO} \times \alpha_{\rm CO}}{(1 - f_{\rm DM})}, \tag{4.4}$$

where the conversion factor $\alpha_{\rm CO}$, the stellar mass-to-light ratio (M_*/L_H) and the dark matter fraction $f_{\rm DM}$ are the unknown parameters. Given the small number of independent data points

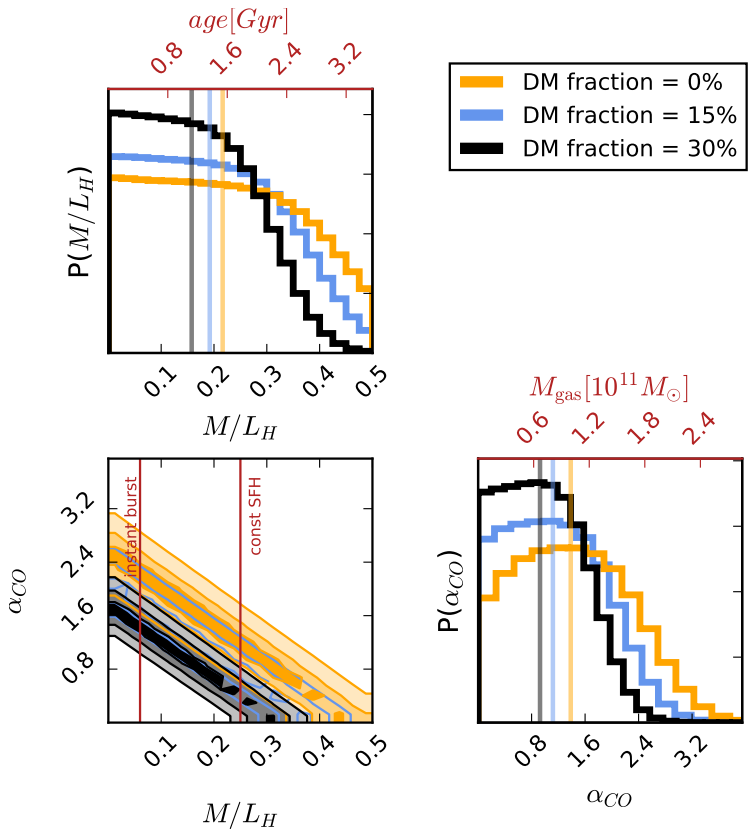

Figure 4.5: One- and two-dimensional posterior probability density functions (PDFs) of the M_*/L_H and $\alpha_{\rm CO}$ parameters for the ALESS sources in this work. *The upper and lower-right panels* show the one-dimensional PDFs as histograms, where the orange, blue and black solid lines correspond to the inference assuming dark matter contributions of 0%, 15% and 30%, respectively. The galaxy age axis (upper panel, in red) equivalent to the M_*/L_H axis is computed using the relation presented by Hainline et al. (2011) for an instantaneous burst SFH. The $M_{\rm gas}$ axis (lower-right panel, in red) is computed by adopting the median $L_{\rm CO}$ of our sample, $< L_{\rm CO} >= 7.7 \times 10^{10}$ K km/s pc^2. The transparent orange, blue and black vertical lines correspond to the median values of the distributions. *The lower-left panel* shows the covariance plot (two-dimensional PDF) of the parameters, were a clear correlation can be recognized through the diagonal shape of the contours, which represent the 25th, 50th and 75th percentiles of the sampled distribution.Two reference lines (red) are drawn, corresponding to the average M_*/L_H ratio found by Simpson et al. (2014) for the ALESS survey as a whole, assuming a constant SFH in contrast to an instantaneous burst SFH.

available (one for each of our four sources), in order to reduce the parameter space we will keep the $f_{\rm DM}$ value fixed, and discuss the effect of low and high $f_{\rm DM}$ values to the other parameters distributions later on.

Firstly, we explore the parameter space built up in Equation 4.4 by applying an MCMC technique, using the open-source algorithm EMCEE (Foreman-Mackey et al. 2013) for the sampling. Based on the likelihood of the measured dynamical masses $M_{\rm dyn}$ (estimated in Section 4.3.3 as a function of $L_{\rm CO}$ and $L_{\rm H}$) given this model, we sample the posterior probability density function (posterior PDF) for $\alpha_{\rm CO}$ and (M_*/L_H). It is important to note that at this point the likelihood function accounts only for the uncertainties in the dynamical masses $M_{\rm dyn}$. To account for the uncertainties in the $L_{\rm CO}$ and $L_{\rm H}$ variables as well, we use a Monte Carlo approach and repeat the inference exercise presented above for 100 iterations, each time using values randomly chosen from within a normal distribution that corresponds to the mean and standard deviation of our $L_{\rm CO}$ and $L_{\rm H}$ measurements.[5] Finally, we average the posterior PDFs gathered in these 100 iterations and obtain a final probability distribution for the parameters which takes into account the uncertainties in the measurements of all observables ($M_{\rm dyn}$, $L_{\rm CO}$ and $L_{\rm H}$).

Fig. 4.5 shows the one- and two-dimensional final posterior PDFs of the (M_*/L_H) and $\alpha_{\rm CO}$ parameters adopting three different dark-matter fractions $f_{\rm DM}$ = 0%, 15% and 30%. The covariance between the parameters can be recognized in the two-dimensional PDF (Figure 4.5) as an elongated ellipse in the central contour level plot. Higher DM fractions decrease the value of $\alpha_{\rm CO}$ and consequently $M_{\rm gas}$. This trend is similarly followed by the $(M_*/L_{\rm H})$ parameter. For a DM fraction of 15% we find a median value of $\alpha_{\rm CO} = 1.1^{+0.8}_{-0.7}$ [M$_\odot$/(K km s^{-1} pc^2)$^{-1}$], while for a larger DM fraction of 30%, these values decrease to $\alpha_{\rm CO} = 0.9^{+0.7}_{-0.6}$ [M$_\odot$/(K km s^{-1} pc^2)$^{-1}$]. For $f_{\rm DM} = 0$ we obtain an upper limit to $\alpha_{\rm CO} \leq 1.4^{+0.9}_{-0.9}$ [M$_\odot$/(K km s^{-1} pc^2)$^{-1}$]. For the mass-to-light ratio parameter we find $(M_*/L_{\rm H}) = 0.22^{+0.16}_{-0.15}M_\odot$/L$_\odot$, $(M_*/L_{\rm H}) = 0.19^{+0.15}_{-0.13}M_\odot$/L$_\odot$ and $(M_*/L_{\rm H}) = 0.16^{+0.12}_{-0.10}M_\odot$/L$_\odot$ for DM fractions of 0%, 15% and 30%. Using these values, the gas reservoirs in our sources have an average gas mass of $\sim 0.9 \times 10^{11}$M$_\odot$(DM contribution of 15%) and $\sim 0.7 \times 10^{11}$M$_\odot$ (DM contribution of 30%), corresponding to average gas-to-total-mass fractions of 0.26% and 0.33%, respectively. These sources show similar gas fractions than those reported for typical star-forming galaxies ($\leq$ 50%, Tacconi et al. 2017). For comparison, Bothwell et al. (2013) presented a study of a representative sample of SMGs at z ~2 from predominantly CO(3-2) observations, finding mean gas masses of $(3.2\pm2.1)\times10^{10}$M$_\odot$assuming $\alpha_{CO} = 1$. Since the resulting PDF for the $M_*/L_{\rm H}$ and *age* parameters for our galaxies is broad and poorly constrained, the galaxy stellar population properties inferred through this method ($\sim 0.1 - 2.0$ Gyr) easily agree with those estimated through SED-fitting by da Cunha et al. (2015), which are also associated with large errors (~70%). They find the age of these galaxies range between ~ 0.04–1.22 Gyr, corresponding to $M_*/L_{\rm H}$ between 0.16–0.2.

As discussed above, the values recovered for the parameters are subject to large uncertainties due to our small sample size. However, we note that one goal of this exercise is to shed light upon the degeneracies among the key parameters and large uncertainties inherent to gas mass calculations. Most importantly, given the increasing availability of dynamical mass measurements for high-redshift galaxies with ALMA, we consider that this approach

[5] We note that while $L_{\rm H}$ is an independent measurement, $M_{\rm dyn}$ and $L_{\rm CO}$ are both a function of the velocity FWHM of the line emission $\Delta V_{\rm FWHM}$, which can affect the robustness of the parameter uncertainties inferred through the MCMC routine. In order to account for the correlated errors induced through this dependence while simulating the uncertainties of $L_{\rm CO}$, each Monte Carlo iteration adopts $M_{\rm dyn}(\Delta V_{\rm FWHM})$ and $L_{\rm CO}(\Delta V_{\rm FWHM})$, where $\Delta V_{\rm FWHM}$ assumes a single value for both functions and is each time randomly sampled from within a normal distribution that corresponds to the mean and standard deviation of $\Delta V_{\rm FWHM}$. In this way the correlated measurements of $M_{\rm dyn}$ and $L_{\rm CO}$ are robustly accounted for during the Monte Carlo sampling.

has potential for constraining the molecular gas properties with more accuracy, especially since larger sample sizes will allow the exploration of a more detailed parameter space in the future.

4.4 Distributions of molecular gas, dust continuum and stellar emission

4.4.1 Offset distributions of ISM tracers and stellar emission in ALESS122.1

An interesting case among our sample is the apparently uncorrelated distribution of dust continuum, gas and stars in ALESS122.1 (Fig. 4.6). The gas and stellar emission extend across regions of similar size, separated by $\sim 0.5''$ (~ 5 kpc at $z = 2$) as measured from their centroids, but are tightly aligned next to each other. There is almost no overlap of gas and stellar emission, even when considering the combined astrometric uncertainties (<0.1″[6]). Moreover, while the gas and stars have half-light radii $r_{1/2} \sim 4$ kpc and are thus extended on scales of ∼10 kpc, the detected dust continuum emission (3mm observed-frame, corresponding to $\sim 850\ \mu$m rest-frame) is confined to a central region of ∼5 kpc, with the emission peak spatially coincident with that of the molecular gas emission. Similar physical offsets between dust continuum, gas and stellar emission, and specifically between ALMA and *HST*, have been previously found in a number of high-redshift sources (e.g., Riechers et al. 2010; Chen et al. 2015; Hodge et al. 2015; Fujimoto et al. 2017; Simpson et al. 2017; Elbaz et al. 2017). For example, based on low-resolution 870μm continuum data (∼1.5″), Chen et al. (2015) reported a statistical offset with the existing stellar component traced by *HST* as large as $\Delta p = 0.4''$ (~ 4 kpc at $z = 2$) in 66% of the ALESS SMGs. Similarly, Hodge et al. (2015) found in the $z = 4$ galaxy, GN20, that the FIR and CO emission are offset by 0.6″ (4 kpc) from the peak of the rest-frame UV emission as traced by the *HST*/WFC3 F105W image.

We consider three scenarios for explaining the mismatch of the distributions of stellar and gas/dust continuum emission in ALESS122.1. The first and most plausible scenario assumes that the optical component extends to the regions of gas and dust continuum emission, while suffering extreme extinction in these regions. Such high-extinction scenarios have been suggested previously in starbursts with extreme SFRs and in cases of partial or total absence of optical counterparts (e.g., Walter et al. 2012; Hodge et al. 2012; Simpson et al. 2015). This is not uncommon in sub-mm selected samples, where optical detection rates are only $\sim 70-80\%$ even with deep data (e.g., Simpson et al. 2014).

The second scenario implies that the observed offset reflects a physical misalignment between the gas/dust continuum distributions and that of the stellar mass. This argument has been tested by Chen et al. (2015) for the full ALESS sample. They tested this hypothesis by comparing the positional offsets found in low-redshift ($z < 2$) to those in high redshift ($z > 2$) subsamples, taking into account that at lower redshift the optical photometry would probe wavelengths less affected by obscuration. They found no statistical difference in the measured positional scatter between the low- and high-redshift samples, implying that obscuration is not the dominant factor for the population as a whole.

The third scenario implies that ALESS122.1 is an ongoing, merging system comprised of two components, one of which is a heavily obscured SMG which has no detected optical counterpart, and the other is an optically bright galaxy in the *HST*-ACS F814W imaging (which corresponds to rest-frame ~ 3000 Å). High-resolution optical-MIR counterparts at

[6]The *HST* astrometric uncertainties are low since the image has been accurately calibrated using *GAIA* measurements of this field.

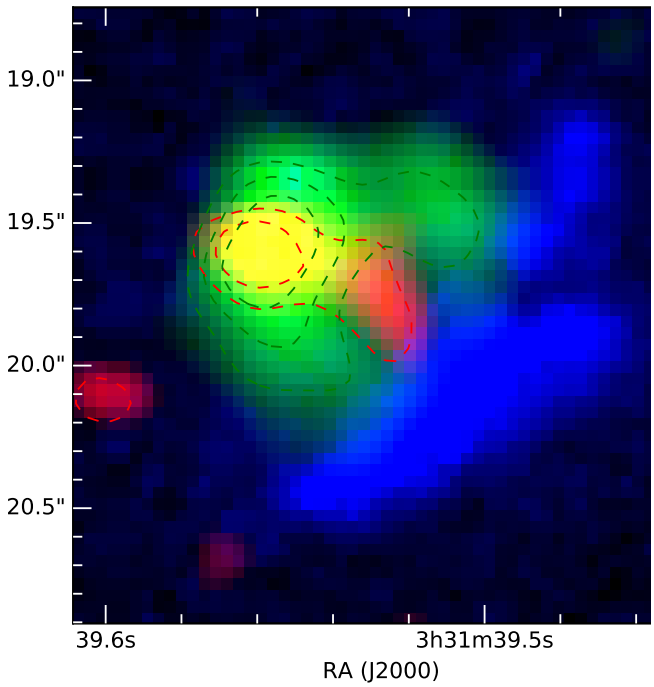

Figure 4.6: False-color image of the molecular gas, dust continuum and stellar emission components in ALESS122.1. The molecular gas (green) shows the CO(3-2) emission and the dust continuum region (red) corresponds to the 3 mm (rest-frame $\sim$ 850 μm) continuum detection (4σ), both masked at $S \geq 3\sigma$. For clarity we overplot dashed contours for both the CO ($6, 8, 10\sigma$) and dust continuum emission (3 and 4σ), to show that their centroids are co-located. The stellar emission (*HST*-ACS F814W) is presented as the blue region and shows a large offset from the gas and dust centroid, with almost no overlap even when considering the combined astrometric uncertainties. The *HST* astrometry in this data is accurate since the images were corrected based on *GAIA* measurements. The increasing evidence of a population of sources with misaligned stellar, dust continuum and gas emission has important implications for energy balance assumptions in SED-fitting. We discuss the striking difference between the observed extent of the gas and dust continuum emission for a larger sample of sources in Section 4.4.2.

other wavelengths are needed in order to confirm the nature of this source and explain the uncorrelated distributions of its physical components.

Regardless of the underlying scenario, the significant anticorrelation between dust continuum and optical imaging disprove some assumptions which are intrinsic to multiwavelength studies such as energy balance in SED-fitting (this has been previously discussed by e.g., Hainline et al. 2011; Chen et al. 2015; Hodge et al. 2016; Simpson et al. 2017; Chen et al. 2017).

4.4.2 Statistical analysis on the relative sizes of dust continuum, molecular gas and stellar emission in SMGs

To gain a general understanding of the distributions of the molecular gas, dust continuum, and stellar emission in SMGs and how they relate, next we conduct a stacking analysis using the CO emission measured in our sources and the available multiwavelength data at similar resolution.

We first produced the stacked radial profiles of the CO emission of the four ALESS sources presented here. To achieve this, we create $10 \times 10''$ thumbnails of our sources, align their centers and scale them to have the same peak flux. We then produce the radial profiles of the individual sources by radially averaging the emission centered at the source peak, and finally, we average the individual radial profiles in our sample (Figure 4.7).[7] To account for the effect of outlier structures of the individual sources, we estimate the uncertainties of the radial profiles through bootstrapping, e.g., by creating 1000 different average profiles, where each iteration used a randomly resampled combination of sources.

Using the same technique, we also stack high-resolution dust continuum emission (0.16″ FWHM at rest-frame 250 μm) of 16 luminous ALESS sources studied by Hodge et al. (2016). This sample of sources are representative of the ALESS survey as a whole (ALESS median $z = 2.5 \pm 0.2$ and $L_{\rm IR} = (3.0 \pm 0.3) \times 10^{12} L_{\odot}$, Simpson et al. 2014; Swinbank et al. 2014) as they have a median redshift of $z = 2.6 \pm 0.5$ and infrared luminosity of $L_{\rm IR} = (3.6 \pm 0.9) \times 10^{12} L_{\odot}$. Most importantly, these properties are also comparable to those of the sample used for the CO stacked profiles (median redshift of $z = 2.5 \pm 0.4$ and infrared luminosity of $L_{\rm IR} = (5.6 \pm 2.2) \times 10^{12} L_{\odot}$), although both samples have only one source in common (ALESS67.1).

Finally, we stack high resolution *HST* imaging (0.17″ in the H_{160} band) available for the same 16 ALESS sources following the procedure described above. The stacked surface brightness profiles for the gas, dust continuum and stellar components are shown in Fig. 4.7 as green, red and blue data points, respectively.

To quantify the extent and distribution of the molecular, sub-mm and optical/near-infrared emission, first we assume that the observed emission can be described by a exponential profile (Sérsic profile with index n=1) convolved with a Gaussian profile, which corrects for the effect of the shape of the beam. Based on this we fit a one-dimensional exponential to the CO and dust continuum profiles and find that they are well described by such a model. We note that for fitting the dust profile we discarded the data points at radius of >7 kpc, since these are evidently affected by artifacts produced by the side lobes of the beam (shown as the shaded area in Fig. 4.7)[8]. The radial profile of the stellar emission results in a bad quality fit when using an exponential, i.e. when fixing the Sérsic index $n = 1$. To improve this, we leave the Sérsic index as a free parameter and achieve a better quality fit with $n = 0.8 \pm 0.2$, which is consistent within the errors with the median value found for the ALESS sample as whole

[7] We note that we investigated the difference between the approach described above and an approach in which a stacked image is produced first and the mean radial profile is then extracted directly from the stacked image. We find that both methods are equivalent and result in identical average radial profiles.

[8] This issue is not relevant for CO, since the side lobes appear only at r>15 kpc

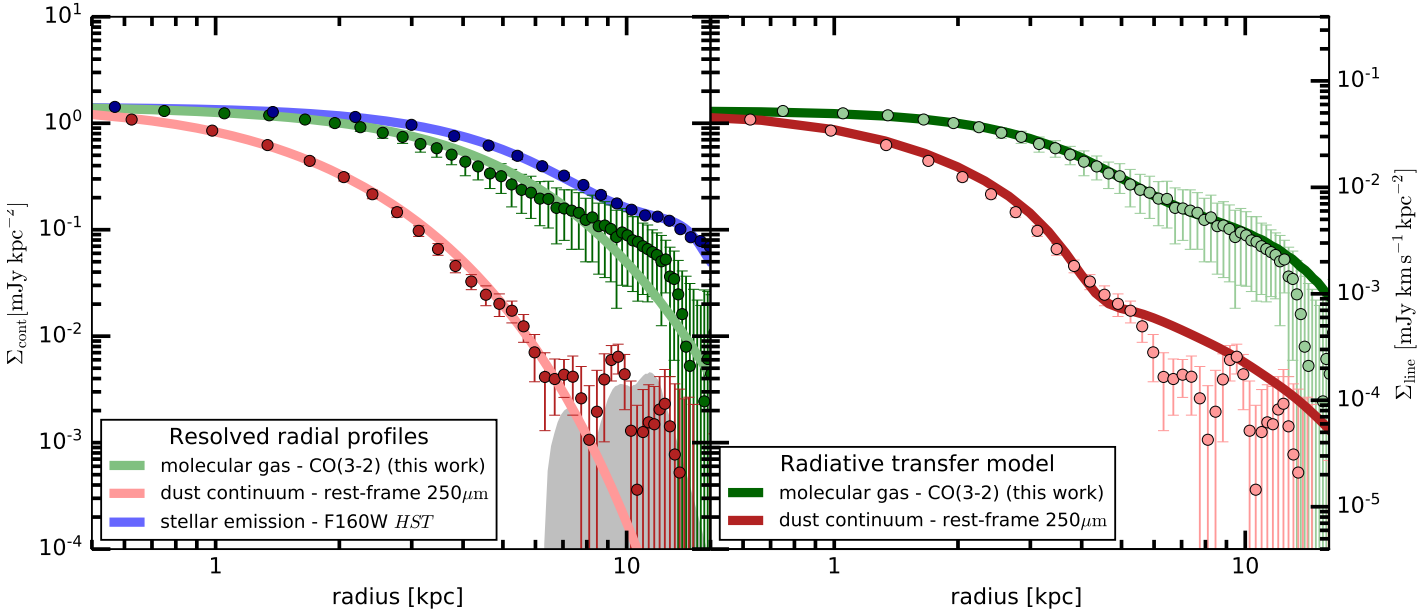

Figure 4.7: Stacked radial profiles and modelling. *Left panel:* one-component exponential profile fits are shown for a) the stacked CO(3-2) emission presented in this paper (green solid line), b) the stacked high-resolution dust continuum emission at 870 μm (rest-frame $\sim$ 250 μm) of 16 luminous ALESS SMGs by Hodge et al. (2016) (red solid line) and c) the stacked high-resolution H-band emission (*HST*) for the same 16 ALESS sources presented by Hodge et al. (2016) (blue solid line). The profiles were normalized to have the same peak flux densities, and the error bars were obtained through bootstrapping. All exponential fits are convolved with Gaussian functions of the size of the beam, to account for the effect of different resolutions. The data points of the dust profile at radii of >7 kpc were discarded for the fitting, since these are evidently affected by artifacts produced by the side lobes of the beam (shown as the grey shaded area). We find that the cool molecular gas and stellar emission are clearly more extended than the rest-frame 250 μm dust continuum by a factor of > 2. *Right panel:* To explain the different sizes, we fit an extended version of the dust and line radiative transfer models of Weiß et al. (2007) to our data. The solid lines are the profiles resulting from the best-fit radiative transfer model. The model assumes an exponentially decreasing column density distribution (Sérsic index of $n = 1$) and a linear temperature gradient decreasing from the center to the outer parts of the disk. Solving the dust and line radiative transfer in several radial bins, we obtain a exponentially decreasing gas and dust radial profile, taking into account the different beam sizes for the dust continuum and CO line observations. Assuming a constant dust-to-gas ratio, the model is thus able to reproduce the apparent size differences between the CO(3-2) and dust continuum emission by only introducing temperature and optical depth gradients.

($n = 1.2 \pm 0.3$, Chen et al. 2015). The best-fit models consist then of exponential profiles with radii of $r = 1.7 \pm 0.1, 3.8 \pm 0.1$ and 4.0 ± 2.0 kpc for the dust continuum, CO and stellar emission respectively.

These results reveal that both the stellar (H_{160}) and molecular gas (CO($J = 3-2$)) emission have similar sizes, but are $> 2\times$ more extended than the dust continuum emission, measured at rest-frame 250 μm. In addition, we note that the estimated size of the CO(3-2) emission should be considered a lower limit for the extent of the total molecular-mass distribution, as the ground-state transition CO(1-0) has been observed to be even more extended than the higher J-transitions (Engel et al. 2010).

4.4.3 Physical implications of the more extended molecular gas distributions as compared to dust continuum emission

A crucial consequence of the different scales probed by the molecular gas, dust and stellar tracers in these galaxies (as shown in Section 4.4.2) is the uncertainty in using conversion factors between the luminosities of individual tracers. The compactness of the dust continuum emission in SMGs has been discussed in the literature (Simpson et al. 2015; Ikarashi et al. 2015; Hodge et al. 2016; Barro et al. 2016; Tadaki et al. 2017a; Simpson et al. 2017), as ALMA continuum observations at high angular resolution (0.13–0.4″) have revealed median radii of $\sim$ 0.7– 1.5 kpc.

Apart from CO and optical imaging, high-resolution observations of other SF tracers such as synchrotron and free-free emission have allowed comparison of relative sizes of dust continuum and gas emission regions. Indeed, radio interferometric observations of SMGs with the Very Large Array at 1.4 GHz (Chapman et al. 2004; Biggs & Ivison 2008), at 3 GHz (Miettinen et al. 2015, 2017) and at 6 GHz (Thomson 2018), have shown that dust continuum sizes appear to be 1.4–4.4 times smaller than the radio.

What is the origin of the significantly smaller sizes (> 2) of the dust continuum emission in SMGs compared to other physical components? There are three parameters that could affect the emission of dust at larger radii: the dust-to-gas ratio, the dust temperature and the optical depth of the dust and gas. The small extent of the dust continuum emission at rest-frame 250 μm is likely to trace the heating of dust by star formation or AGN, as it is confined to central compact regions, as expected for highly star-forming systems. A decrease in optical depth at larger radii, would similarly affect the observed sub-mm continuum emission, as would a radially dependent dust-to-gas ratio. Studies in the nearby Universe, however, (e.g., Sandstrom et al. 2013; Groves et al. 2015) suggest that no large variations in the latter are expected across the galaxy, making this scenario less plausible.

The different spacial extent for the rest-frame 250 μm dust continuum emission and the CO line emission can be explained in the context of self-consistent radiative transfer of the CO(3-2) and dust continuum emission. Weiß et al. (2007) presented such a model, where the line and dust continuum emission are linked through a constant dust-to-gas mass ratio throughout the galaxy, specifically, by connecting the gas column density $N_{\mathrm{H_2}}$ to the optical depth of the dust, $\tau_{\mathrm{dust}}(r) \sim N_{\mathrm{dust}} \sim N_{\mathrm{H_2}}$. The different dust continuum and CO sizes can then be explained by assuming a radially decreasing gas column density and a radially decreasing temperature distribution $T(r)$. Following the radiative transfer equation, and neglecting the background temperature, we have

$$S(r) \propto T(r) \cdot (1 - e^{-\tau}), \tag{4.5}$$

where $T(r)$ implies $T(r) = T_{\mathrm{dust}}(r)$ for the dust and $T(r) = T_{\mathrm{ex}}(r)$ for the molecular gas. We can expect that the long wavelength dust continuum emission, which is optically thin

($\tau \ll 0$), will be sensitive to both the column density and the temperature gradients ($S_{\rm cont}(r) \propto T_{\rm dust}(r) \cdot \tau_{\rm dust}(r)$), whereas the optically thick CO line emission ($\tau \gg 1$) will to first order only respond to the temperature gradient ($S_{\rm CO}(r) \propto T_{\rm ex}(r) \sim T_{\rm kin}(r)$ for the low-J CO transitions, which are close to thermalisation. This would have the effect that the dust continuum emission becomes fainter more rapidly as a function of radius than the gas emission.

Based on these arguments, we have used an extended version of the dust and line radiative transfer models of Weiß et al. (2007) to demonstrate this effect for the radial distribution of the stacked CO(3-2) and rest-frame 250 μm dust continuum data shown in Figure 4.7. In the model we use an exponentially decreasing column density distribution (Sérsic index of $n = 1$) and a linear temperature gradient from the center to the outer parts of the disk, and we solve the dust and line radiative transfer in several radial bins (more details on the model will be presented in Weiß et al. (in prep)). Figure 4.7 shows a fit of a exponentially decreasing gas component, taking into account the different beam sizes for the dust continuum and CO line observations. Given the uncertainties of the data, the model can reproduce the different radial behaviour of the dust continuum and the CO(3-2) line emission. From this fit we derive an intrinsic exponential scale length of 3.4 kpc (0.4″) for the underlying H_2 distribution, intermediate between the intrinsic sizes we have estimated earlier based on the de-convolved intensity profiles for the dust and the CO(3-2) line emission.

In this section we have proposed that assuming a unique intrinsic distribution of dust and gas, temperature and optical depth gradients alone could give rise to the apparent size differences observed between the CO and dust continuum emission. If these parameters are the origin of the compactness of dust continuum emission observed in the high-redshift Universe (here probed at rest-frame ~ 250 μm), caution must be exercised when extrapolating properties of high-resolution continuum observations to conclusions on the molecular phase of the ISM. Specifically, these results advise against combining unresolved molecular gas observations with radius estimates from resolved dust continuum observations when calculating key parameters such as dynamical masses. In order to empirically test the assumptions placed into this model on the temperature and optical depth gradients, high-resolution observations of the dust continuum at different frequencies would be necessary, as a gradient in observed sizes of the emission regions is a direct tracer of the dust optical depth across the SED.

4.5 Summary

- We have presented ALMA observations of the gas and dust of four luminous submillimetre galaxies at $z \sim 2-3$ to investigate the spatially resolved properties of the inter-stellar medium (ISM) on scales of a few kpc. The molecular gas in these sources, traced by the ^{12}CO(J=3-2) emission, is extended over FWHM~5 –14 kpc.

- We investigated the dynamics of the molecular gas in our sources and modelled the kinematics of one of them, ALESS122.1, finding that the velocity fields of three of our four sources are consistent with disk rotation to first order. We clarify that this scenario does not preclude the connection of our sources to mergers as observations of nearby merger remnant and simulations show that gas disks reform rapidly within <100 Myr of the peak star formation associated with a merger.

- The resolved CO imaging provides size measurements that allow us to derive dynamical masses for our sample. The dynamical masses found are in the range of (1.1–5.3)$\times 10^{11}$M$_\odot$, as calculated within 2× the half-light radii of our sources, which is in agreement with other dynamical mass estimates for SMGs.

- To provide dynamical constraints to the gas masses, we explore the uncertainties introduced by the estimation of stellar masses, the assumptions on the dark matter fractions and the CO-to-H_2 conversion factor α_{CO}. Taking into account the covariance between the mass-to-light ratio and α_{CO} parameters, we estimate an average CO-to-H_2 conversion factor of $\alpha_{CO} = 1.1^{+0.8}_{-0.7}$ and $\alpha_{CO} = 0.9^{+0.7}_{-0.6}$ for dark matter fractions of 15% and 30% respectively, and an upper limit of $\alpha_{CO} \leq 1.4^{+0.9}_{-0.9}$ for a dark matter fractions of 0%. These values imply gas fractions of ~30% for our sources, which are similar to those estimated for main-sequence star-forming galaxies and other SMGs.

- Our high resolution study allows us to investigate the correlation between the spatial distribution of the physical components of the ISM (the dust continuum and gas) and the stellar distributions. The sizes of gas and stars are comparable but spatially uncorrelated, while the rest-frame 250 μm dust continuum is significantly more compact. The observation of the anti-correlated distributions of the dust continuum and gas emission with respect to the unobscured stellar emission may challenge energy balance assumptions in global SED fitting routines and suggests that caution must be exercised particularly for dusty star-forming galaxies, such as SMGs.

- To investigate this question statistically, we conduct a stacking analysis of available high resolution ancillary data for SMG populations of similar properties. We find that the cool molecular gas and stellar emission are clearly more extended than the rest-frame 250 μm dust continuum by a factor of > 2.

- We reproduce our observations with a radiative transfer model, finding that the different sizes are consistent with the expected response of optically thin dust and optically thick gas to radially decreasing optical depth and temperature gradients, when a constant dust-to-gas ratio is assumed. We suggest that extrapolations from morphological properties of high-resolution continuum observations to conclusions on the molecular phase of the ISM should be thus treated cautiously.

Acknowledgements

We thank the anonymous referee for the useful comments to improve the clarity of this manuscript. We would like to thank Jarle Brinchmann, Erwin de Blok, Alison Peck and the Allegro group in Leiden, especially Luke Maud, for valuable help and advice at different stages of the project. GCR acknowledge support from the European Research Council under the European Unions Seventh Framework Programme (FP/2007- 2013) /ERC Advanced Grant NEW-CLUSTERS-321271. JH acknowledges support of the VIDI research programme with project number 639.042.611, which is (partly) financed by the Netherlands Organisation for Scientific Research (NWO). IRS acknowledges support from the ERC Advanced Grant DUSTYGAL (321334), a Royal Society/Wolfson Merit Award and STFC (ST/P000541/1). JLW acknowledges support of an STFC Ernest Rutherford Fellowship (ST/P004784/1) and additional support from STFC (ST/P000541/1). F.W and B.P.V acknowledge funding through ERC grants "Cosmic Dawn" and "Cosmic Gas". H.D. acknowledges financial support from the Spanish Ministry of Economy and Competitiveness (MINECO) under the 2014 Ramón y Cajal program MINECO RYC-2014-15686. This paper makes use of the following ALMA data: ADS/JAO.ALMA#2013.1.00470.S and #2016.1.00754.S. ALMA is a partnership of ESO (representing its member states), NSF (USA) and NINS (Japan), together with NRC (Canada), MOST and ASIAA (Taiwan), and KASI (Republic of Korea), in cooperation with the Republic of Chile. The Joint ALMA Observatory is operated by ESO, AUI/NRAO and

NAOJ. This research made use of ASTROPY, a community-developed core Python package for Astronomy (Astropy Collaboration et al. 2013), and the open-source plotting packages for Python APLPY (Robitaille & Bressert 2012), and CORNER (Foreman-Mackey 2016).

Bibliography

Accurso, G., Saintonge, A., Catinella, B., et al. 2017, MNRAS, 470, 4750

Aravena, M., Hodge, J. A., Wagg, J., et al. 2014, MNRAS, 442, 558

Astropy Collaboration, Robitaille, T. P., Tollerud, E. J., et al. 2013, A&A, 558, A33

Barro, G., Kriek, M., Pérez-González, P. G., et al. 2016, ApJ, 827, L32

Biggs, A. D., & Ivison, R. J. 2008, MNRAS, 385, 893

Blain, A. W., Smail, I., Ivison, R. J., Kneib, J.-P., & Frayer, D. T. 2002, Phys. Rep., 369, 111

Bolatto, A. D., Wolfire, M., & Leroy, A. K. 2013, ARA&A, 51, 207

Bothwell, M. S., Smail, I., Chapman, S. C., et al. 2013, MNRAS, 429, 3047

Bouché, N., Carfantan, H., Schroetter, I., Michel-Dansac, L., & Contini, T. 2015, AJ, 150, 92

Carilli, C. L., & Walter, F. 2013, ARA&A, 51, 105

Casey, C. M., Narayanan, D., & Cooray, A. 2014, Phys. Rep., 541, 45

Chapman, S. C., Smail, I., Windhorst, R., Muxlow, T., & Ivison, R. J. 2004, ApJ, 611, 732

Chen, C.-C., Smail, I., Swinbank, A. M., et al. 2015, ApJ, 799, 194

Chen, C.-C., Hodge, J. A., Smail, I., et al. 2017, ApJ, 846, 108

Courteau, S., & Dutton, A. A. 2015, ApJ, 801, L20

da Cunha, E., Walter, F., Smail, I. R., et al. 2015, ApJ, 806, 110

Danielson, A. L. R., Swinbank, A. M., Smail, I., et al. 2011, MNRAS, 410, 1687

—. 2017, ApJ, 840, 78

Dannerbauer, H., Lehnert, M. D., Emonts, B., et al. 2017, A&A, 608, A48

de Blok, W. J. G., & Walter, F. 2014, AJ, 147, 96

Decarli, R., Walter, F., Aravena, M., et al. 2016, ApJ, 833, 70

Elbaz, D., Leiton, R., Nagar, N., et al. 2017, ArXiv e-prints, arXiv:1711.10047

Emonts, B. H. C., Lehnert, M. D., Villar-Martín, M., et al. 2016, Science, 354, 1128

Engel, H., Tacconi, L. J., Davies, R. I., et al. 2010, ApJ, 724, 233

Erb, D. K., Steidel, C. C., Shapley, A. E., et al. 2006, ApJ, 647, 128

Foreman-Mackey, D. 2016, The Journal of Open Source Software, 24, doi:10.21105/joss.00024

Foreman-Mackey, D., Hogg, D. W., Lang, D., & Goodman, J. 2013, PASP, 125, 306

Fujimoto, S., Ouchi, M., Shibuya, T., & Nagai, H. 2017, ApJ, 850, 83

Gaia Collaboration, Brown, A. G. A., Vallenari, A., et al. 2016, A&A, 595, A2

Genzel, R., Tacconi, L. J., Combes, F., et al. 2012, ApJ, 746, 69

Genzel, R., Tacconi, L. J., Lutz, D., et al. 2015, ApJ, 800, 20

Genzel, R., Schreiber, N. M. F., Übler, H., et al. 2017, Nature, 543, 397

Ginolfi, M., Maiolino, R., Nagao, T., et al. 2017, MNRAS, 468, 3468

Greve, T. R., Vieira, J. D., Weiß, A., et al. 2012, ApJ, 756, 101

Groves, B. A., Schinnerer, E., Leroy, A., et al. 2015, ApJ, 799, 96

Hainline, L. J., Blain, A. W., Smail, I., et al. 2011, ApJ, 740, 96

Harris, A. I., Baker, A. J., Frayer, D. T., et al. 2012, ApJ, 752, 152

Hezaveh, Y. D., Marrone, D. P., & Holder, G. P. 2012, ApJ, 761, 20

Hildebrand, R. H. 1983, QJRAS, 24, 267

Hodge, J. A., Carilli, C. L., Walter, F., Daddi, E., & Riechers, D. 2013a, ApJ, 776, 22

Hodge, J. A., Carilli, C. L., Walter, F., et al. 2012, ApJ, 760, 11

Hodge, J. A., Riechers, D., Decarli, R., et al. 2015, ApJ, 798, L18

Hodge, J. A., Karim, A., Smail, I., et al. 2013b, ApJ, 768, 91

Hodge, J. A., Swinbank, A. M., Simpson, J. M., et al. 2016, ApJ, 833, 103

Hopkins, P. F., Cox, T. J., Hernquist, L., et al. 2013, MNRAS, 430, 1901

Hopkins, P. F., Cox, T. J., Younger, J. D., & Hernquist, L. 2009, ApJ, 691, 1168

Hubble, E. P. 1926, ApJ, 64, doi:10.1086/143018

Huynh, M. T., Emonts, B. H. C., Kimball, A. E., et al. 2017, MNRAS, 467, 1222

Ikarashi, S., Ivison, R. J., Caputi, K. I., et al. 2015, ApJ, 810, 133

Ivison, R. J., Papadopoulos, P. P., Smail, I., et al. 2011, MNRAS, 412, 1913

Ivison, R. J., Smail, I., Papadopoulos, P. P., et al. 2010, MNRAS, 404, 198

Karim, A., Swinbank, A. M., Hodge, J. A., et al. 2013, MNRAS, 432, 2

Lagos, C. d. P., Bayet, E., Baugh, C. M., et al. 2012, MNRAS, 426, 2142

Lehmer, B. D., Brandt, W. N., Alexander, D. M., et al. 2005, ApJS, 161, 21

Leroy, A. K., Bolatto, A., Gordon, K., et al. 2011, ApJ, 737, 12

Lovell, M. R., Pillepich, A., Genel, S., et al. 2018, ArXiv e-prints, arXiv:1801.10170

Madau, P., & Dickinson, M. 2014, ARA&A, 52, 415

Magdis, G. E., Daddi, E., Elbaz, D., et al. 2011, ApJ, 740, L15

McMullin, J. P., Waters, B., Schiebel, D., Young, W., & Golap, K. 2007, in Astronomical Society of the Pacific Conference Series, Vol. 376, Astronomical Data Analysis Software and Systems XVI, ed. R. A. Shaw, F. Hill, & D. J. Bell, 127

Michałowski, M. J., Dunlop, J. S., Cirasuolo, M., et al. 2012, A&A, 541, A85

Miettinen, O., Novak, M., Smolčić, V., et al. 2015, A&A, 584, A32

—. 2017, A&A, 602, A54

Narayanan, D., Krumholz, M., Ostriker, E. C., & Hernquist, L. 2011, MNRAS, 418, 664

Narayanan, D., & Krumholz, M. R. 2014, MNRAS, 442, 1411

Narayanan, D., Krumholz, M. R., Ostriker, E. C., & Hernquist, L. 2012, MNRAS, 421, 3127

Nedyalkov, P. L. 1993, Astronomy Letters, 19, 115

Oteo, I., Ivison, R. J., Negrello, M., et al. 2017, ArXiv e-prints, arXiv:1709.04191

Planck Collaboration, Ade, P. A. R., Aghanim, N., et al. 2014, A&A, 571, A16

Price, S. H., Kriek, M., Shapley, A. E., et al. 2016, ApJ, 819, 80

Riechers, D. A., Hodge, J., Walter, F., Carilli, C. L., & Bertoldi, F. 2011, ApJ, 739, L31

Riechers, D. A., Capak, P. L., Carilli, C. L., et al. 2010, ApJ, 720, L131

Robertson, B., Bullock, J. S., Cox, T. J., et al. 2006, ApJ, 645, 986

Robitaille, T., & Bressert, E. 2012, APLpy: Astronomical Plotting Library in Python, Astrophysics Source Code Library, ascl:1208.017

Sandstrom, K. M., Leroy, A. K., Walter, F., et al. 2013, ApJ, 777, 5

Scoville, N., Aussel, H., Sheth, K., et al. 2014, ApJ, 783, 84

Scoville, N., Sheth, K., Aussel, H., et al. 2016, ApJ, 820, 83

Scoville, N., Lee, N., Vanden Bout, P., et al. 2017, ApJ, 837, 150

Serjeant, S. 2012, MNRAS, 424, 2429

Sharon, C. E., Riechers, D. A., Hodge, J., et al. 2016, ApJ, 827, 18

Simpson, J. M., Swinbank, A. M., Smail, I., et al. 2014, ApJ, 788, 125

Simpson, J. M., Smail, I., Swinbank, A. M., et al. 2015, ApJ, 799, 81

—. 2017, ApJ, 839, 58

Solomon, P. M., & Vanden Bout, P. A. 2005, ARA&A, 43, 677

Sorba, R., & Sawicki, M. 2018, MNRAS, arXiv:1801.07368

Spilker, J. S., Marrone, D. P., Aravena, M., et al. 2016, ApJ, 826, 112

Strandet, M. L., Weiss, A., De Breuck, C., et al. 2017, ApJ, 842, L15

Swinbank, A. M., Simpson, J. M., Smail, I., et al. 2014, MNRAS, 438, 1267

Tacconi, L. J., Genzel, R., Smail, I., et al. 2008, ApJ, 680, 246

Tacconi, L. J., Genzel, R., Saintonge, A., et al. 2017, ArXiv e-prints, arXiv:1702.01140

Tadaki, K.-i., Genzel, R., Kodama, T., et al. 2017a, ApJ, 834, 135

Tadaki, K.-i., Kodama, T., Nelson, E. J., et al. 2017b, ApJ, 841, L25

Thomson. 2018, MNRAS

Ueda, J., Iono, D., Yun, M. S., et al. 2014, ApJS, 214, 1

Vieira, J. D., Marrone, D. P., Chapman, S. C., et al. 2013, Nature, 495, 344

Walter, F., Decarli, R., Carilli, C., et al. 2012, Nature, 486, 233

Walter, F., Decarli, R., Aravena, M., et al. 2016, ApJ, 833, 67

Wang, S. X., Brandt, W. N., Luo, B., et al. 2013, ApJ, 778, 179

Wardlow, J. L., Cooray, A., De Bernardis, F., et al. 2013, ApJ, 762, 59

Weiß, A., Downes, D., Neri, R., et al. 2007, A&A, 467, 955

Weiß, A., Kovács, A., Coppin, K., et al. 2009, ApJ, 707, 1201

Wuyts, S., Förster Schreiber, N. M., Wisnioski, E., et al. 2016, ApJ, 831, 149

Xue, Y. Q., Luo, B., Brandt, W. N., et al. 2011, ApJS, 195, 10

5

The Resolution Frontier II: Strong FUV fields drive the [CII]/FIR deficit in $z \sim 3$ dusty, star-forming galaxies

We present 0.15-arcsec (1 kpc) resolution ALMA observations of the [C II] 157.74 μm line and rest-frame 160-μm continuum emission in two of the $z \sim 3$ dusty, star-forming galaxies presented in the previous chapter - ALESS 49.1 and ALESS 57.1. The [C II] surface brightness distribution is dominated by a compact core ≤1 kpc in radius, a factor of 2–3 smaller than the CO (3–2) emission. In ALESS 49.1, we find an extended (8-kpc radius), low surface-brightness [C II] component. Based on an analysis of mock ALMA observations, the [C II]/160-μm continuum surface brightness distributions are inconsistent with a single-Gaussian surface brightness distribution with the same size as CO (3–2) emission. The [C II] rotation curves flatten only at few-kpc radius, suggesting the kinematics of the central regions are dominated by a baryonic disc. Both galaxies exhibit a strong [C II]/FIR deficit on 1-kpc scales, with FIR-surface-brightness to [C II]/FIR slope steeper than in local star-forming galaxies. A comparison of the [C II]/CO(3–2) observations with PDR models suggests a strong FUV radiation field ($G_0 \sim 10^4$) and high gas density (n(H) $\sim 10^4$ cm^{-3}) in the central regions of ALESS 49.1 and 57.1. The most direct interpretation of the pronounced [C II]/FIR deficit is a thermal saturation of the C^+ fine-structure levels at temperatures ≥ 500 K, driven by the strong FUV field.

M. Rybak, G. Calistro Rivera, J. A. Hodge, Ian Smail, F. Walter, P. van der Werf, et al.
ApJ, **(submitted)**.[1]

[1]This chapter is part of this PhD Thesis due to my significant contribution to this project at all levels. The main results of this chapter are based on the comparison of the [C II] data to the CO observations and analysis that was carried out and presented in Chapter 4. Additionally, I have been active in both the realization and discussion of this comparative analysis. I have carried out the kinematic modelling of the [C II] data presented in section 2.3 and have written the description of the process in this chapter. Finally, I have proof-read and edited different versions of this chapter, and have led the ALMA Cycle 4 proposal to complete the [C II] observations for the two remaining sources from Calistro-Rivera et al. (2018).

5.1 Introduction

Dusty, star-forming galaxies (DSFGs) are a major contributor to the global star-formation rate between redshifts $z = 2 - 4$, at an epoch when the star-forming activity of the Universe was at its peak (e.g. Casey et al. 2014). Although low in numbers, thanks to their high star-formation rates (SFR >100 $M_\odot$ yr^{-1}), up to 20 per cent of all the star formation at $z \sim 3$ takes place in DSFGs (Swinbank et al. 2014).

The eponymous massive dust reservoirs in DSFGs absorb the UV/optical radiation from the newborn stars, mostly re-radiating it thermally as a rest-frame FIR/sub-mm continuum. Therefore, studying the structure and physical properties in these extreme sources requires relying on sub-mm/mm bright tracers - the dust continuum (which directly traces the obscured star formation) and low-J CO rotational transitions[2] (which trace the cold, molecular gas that fuels the star formation, Carilli & Walter 2013).

Besides the FIR continuum and CO emission, the third bright rest-frame FIR tracer of the star-forming interstellar medium (ISM) is the [C 2] 157.74 μm line, a fine-structure transition of C^+ ions. Due to its low ionization energy (11.3 eV) and a relatively low critical density, [C 2] traces of a wide range of ISM phases - from the ionized H 2 regions to warm molecular clouds to diffuse gas. Depending on the environmental conditions, the upper fine-structure level is populated predominantly by collisions with H, H_2 or e^- (Goldsmith et al. 2012).

Starting in the early 1990's, systematic studies of [C 2] emission in local galaxies were enabled by the *Infrared Space Observatory* and the Kuiper Airborne Observatory. These observations revealed a tight correlation between the [C 2] line and FIR continuum emission from the heated dust at low SFR surface densities (e.g. Stacey et al. 1991). However, this correlation was found to break at larger FIR surface brightness Σ_{FIR} – the so-called "*[CII]/FIR deficit*" (e.g. Malhotra et al. 1997; Luhman et al. 1998; Malhotra et al. 2001; Luhman et al. 2003) – with the [C 2]/FIR ratio decreasing with increasing Σ_{FIR}.

In the last decade, the study of [C 2] emission in the nearby Universe was further revolutionized by *Herschel*. [C 2] emission in a large number of nearby galaxies was targeted by *Herschel*: the largest such sample of [C 2] was presented by Díaz-Santos et al. (2013), who obtained PACS spectroscopic observations of the 241 galaxies from the Great Observatories All-sky LIRG Survey (GOALS) (Armus et al. 2009). Further systematic studies of the [C 2] emission in nearby galaxies have been presented by Graciá-Carpio et al. (2011); Díaz-Santos et al. (2017); Smith et al. (2017); Herrera-Camus et al. (2018), confirming a strong correlation of the [C 2]/FIR deficit with Σ_{SFR} down to 200-pc scales in a wide range of environments.

At the highest redshifts ($z > 4$), the importance of the [C 2] line increases dramatically, as the raised CMB temperature renders the low-J CO emission undetectable, while the [C 2] line remains relatively unaffected (da Cunha et al. 2013; Vallini et al. 2015; Lagache et al. 2018). Indeed, with the advent of Atacama Large Millimeter/submillimeter Array (ALMA), [C 2] observations are now being routinely used to determine redshifts and dynamical masses of high-redshift galaxies, including some of the most distant systems (Walter et al. 2009; Brisbin et al. 2015; Gullberg et al. 2015; Oteo et al. 2016; Carniani et al. 2017; Decarli et al. 2018; Smit et al. 2018). Most recently, Gullberg et al. (2018) presented deep, 30-mas resolution (200 pc physical size) ALMA observations of the [C 2] line in four z=4.4–4.8 galaxies. Although their observation suffered from a very sparse *uv*-plane coverage, they found the resolved [C 2]-FIR deficit at $z \sim$4.5 to follow the trend seen in local galaxies.

Despite the recent progress, it is still unclear how well the results and relations derived from local observations hold for the high-redshift population, especially the intensely star-forming high-redshift DSFGs, with Σ_{SFR} some two to three orders of magnitude higher than

[2] In this work, we use the term "low-J" transitions for the rotational transitions with $J_{upp} \leq 3$.

the local star-forming galaxies (10^{-3} – 10^{0} $M_{\odot}$ yr^{-1} kpc^{-2}, e.g. Smith et al. 2017). To directly compare the [C 2] emission in high-redshift DSFGs to the local galaxies and study its connection to the star-formation, high-resolution (kpc-scale) observations of the [C 2] emission, alongside the rest-frame FIR continuum (tracing the obscured star formation) and the low-J CO emission tracing the molecular gas are necessary.

At high redshift, such resolved, multi-tracer studies are typically limited by the angular extent of the source (few arcsec at most), and the need for robust redshifts to ensure that both [C 2] and low-J CO emission are observable from the ground. For example, Stacey et al. (2010) compared unresolved [C 2]/FIR/ CO ($J_{upp} \leq 4$) observations of a heterogeneous sample of $z = 1 - 2$ galaxies. Gullberg et al. (2015) compared [C 2], FIR and CO (2–1)/(1–0) observations in 20 strongly lensed DSFGs ($z_{\rm source}$=2.1–5.7); they found the [C 2] and CO line profiles to be very similar, suggesting that they originate from the same source-plane regions. However, the limited resolution of these observations prevented a robust source-plane reconstruction of the CO/[C 2] emission; the *differential magnification* bias therefore could not be eliminated (e.g. Serjeant 2012). In addition, several individual sources at $z > 4.5$ have been studied in both [C 2] and low-J CO emission (e.g. Walter et al. 2009; Huynh et al. 2014; Cicone et al. 2015), though these tend to be extreme sources in terms of brightness and AGN activity.

Finally,the [C 2] line has been proposed as an alternative molecular gas tracer to CO emission. (e.g. Zanella et al. 2018). However, in DSFGs, the spatial extent of CO emission has been shown to vary strongly with $J_{\rm upp}$ (e.g. Ivison et al. 2011; Riechers et al. 2011). If [C 2] emission traces only a subset of the molecular gas reservoir, [C 2]-based mass estimates might be severely biased.

In this paper, we explore a new regime in resolved, multi-tracer studies by investigating resolved [C 2], FIR continuum and CO (3–2) emission on kpc-scales in two (non-lensed) $z \sim 3$ sources. This allows us to address the following questions:

- How does the resolved [C 2]/FIR ratio at z∼3 compare to that seen in local and high-redshift star-forming galaxies?
- What drives the [C 2]/FIR deficit in DSFGs?
- How well does the [C 2] emission trace the molecular gas reservoir in DSFGs?

Compared to the high-redshift, high-resolution [C 2]-only studies (e.g. Gullberg et al. 2018; Zanella et al. 2018), resolved emission line maps of two different species (C^{+} and ^{12}CO) allow us to study the relation between [C 2] emission and the colder molecular gas.

This paper is structured as follows: in Section 5.2, we give the details of ALMA observations. Section 5.3 details the processing of the data in both the image- and *uv*-plane, the assessment of the systematic errors and kinematic modelling. Section 5.4 presents the spatial and kinematic comparison of the interpretation of the [C 2]/CO(3–2)/FIR observations, results of PDR modelling and a discussion of the physical processes driving the [C 2]/FIR deficit. Finally, Section 5.5 summarizes the conclusions of this paper.

Throughout this paper, we use a flat ΛCDM cosmology from Planck Collaboration et al. (2016). We adopt the CO (3–2) spectroscopic redshifts from Calistro Rivera et al. (2018): z=2.943±0.001 and z=2.943±0.002 for ALESS 49.1 and 57.1. Consequently, 1 arcsec corresponds to 7.9 kpc for both ALESS 49.1 and ALESS 57.1; the luminosity distance to both sources is 25445 Mpc (Wright 2006).

5.2 Observations and data reduction

5.2.1 Sample selection

The two galaxies analysed in this paper were identified by Hodge et al. (2013) as a part of the ALESS survey. The ALESS survey was an ALMA Cycle 0 870 μm imaging campaign targeting all 126 sources discovered in the LABOCA Extended *Chandra* Deep Field South Submillimeter Survey (LESS, Weiß et al. 2009). With ALMA Cycle 0 observations providing a significant improvement over the LABOCA bolometer in both resolution (beam area reduced by a factor of ∼200) and sensitivity (increased by a factor of ∼3), the ALESS survey identified 99 distinct sub-mm bright sources in its primary sample (Hodge et al. 2013). Out of these, at the time of the proposal (2015 April) only four – ALESS 49.1, 57.1, 67.1 and 122.1 – had robust redshifts that allowed for ALMA observations of both the low-J CO and [C 2] lines. The spectroscopic redshifts were acquired using VLT-FORS2/VIMOS and Keck-DEIMOS, and are based on multiple line detections (Danielson et al. 2017).

In this paper, we present the ALMA Band 8 observations targeting the [C 2] line and rest-frame 160-μm continuum. The corresponding Band 3 observations, targeting the CO (3-2) ($\nu_{\rm rest}$=345.795 GHz) emission, were recently presented by Calistro Rivera et al. (2018).

5.2.2 ALMA Band 8 observations

The observations were carried out as part of the ALMA Cycle 3 Project #2015.1.00019.S (PI: J. Hodge) on 2016 August 12. Only ALESS 49.1 and 57.1 ([C 2] line in ALMA Band 8) were observed; ALESS 67.1 and 122.1 have [C 2] line in ALMA Band 9, and were not observed. The total time including calibration and overheads was 72 mins, with an on-source time of 11 mins per target. The array configuration consisted of 38 12-m antennas, with baselines extending up to 1400 m. The largest angular scale of the observations is ∼1.9 arcsec for both sources[3]. The primary beam FWHM is 14.1 arcsec. Synthesized beam sizes and σ_{rms} for the 160-μm continuum and the [C 2] emission are listed in Table 5.1. The target elevation range was 66–73 deg for ALESS 49.1 and 67–76 deg for ALESS 57.1.

The frequency setup was configured in four spectral windows (SPWs) in Band 8. The individual SPWs were centered at 481.953, 483.183, 493.506, 495.386 GHz. Each SPW was split into 480 frequency channels 3.90625 MHz wide, for a total bandwidth of 1.875 GHz per SPW. The radio-velocity resolution was 2.42 km s^{-1}. Both the Stokes XX and YY parameters were observed.

The data were calibrated using the standard ALMA pipeline, with additional flagging necessary to remove atmospheric features (see below). All the visibility data processing apart from imaging was performed using CASA versions 4.7 and 5.0 (McMullin et al. 2007).

The spectral structure of the [C 2] line overlaps with atmospheric absorption features at 481.2 and 481.6 GHz. Consequently, the noise level in the affected channels is raised by factor of ∼2. This issue is particularly severe for ALESS 49.1. Another atmospheric feature is located in a line-free SPW at 496.35 GHz; here, the affected channels were flagged to improve the continuum SNR. As will be outlined in Section 5.3.1, we use a channel-dependent threshold for the deconvolution process to avoid introducing noise features from the affected channels.

To increase the signal-to-noise ratio, each line was split into frequency bins ∼120 km s^{-1} wide. Additionally, we time-averaged the data using a 30-second bin; this corresponds to an average intensity loss of <0.5 per cent at 5 arcsec from the phase-tracking centre, which we

[3]The largest angular scale is estimated as $0.983/\lambda_{5\%}$, where $\lambda_{5\%}$ is the 5-th percentile uv-distance (ALMA Cycle 5 Technical Handbook).

Table 5.1: Source positions (corresponding to the 160-μm continuum surface brightness maximum), redshifts, ALMA Band 8 naturally-weighted beam sizes and noise levels, observed 160-μm continuum/[C 2] flux-densities and [C 2] and FWHM.. The redshifts are based on CO (3–2) observations Calistro Rivera et al. (2018). The spatially-integrated flux-densities $S_{160\mu m}/S_{[CII]}$ are measured within a circular aperture with 1-arcsec diameter, centered on the continuum surface brightness maximum.

Source		ALESS 49.1	ALESS 57.1
RA (J2000)		3:31:24.71	3:31:51.94
DEC (J2000)		−27:50:46.9	−27:53:27.0
z		2.943±0.001	2.943±0.002
Beam FWHM	[arcsec]	0.16×0.12	0.16×0.12
Beam PA	[deg]	53	56
$S_{160\mu m}$	[mJy]	10.7±1.0	8.2±0.5
$I^{max}_{160\mu m}$	[mJy beam^{-1}]	3.42±0.16	1.53±0.17
$S_{[CII]}$	[mJy]	15.4±2.8	8.8±2.5
$I^{max\ a}_{[CII]}$	[mJy beaam^{-1}]	2.0±0.4	3.0±0.4
FWHM$_{[CII]}$	[km s^{-1}]	600±130	390±70
FWHM$_{CO}$ [c]	[km s^{-1}]	610±30	360±90

[a] per 120 km s^{-1} velocity bin.
[b] integrated over 800and 710km s^{-1} for ALESS 49.1 and 57.1, respectively.
[c] adopted from Calistro Rivera et al. (2018).

consider negligible[4]. The time-bin size was chosen so as to prevent significant time-averaging smearing. The two linear polarizations were combined into the Stokes intensity I.

5.2.3 ALMA Band 3 observations

ALMA Cycle 2/4 Band 3 observations of the CO (3–2) and rest-frame 1.0-mm continuum in ALESS 49.1 and 57.1 was presented by Calistro Rivera et al. (2018). These consisted Cycle 2 observations of ALESS 49.1 and 57.1 (Project #2013.1.00470.S; PI:Hodge) at 0.34-0.67 arcsec resolution; and additional Cycle 4 observations of ALESS 49.1 (Project #2016.1.00754.S; PI: Wardlow) at 1.1-arcsec resolution. The naturally-weighted Band 3 synthesized beam size is 0.69×0.63 arcsec for ALESS 49.1 (after concatenating Cycles 2 and 4 data) and 0.67×0.60 arcsec for ALESS 57.1, with a continuum σ_{rms} of 17.6 and 19.5 μJy beam^{-1}, respectively. For a detailed description of the data and the resulting analysis, we refer the reader to Calistro Rivera et al. (2018).

5.3 Results

5.3.1 Image analysis

Imaging

We perform synthesis imaging of the visibility data using the WS-CLEAN algorithm introduced by Offringa et al. (2014), specifically its multi-scale version (Offringa & Smirnov

[4]Taylor et al. (1999), equation (18–42).

2017). The multi-scale WS-CLEAN is an advanced deconvolution algorithm with a multi-scale, multi-frequency capability (Offringa & Smirnov 2017). Another advantage of the WS-CLEAN as opposed to the CASA implementation is the channel-dependent deconvolution threshold. As the noise level changes appreciably with frequency due to atmospheric lines, this prevents us from introducing noise-peaks from the affected channels into the reconstructed images.

For the line imaging, we first subtract the continuum by linearly interpolating the line-free channels in SPWs 1, 2, and 3 and subtract the continuum slope from the line-containing channels. The continuum channels overlapping with the atmospheric lines were flagged before the continuum subtraction. For the continuum imaging, we discard the entire SPW 0 and the line-containing channels in SPW1, as well as the channels affected by the atmospheric feature around 496.35 GHz.

The data were deconvolved on a sky-plane grid of 1024 × 1024 5-mas pixels (total FoV size = 5.115×5.115 arcsec), using natural weighting. We use the automatic SNR-based masking, with `auto-mask` SNR threshold of 2. Table 5.1 lists the source positions, redshifts and the rms noise for the synthesized images.

ALMA 160-μm continuum

The rest-frame 160-μm continuum is detected in both sources at >10 σ-confidence (Figure 5.1). In both sources, the continuum emission shows only a single brightness peak at 0.15-arcsec resolution. In ALESS 49.1, the continuum emission is almost circularly symmetric, with a minor extension in the east-west direction. In ALESS 57.1, the continuum is noticeably extended in the east-west direction (axis ratio at FWHM 2:1). The spatially-integrated 160-μm continuum flux-density for ALESS 49.1 and 57.1 is given in Table 5.1. The 160-μm flux-density is calculated from an aperture with a 1.0 arcsec radius, centered on the 160-μm continuum surface brightness maximum. The aperture size was chosen based on the CO (3–2) sizes measured in Calistro Rivera et al. (2018); additionally, based on the *uv*-plane size measurements (Section 5.3.2), we do not expect significant surface brightness contribution ≥1 arcsec from the centre of the source.

[CII] emission

The velocity-integrated maps of the [C 2] emission are presented in Figure 5.1. The [C 2] emission is detected at 5 and 8-σ significance in ALESS 49.1 and 57.1, respectively. The [C 2] emission is relatively compact (<0.5 arcsec diameter), similar in extent to the 160-μm continuum. The [C 2] emission in ALESS 57.1 is highly elliptical (axis ratio ≥2:1) and elongated in the east-west direction; the [C 2] does not show any significant offset from the 160-μm peak. Note that the low-significance clumpy substructure such as that seen in ALESS 49.1 [C 2] maps is often an artifact of low SNR (e.g. Hodge et al. 2016; Gullberg et al. 2018), rather than a real physical feature.

5.3.2 *uv*-plane analysis

We estimate the size of the continuum and [C 2] emission regions by directly fitting the observed visibility function. Given the relatively low SNR of the data, we assume the surface brightness distribution to follow a circularly symmetric Gaussian profile.

The size is measured using the frequency-integrated continuum and line datasets. To correct the offset between the phase-tracking centre and the centroid of the surface brightness distribution given in Table 5.1, each dataset is phase-shifted to center the field-of-view on the

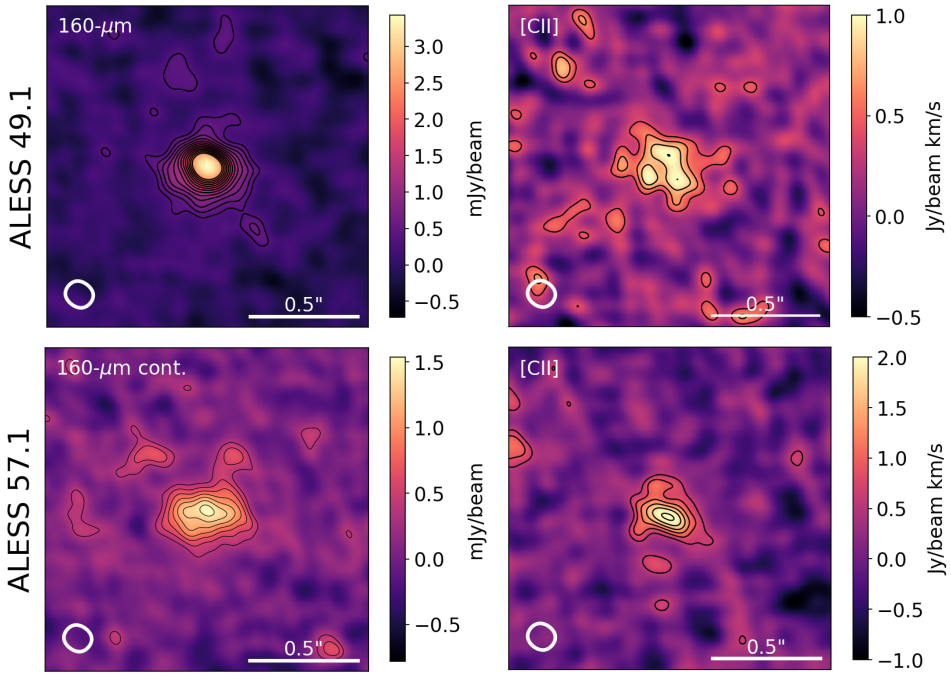

Figure 5.1: ALESS 49.1 and 57.1 imaging: continuum (right) and integrated [C 2] emission (left) maps. The contours start at 2-σ level and increase by 1-σ. The FWHM beam size is indicated by the ellipse in the lower left corner. The [C 2] and 160-μm emission is well-resolved in both sources, and almost co-spatial.

centroid of the source. The data are then radially binned into bins of equal width. To test the robustness of the *uv*-plane fitting against the *uv*-bin size, we vary the *uv*-bin size from 5 to 50 kλ.

We fit each *uv*-plane dataset with (1) a single Gaussian profile, (2) two Gaussian components to investigate the possibility of having compact, bright [C 2] emission embedded in an extended, low surface-brightness component; (3) a combination of a single Gaussian profile and a constant term, corresponding to a point-source in the image plane. To determine whether the two-component model significantly improves the goodness-of-fit compared to the one-component model, we compare the two models using the F-test (Bevington 1969). The single-component model is preferred for the continuum emission in ALESS 49.1 and [C 2] emission in ALESS 57.1, independently of the *uv*-bin size. We will address the robustness of the inferred $R_{1/2}$ in Section 5.3.2. The two-component model is strongly ($p > 0.95$) preferred for the [C 2] emission in ALESS 49.1 and the continuum emission in ALESS 57.1. We do not find the Gaussian-and-constant-term (point-source) model to be preferred over the single-Gaussian model for any dataset considered. The best-fitting values for the two-component model are listed in Table 5.2. Figure 5.2 shows the visibility function for the [C 2] and 160-μm continuum, as well as the CO (3–2) observations from Calistro Rivera et al. (2018), and the corresponding best-fitting profiles.

In physical units, for the single-Gaussian models, the [C 2] and 160-μm emission are rather compact (0.8–1.4 kpc) in both sources. The [C 2] and 160-μm continuum sizes from the single-Gaussian fitting agree within 1–2-σ uncertainty. For the two-Gaussian models, the compact and extended [C 2] components in ALESS 49.1 have half-light radii of 1.01±0.12 kpc and 8.7±1.6 kpc, respectively. The compact and extended 160-μm components in ALESS 57.1 have half-light radii of 0.86±0.07 and 5.3±1 kpc, respectively.

For the two-component [C 2] model in ALESS 49.1, the extended [C 2] components accounts for up to 80 cent of the total [C 2] luminosity. Note that the systematic uncertainty on this estimate might be significant, as it is unclear how much does the extended component depart from the assumption of a circular Gaussian profile. For ALESS 57.1, the single-Gaussian model is preferred. However, if ALESS 57.1 has a very faint extended [C 2] component with the same size as in ALESS 49.1, the upper 3-σ limit on the total flux-density contributed by this hypothetical component is 80 per cent.

How will the extended components in ALESS 49.1 [C 2] emission and ALESS 57.1 160-μm continuum contribute to the observed [C 2]/160-μm surface brightness distribution? The half-light radius of the ALESS 57.1 160-μm extended component is well below the maximum recoverable scale and therefore should be fully accounted for in the synthesized images. This is supported by the results from the spectral energy distribution modeling (Section 5.3.4), which indicate that the 160-μm continuum is not significantly resolved out. For the [C 2] emission, the half-light radius of the extended component in ALESS 49.1 is comparable to the maximum recoverable scale (1.9 arcsec) and some emission is likely resolved out in the synthesized images. However, while the extended [C 2] component in ALESS 49.1 dominates the total [C 2] luminosity, it contributes only between 5–20 per cent of the surface brightness across the inner $R < 2$ kpc region. It is for this reason that our analysis in Sections 4.2, 4.3 and 4.4 focuses on the central regions ($R \leq 2$ kpc) of ALESS 49.1 and 57.1, including the uncertainty from the extended components in further analysis.

How robust are the source sizes determined from the uv-plane fitting?

Before analyzing our resolved [C 2] and 160-μm continuum observations, we assess the reliability of the inferred source sizes. In particular, we investigate a possibility that the [C 2]/160-μm emissions follow CO (3–2) surface distribution, and that the source sizes inferred in Sec-

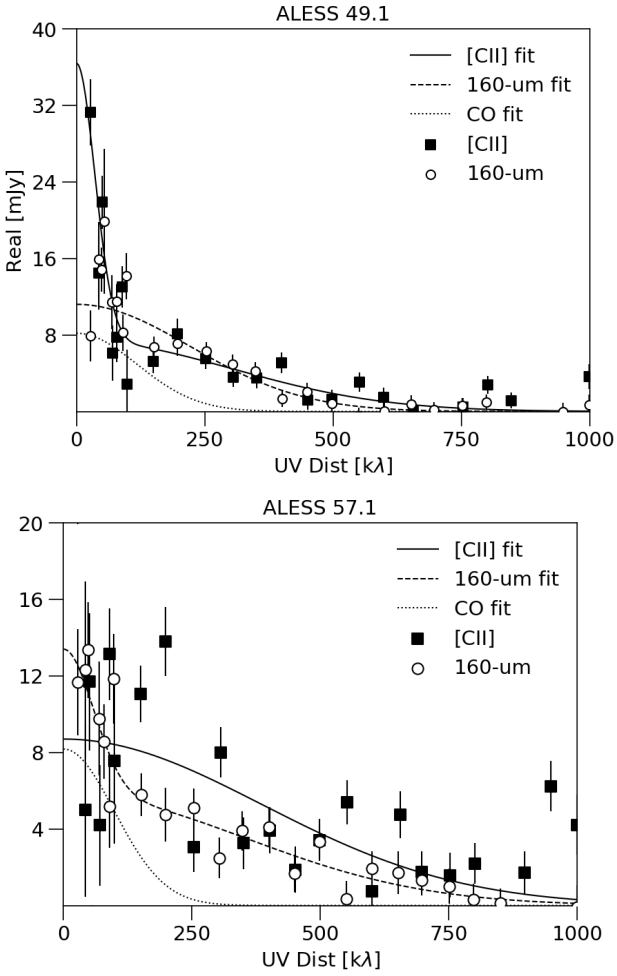

Figure 5.2: Azimuthally averaged visibility function for ALESS 49.1 (left) and ALESS 57.1 (right), for the [C 2], 160-μm continuum with best-fitting model (full and dashed lines), and best-fitting single-Gaussian profiles to the CO (3–2) data (dotted line, increased by a factor of 10,Calistro Rivera et al. 2018). For added clarity, the data is binned with a 10 – 50 kλ bin size and truncated at 1000 kλ. In ALESS 49.1, the excess [C 2] flux at short baselines - corresponding to the extended component - is clearly visible.

tion 5.3.2 are an artifact of the limited short-spacing coverage of our Band 8 observations. We estimate this uncertainty using simulated ALMA observations.

The mock observations are created as follows. First, we calculate the mean and rms scatter for the [C 2] / 160-μm continuum visibilities within a given *uv*-bin. We then subtract the mean signal from the data, which gives us a *uv*-plane coverage corresponding exactly to a given observation, along with a realistic noise measurement for each baseline. We choose this approach to account for the different noise levels for each dataset, and the effect of the atmospheric lines on our [C 2] data. We then inject an artificial source into the data, generating 1000 datasets with different noise realizations for each source. We consider sources with a half-light radius of 0.1–1.0 arcsec and peak surface brightness of 0.05 – 4.0 mJy beam^{-1}. Finally, we bin the mock visibilities in the *uv*-plane using exactly the same procedure as applied to real data in Section 5.3.2.

Figure 5.3 shows the inferred radius as a function of the surface brightness maximum alongside the 1-σ uncertainty from the *uv*-plane fitting. The measured [C 2] and 160-μm continuum sizes in ALESS 49.1 and 57.1 are all smaller than sizes inferred for input sources with $R_{1/2} \geq 0.2$ arcsec in the relevant peak surface brightness range. In other words, given the observed peak surface brightness, $R_{1/2}^{[\mathrm{CII}]}$ >0.2 arcsec would be recovered within 10 per cent uncertainty for both ALESS 49.1 and 57.1. For comparison, the CO (3–2) half-light radii in ALESS 49.1 and 57.1 are $R_{1/2}^{\mathrm{CO}}$=0.33±0.06 and 0.39±0.06 arcsec, respectively.

Therefore, we consider it unlikely that the [C 2]/160-μm continuum follow a single-Gaussian surface brightness distribution with the same size as CO (3–2) emission (0.33±0.05 and 0.39±0.06 arcsec for ALESS 49.1 and 57.1, respectively). Nevertheless, we can not exclude a combination of a bright compact and faint extended components. In the following analysis, we will focus on the center of the sources where the extended [C 2] component is not expected to contribute significantly.

5.3.3 [CII] spectra and kinematics

Figure 5.4 presents the [C 2] moment-one (intensity-weighted velocity) maps and the comparison of [C 2]/CO (3-2) line profiles in ALESS 49.1 and 57.1. The spectra were extracted from the naturally-weighted channel maps, using an aperture 1 arcsec (~8 kpc) in radius.

The [C 2] line profile in ALESS 49.1 largely traces the CO (3–2) profile, exhibiting an increased brightness in the blue channels. The [C 2] and CO (3–2) line profiles are consistent within errors for both sources. The moment-one maps reveal a clear velocity gradient across both ALESS 49.1 and 57.1.

We model the velocity-fields using the GalPak3D software (Bouché et al. 2015). GalPak3D uses a Monte-Carlo approach to extract the kinematic and morphological parameters from three-dimensional image cubes, accounting for both the spatial and spectral response of the instrument, assuming a parametric model for a rotating disc. For our simulations, we assume an exponential disc profile - an appropriate choice for ALESS DSFGs, which show a mean Sérsic index of $n = 0.9 \pm 0.2$ (Hodge et al. 2016, $n = 1$ corresponds to an exponential profile.). To improve the SNR and the speed of the calculations, we re-sampled our data onto cubes with a pixel size of 25 mas, using natural weighting.

Figure 5.5 shows the input and reconstructed moment-0 and moment-1 maps for ALESS 49.1 and 57.1. At the SNR of our Band 8 observations, velocity fields in both sources are consistent with an ordered, disc-like rotation. The deconvolved [C 2] rotational curves are shown in Figure 5.6, which also lists the FWHM velocity measurements obtained from the fitting of the spatially-integrated CO (3–2) spectra (Calistro Rivera et al. 2018). The source inclinations are inferred by fitting the moment-0 map and agree with those derived from CO (3–2) imaging by Calistro Rivera et al. (2018) within 1–2σ uncertainty.

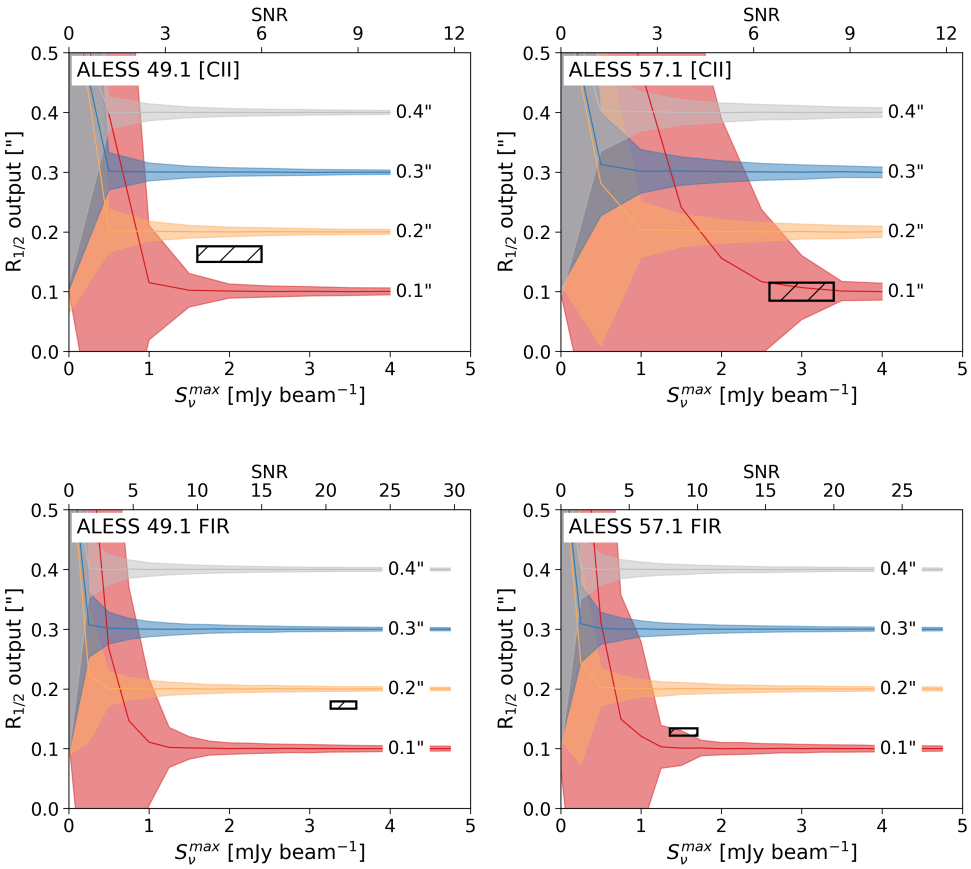

Figure 5.3: Comparison of the inferred and true $R_{1/2}$ for the [C 2] line (upper) and 160-μm data continuum (lower). The bold lines denote the mean inferred $R_{1/2}$ for input $R_{1/2}$=0.1–0.4 arcsec, with coloured regions denoting the 1-σ uncertainty from the *uv*-plane fitting only. For $R_{1/2}$ >0.4 arcsec, the source sizes are inferred robustly and are now shown for clarity. The boxed regions indicate the measured source sizes and peak surface brightness for ALESS 49.1 and 57.1 with 1 σ uncertainties. Given the SNR of our observations, we rule out the possibility that [C 2] and 160-μm continuum follow the same single Gaussian profile as the CO (3–2) emission.

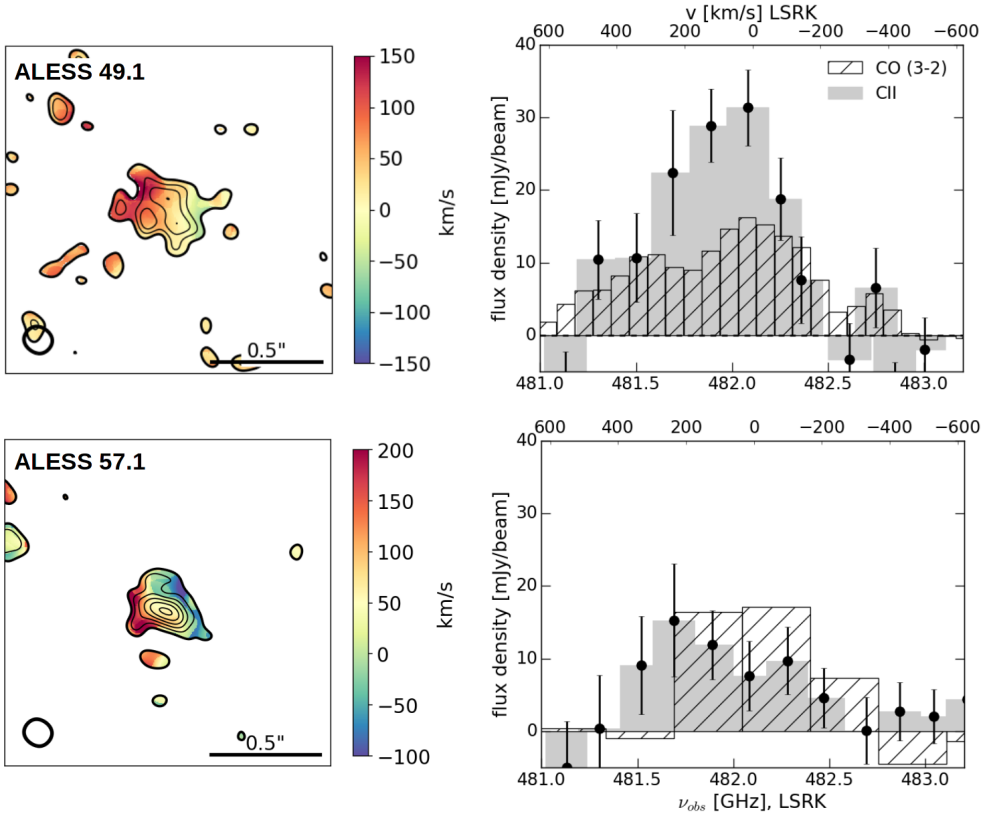

Figure 5.4: Moment-one (velocity) maps and [C 2] line profiles for ALESS 49.1 and ALESS 57.1. The contours correspond to [C 2] moment-zero maps as shown in Figure 5.1. The [C 2] velocity fields in both galaxies show a clear gradient across the source, without any major perturbations. The CO (3–2) spectra are taken from Calistro Rivera et al. (2018); the CO (3–2) flux-density is scaled up by a factor of 10 for clarity. The velocity is given in the LSRK frame with respect to the redshift of $z = 2.943$, using the radio definition of velocity. The line intensity was measured from images obtained using natural weighting, for an aperture with 1 arcsec diameter, centered on the surface-brightness maximum of the integrated [C 2] line. The error-bars indicate 1-σ uncertainty. The frequency coverage of our Band 8 observations does not extend below 481.0 GHz. The [C 2] and CO (3–2) line widths match each other (Table 5.1).

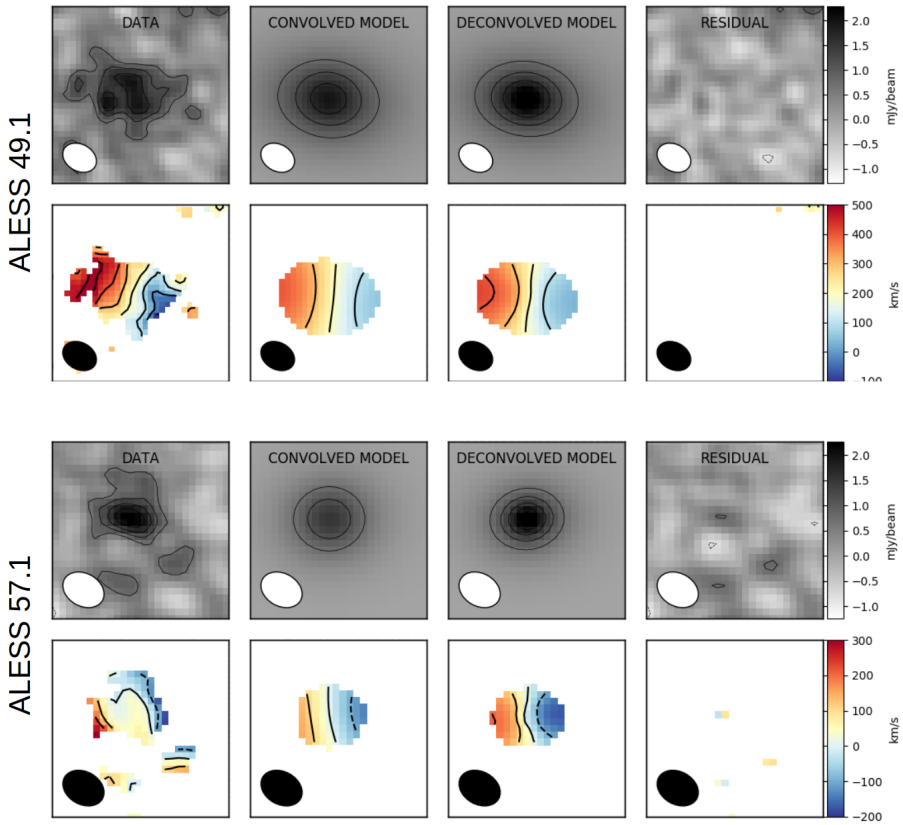

Figure 5.5: GALPAK3D models of the [C 2] velocity field in ALESS 49.1 (upper) and ALESS 57.1 (lower), using an exponential disc model. The upper row shows, respectively, the velocity moment-0 (surface brightness) data, best moment-0 model convolved with the beam, best moment-0 model (deconvolved) and the moment-0 residuals. The moment-zero contours start at $\pm 2\sigma_{\rm rms}$ level and increase in steps of $1\sigma_{\rm rms}$. The moment-one contours are drawn in steps of ± 100 km s^{-1}. The lower row shows the reconstructed moment-one (velocity) maps for regions with surface brightness $> 2\sigma_{\rm rms}$. The data is fully consistent with the exponential disc model, with no residuals at $> 2\sigma_{\rm rms}$ significance. The field-of-view size is 1.6×1.6 arcsec and 1.4×1.4 arcsec, respectively.

Table 5.2: Inferred source properties for ALESS 49.1 and ALESS 57.1. For the global source properties derived from the SED-fitting, we provide the median value of the posterior probability density function. The [C 2] and CO (3–2) line luminosities are spectrally integrated over the full extent of the [C 2], rather than over FWHM only (as in Calistro Rivera et al. 2018) as the [C 2] line exhibits a non-Gaussian profile.

Source		ALESS 49.1	ALESS 57.1
SED fitting			
$L_{3-2000\mu m}$	[10^{12} $L_\odot$]	$7.1^{+0.8}_{-0.9}$	$7.4^{+0.9}_{-0.9}$
SFR	[$M_\odot$ yr^{-1}]	490^{+30}_{-60}	480^{+70}_{-60}
T_{dust}	[K]	46^{+6}_{-2}	51^{+7}_{-4}
$M_\star$	[10^{10} $M_\odot$]	$4.4^{+1.8}_{-0.3}$	$4.3^{+1.7}_{-0.8}$
$M_{\rm gas}$ [b]	[10^{10} $M_\odot$]	5 ± 2	5 ± 2
$M_{\rm dust}$	[10^8 $M_\odot$]	$4.4^{+0.5}_{-0.7}$	$4.1^{+0.5}_{-0.6}$
Line Luminosities			
$L_{\rm [CII]}$	[10^9 $L_\odot$]	3.0±0.8	1.1±0.4
$L'_{\rm [CII]}$	[10^{10} K km s^{-1} pc^2]	14±4	5.1±1.7
$L_{\rm CO(3-2)}$ [a]	[10^9 $L_\odot$]	0.070±0.005	0.062±0.016
$L'_{\rm CO(3-2)}$ [a]	[10^{11} K km s^{-1} pc^2]	0.51±0.04	0.05±0.01
$L_{\rm CO(1-0)}$ [a]	[10^6 $L_\odot$]	2.1±0.2	2.6±0.7
Source sizes - single Gaussian			
$R^{\rm [CII]}_{1/2}$	[arcsec]	0.163±0.013	0.101±0.010
$S^{\rm [CII]}$	[mJy]	10.9±0.9	8.6±0.9
$R^{160\mu m}_{1/2}$	[arcsec]	0.173±0.009	0.128±0.006
$S^{160\mu m}$	[mJy]	11.2±0.4	7.6±0.4
$R^{\rm CO}_{1/2}$ [a]	[arcsec]	0.33±0.5	0.39±0.06
Source sizes - two Gaussians			
$R^{\rm [CII]}_{1/2}$ (compact)	[arcsec]	0.128±0.015	–
$R^{\rm [CII]}_{1/2}$ (extended)	[arcsec]	1.1±0.3	–
$S^{\rm [CII]}$ (compact)	[mJy]	7.4±1.1	–
$S^{\rm [CII]}$ (extended)	[mJy]	29±8	–
$R^{160\mu m}_{1/2}$ (compact)	[arcsec]	–	0.109±0.007
$R^{160\mu m}_{1/2}$ (extended)	[arcsec]	–	0.67±0.11
$S^{160\mu m}$ (compact)	[mJy]	–	5.8±0.5
$S^{160\mu m}$ (extended)	[mJy]	–	7.6±1.4
[C 2] and CO (3–2) kinematics			
$i_{\rm [CII]}$	[deg]	39±5	58±5
$M^{\rm [CII]}_{\rm dyn}$ ($R \leq 2$ kpc)	[10^{10} $M_\odot$]	6.2 ± 5.5	2.7 ± 1.6
$M^{\rm CO}_{\rm dyn}(R < R^{\rm CO}_{1/2})$	[$10^{10} M_\odot$]	11 ± 2	11 ± 5

[a] Calistro Rivera et al. (2018): L_{line} integrated over the entire line width as opposed to integrating only over FWHM as in Calistro Rivera et al. (2018)
[b] Calistro Rivera et al. (2018). M_{gas} estimated assuming $\alpha_{\rm CO} = 1.0$.

5.3.4 Spectral energy distribution modelling

We infer the global stellar and interstellar medium properties of ALESS 49.1 and 57.1 from the spatially-integrated spectral energy distributions (SEDs) using the MAGPHYS package (da Cunha et al. 2008). These differ from the previously published models (da Cunha et al. 2015) by using the CO (3–2)-derived spectroscopic redshifts compared to the photometric ones from da Cunha et al. (2015), and inclusion of ALMA Bands 3/4/8 continuum flux-densities. Namely, we include Band 4 continuum measurements ($S_{2.1\mathrm{mm}} = 380\pm100$ μJy and 65 ± 50 μJy for ALESS 49.1 and 57.1; da Cunha et al., in prep.), as well as the ALMA Band 3 continuum measurement for ALESS 49.1, $S_{3.3\mathrm{mm}} = 37 \pm 5$ μJy (Wardlow et al. 2018), as well as the Band 8 continuum measurements from Table 5.1. The updated source properties are listed in Table 5.2. The estimated dust temperatures $T_{\mathrm{dust}} = 47^{+5}_{-9}/52^{+10}_{-6}$ K in ALESS 49.1 and 57.1 are warmer than the median T_{dust}=42±2 K of the ALESS DSFGs inferred from MAGPHYS modelling (da Cunha et al. 2015). However, median $T_{\mathrm{dust}} = 55 \pm 4$ K was found in a sample of $z \sim 4.5$ emitters by Cooke et al. (2018), who interpreted the high T_{dust} as evidence for high Σ_{SFR} at high redshift. Compared to the MAGPHYS models of entire ALESS sample (da Cunha et al. 2015), ALESS 49.1 and 57.1 have SFR higher by a factor of ∼2 (da Cunha et al. 2015: median SFR = 280±70 $\mathrm{M}_\odot$ yr^{-1}) and stellar mass factor of 2 lower (da Cunha et al. 2015: $M_* = (8.9 \pm 0.1) \times 10^{10}$ $\mathrm{M}_\odot$ yr^{-1}); the dust mass is consistent with the median da Cunha et al. (2015) value ($(5.6 \pm 1.0) \times 10^{10}$ $\mathrm{M}_\odot$). The gas depletion timescale (M_{gas}/SFR is 100±40 Myr in both ALESS 49.1 and 57.1, in line with redshift 2–4 DSFGs (Huynh et al. 2017; Bothwell et al. 2013), and few times lower than in $z = 1 - 3$ massive main-sequence galaxies from the PHIBBS survey (0.7 ± 0.1 Myr, Tacconi et al. 2018).

Using the SED models, we can estimate the raction of the 160-μm continuum that is resolved out by comparing the observed rest-frame 160-μm continuum fluxes with SED modeling predictions, assuming that T_{dust} and optical depth are constant across the source. Namely, we use MAGPHYS (da Cunha et al. 2008) to perform SED modeling using all the photometry points apart from the rest-frame 160-μm continuum. The predicted 160-μm flux-densities are 11.8 and 7.6 mJy for ALESS 49.1 and 57.1, respectively; the observed flux densities match the predicted ones to <10 per cent. Therefore, we conclude that our observations recover the bulk of the 160-μm emission.

5.4 Discussion

5.4.1 Comparison with CO (3–2) emission

Based on the *uv*-plane analysis in Section 5.3.2 and test on mock ALMA data in Section 5.3.2, we found the [C 2]/160-μm continuum surface brightness distribution to be dominated by a compact component, embedded within a low-surface-brightness, extended emission. We now compare these morphologies to the CO (3–2) surface brightness profiles, and other low- and high-redshift observations and simulations.

160-μm continuum size

Comparing the 160-μm continuum emission sizes with the CO (3–2) sizes (Table 5.2), the 160-μm continuum is 1.9±0.3 (ALESS 49.1) and 3.1±0.7 (ALESS 57.1) more compact than the CO (3–2) emission.

Compact dust continuum emission embedded in a larger molecular gas reservoir has been observed in a number of high-resolution studies of $z = 2 - 4$ DSFGs. For example, PdBI/VLA imaging of GN20 ($z = 4.05$) revealed a compact dusty, star-forming region within a large disc

as traced by the CO (2–1) emission (Hodge et al. 2012, 2015). At very high spatial resolutions ($\sim$ 100 pc), similar morphology has been seen in the strongly-lensed z = 3 DSFG SDP.81 (ALMA Partnership et al. 2015), which shows a compact (~3 kpc across), dusty star-forming disc (Rybak et al. 2015a), embedded in a large ($\geq$ 10 kpc) molecular gas reservoir, as traced by the CO (1–0) emission (Valtchanov et al. 2011; Rybak et al. 2015b). Similarly, Spilker et al. (2015) observed compact ALMA Band 7 continuum and extended CO(3–2)/(1–0) emission in two strongly lensed galaxies from the South Pole Telescope sample; note that in DSFGs, the CO (3–2) is typically significantly less extended than the CO (1–0) line (e.g. Ivison et al. 2011; Riechers et al. 2011). Using ALMA 860-μm continuum, VLA CO (3–2) and SINFONI Hα observations of ALESS 67.1 (z=2.1), Chen et al. (2017) found the ALMA continuum to be a factor of ~5 more compact than CO (3–2) and Hα emission (which are similar in size). Finally, Calistro Rivera et al. (2018) compared stacked CO (3–2) and Hodge et al. (2016) 860-μm ALMA observations of a sample of 4/18 DSFGs from the ALESS sample, showing the FIR continuum to be more compact by a factor of >2. Based on a radiative transfer modelling, Calistro Rivera et al. (2018) found that the compact FIR and extended CO (3–2) sizes are consistent with a decrease in dust temperature and optical depth towards the outskirts of the source. The compact continuum sizes in ALESS 49.1 and 57.1 thus add to the growing evidence for variations ISM conditions in DSFGs on scales of few kpc.

[CII] emission size

Based on the source sizes inferred from *uv*-plane fitting, the [C 2] emission is 2.0 ± 0.4 (ALESS 49.1) and 3.9 ± 0.7 (ALESS 57.1) times more compact than CO (3–2). The compact size of the high surface-brightness [C 2] component contrasts with a relatively similar extent of the [C 2] and low-J CO emission in local galaxies, as recently presented by de Blok et al. (2016), who found the [C 2] to be "*slightly less compact than the CO*" (scale radius $\sim$ 70 ± 20 per cent larger). Note that the de Blok et al. (2016) galaxies have $\Sigma_{\rm SFR}$ much lower than ALESS 49.1 and 57.1 ($10^{-3} - 10^{-2}$ M$_\odot$ yr^{-1} kpc^{-2} vs. $10^{1} - 10^{2}$ M$_\odot$ yr^{-1} kpc^{-2}).

The [C 2] morphologies consisting of a high surface-brightness compact, and a low surface-brightness extended component have been observed in several local star-forming galaxies. For example, early Kuiper Airborne Observatory imaging of [C 2] emission in NGC 6946 (Madden et al. 1993) resolved three distinct components: (1) a bright, compact nucleus (R < 300 kpc); (2) a faint, diffuse component at least 12 kpc in radius, contributing ~40 per cent of the total [C 2] flux (Contursi et al. 2002) and (3) local enhancements corresponding to the spiral arms.

Furthermore, one of the best-studied $z \geq 5$ sources with resolved [C 2]/low-J CO observations - z ~6.42 quasar SDSS J1148+5251 (Walter et al. 2004, 2009) - has a compact ($R \sim$ 0.75 kpc) [C 2] emission embedded within a much more extended ($R \sim$ 2.5 kpc) CO (3–2) reservoir (Walter et al. 2009; Stefan et al. 2015). Cicone et al. (2015) found an extremely extended (out to ~30 kpc) [C 2] emission associated with powerful outflows likely driven by the central engine in J1148+5251.

Apart from observational evidence, a compact, high surface-brightness [C 2] component in star-forming galaxies has been predicted by simulations. In particular, Olsen et al. (2015) predicted using zoomed-in cosmological SPH simulations of several mildly star-forming $z \sim 2$ galaxies (SFR=5–60 M$_\odot$ yr^{-1}) that the [C 2] emission is concentrated into a compact central region ($R \sim$ 1 kpc), with a much fainter (by up to 1 dex) extended component – similar to our double-component model of [C 2] emission in ALESS 49.1. In the Olsen et al. (2015) simulations, the compact size of the [C 2] emission is due to gas inflows into the central star-forming regions, and the [C 2] emission is dominated by the dense, molecular phase of the ISM. This contrasts with low-SFR galaxies, where the bulk of the star-formation takes place

in the spiral arms at large galactocentric radii (e.g. Pineda et al. 2013).

Inferring FIR source sizes using the Stacey et al., 2010 relation

Given the limited angular resolution of many high-redshift [C 2] detections, the source size can not be inferred directly from unresolved/marginally resolved data. However, parallel [C 2]/CO/FIR continuum observations have been used to constrain the source size, assuming the bulk of the line and continuum emission originates in PDR regions.

This technique, introduced by Stacey et al. (2010), compares the observed [C 2]/CO/FIR fluxes with predictions from the PDR models of (Kaufman et al. 1999, see Section 5.4.4) to infer the FUV field strength G_0 and the density n. The observed $L_{\rm FIR}$ and inferred G_0 are then used to infer the FIR size $R_{\rm FIR}$ using the Wolfire et al. (1990) relations. In particular, Wolfire et al. (1990) distinguish two main regimes:

1. $\langle\lambda_{\rm FUV}\rangle < R_{\rm FIR}$

$$\langle G_0\rangle = 3\times10^4\Big(\frac{L_{\rm FIR}}{10^{10}{\rm L}_\odot}\Big)\Big(\frac{\langle\lambda_{\rm FUV}\rangle}{100{\rm pc}}\Big)\Big(\frac{100{\rm pc}}{R_{\rm FIR}}\Big)^3 (1-\exp(-R_{\rm FIR}/\langle\lambda_{\rm FUV}\rangle)), \quad (5.1)$$

2. $\langle\lambda_{\rm FUV}\rangle \geq R_{\rm FIR}$

$$\langle G_0\rangle = 3\times10^4\Big(\frac{L_{\rm FIR}}{10^{10}{\rm L}_\odot}\Big)\Big(\frac{100{\rm pc}}{R_{\rm FIR}}\Big)^2, \quad (5.2)$$

where G_0 is given in the units of the Habing field (1.6×10^{-3} erg cm^{-2} s^{-1}) and $R_{\rm FIR}$ and the FUV photon mean free path $\langle\lambda_{\rm FUV}\rangle$ are in pc. Stacey et al. (2010) assume that $\langle\lambda_{\rm FUV}\rangle$ in $z = 1-2$ star-forming galaxies is the same as in a nearby starburst M82. For M82, Stacey et al. (2010) assume $L_{\rm FIR} = 2.8\times10^{10}$ L$_\odot$, $G_0 = 10^3$, $R_{\rm FIR} = 150$ pc.

With high-resolution [C 2], CO (3–2) and FIR observations and robust source sizes in hand, we now investigate the applicability of the Stacey et al. (2010) relations to high-redshift DSFGs. Assuming that $\langle\lambda_{\rm FUV}\rangle$ is smaller than $R_{\rm FIR}$ (an appropriate choice given the heavily obscured, dusty environment), we infer $R_{\rm FIR} = 410\pm50$ and 420 ± 70 pc for ALESS 49.1 and 57.1, respectively; a factor of 2.5–3.5 smaller than the actual FIR half-light radii measured from the *uv*-plane fitting (Section 5.3.2). We note that the M82 $L_{\rm FIR}$, G_0 and $R_{\rm FIR}$ estimates from the literature show a considerable scatter; alternatively, the $\langle\lambda_{\rm FUV}\rangle$ in DSFGs differs from that in M82. Crucially, if the FIR sizes of high-redshift DSFGs are systematically underestimated by similar factors, the star-formation rate surface density $\Sigma_{\rm SFR} \propto L_{\rm FIR}/R_{\rm FIR}^2$ will be *overestimated* by 0.5–1.0 dex - a shift that might affect a number of unresolved datapoints in e.g. the [C 2]/FIR – $\Sigma_{\rm SFR}$ plane (Figure 5.7).

5.4.2 Molecular gas kinematics

The [C 2] and CO (3–2) lines provide two independent measurements of the molecular gas velocity structure. Due to their different spatial extents (Section 5.3.2), the [C 2] and CO (3–2) emission trace the velocity field at different radii. Figure 5.6 shows the line-of-sight velocity as traced by the [C 2] and CO (3–2) emission, and the GALPAK3D model of the [C 2] disc. In particular, the [C 2] emission probes the velocity field within the inner 2-kpc region. Typically, rotational curves of disc-like galaxies are decomposed into contributions from the

dark matter halo, and baryons in the form of a galactic bulge and disc. Given the baryonic mass $M_{\rm bar} = M_* + M_{\rm gas}$ is comparable to the dynamical mass enclosed within twice the CO (3–2) half-light radius (5.2 and 6.0 kpc in ALESS 49.1 and 57.1, respectively; Table 5.2), we conclude that the inner rotation curve is baryon-dominated.

In both ALESS 49.1 and 57.1, the line-of-sight velocity $v_{\rm los}$ flattens at 2–4 kpc radius. As a dominant bulge would cause the $v_{\rm los}$ to increase rapidly on sub-kpc scales, we speculate that the inner ($R \leq 2$ kpc) rotational curves in ALESS 49.1 and 57.1 are disc-dominated. However, higher-SNR data are necessary to confirm this hypothesis.

The rotation curves have been studied at a comparable resolution in only a handful of DSFGs. In this respect, ALESS 49.1 and 57.1 velocity fields are most directly comparable to those in $z = 2.4$ twin hyperluminous DSFGs H-ATLAS J084933 (Ivison et al. 2013) and strongly lensed DSFGs SMM J2135-0102 ($z = 2.032$, Swinbank et al. 2011) and SDP.81 ($z = 3.042$, Dye et al. 2015; Rybak et al. 2015b), which flatten out at ∼200 km s^{-1} within the inner 2-kpc radius. The dynamical mass enclosed within the central 2-kpc radius region of ALESS 49.1 and 57.1 is M_{dyn} ($R \leq$2 kpc) = $(6.2 \pm 5.5) \times 10^{10}$ and $(2.7 \pm 1.6) \times 10^{10}$ M$\odot$, respectively; although CO (3–2) observations provide mass estimates at 5–6 kpc radius, the large uncertainties prevent us from investigating the mass profiles of the two sources. The limited extent of the bright [C 2] component and the possibility that an extended [C 2] emission in ALESS 49.1 is resolved out highlight the limits of using very high-angular-resolution observations to trace the kinematics of the cold gas reservoir.

Finally, given the ordered rotation in ALESS 49.1 and 57.1, we can use the [C 2]/CO(3–2) ratio to search for variations in gas physical conditions in different regions of the source. We bin the one-dimensional spectra from Figure 5.4 into bins 250 km s^{-1} wide. Although by eye the [C 2] and CO (3–2) ratio in ALESS 49.1 seems to vary between across the spectrum, we do not find any change in [C 2]/CO(3–2) ratio in either source at ≥2-σ level given the current depth of the Bands 3 and 8 observations.

5.4.3 The resolved [CII]-FIR ratio

The high resolution of ALMA Band 8 data allows us to investigate the $L_{\rm [CII]}/L_{\rm FIR}$ ratio at $z \sim 3$ on 1-kpc scales. Here, we focus on the *central region* ($R \leq$2 kpc), in which the contribution of any extended [C 2] component is below 20 per cent. This discussion does not include the *global* tracer ratios, as the Band 8 observations might resolve out significant fraction of the total [C 2] flux from an extended component.

The star-formation rate surface density $\Sigma_{\rm SFR}$ is estimated by adopting the global SFR from our SED fits 5.3.4, assuming (1) a linear mapping between the rest-frame 160-μm emission and SFR; (2) no AGN contribution to the rest-frame FIR luminosity; (3) universal IMF (c.f Zhang et al. 2018a). The linear mapping between the FIR continuum and SFR density assumes a constant dust temperature and opacity across the source. Further high-resolution, multi-band observations of the dust continuum and spatially-resolved SED modelling would be required for a more precise $\Sigma_{\rm SFR}$ estimate for different parts of the source. The [C 2]/FIR ratio was extracted by binning the [C 2] and 160-μm continuum maps (Fig. 5.1) into pixels 1 beamwidth large; only pixels for which both the [C 2] and 160-μm continuum have SNR≥2 are considered.

Figure 5.7 shows the resolved $L_{\rm [CII]}/L_{\rm FIR}$ for ALESS 49.1 and 57.1 as a function of the SFR surface density $\Sigma_{\rm SFR}$, compared to resolved and unresolved measurements from both local and high-redshift sources (Smith et al. 2017; Díaz-Santos et al. 2017; Gullberg et al. 2018 and references therein). In both ALESS 49.1 and 57.1, the resolved ratio decreases sharply with $\Sigma_{\rm SFR}$, confirming the [C 2]/FIR deficit on 1-kpc scales.

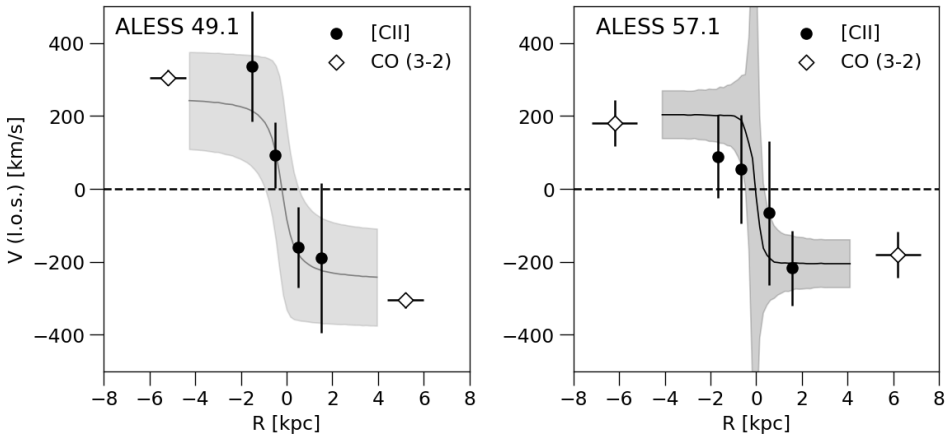

Figure 5.6: Line-of-sight velocity curves for ALESS 49.1 and 57.1, showing the [C 2] velocity and velocity dispersions measured from the image cubes (full dots), with inferred rotation curve from GALPAK3D (full line, velocity dispersion estimate indicated by the shaded region), alongside the CO (3–2) measurements (empty diamonds, Calistro Rivera et al. 2018). The [C 2] measurements were extracted along the major kinematic axis determined by the GALPAK3D modelling from an aperture 1 beamwidth wide. The line-of-sight velocity flattens out at ∼2-kpc radius, suggesting disc-dominated kinematics. The large GALPAK3D-predicted velocity dispersion at the centre of ALESS 57.1 is a numerical artefact.

Comparing our measurements with an empirical relation between [C 2]/FIR ratio and $\Sigma_{\rm SFR}$ proposed by Smith et al. (2017),

$$\Sigma_{\rm SFR} = (12.7 \pm 3.2)\Big(\frac{L_{\rm [CII]}/L_{\rm FIR}}{0.001}\Big)^{-4.7\pm0.8}\,{\rm M_\odot yr^{-1}kpc^{-2}}. \quad (5.3)$$

we find that the bulk of the ALESS 49.1 and 57.1 [C 2]/FIR measurements are below the 1-σ scatter of the Smith et al. (2017) relation, with $\Sigma_{\rm SFR}$ almost 1–2 dex lower than those predicted by the Smith et al. (2017) relation. This suggests that the Smith et al. (2017) $\Sigma_{\rm SFR} - L_{\rm [CII]}/L_{\rm [CII]}$ might not be directly applicable in the high-Σ_{SFR} regime in ALESS 49.1 and 57.1.

We note that the ALESS 49.1 and 57.1 [C 2]/FIR measurements fall below the redshift $\sim$ 4.5 resolved measurements of Gullberg et al. (2018). This can be attributed to several factors: (1) different object selection; (2) aperture-averaging effects in Gullberg et al. (2018), as the [C 2]/FIR ratio is calculated for apertures several kpc wide; (3) systematic uncertainties such as assuming uniform $T_{\rm dust}$ for each source. Regarding object selection, ALESS 49.1 and 57.1 have $L_{\rm FIR}$ more than 2× higher than Gullberg et al. (2018) sources, while being more compact in the rest-frame FIR continuum; consequently, our measurements might probe a higher $\Sigma_{\rm FIR}$ regime, which would correspond to lower [C 2]/FIR ratio and potentially higher $T_{\rm gas}$ (see Section 5.4.4).

The radial variation of $L_{\rm [CII]}/L_{\rm FIR}$ in ALESS 49.1 and 57.1 is shown in Figure 5.8. A decrease in the [C 2]/FIR ratio towards the centre of the source is seen in both local star-forming galaxies (e.g. Madden et al. 1993; Smith et al. 2017) and high-redshift sources (Gullberg et al. 2018) and indicates that the [C 2]/FIR deficit is driven by local processes, as opposed to global properties of the sources. In particular, Smith et al. (2017) found the [C 2]/FIR ratio to be suppressed by on average 30±15 per cent in the central $R \leq 400$ pc regions of galaxies without an AGN. On the other hand, [C 2]/FIR ratio drops by a factor of a few over the inner 2 kpc in nu-

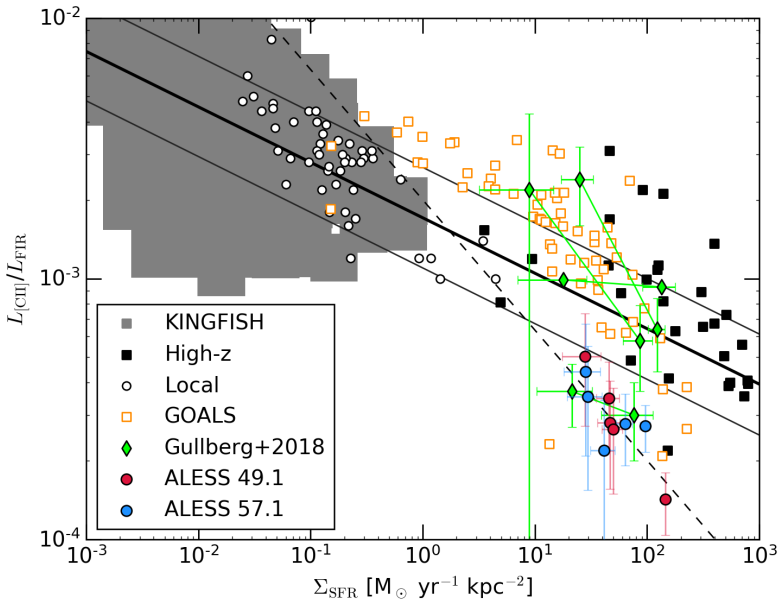

Figure 5.7: Resolved [C 2]/FIR deficit in ALESS 49.1 and 57.1, compared to the KINGFISH Smith et al. (2017) and GOALS Díaz-Santos et al. (2017) samples and other local (empty circles) and high-redshift measurements (black squares), adapted from Smith et al. (2017) and Gullberg et al. (2018). For each of the Gullberg et al. (2018) sources, we show the ratio for the inner and outer region, connected by a line. The thick black lines indicates the Smith et al. (2017) empirical fit to the [C 2]/FIR data (equation (5.3) and the corresponding 1-σ scatter; the dashed line indicates the prediction from the Muñoz & Oh (2016) temperature-saturation model (equation (5.5)), for $f_{[CII]}$=0.13. The resolved ALESS 49.1 and 57.1 data-points fall below the Smith et al. (2017) trend, and follow a much steeper slope, indicating a [C 2]-saturation regime. The errorbars on ALESS 49.1 and 57.1 measurements include a contribution from an extended [C 2]/160-μm continuum components.

clear starbursts in M82 and M83 (Herrera-Camus et al. 2018). Fitting the resolved [C 2]/FIR data with a power-law $L_{[CII]}/L_{[CII]} \propto R^{\alpha}$, we find a strong evidence for a radial variation of the [C 2]/FIR ratio in ALESS 49.1 ($\alpha = 0.41 \pm 0.06$), while in ALESS 57.1, the data is consistent with being uniform ($\alpha = 0.05 \pm 0.05$). While the obscured *Chandra*-detected AGN in ALESS 57.1 (Wang et al. 2013) might be expected to suppress the [C 2] emission in the circumnuclear region, we do not detect any strong [C 2] suppression in ALESS 57.1 on 1-kpc scales. The difference in the [C 2]/FIR radial profiles in ALESS 49.1 and 57.1 is due to the larger scatter in [C 2]/FIR ratio for a given Σ_{SFR} in ALESS 57.1 (see Figure 5.7), which is a result of the complex [C 2] and 160-μm morphology (Figure 5.1). Note that the limited SNR of our data at $R \geq 2$ kpc prevents us to study the [C 2]/FIR radial dependence at larger radii.

5.4.4 Comparison with PDR models

The relative intensities of the [C 2], CO (3–2) and FIR emission from hot-dissociation regions (PDRs) depend on the ionizing FUV field strength G_0 and the gas density n(H), which determine the depth of the outer C^+ layer. We now use our resolved [C 2]/CO(3–2)/FIR observations to infer the G_0 and n using the PDR models from the PDRTOOLBOX library (Kaufman

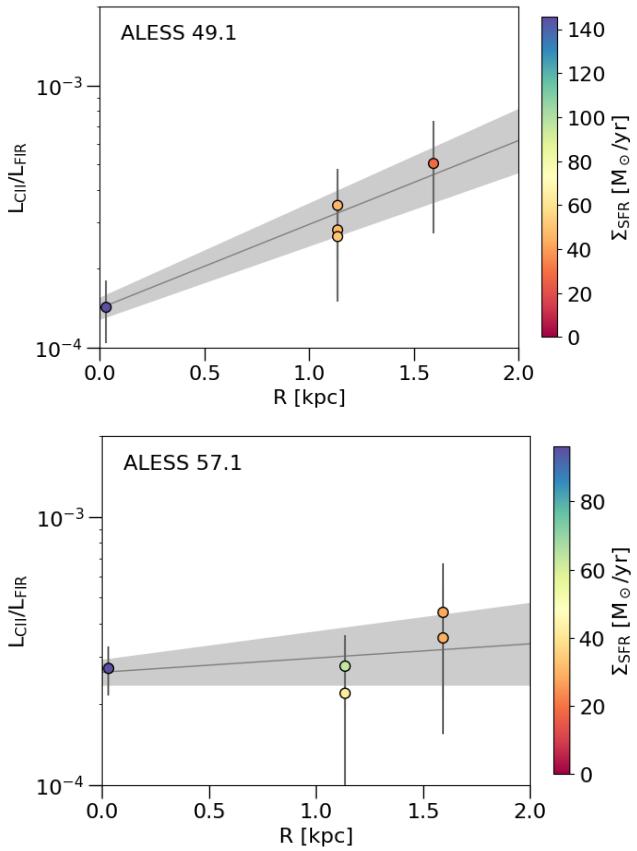

Figure 5.8: [C 2]/FIR deficit radial trends in ALESS 49.1 and 57.1, colour-coded by the star-formation rate surface density Σ_{SFR}; each point corresponds to a separate resolution element. The lines and shaded regions indicate the best-fitting slopes and corresponding uncertainties, respectively. The radial distances R are measured from the 160-μm continuum surface brightness maximum.

Table 5.3: Comparison with PDRTOOLBOX PDR models: observed [C 2]/CO(3–2) and [C 2]/FIR continuum ratios, along with inferred FUV field strength G_0, density n(H) and PDR surface temperature $T_{\rm PDR}$ for ALESS 49.1 and 57.1. We consider both optically thin and thick [C 2] scenarios. The [C 2] luminosities are given before subtracting the contribution from non-PDR sources.

Source		ALESS 49.1	ALESS 57.1
[C 2]/FIR		$(3.3 \pm 1.5) \times 10^{-4}$	$(3.4 \pm 1.2) \times 10^{-4}$
[C 2]/CO(3–2)		310 ± 100	600 ± 240
[C 2] optically thin			
$\log G_0$		$4.1^{+0.3}_{-0.2}$	$4.1^{+0.9}_{-0.4}$
$\log n$(H)	[cm^{-3}]	$4.2^{+0.5}_{-0.2}$	$3.6^{+0.5}_{-0.3}$
$T_{\rm gas}$	[K]	720 ± 200	670 ± 170
[C 2] optically thick			
$\log G_0$		$3.7^{+0.4}_{-0.3}$	$3.7^{+0.9}_{-0.4}$
$\log n$(H)	[cm^{-3}]	$3.4^{+0.4}_{-0.2}$	$2.8^{+0.5}_{-0.2}$
$T_{\rm gas}$	[K]	430 ± 30	480 ± 90

5

et al. 2006; Pound & Wolfire 2008). We focus on the central regions of the source ($R \leq 2$ kpc) adopting the one/two-component Gaussian models from Section 5.3.2.

For a proper comparison, several corrections need to be applied. First, the [C 2] emission from the ionized ISM needs to be subtracted from the observed [C 2] signal. The contribution from the ionized gas can be estimated from [N 2] 122/205-μm lines, which have similar critical density for collisions with electrons (300 cm^{-3}/32 cm^{-3}) as the [C 2] line (50 cm^{-3}, Goldsmith et al. 2012), but ionization energy > 13.6 eV and hence traces only the ionized gas. Croxall et al. (2017) carried out a systematic study of the [N 2] 122/205 μm lines in a sample of 21 nearby star-forming galaxies, estimating the fraction of [C 2] in PDRs as $f^{\rm PDR}_{\rm [CII]} \geq 0.8$ for sources with $\Sigma_{\rm SFR} \geq 10^{-2}$ M$_\odot$ yr^{-1} kpc^{-2}. At high redshift, Zhang et al. (2018b) used [N 2] 122-μm line observations in $z = 1 - 3$ DSFGs to derive 10–15 per cent ionized gas contribution to [C 2] luminosity, assuming Galactic diffuse gas N and C abundancies. We adopt a conservative estimate of $f^{\rm PDR}_{\rm [CII]} = 0.8$.

Second, PDRTOOLBOX models are derived for a one-dimensional, semi-infinite slab, illuminated from the face side only. In the intensely star-forming DSFGs, we expect the clouds to be illuminated from multiple sides and the optical thickness of individual tracers needs to be considered. Namely, for optically thick emission, only the emission from the side of the cloud facing the observer is observed; while for the optically thin emission, the distant side of the cloud adds to the observed fluxes and the line intensities expected from PDR models need to be multiplied by a factor of 2 Kaufman et al. (1999). The 160-μm continuum is generally assumed to be optically thin. Based on the models of Narayanan & Krumholz (2014), CO (3–2) line is optically thick with a median optical depth ≥ 10 for $\Sigma_{\rm SFR} = 10^{-1} - 10^{3}$ M$_\odot$ yr^{-1}. The [C 2] emission is optically thin in most environments; although there is evidence for moderately optically thick [C 2] (optical depth ~1) in both Galactic PDRs (Graf et al. 2012; Sandell et al. 2015) and high-redshift sources (Gullberg et al. 2015). We consider both optically-thin and optically-thick [C 2] scenarios, adopting the former for the rest of this paper.

Figure 5.9 shows the contours in the G_0/n space for the central $R \leq 2$ kpc region of ALESS 49.1 and 57.1, with best-fitting values listed in Table 5.3. The combination of the three tracers provides orthogonal constraints on G_0 and n. In particular, G_0 is largely determined by the [C 2]/FIR ratio, and n by [C 2]/CO (3–2). Table 5.3 lists the inferred G_0 and

n values for the optically thin and optically thick [C 2] scenarios, along with the PDR surface temperature. For the optically-thin [C 2] case, the conditions in ALESS 49.1 and 57.1 are almost identical, with $\log G_0 \sim 4.1$ and $\log n \sim 4.0$, implying PDRsurface temperature $T_{\rm PDR}$ of ∼700 K. Increasing the fraction of [C 2] emission from the PDRs from 0.8 to 1.0 causes the inferred G_0 and n values to decrease by ≤0.25 dex. For the optically-thick [C 2] case, the inferred G_0 and n decrease almost 0.5 and 1.0 dex, respectively; $T_{\rm PDR}$ is reduced to 400–500 K.

The G_0, n values in the central region of ALESS 49.1 and 57.1 are comparable to those inferred from unresolved SMG observations ($n = 10^2 - 10^4$ cm^{-3}, $G_0 = 10^3 - 10^{4.5}$, Stacey et al. 2010; Danielson et al. 2013; Wardlow et al. 2017; Alaghband-Zadeh et al. 2013; Zhang et al. 2018b). Gullberg et al. (2015) found a larger scatter of FUV strength ($G_0 = 10^2 - 8\times10^3$) and density ($n = 10^2 - 10^5$ cm^{-3}), although the effect of differential magnification might be substantial. For nearby star-forming galaxies, a comparison of observed spatially integrated [C 2], [O 1] 63-μm and FIR luminosities with the PDRTOOLBOX models was carried out by Malhotra et al. (2001) and Díaz-Santos et al. (2017). ALESS 49.1 and 57.1 are consistent with the high-density Malhotra et al. (2001) sources; however, G_0 and n in ALESS 49.1 and 57.1 are higher than in the most dense ultra-luminous infrared galaxies (ULIRGs) from the Díaz-Santos et al. (2017) sample. which have $G_0 \sim 10^3$, $n = 1 - 10^3$ cm^{-3}. Note that the globally-averaged G_0 and n in ALESS 49.1 and 57.1 might be lower than those inferred from the $R \leq 2$ kpc region. On kpc-scales, G_0 and n in the central regions of ALESS 49.1 and 57.1 are more comparable to the resolved observations of central star-forming regions in nearby starburst galaxies NGC 6946 and NGC 1313 ($G_0 = 10^3 - 10^4$, $n = 10^{3.0} - 10^{3.5}$ cm^{-3}, Contursi et al. 2002).

What drives the strong FUV fields in ALESS 49.1 and 57.1: a central AGN, or star-formation? Although *Chandra* X-ray observations of ALESS 49.1 and 57.1 (Wang et al. 2013) revealed an obscured AGN in ALESS 57.1 (no emission from ALESS 49.1 was detected), it is unlikely that an obscured AGN would be driving a strong FUV field on few-kpc scales. On the other hand, the G_0 in the vicinity of H 2 regions is of the order $10^3 - 10^5$ (e.g. Tielens & Hollenbach 1985; Hollenbach & Tielens 1999), comparable to the values inferred from PDR models. Similarly, typical G_0 and n values for Galactic star-forming regions are of the order of $G_0 = 10^3 - 10^5$, $n = 10^3 - 10^6$ cm^{-3}(Stacey et al. 1991, 2010). We therefore conclude that the strong FUV field in ALESS 49.1 and 57.1 is due to star formation, rather than a central AGN.

5.4.5 Origin of the [CII]/FIR deficit

With estimates of G_0 and n in the central regions of ALESS 49.1 and 57.1, we now turn to the mechanism driving the [C 2]/FIR deficit. We focus on the thermal saturation model proposed by Muñoz & Oh (2016), and the reduction of the photoelectric heating of the gas by small dust grains (e.g. Bakes & Tielens 1994; Malhotra et al. 2001); we briefly discuss other potentially relevant mechanisms – AGN contribution and dust-bound HII regions – in Section 4.5.3. For a more exhaustive list of potential mechanisms behind the [C 2]/FIR deficit, we refer the reader to Smith et al. (2017).

Thermal saturation of the [CII] line

Muñoz & Oh (2016) have proposed the thermal saturation of the upper level of the C^+ fine-structure transition as the main driver of the [C 2]/FIR deficit. In other words, when T_{gas} exceeds the C^+ ionization temperature (92 K), the upper/lower level population ratio (and the [C 2] luminosity) depends only weakly on T_{gas}, while the FIR luminosity keeps on increasing.

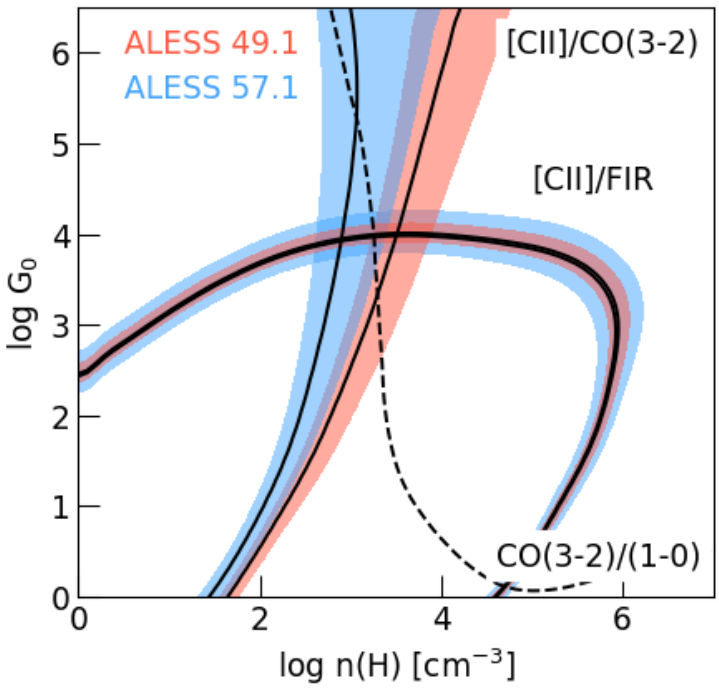

Figure 5.9: Constraints on the FUV field strength G_0 and density n for the central $R \leq 2$ kpc region derived from comparison with Kaufman et al. (2006) PDR models. For the [C 2]/FIR/CO(3–2) emission, we adopt surface brightness profiles derived from the *uv*-plane fitting. The [C 2] emission is assumed to be optically thin, with PDR contributing 80 per cent of the observed signal. The coloured areas indicate 1-σ confidence regions. For the central regions of ALESS 49.1 and 57.1, we infer $G_0 \sim 10^{3.5} - 10^{4.0}$ and $n = 10^{3.6} - 10^{4.2}$ cm^{-3}.

The PDRTOOLBOX models, which imply high FUV fields strength ($G_0 \sim 10^4$) and densities ($n = 10^{3.5} - 10^4$) and surface temperatures larger than 500 K (Table 5.3. The [C 2] transition is saturated in this regime. Following Muñoz & Oh (2016), the thermal cooling rate per Hydrogen atom via the [C 2] line depends on T_{gas} via

$$\Lambda_{[\rm CII]} = 2.3 \times 10^{-6}\, k_{\rm B}\, T_{[\rm CII]} \frac{2}{2 + \exp(T_{\rm CII}/T_{\rm gas})\frac{C}{H}}, \tag{5.4}$$

where $k_{\rm B}$ is the Boltzmann constant and $T_{[\rm CII]}$ is the [C 2] ionization temperature. Following the equation (5.4), the [C 2] cooling rate increases by only ∼40 per cent between T_{gas}=100 K and 500 K, whereas the $L_{\rm FIR}$ increases by a factor of few hundred, assuming T_{dust} scales proportionally with T_{gas} and $L_{\rm FIR} \propto T_{dust}^{4+\beta}$, where we assumed dust opacity $\beta = 1.5$.

For a more direct comparison with Muñoz & Oh (2016) model, we compare the resolved [C 2]/FIR observations in ALESS 49.1 and 57.1 (Figure 5.7) to the predicted $\Sigma_{\rm SFR}$-[C 2]/FIR slope. According to Muñoz & Oh (2016), $L_{[\rm CII]}/L_{\rm FIR}$ ratio scales as:

$$\frac{L_{[\rm CII]}}{L_{\rm FIR}} = 2.2 \times 10^{-3} \frac{f_{\rm CII}}{0.13} \Big(\frac{\Sigma_{\rm FIR}}{10^{11} {\rm L}_\odot {\rm kpc}^{-2}} \Big)^{-1/2}, \tag{5.5}$$

where $f_{\rm CII}$ is the fraction of gas emitting in [C 2] and C/H the relative abundances of Carbon/Hydrogen atoms. Fitting our datapoints with a power-law following the equation (5.5), we obtain a best-fitting slope of $\gamma = -0.53 \pm 0.12$. This is in agreement with the thermal-saturation model slope of $\gamma = -0.5$ (equation (5.5)).

We note that Díaz-Santos et al. (2017) discount the thermal saturation of the [C 2] line as a source of the [C 2]/FIR deficit in local star-forming galaxies. Namely, comparing the [O 1] 63 μm and [C 2] line ratios with a statistical equilibrium radiative transfer model, they obtain a scaling between dust and gas kinetic temperature $T_{gas} = 1.6 - 2.1 \times T_{dust}$. Given $T_{\rm dust}$ of 21–48 K, they find $T_{gas} \leq$92 K, i.e. below the thermal-saturation regime. However, ALESS 49.1 and 57.1 show relatively high global $T_{dust} = 47^{+5}_{-9}/52^{+10}_{-6}$ K (Table 5.2). Given the conversion factors from Díaz-Santos et al. (2017) and evidence for increase in dust and gas temperature towards the centre of DSFGs (Calistro Rivera et al. 2018), T_{gas} in the central regions of ALESS 49.1 and 57.1 exceeds 92 K.

Suppression of the [CII] emission due to positive grain charging

In addition to the temperature saturation, another potentially important effect at the G_0, n values inferred from our PDR analysis is the reduced photoelectric heating of the gas by electrons ejected from the small dust grains by the FUV photons (e.g. Bakes & Tielens 1994; Malhotra et al. 2001; Wolfire et al. 2003). At high G_0/n ratios, the grains become positively charged, thus raising the potential barrier for the electrons to escape. Qualitatively, a reduced photoelectric heating will manifest in moderate $T_{\rm gas}/T_{\rm dust}$ ratios. Although ALESS 49.1 and 57.1 have elevated dust temperatures compared to other high-redshift DSFGs (Swinbank et al. 2014; da Cunha et al. 2015) and local ULIRGs (Díaz-Santos et al. 2017), the high PDR surface temperatures indicate that the gas is already heated to high temperature, at which point the [C 2] line becomes saturated.

Quantitatively, following Wolfire et al. (2003), the photoelectric heating rate per hydrogen atom is give as:

$$\Gamma_{\rm PE} = \frac{1.1\times10^{-25} G' Z_d}{1 + 3.2\times10^{-2}\left[G'(T_{\rm gas}/100\ K)^{1/2} n_e^{-1}\phi_{\rm PAH}\right]^{0.73}} \quad {\rm erg\,s^{-1}}, \quad (5.6)$$

where $G' = 1.7 \times G_0$, Z_d is the dust-to-gas ratio (normalized to the Galactic value), n_e the electron density and $\phi_{\rm PAH}$ a factor associated with the PAH molecules. The second term in the denominator corresponds to the positive grain charging. We follow Muñoz & Oh (2016) by adopting $n_e = 1.1\times10^{-4} n$, $\phi_{PAH} = 0.5$. Note that equation (5.6) assumes $T_{\rm gas} \leq$1000 K, which is satisfied for both ALESS 49.1 and 57.1. While for the ALESS 49.1 and 57.1 values of G_0, n the second term in the denominator corresponding to the reduction in photoelectric heating, becomes dominant, the numerator is also proportional to G_0. Comparing a typical nearby star-forming galaxy with $G_0 = 10^2$, $n = 10^4$ cm^{-3}, (c.f. Muñoz & Oh 2016) and ALESS 49.1 and 57.1 with $G_0 = 10^4$, $n = 10^4$ cm^{-3}, the second term in the determinant increases from ∼0.3 to ∼ 18, indicating a significant reduction in the gas heating due to grain charging. However, at the same time, the overall $\Gamma_{\rm PE}$ increases by a factor of ∼6.

Therefore, we attribute the pronounced [C 2]/FIR deficit in the central regions of ALESS 49.1 and 57.1 to the high gas temperature which results in a quantum-level saturation of the C^+ fine structure.

Other mechanisms for [CII]/FIR deficit

Finally, we briefly consider other proposed mechanisms for the [C 2] deficit.

AGNs can contribute to the [C 2] deficit, both by increasing the FIR luminosity and reduce the C^+ abundance and the [C 2] emission by ionizing the carbon atoms to higher ionization states (C^{2+}, C^{3+} etc.) via soft X-ray radiation (Langer & Pineda 2015). *Chandra* of ALESS 49.1 and 57.1 revealed an obscured AGN with an extinction-corrected X-ray luminosity of $\log L_{0.5-8.0{\rm keV}} = 44.3$ and no X-ray emission in ALESS 49.1 (Wang et al. 2013). According to Langer & Pineda (2015) models, for $n \sim 10^3$ cm^{-3} (model closest to the conditions in ALESS 49.1 and 57.1), a 10 per cent decrease in the fraction of carbon in the C^+ state requires an X-ray flux of $f_X \simeq 10^{3.5}$ erg cm^{-2} s^{-1}. Assuming an X-ray flux dilutes with distance D as $1/4\pi D^2$, the AGN in ALESS 57.1 will affect only the innermost ∼100 pc radius, well below the spatial resolution of our data. Consequently, we do not expect a significant AGN contribution to the observed [C 2] deficit.

Another potential explanation for the [C 2]/FIR deficit is the increased absorption of ionizing UV photons by the dust in dust-bounded H 2 regions, which would result in increased FIR and decreased [C 2] luminosity, respectively (Luhman et al. 2003). Abel et al. (2009) used radiative transfer models of dust-bounded H 2 region to qualitatively reproduce the [C 2]/FIR deficit trend. However, for the observed [C 2]/FIR values in ALESS 49.1 and 57.1, the Abel et al. (2009) models require densities of $n \leq 1 - 2 \times 10^3$ cm^{-3}, i.e. much lower than those inferred from the PDR modelling. Furthermore, as already noted by Muñoz & Oh (2016), the dust drift time for high G_0, n values becomes very short compared to O/B stars lifetime. We follow Draine (2011) to estimate a dust drift time for a cluster of 10^3 O/B stars, providing an ionizing photons flux $Q_0 = 10^{52}$ s^{-1}. Given the density of $10^{3.5} - 10^{4.0}$ cm^{-3}, the dust drift time becomes $t_{\rm drift} = 1.0 - 1.5 \times 10^5$ yr (Figure 9 of Draine 2011). Even if the H 2 regions in ALESS 49.1 and 57.1 are originally dust-bound, given the duration of the starburst, we do not expect a significant fraction of the to be dust-bound at a given moment and hence do not expect the dust-bounded H 2 regions to dominate the [C 2]/FIR deficit in ALESS 49.1 and 57.1.

5.5 Conclusions

We have investigated the morphology and kinematics of the [C 2] 157.74-μm line emission and associated 160-μm rest-frame continuum in two $z \sim 3$ sources from the ALESS sample, based on the 0.15 arcsec ALMA Band 8 imaging. The morphology and [C 2] velocity field in both galaxies is consistent with an inclined rotating exponential disc. The [C 2] rotation curves show a flattening within the inner 2-3 kpc radius, indicative of a potential dominated by a baryonic disc.

Comparing the resolved maps of the [C 2] emission with those of CO (3–2) (Calistro Rivera et al. 2018), we found the [C 2] surface brightness distribution to be concentrated into a region a factor of 2–3 more compact the CO (3–2). In ALESS 49.1, we found evidence for a low surface-brightness, extended ($R_{1/2} \sim 8$ kpc) [C 2] component, accounting for up to 80 percent of the [C 2] brightness. Based on mock ALMA observations, we excluded the possibility that [C 2] and 160-μm continuum follow the same single-Gaussian surface brightness as the CO (3–2) emission.

We compared of the [C 2]/FIR and CO (3–2) observations to the PDRTOOLBOX photo-dissociation regions models (Kaufman et al. 2006; Pound & Wolfire 2008). These indicate intense FUV radiation field ($G_0 \sim 10^4$) and moderately high gas densities (n(H) = $10^{3.5} - 10^{4.0}$ cm^{-3}). These are comparable to the G_0 and n values found in the central regions of nearby starbursts (e.g. Contursi et al. 2002), as well as in other $z > 2$ SMGs (Stacey et al. 2010). We attribute the strong FUV field to to massive the star-formation, rather than by an obscured AGN.

We tested the applicability of the Stacey et al. (2010) technique for estimating FIR source size from unresolved [C 2]/low-J CO / FIR observations to ALESS 49.1 and 57.1. The Stacey et al. (2010) method yields estimates a factor of 2.5–3.5 more compact than the FIR sizes measured from the uv-plane fitting; this bias causes the SFR surface-density to be overestimated by up to 1 dex, having a potentially significant impact on the interpretation of low-resolution observations.

Both ALESS 49.1 and 57.1 show a pronounced [C 2]/FIR deficit. The resolved [C 2]/FIR luminosity ratios fall below the empirical trend of Smith et al. (2017), indicating a change in physical conditions compared to the nearby star-forming galaxies. A comparison with PDR models indicated surface temperatures of 400–800 K; at such a high temperature, the occupancy of the upper fine-structure level of C^+ ions (and the [C 2] luminosity) saturates, while FIR luminosity increases sharply. The most direct interpretation is that the strong [C 2] deficit is a result of the [C 2] temperature saturation (Muñoz & Oh 2016). In addition, in the resolved [C 2]/FIR measurements in ALESS 49.1 and 57.1 scale with star-formation rate surface density $\Sigma_{\rm SFR}^{-0.53\pm0.12}$, in agreement with the thermal-saturation scenario slope of -0.5 (Muñoz & Oh 2016). Although the photoelectric heating of the gas is reduced due to positive grain charging, for the G_0, n values in ALESS 49.1 and 57.1, the thermal saturation is the main driving mechanism of the [C 2]/FIR deficit. This contrasts with the local star-forming galaxies, which are found to have gas temperatures below the C^+ ionization energy (e.g. Díaz-Santos et al. 2017).

With only two galaxies in our sample, it is difficult to generalize our conclusions to the entire population of dusty, star-forming galaxies. With ALMA now enabling routine observations of [C 2] emission at redshift 3 and beyond, and with a rapid increase of high-redshift sources with robust spectroscopic redshifts that are necessary for parallel [C 2]/CO observations, this study is a precursor to future multi-tracer, resolved studies of ISM at high redshift, and a necessary stepping stone to interpreting the [C 2] observations at very high redshift.

Acknowledgements

The authors thank Frank Israel and Desika Narayanan for helpful discussions about the [C 2]/CO extent. This paper makes use of the following ALMA data: ADS/JAO.ALMA#2013.1.00470.S, #2015.1.00019.S, #2015.1.00948.S and #2016.1.00754.S. ALMA is a partnership of ESO (representing its member states), NSF (USA) and NINS (Japan), together with NRC (Canada), MOST and ASIAA (Taiwan), and KASI (Republic of Korea), in cooperation with the Republic of Chile. The Joint ALMA Observatory is operated by ESO, AUI/NRAO and NAOJ. MR and JH acknowledge support of the VIDI research programme with project number 639.042.611, which is (partly) financed by the Netherlands Organisation for Scientific Research (NWO). IRS acknowledges support from the ERC Advanced Grant DUSTYGAL (321334) and STFC (ST/P000541/1). HD acknowledges financial support from the Spanish Ministry of Economy and Competitiveness (MINECO) under the 2014 Ramón y Cajal program MINECO RYC-2014-15686. JLW acknowledges support from an STFC Ernest Rutherford Fellowship (ST/P004784/1).

Bibliography

Abel, N. P., Dudley, C., Fischer, J., Satyapal, S., & van Hoof, P. A. M. 2009, ApJ, 701, 1147

Alaghband-Zadeh, S., Chapman, S. C., Swinbank, A. M., et al. 2013, MNRAS, 435, 1493

ALMA Partnership, Vlahakis, C., Hunter, T. R., et al. 2015, Apjl, 808, L4

Armus, L., Mazzarella, J. M., Evans, A. S., et al. 2009, PASP, 121, 559

Bakes, E. L. O., & Tielens, A. G. G. M. 1994, ApJ, 427, 822

Bevington, P. R. 1969, Data reduction and error analysis for the physical sciences

Bothwell, M. S., Smail, I., Chapman, S. C., et al. 2013, MNRAS, 429, 3047

Bouché, N., Carfantan, H., Schroetter, I., Michel- Dansac, L., & Contini, T. 2015, AJ, 150, doi:10.1088/0004-6256/150/3/92

Brisbin, D., Ferkinhoff, C., Nikola, T., et al. 2015, ApJ, 799, 13

Calistro Rivera, G., Hodge, J. A., Smail, I., et al. 2018, ApJ, 863, 56

Carilli, C. L., & Walter, F. 2013, ARA&A, 51, 105

Carniani, S., Maiolino, R., Amorin, R., et al. 2017, ArXiv e-prints, arXiv:1712.03985

Casey, C. M., Narayanan, D., & Cooray, A. 2014, Phys. Rep., 541, 45

Chen, C.-C., Hodge, J. A., Smail, I., et al. 2017, ApJ, 846, doi:10.3847/1538-4357/aa863a

Cicone, C., Maiolino, R., Gallerani, S., et al. 2015, A&A, 574, A14

Contursi, A., Kaufman, M. J., Helou, G., et al. 2002, AJ, 124, 751

Cooke, E. A., Smail, I., Swinbank, A. M., et al. 2018, ApJ, 861, 100

Croxall, K. V., Smith, J. D., Pellegrini, E., et al. 2017, ApJ, 845, 96

da Cunha, E., Charlot, S., & Elbaz, D. 2008, MNRAS, 388, 1595

da Cunha, E., Groves, B., Walter, F., et al. 2013, ApJ, 766, doi:10.1088/0004-637X/766/1/13

da Cunha, E., Walter, F., Smail, I. R., et al. 2015, ApJ, 806, 110

Danielson, A. L. R., Swinbank, A. M., Smail, I., et al. 2013, MNRAS, 436, 2793

—. 2017, ApJ, 840, 78

de Blok, W. J. G., Walter, F., Smith, J.-D. T., et al. 2016, AJ, 152, 51

Decarli, R., Walter, F., Venemans, B. P., et al. 2018, ApJ, 854, doi:10.3847/1538-4357/aaa5aa

Díaz-Santos, T., Armus, L., Charmandaris, V., et al. 2013, ApJ, 774, 68

Díaz-Santos, T., Armus, L., Charmandaris, V., et al. 2017, ApJ, 846, 32

Draine, B. T. 2011, ApJ, 732, 100

Dye, S., Furlanetto, C., Swinbank, A. M., et al. 2015, MNRAS, 452, 2258

Goldsmith, P. F., Langer, W. D., Pineda, J. L., & Velusamy, T. 2012, The Astrophysical Journal Supplement Series, 203, doi:10.1088/0067-0049/203/1/13

Graciá-Carpio, J., Sturm, E., Hailey-Dunsheath, S., et al. 2011, ApJ, 728, L7

Graf, U. U., Simon, R., Stutzki, J., et al. 2012, A&A, 542, L16

Gullberg, B., De Breuck, C., Vieira, J. D., et al. 2015, MNRAS, 449, 2883

Gullberg, B., Swinbank, A. M., Smail, I., et al. 2018, ArXiv e-prints, arXiv:1804.03663

Herrera-Camus, R., Sturm, E., Graciá-Carpio, J., et al. 2018, ArXiv e-prints, arXiv:1803.04419

Hodge, J. A., Carilli, C. L., Walter, F., et al. 2012, ApJ, 760, doi:10.1088/0004-637X/760/1/11

Hodge, J. A., Riechers, D., Decarli, R., et al. 2015, ApJ, 798, L18

Hodge, J. A., Karim, A., Smail, I., et al. 2013, ApJ, 768, 91

Hodge, J. A., Swinbank, A. M., Simpson, J. M., et al. 2016, ApJ, 833, 103

Hollenbach, D. J., & Tielens, A. G. G. M. 1999, Reviews of Modern Physics, 71, 173

Huynh, M. T., Kimball, A. E., Norris, R. P., et al. 2014, MNRAS, 443, L54

Huynh, M. T., Emonts, B. H. C., Kimball, A. E., et al. 2017, MNRAS, 467, 1222

Ivison, R. J., Papadopoulos, P. P., Smail, I., et al. 2011, MNRAS, 412, 1913

Ivison, R. J., Swinbank, A. M., Smail, I., et al. 2013, ApJ, 772, 137

Kaufman, M. J., Wolfire, M. G., & Hollenbach, D. J. 2006, ApJ, 644, 283

Kaufman, M. J., Wolfire, M. G., Hollenbach, D. J., & Luhman, M. L. 1999, ApJ, 527, 795

Lagache, G., Cousin, M., & Chatzikos, M. 2018, A&A, 609, doi:10.1051/0004-6361/201732019

Langer, W. D., & Pineda, J. L. 2015, A&A, 580, A5

Luhman, M. L., Satyapal, S., Fischer, J., et al. 2003, ApJ, 594, 758

—. 1998, ApJ, 504, L11

Madden, S. C., Geis, N., Genzel, R., et al. 1993, ApJ, 407, 579

Malhotra, S., Helou, G., Stacey, G., et al. 1997, ApJ, 491, L27

Malhotra, S., Kaufman, M. J., Hollenbach, D., et al. 2001, ApJ, 561, 766

McMullin, J. P., Waters, B., Schiebel, D., Young, W., & Golap, K. 2007, in Astronomical Data Analysis Software and Systems XVI ASP Conference Series, Vol. 376, proceedings of the conference held 15-18 October 2006 in Tucson, Arizona, USA. Edited by Richard A. Shaw, Frank Hill and David J. Bell., p.127, Vol. 376, 127

Muñoz, J. A., & Oh, S. P. 2016, MNRAS, 463, 2085

Narayanan, D., & Krumholz, M. R. 2014, MNRAS, 442, 1411

Offringa, A. R., & Smirnov, O. 2017, MNRAS, 471, 301

Offringa, A. R., McKinley, B., Hurley-Walker, N., et al. 2014, MNRAS, 444, 606

Olsen, K. P., Greve, T. R., Narayanan, D., et al. 2015, ApJ, 814, 76

Oteo, I., Ivison, R. J., Dunne, L., et al. 2016, ApJ, 827, 34

Pineda, J. L., Langer, W. D., Velusamy, T., & Goldsmith, P. F. 2013, A&A, 554, A103

Planck Collaboration, Ade, P. A. R., Aghanim, N., et al. 2016, A&A, 594, A13

Pound, M. W., & Wolfire, M. G. 2008, in Astronomical Society of the Pacific Conference Series, Vol. 394, Astronomical Data Analysis Software and Systems XVII, ed. R. W. Argyle, P. S. Bunclark, & J. R. Lewis, 654

Riechers, D. A., Hodge, J., Walter, F., Carilli, C. L., & Bertoldi, F. 2011, ApJ, 739, L31

Rybak, M., McKean, J. P., Vegetti, S., Andreani, P., & White, S. D. M. 2015a, MNRAS, 451, L40

Rybak, M., Vegetti, S., McKean, J. P., Andreani, P., & White, S. D. M. 2015b, MNRAS, 453, L26

Sandell, G., Mookerjea, B., Güsten, R., et al. 2015, A&A, 578, A41

Serjeant, S. 2012, MNRAS, 424, 2429

Smit, R., Bouwens, R. J., Carniani, S., et al. 2018, Nature, 553, 178

Smith, J. D. T., Croxall, K., Draine, B., et al. 2017, ApJ, 834, 5

Spilker, J. S., Aravena, M., Marrone, D. P., et al. 2015, ApJ, 811, 124

Stacey, G. J., Geis, N., Genzel, R., et al. 1991, ApJ, 373, 423

Stacey, G. J., Hailey-Dunsheath, S., Ferkinhoff, C., et al. 2010, ApJ, 724, 957

Stefan, I. I., Carilli, C. L., Wagg, J., et al. 2015, MNRAS, 451, 1713

Swinbank, A. M., Papadopoulos, P. P., Cox, P., et al. 2011, ApJ, 742, 11

Swinbank, A. M., Simpson, J. M., Smail, I., et al. 2014, MNRAS, 438, 1267

Tacconi, L. J., Genzel, R., Saintonge, A., et al. 2018, ApJ, 853, 179

Taylor, G. B., Carilli, C. L., & Perley, R. A., eds. 1999, Astronomical Society of the Pacific Conference Series, Vol. 180, Synthesis Imaging in Radio Astronomy II

Tielens, A. G. G. M., & Hollenbach, D. 1985, ApJ, 291, 722

Vallini, L., Gallerani, S., Ferrara, A., Pallottini, A., & Yue, B. 2015, ApJ, 813, 36

Valtchanov, I., Virdee, J., Ivison, R. J., et al. 2011, MNRAS, 415, 3473

Walter, F., Carilli, C., Bertoldi, F., et al. 2004, ApJ, 615, L17

Walter, F., Riechers, D., Cox, P., et al. 2009, Nature, 457, 699

Wang, S. X., Brandt, W. N., Luo, B., et al. 2013, ApJ, 778, doi:10.1088/0004-637X/778/2/179

Wardlow, J. L., Cooray, A., Osage, W., et al. 2017, ApJ, 837, doi:10.3847/1538-4357/837/1/12

Wardlow, J. L., Simpson, J. M., Smail, I., et al. 2018, MNRAS, 479, 3879

Weiß, A., Kovács, A., Coppin, K., et al. 2009, ApJ, 707, 1201

Wolfire, M. G., McKee, C. F., Hollenbach, D., & Tielens, A. G. G. M. 2003, ApJ, 587, 278

Wolfire, M. G., Tielens, A. G. G. M., & Hollenbach, D. 1990, ApJ, 358, 116

Wright, E. L. 2006, PASP, 118, 1711

Zanella, A., Daddi, E., Magdis, G., et al. 2018, MNRAS, 481, 1976

Zhang, Z.-Y., Romano, D., Ivison, R. J., Papadopoulos, P. P., & Matteucci, F. 2018a, Nature, 558, 260

Zhang, Z.-Y., Ivison, R. J., George, R. D., et al. 2018b, MNRAS, 481, 59

5.A Companion sources in LESS 49 field

Hodge et al. (2013) identified a nearby counterpart to ALESS 49.1 - ALESS 49.2. Detected at 4-σ confidence level in 870 μm continuum, it is included in the "main" sample of ALMA counterparts of ALESS sources. With a reported position of J2000 03:31:24.47 -27° 50' 38.1", ALESS 49.2 is located within the primary beam of our ALMA Band 8 observations. Hodge et al. (2013) observed ALESS 49.2 to have a 870 μm continuum flux a factor of 3.3 lower than that of ALESS 49.1. ALESS 49.2 is undetected in Wardlow et al. (2018) ALMA Band 4 observations which cover the CO (3–2) line in ALESS 49.1, suggesting ALESS 49.2 is at a different redshift than ALESS 49.1.

We do not find any significant emission ($> 2\sigma_{rms}$) within a 1-arcsec radius of the position reported by Hodge et al. (2013). Therefore, we impose a 0.33 mJy upper limit on the ALESS 49.2 observed 620-μm continuum flux-density (at 3-σ level).

In addition to ALESS 49.2, Wardlow et al. (2018) identified several additional sources in the vicinity of ALESS 49.1. In particular, the ALESS 49.L source from Wardlow et al. (2018) is located at the same redshift as ALESS 49.1, based on a CO line detection. However, we do not detect any emission at ≥4 significance in either Band 8 continuum or [C 2] emission at the position of any of the Wardlow et al. (2018) sources.

Nederlandse Samenvatting

Het zichtbare universum

U leest deze zinnen op een plek op aarde, één van de acht planeten die om de dichtstbijzijnde ster draaien: de zon. De zon is op haar beurt slechts een onderdeel van een groter geheel bestaande uit honderden miljarden sterren[5] bijeengehouden door de zwaartekracht. Dit geheel wordt gedefinieerd als een sterrenstelsel en de onze wordt de Melkweg genoemd. Naast de Melkweg zijn er triljoenen sterrenstelsels [6] met een grote diversiteit in grootte, vorm en massa, die de bouwstenen vormen van ons zichtbare universum.

Het onderzoeken van het zichtbare universum is een streven inherent aan het mens zijn. Sinds oudsher hebben menselijke beschavingen, van de Babyloniërs tot de Inca's, hun vaardigheden en verbeelding gebruikt om de hemel te observeren en te beschrijven. De wetenschappelijke studie van het zichtbare heelal is echter pas begonnen na het uitvinden/bouwen van de telescoop door Galileo Galilei. De telescoop maakte een ongekende ontwikkeling door die hand in hand ging met de algemene technische vooruitgang, Dit leidde uiteindelijk tot de ontwikkeling van geweldige machines voor het verkennen van het heelal. Deze machines zorgen er niet alleen voor dat ons zicht nu tot onvoorstelbare afstanden reikt, maar breiden ook het zichtbare spectrum uit waardoor we het universum kunnen zien en begrijpen met kleuren die voor mensen niet zichtbaar zijn.

Licht is de belangrijkste bron van informatie voor het bestuderen van het universum. De constante lichtsnelheid, $c \sim 3 \times 10^8$ m/s, is van grote waarde, omdat dit het mogelijk maakt om terug in de tijd te kijken. Licht geproduceerd in het begin van het universum, bereikt ons nu pas doordat het een constante snelheid heeft. Hierdoor geeft licht ons de mogelijkheid om de gebeurtenissen in het nog jonge universum waar te nemen. De constante snelheid definieert ook de limieten van het waarneembare heelal gezien vanuit onze positie. Licht dat naar ons toe beweegt, wordt door het uitdijen van het heelal ook uitgerekt zodat het een langere golflengte krijgt. Dit fenomeen heet roodverschuiving. Het versnelde uitdijen van het heelal zorgt ervoor dat licht uitgezonden in het jongere universum altijd een hogere roodverschuiving heeft. Roodverschuiving kan dus als een maat voor tijd worden gebruikt, zodat waarnemen met telescopen kan worden beschouwd als tijdreizen. Wanneer we de roodverschuiving van het licht weten, kunnen we ook onze tijdsbestemming bepalen.

De kleur van licht is karakteristiek; het bevat cruciale informatie over de roodverschuiving of de fysieke oorsprong van de straling. De verschillende kleuren zijn afkomstig uit het scala aan golflengten die behoren tot het elektromagnetische spectrum waaruit licht wordt opgemaakt. Het menselijk oog kan slechts een klein deel van het spectrum waarnemen: de optische golflengten. Een groot deel van de informatie over de fysische oorsprong van de emissie ligt verborgen in de onzichtbaar gewaande golflengten. Laag energetische processen produceren meestal emissie van radio, microgolf en infrarode golven. Hoog energetische processen produceren daarentegen ultraviolette- (UV), Röntgen- en Gammastraling. In deze scriptie hebben we gebruik gemaakt van verschillende telescopen om aan de hand van de emissie van sterrenstelsels over het gehele elektromagnetische spectrum het vroege universum in al zijn verschillende kleuren te beschrijven. We hebben de bestaande grenzen in het onderzoek naar sterrenstelsels met behulp van verschillende golflengten hiermee verlegd. We

[5] GAIA DR2 (Gaia Collaboration et al. 2018)
[6] Conselice et al. (2016)

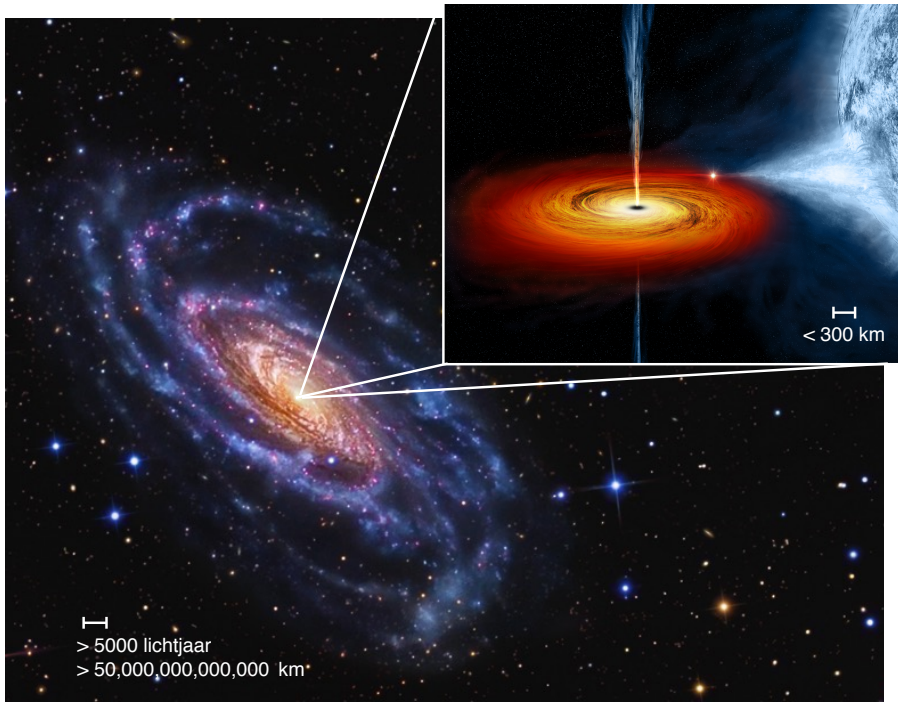

Figure S.10: Vergelijking op schaal van een accreterend zwart gat en het bijbehorende sterrenstelsel. Het grotere figuur is een foto van de optische emissie van het nabije sterrenstelsel NGC 5033 dat twee superzware zwarte gaten bevat in zijn kern. NGC 5033 is populair onder amateur astronomen omdat het door zijn karakteristieke grootte en helderheid gemakkelijk te observeren en af te beelden is. De ingezoomde figuur laat een artist impression zien van het eerste object waarvan algemeen aanvaard werd dat het een zwart gat was (Cygnus X-1). (Credit voor NGC 5033: R. Jay GaBany, Cosmotography, en credit voor de representatie van een zwart gat: NASA/CXC/M.Weiss.)

.

hebben ook laten zien hoe dit ons een meer compleet fysisch begrip heeft gegeven van het extreme en verre universum.

De kleuren van sterrenstelsels en zwarte gaten

De fysica van sterrenstelsels is een van de meest bijzondere voorbeelden van fenomenen met een groot golflengtebereik in het universum, aangezien sterrenstelsels helder en karakteristiek licht produceren over alle golflengten. Dit spectrum kan nog verder worden uitgebreid zoals recentelijk is ontdekt in de fysica van compacte objecten, zoals zwarte gaten. Deze objecten produceren niet alleen elektromagnetische golven maar ook gravitatiegolven en leidden het begin in van het multi-messenger tijdperk in de astronomie.

Sterrenstelsels worden in door gravitatie gebonden donkere materie halo's gevormd. Deze materie wordt nog steeds slecht begrepen maar bekend is dat het geen andere interactie kent dan de zwaartekracht. Donkere materie is namelijk, zoals de naam al suggereert, onzichtbaar en produceert geen elektromagnetische golven. De emissie van sterrenstelsels over een groot golflengtebereik is zodanig afkomstig van de baryonische (atomen van elke aard) com-

ponent. De baryonische component van sterrenstelsels is doorgaans verdeeld over de bulge en de schijf structuur en bestaat voornamelijk uit het interstellair medium en sterren. Het interstellair medium bestaat uit een grote hoeveelheid atomisch en moleculair gas en stof en wordt gedomineerd door waterstofatomen. Het produceert emissie met radio, submillimeter en infrarode golflengten. Het geïoniseerde deel van het interstellair medium produceert ook emissie met optische en UV golflengten. Van de moleculaire fase van het interstellair medium wordt aangenomen dat het de grondstof is voor de groei van sterrenstelsels, aangezien dit gas het formatieproces van sterren voedt. De verschillende populaties sterren in sterrenstelsels vormen de meest veelvoorkomende bron van optisch en UV licht in het universum. Dit zien we ook wanneer we op een heldere nacht naar de hemel kijken.

Een van de grootste ontdekkingen in de extragalactische astrofysica is dat de meeste (zo niet alle) sterrenstelsels een zwaar zwart gat in hun centrum hebben. Ook onze eigen Melkweg heeft een dergelijk zwart gat in diens centrum: Sagittarius A*. Dit zwarte gat is 4 miljoen keer zo zwaar als onze zon. Zwarte gaten zijn zware compacte objecten die zo'n extreem grote potentiaalput hebben dat materie of licht dat zich binnen de waarnemingshorizon bevindt niet kan ontsnappen. Vlak voordat materie deze horizon overschrijdt, vormt het onder de invloed van de zwaartekracht een schijf met daarin alle materie dat uiteindelijk in het zwarte gat valt. Figuur 4.1 toont een vergelijking op schaal van een sterrenstelsel en het zwarte gat dat zich in het centrum bevindt. De immense kinetische energie van de invallende schijf kan de meest (voortdurend stralend) heldere en hoog energetische processen in het universum produceren. Sterrenstelsel met deze accretieschijven worden actieve sterrenstelsels genoemd (Engels: Active Galactic Nuclei, AGN). Deze actieve sterrenstelsels zijn op zichzelf een fenomeen met emissie over een groot golflengtebereik en produceren dus straling over het hele elektromagnetische spectrum. De hoog energetische emissie wordt geproduceerd door het invallen van materie in het zwarte gat, wat UV- en Röntgenstraling creëert. Geabsorbeerde en weer uitgezonden emissie en indirecte emissie ontstaan door interacties met bijv. stof of magnetische velden produceren daarnaast emissie van infrarode en radio golven.

Een nieuwe methode voor het karakteriseren van de emissie van sterrenstelsels en accreterende zwarte gaten over een groot bereik van golflengten.

Een van de meeste efficiënte methodes voor het bepalen van fysische eigenschappen van sterrenstelsels en zwarte gaten is het modelleren van de emissie van zulke objecten over een groot bereik van golflengten, de zogeheten Spectral Energy Distribution (SED, NL: Spectrale Energieverdeling). In Hoofdstuk 2 hebben we de software AGNfitter ontwikkeld om zulke SEDs van sterrenstelsels en AGN op consistente wijze te modelleren. AGNfitter maakt gebruik van Bayesische statistiek om te zien welk model de gemeten SED het beste beschrijft, vanaf het ultraviolet tot aan het submillimeter. Hierbij wordt gebruik gemaakt van semi-empirische en theoretische modellen van de verschillende fysische componenten. De door ons gepresenteerde methode is nieuw, aangezien we de kansdichtheidsverdelingen van de fundamentele fysische parameters van sterrenstelsels en AGN berekenen, zoals de totale massa van de sterren, de mate van stervorming en de totale lichtkracht van de AGN, welk op zijn beurt weer afhangt van de massa van het zwarte gat en de mate van verduistering door kosmisch stof. De foutmarges op deze parameters worden op een robuuste manier bepaald, door de manier waarop de volledige parameterruimte wordt doorlopen, daarbij gebruikmakend van de fotometrische waarnemingen gedaan bij meerdere golflengten en de bijbehorende meetonzekerheden. AGNfitter is een modulaire en open-source Python code, en heeft sterk bijgedragen

aan ten minste 20 verschillende onderzoeken in de afgelopen twee jaar, zowel binnen onze collaboratie als daarbuiten. In Hoofdstuk 2 hebben we bovendien deze methode getest en gevalideerd door middel van het generen van 2000 SEDs voor AGN - actief toen het heelal slechts een kwart van de huidige leeftijd had - welk zijn geselecteerd door middel van hun Röntgenstraling. Ons onderzoek heeft aangetoond dat het modelleren van de SED van AGN, lopende van de ver-infrarode (VIR) tot de ultraviolette golflengten, op robuuste wijze de fysische eigenschappen en parameters kan bepalen van zowel emissie afkomstig van het zwarte gat als van de sterren zelf, ondanks dat feit dat deze processen zich op schalen afspelen die met ~ 7 ordes van grootte verschillen.

Een nieuwe blik op de fysica van sterrenstelsels en zwarte gaten

De unieke combinatie van resolutie, zichtveld en gevoeligheid van de LOFAR telescoop (Low Frequency Array, NL: Lage Frequentie Ontvanger), maakt het mogelijk om grote vooruitgang te boeken in het gebruik van het lage-frequentie radiobereik voor het bestuderen van de groei en evolutie van sterrenstelsels in het vroege universum, zoals hun mate van stervorming. In Hoofdstuk 3 hebben we de eerste studie naar de evolutie van sterrenstelsels en AGN op lage radiofrequenties uitgevoerd. Hiermee hebben we de fysische eigenschappen van zowel stervormende sterrenstelsels als AGN bepaald. Beide soorten sterrenstelsels zijn geselecteerd op basis van hun emissie op radio-golflengten, tot op een roodverschuiving van $z \sim 2.5$, toen het universum slechts een vijfde van de huidige leeftijd had. We hebben hiervoor de diepste radiowaarnemingen op meerdere frequenties bijeengevoegd, en gebruik gemaakt van nauwkeurige extractie van radiobronnen en kalibratietechnieken op omvangrijke radioafbeeldingen, afkomstig van verschillende radiotelescopen, zoals LOFAR, de VLA, WRST en GMRT. Het onderzoek focuste op stervormende stelsels, waarbij de radiostraling voornamelijk afkomstig is van recent gevormde sterren. De radio emissie van het zwarte gat is dan in vergelijking hierbij te verwaarlozen. Met de geselecteerde stervormende stelsels hebben we op verscheiden frequenties een karakteristieke eigenschap van zulke stelsels onderzocht; de ver-infrarood(VIR)-radio correlatie. De resultaten van Hoofdstuk 3 onthulden dat de VIR-radio correlatie blijkt te evolueren als functie van kosmische tijd, wat in tegenstelling is tot wat is gesuggereerd door eerdere studies. Daarnaast hebben we radio emissie op lage frequenties (150 MHz) gerelateerd aan stervorming en accretie op het centrale zwarte gat door middel van het modelleren van de VIR-UV spectrale energieverdelingen. Hiermee hebben we de eerste calibratie van de 150 MHz radio-emissie opgesteld als maat voor de hoeveelheid stervorming die plaatsvindt.

Een nieuw perspectief op het interstellair medium door middel van hoge resolutie waarnemingen

Het interstellair medium van sterrenstelsels vormt de voedingsbron voor zowel de formatie van sterren als de groei van zwarte gaten, en is daardoor een belangrijk ingrediënt in de evolutie van sterrenstelsels. Met de komst van de grootste submillimetertelescoop op aarde, het Atacama Large (sub-)Millimeter Array (ALMA; de Atacama Grote (sub-)Millimeter Ontvanger), is het nu mogelijk om het interstellair medium in detail te karakteriseren. Om het interstellair medium van sterrenstelsels in het vroege universum te bestuderen, wordt voornamelijk gebruikgemaakt van de rotationele emissielijnen van het molecuul koolstofmonoxide (CO),

de fijnstructuur emissielijn [CII] of de continuümstraling van kosmisch stof (in het zogeheten Rayleigh-Jeans regime). Deze lijnen behoeven echter verschillende aannames over de fysische toestanden van het gas en stof in sterrenstelsels, betreffende de optische diepte, temperatuur en dichtheid van het gas alsmede de ratio tussen de hoeveelheid stof en gas. Slechts met zulke aannames kunnen de lijnen worden gebruikt voor het karakteriseren van het interstellair medium, zodat de fysische toestanden die hieruit worden afgeleid grote onzekerheden met zich meebrengen. In Hoofdstukken 4 en 5 hebben we de CO(3-2) en [CII] emissielijnen gekarakteriseerd met behulp van hoge-resolutie waarnemingen van ALMA, voor een verzameling sterrenstelsels geselecteerd op basis van hun submillimeter emissie (zogeheten submillimeter galaxies; SMGs), met als doel het ophelderen van deze onzekerheden. Door het modelleren van de dynamica hebben we de snelheidsvelden van deze stelsels bepaald, welke laten zien dat de CO-emissie van de SMGs consistent is met dat van een geordende, roterende schijf, ondanks de ogenschijnlijk verstoorde morfologie van de stelsels die is te zien in optische waarnemingen. Dit suggereert dat dat een schijf van moleculair gas zich snel kan hervormen na een botsing tussen twee sterrenstelsels. Met verder onderzoek naar de [CII]-emissie en het ver-infrarood continuüm in Hoofdstuk 5 hebben we aangetoond dat deze sterrenstelsels een sterk tekort vertonen in hun [CII]/VIR-ratio in vergelijking met resultaten afkomstig van eerdere studies. Door onze resultaten te vergelijken met modellen van foto-dissociatie regio's, laten we zien dat dit tekort waarschijnlijk wordt veroorzaakt door thermische saturatie van de [CII] energieniveaus, en door een sterke vermindering in de verwarming van het gas door het foto-elektrisch effect.

Een nieuw perspectief op de emissie van sterrenstelsels over een groot golflengtebereik door middel van hoge resolutie waarnemingen

Een zuivere karakterisering van de fysische toestand van sterrenstelsels behoeft waarnemingen op meerdere golflengten, en dit geldt evenzo voor studies die gebruikmaken van observaties met hoge resolutie. Slechts met een klein aantal telescopen is het echter mogelijk om resoluties te bereiken die scherper zijn dan een boogseconde, zodat het lastig is om de verschillende onderdelen van sterrenstelsels op hoge roodverschuiving te onderscheiden, aangezien deze worden vertroebeld door de eindige resolutie van een telescoop. In Hoofdstukken 4 en 5 hebben we ALMA waarnemingen gecombineerd met hoge-resolutie afbeeldingen van de Hubble Space Telescope (HST; de Hubble Ruimtetelescoop) om de emissie van sterren, het stof en de CO en [CII] emissielijnen te bestuderen in sterrenstelsels in het vroege universum, welke zijn geselecteerd op basis van hun submillimeter emissie. Na het corrigeren van de astrometrie met behulp van GAIA waarnemingen, heeft ons werk aangetoond dat de ruimtelijke distributie van het stof en moleculaire gas sterk gescheiden kan zijn van de regio's waarin de waargenomen straling voornamelijk wordt geproduceerd door sterren. Deze bevindingen trekken veelgebruikte aannames met betrekking tot een energiebalans tussen de emissie van sterren en stof in twijfel. Daarnaast benadrukken de bevindingen het vermogen van gecombineerde ALMA en HST waarnemingen om onze kennis van de fysica van sterrenstelsels op hoge roodverschuiving te vergroten. Ten slotte hebben we een statistische analyse uitgevoerd door het opeenstapelen (Engels: stacking) van de waargenomen afmetingen van de regionen van stof-continuümstraling, moleculair gas en emissie van sterren in onze SMGs. Dit werk heeft aangetoond dat het koude moleculaire gas en de stellaire emissie van onze sterrenstelsels verder reiken in ruimtelijke zin dan zowel het stof als de regio van [CII]-emissie, met meer dan een factor twee verschil. Om deze waarneming verder te begrijpen, en te onder-

zoeken of er een fysisch verschil is in de distributie van gas en stof, hebben we een model van stralingstransport toegepast op de gemiddelde radiële profielen van onze stelsels. Dit heeft aangetoond dat dit verschil in de waargenomen afmetingen van het gas en stof kan worden verklaard door sterke gradiënten in de temperatuur en optische diepte in onze sterrenstelsels.

English Summary

The observable Universe

You are probably reading these lines on some spot on Earth, one of the eight planets that orbit our closest star, the Sun. The Sun is, in turn, one element in a structure of a few hundreds of billions of stars[7] bound by gravity and defined as a galaxy, our galaxy, the Milky Way. Such as the Milky Way, trillions of galaxies[8] of different sizes, shapes, and masses, are the building blocks of our vast observable Universe.

The exploration of the observable Universe is an endeavour inherent to the human nature and thus from ancient times human civilizations, from the Babylonians to the Incas, have targeted their skills and imagination to observe and map the skies. However, the scientific study of the observable Universe has seen an unprecedented development only recently, after the telescope constructed by Galileo Galilei evolved, hand in hand with technology, into magnificent machines of exploration. These machines do not only deepen our view to look into inconceivable distances, but also broaden the observable spectrum, allowing us to see and understand the Universe through colours not even humanly perceivable.

Light is the main channel of information to learn about the Universe. The constant speed of light, at $c \sim 3 \times 10^8$ m/s, is of great value since it allows us to look back in time. Due to its constant velocity, light produced at early times of cosmic history would reach us only now, allowing us to witness these early events. This velocity also defines the limits of the Universe observable to our position in space-time. Additionally, light travelling towards us is 'stretched' to longer wavelengths by the expansion of the Universe, in a phenomenon call redshift. The accelerated expansion of the Universe produces a redshift that is always higher at earlier epochs, serving as a tag for the time when an event has occurred. Observing with telescopes is thus sort of travelling in time, and when the redshift of the detected light is available, we can also know the epoch we are travelling back to.

Crucial information – such as the redshift or the physical origin of the emission – is encoded in the characteristic 'colours'. These colours arise from the different wavelengths of the electromagnetic spectrum that composes light. While the human eye can perceive solely a small part of the spectrum (optical wavelengths), vast information on the physics producing the emission is contained across 'invisible' wavelengths. Lower energy physics usually produce emission at radio, microwave, and infrared wavelengths, while higher energy events produce Ultra-Violet (UV), X-ray and Gamma-ray emission. In this thesis, we have made parallel use of telescopes detecting the emission of galaxies across the electromagnetic spectrum to portray the early Universe in its different colours. We have pushed some of the current frontiers of the multiwavelength study of galaxies and showed how it provides us with a more complete physical understanding of the extreme and distant Universe.

The colours of galaxies and black holes

The physics of galaxies and black holes is one of the most remarkable examples of multiwavelength phenomena in the Universe, since they produce bright and characteristic emission

[7] GAIA DR2 (Gaia Collaboration et al. 2018)
[8] Conselice et al. (2016)

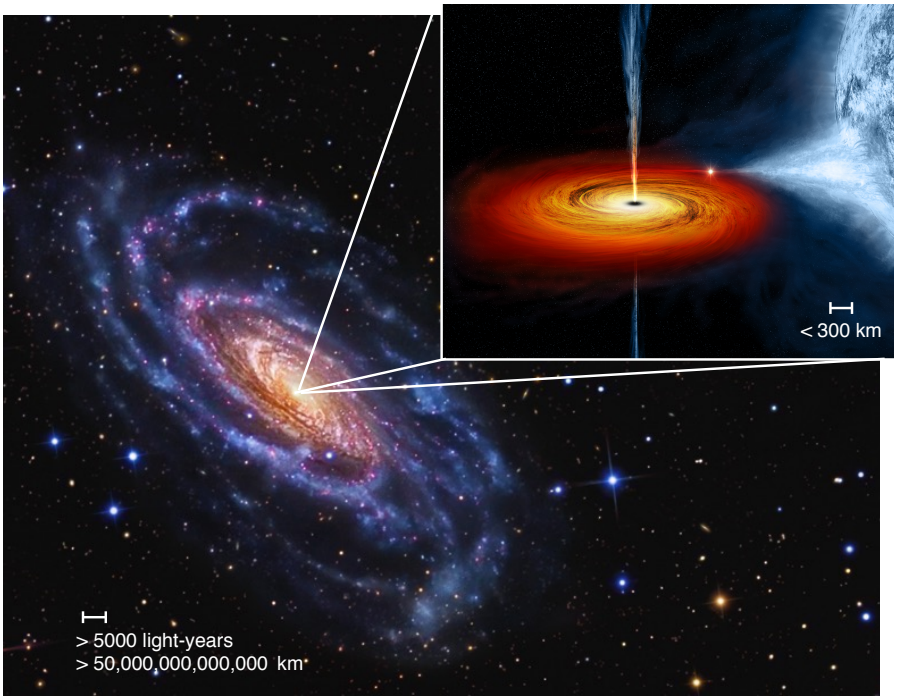

Figure S.11: Comparing the scales of a host galaxy and an accreting black hole. The *larger figure* is a photograph of the optical emission of the nearby galaxy NGC 5033, known to host two supermassive black holes in its center. NGC 5033 is a popular galaxy among amateur astronomers since its characteristic size and brigthness allows it to be easily seen and imaged. The *zoom-in figure* shows an artistic representation of the first source widely accepted to be a black hole (Cygnus X-1). (Credit for NGC 5033: R. Jay GaBany, Cosmotography, and credit for black hole representation: NASA/CXC/M.Weiss)

.

across all these wavelengths. The physics of compact objects such as black holes has been recently shown to go even further, and not only produce electromagnetic waves but also gravitational waves, opening the era of multi-messenger Astronomy.

Although galaxies are formed within gravitationally bound structures of a poorly-understood material called dark matter, this main galaxy component does not undergo any other interaction than gravity, and is as suggested by it's name, invisible, producing no electromagnetic wave signature. The multi-wavelength emission in galaxies arise instead from their different baryonic components (atoms of any sort). The baryonic components of galaxies are usually distributed within bulge and disk structures, composed mainly by an interstellar medium and stars. The interstellar medium is a large content of atomic and molecular gas and dust, largely dominated by Hydrogen atoms, and produces emission in the radio, sub-millimeter and infrared regime. The ionized fraction of the interstellar medium can also emit light of optical/UV wavelengths. The molecular phase of the interstellar medium is believed to be the main raw material for the growth of the galaxy, since this gas fuels the production of new stars. The populations of stars within galaxies are the most common sources of the visible optical/UV light in the Universe, as we can witness by looking up to the sky in a clear night.

Additionally, one of the main discoveries in extragalactic astrophysics has been that most (if not all) galaxies host massive black holes in their centres. Indeed, our own Milky Way hosts a black hole in its centre called Sagittarius A*, which has been measured to be 4 million times more massive than our Sun. Black holes are massive compact objects that exhibit such an extremely large gravitational potential, that no matter *or light* within a boundary, called the black hole's event horizon, can escape from it. However, just before matter crosses this horizon, the gravitational pull creates a disk of all matter that is accreted into the black hole. See Figure S.11 for a comparison of the scales of a galaxy and its accreting black hole. The immense kinetic energy of this accretion disk can produce the most (constantly-emitting) luminous and highly energetic events in the Universe, which are called active galactic nuclei (AGN). These galactic nuclei themselves are multi-wavelength phenomena producing emission across the electromagnetic spectrum: the very energetic emission produced in the accretion is exhibited in the UV and X-ray regimes, while the reprocessed and indirect emission originated in the interaction with e.g., dust or magnetic fields, is emitted in infrared and radio wavelengths.

A new method to characterize the multi-wavelength emission of galaxies and accreting black holes

One of the most efficient methods for extracting the physical properties of galaxies and black holes is modelling this multi-wavelength emission of galaxies, synthesized as their spectral energy distributions (SEDs). In Chapter 2, we have developed a software, AGNFITTER, to consistently model the multi-wavelength emission of galaxies and AGN. AGNFITTER applies Bayesian statistics to fit the observed SEDs, from the UV to the (sub)mm, with semi-empirical and theoretical models of the different physical components. The method we have presented is novel since it recovers the probability density functions of fundamental physical parameters of galaxies and AGN, robustly handling uncertainties and in-homogeneous sampling of the multi-wavelength photometric observations. These parameters include the total masses of the stellar populations, the star formation rates, the total AGN luminosities that correlate with the masses of the black hole and obscuration by dust.. AGNFITTER is a modular and open-source code written in the Python language, and has made compelling contributions to at least 20 different research projects in the last two years, both within and outside our collaboration circles. In Chapter 2, we have also tested and validated this approach by constructing the

multi-wavelength SEDs of a sample of ∼ 2000 AGNs, active when the Universe was around one quarter of its current age, selected by their X-ray emission. Our work revealed that modelling the FIR-to-UV SED of AGN can robustly recover the parameters ruling both galaxy and nuclear (AGN) emission, despite the ∼7 orders of magnitude difference in scale.

A new window on the physics of galaxies and black holes

Thanks to the unique combination of the field-of-view, resolution and sensitivity of the LOFAR (Low Frequency ARray) telescope, in the LOFAR-Surveys collaboration we have been taking an important step forward in using the radio regime at low-frequency to trace the growth-properties of galaxies, such as star formation, in the Early Universe. In Chapter 2, we have conducted the first study of the evolution of galaxies and AGN as seen at low radio frequencies. We have characterized the physical properties of star-forming galaxies and AGN selected by their radio emission, back to redshifts of $z \sim 2.5$, when the Universe was one fifth of its current age. We have built the deepest sample of multi-frequency radio spectra, by applying careful source extraction and flux calibration techniques to large radio maps observed by several different radio telescopes, including the LOFAR, VLA, WSRT and GMRT telescopes. Focussing on star forming galaxies with negligible black hole accretion, e.g., whose radio emission is dominated by the emission indirectly arising from new-born stars, we have investigated a characteristic property, the far-infrared-radio correlation, at multiple radio frequencies. The results from Chapter 3 revealed that the FIR-radio correlation at both high and low frequencies is not constant, as suggested by previous literature, but evolves as a function of cosmic time. Most importantly, we have linked the radio emission at low-frequencies (150 MHz) to star formation and black hole accretion activity through the modelling of the FIR-UV SEDs and delivered the first calibration of the radio emission at 150 MHz as a diagnostic of star formation.

A new high-resolution perspective on the interstellar medium

The interstellar medium in galaxies feeds both the formation of stars and the growth of black holes, making it a key ingredient in the evolution of galaxies. With the advent of the largest sub-millimeter telescope on Earth, the Atacama Large (sub)Millimeter Array (ALMA), we can now probe the interstellar medium in increasingly exquisite detail. Studies of the interstellar medium in the early Universe are most commonly conducted by observing the emission of the rotational transitions of the carbon monoxide molecule (CO), the fine-structure [CII] line, or the emission of the dust continuum (the Rayleigh-Jeans tail). The use of these tracers as a probe of the interstellar medium, however, involve several assumptions on the physical conditions of the gas and dust, such as optical depth, temperature and density of gas and dust-to-gas ratios. These assumptions could introduce large uncertainties to conclusions on the properties of the interstellar medium. In Chapters 4 and 5, we have used the ALMA telescope to make progress settling this issue by characterizing the CO(3-2) molecular emission, and the [CII] emission at high resolution, in a sample of galaxies selected by their sub-millimeter emission (sub-millimeter galaxies, SMGs). We have applied kinematic and dynamical modelling on the data to characterize the velocity fields of these sources, finding that the CO emission in our SMGs are consistent with ordered rotating disk, despite having apparent disrupted optical morphologies. This observation may suggest that molecular gas disks can quickly reform after a merger event. Our parallel study of the [CII] and far-infrared (FIR) dust continuum emission in Chapter 5 showed that galaxies exhibit a strong deficit in the [CII]/FIR ratio compared

to the values expected in the literature. Comparing our observations with models of photo-dissociation regions show that this deficit is probably originated in the a thermal saturation of [CII] levels, and a significantly reduced heating of the gas via the photoelectric effect.

A new high-resolution perspective on the multi-wavelength emission of galaxies

An unbiased characterization of the physics of a galaxy requires multiwavelength studies, and this applies as well to high-resolution studies. However, since only a few telescopes provide sub-arcsecond resolution, multi-wavelength resolved studies of galaxies in the early Universe are challenging. In Chapters 4 and 5, we combined our ALMA observation with high-resolution images from the *Hubble Space Telescope* to study the stellar, dust continuum, CO and [CII] gas emission in submillimeter-selected galaxies in the early Universe. After applying robust astrometry corrections based on *GAIA* observations, our work has revealed that the resolved spatial distributions of the dust and molecular gas emission can be *entirely offset* to the stellar emission within these galaxies. This finding challenges common assumptions on energy balance between stellar and cold dust emission, highlighting the potential of combined *HST* and ALMA observations to push forward our understanding of galaxy physics at high redshift. Finally, we have conducted a statistical analysis through stacking of the observed sizes of the dust continuum, molecular gas and stellar emission in our sample of submillimeter galaxies. Our work has revealed that both the cool molecular gas emission and the stellar emission in these sources is clearly more extended than both, the dust continuum, and the [CII] main emission component *by a factor* > 2. To further understand this observation – whether there is a physical difference in the distribution of gas and dust – we have applied a radiative transfer model on the observed average radial profiles of our galaxies. Our work has revealed that this apparent size difference of gas and dust can be produced by large temperature and optical-depth gradients alone.

Resumen en español

El Universo observable

Usted está leyendo estas lineas desde algún rincón de la Tierra, uno de los ocho planetas que orbitan nuestra estrella más cercana, el Sol. El Sol es, a su vez, solo un elemento dentro de una estructura compuesta de cientos de billones de estrellas que, unidas por la gravedad, definen a una galaxia, nuestra galaxia, la Via Láctea. Como la Vía Láctea, trillones de galaxias, de diferentes formas, tamaños, y masas, forman las piezas que constituyen nuestro vasto Universo observable.

La exploración del Universo observable es una actividad inherente a la naturaleza humana, y por ello desde tiempos ancestrales, civilizaciones humanas, desde los babiloneos a los Incas, han enfocado su destreza e imaginación en observar y mapear los cielos. Sin embargo, el estudio científico del Universo observable se ha desarrollado de manera sin precedente a consecuencia de que el telescopio construido por Galileo Galilei evolucionó, mano a mano con la tecnología, en magníficos instrumentos de exploración. Estos instrumentos no sÍo nos permiten una visión más profunda del Universo lejano, sino también amplía nuestro espectro observado, permitiéndonos ver y entender el Universo por medio de colores biológicamente invisibles para el ser humano.

La luz que viaja desde el espacio hacia nosotros, los observadores, es la fuente principal de información que tenemos sobre la física del Universo. La velocidad constante de la luz a $\sim 3\times10^8$ m/s, es de gran valor para la astronomía, pues nos permite mirar hacia el pasado. La luz producida en posiciones lejanas del espacio-tiempo, por ejemplo cerca al origen del Universo, tarda en llegar hasta el observador a causa de esta velocidad limitada, permitiéndonos presenciar eventos pasados al observar el espacio más profundo. Esta velocidad es también la que define los límites del Universo observable desde nuestra posición en el espacio-tiempo. Adicionalmente, las ondas de luz que viajan hacia nosotros son además 'expandidas' a longitudes de onda más largas a consecuencia de la expansión del Universo. Este efecto sobre las ondas de luz es denominado 'corrimiento al rojo'. Como la expansión del Universo es además acelerada, esto produce un corrimiento al rojo que es siempre mayor en épocas más remotas, sirviendo de este modo como una etiqueta que marca la época en la cual este evento ha ocurrido. Observar con un telescopio es, por consiguiente, similar a viajar con una máquina del tiempo. Y cuando conocemos el corrimiento al rojo de la luz detectada, podemos además saber la época exacta hacia la que estamos regresando. Este fenómeno es de gran utilidad para la astronomía extragaláctica, ya que permite el estudio de la historia cósmica y la formación y evolución de las galaxias, desde los inicios del Universo hasta el tiempo presente.

Mucha información importante – tal como el corrimiento al rojo o el orígen físico de la emisión observada – se encuentra codificada dentro de los colores característicos de la luz. Estos colores se originan en las diferentes longitudes de onda del espectro electromagnético que compone la luz. Mientras que el ojo humano puede percivir solamente una parte del espectro – la longitud de onda óptica –, longitudes de onda 'invisibles' no solo contienen una gran cantidad de información sobre la física que origina la emisión, sino son fundamentales para tener una visión completa de ésta. Fenómenos físicos de poca energía producen emisión en longitudes de onda radio, microondas e infrarojas, mientras aquellos de alta energía emiten luz ultra-violeta, rayos-x y rayos-gama. En esta tesis, hemos hecho uso paralelo de diferentes telescopios que detectan la emisión de galaxias a través de todo el espectro electromagnético, para de esta forma retratar el Universo temprano en sus diferentes colores. En esta tesis

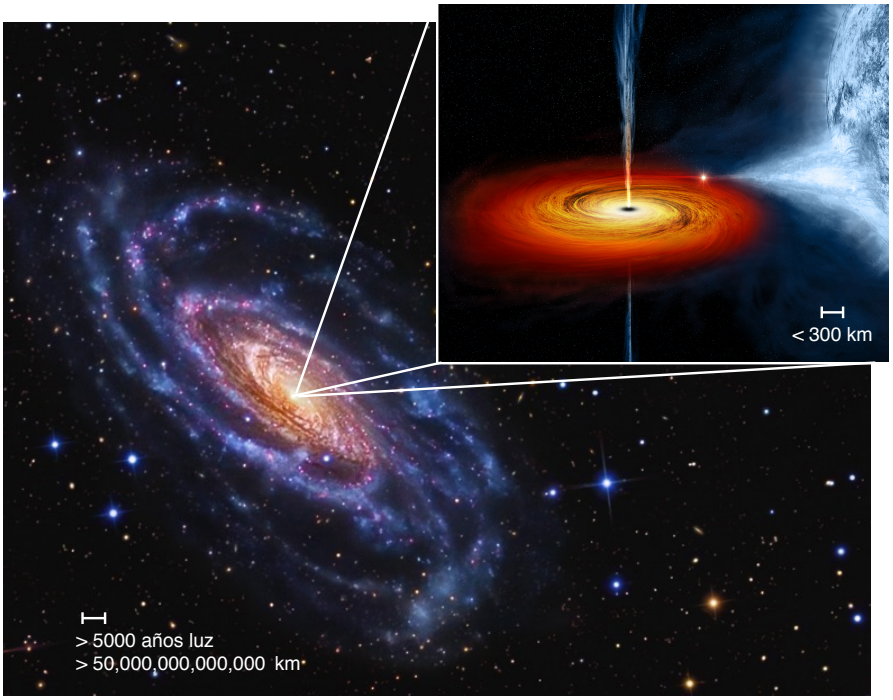

Figure S.12: La escala correspondiente a una galaxia en comparación a la escala del *horizonte de sucesos* de un agujero negro. La *figura principal* es la fotografía de la emisión optical de la galaxia cercana NGC 5033, conocida por albergar dos agujeros negros masivos en su centro. NGC 5033 es una galaxia popular entre astrónomos aficionados pues su tamaño característico y luminosidad permite que sea observada y fotografeada fácilmente. La *figura amplificada* presenta una representación artística de la primera fuente que fue aceptada como un agujero negro (Cygnus X-1). (Crédito por la imagen de NGC 5033: R. Jay GaBany, Cosmotography, y crédito por la representación del agujero negro: NASA/CXC/M.Weiss)

.

hemos ampliado los límites de la astronomía multi-onda extragaláctica y hemos demostrado cómo estos métodos nos proveen de un entendimiento más completo del Universo distante y extremo.

Los colores de las galaxias y agujeros negros

La física de las galaxias y los agujeros negros es uno de los ejemplos más notables de fenómenos multi-onda en el Universo, pues estos objetos producen una emisión luminosa y característica a través de todo el espectro electromagnético. En efecto, la física de objetos compactos, tal como los agujeros negros, ha demonstrado recientemente que van incluso más alla, no solo produciendo ondas electromagnéticas sino también ondas gravitacionales, inaugurando de esta forma la era de la astronomía multi-mensajera.

Aunque las galaxias se forman dentro de halos de materia oscura (un material enigmático) sostenido por la gravedad, este componente no se somete a ninguna otra interacción física más que la gravedad, y por esta razón, tal cómo sugiere su nombre, no produce ninguna señal electromagnética. La emisión multi-onda en las galaxias se origina en sus diferentes componentes bariónicos (átomos de diferentes tipos). Los componentes bariónicos de las galaxias están

usualmente distribuidos en estructuras en forma de bultos y discos, compuestas principalmente de un medio interestelar y de estrellas. El medio interestelar es un conglomerado de gas atómico y molecular, y de partículas de polvo, que producen emisión radio, sub-milimétrica e infraroja. La fracción de gas del medio interestelar que está ionizada puede producir también emisión óptica o ultra-violeta. Se cree que la fase molecular del medio interestelar es la materia prima principal para el crecimiento y desarrollo de las galaxias, pues este gas alimenta la producción de nuevas estrellas. Finalmente, las poblaciones de estrellas en las galaxias, además de ser los hornos en los que se forman los elementos complejos que forman entre otras estructuras, la vida, son la fuente más común de luz óptica y ultravioleta en el Universo, como podemos apreciar observando a simple vista el cielo en una noche clara.

Uno de los descubrimientos principales en la astrofísica extragaláctica ha sido que la mayor parte de las galaxias (si no todas) hospedan agujeros negros masivos en sus núcleos. En efecto, nuestra propio Vía Láctea hospeda un agujero negro en su centro, llamado Sagitario A*, el cuál es 4 millones de veces más masivo que el Sol, según cálculos basados en el efecto gravitacional que este causa sobre objetos a su alredor. Los agujeros negros son objetos compactos extremadamente masivos, que exhiben un potencial gravitacional tan elevado, que ninguna materia o luz que traspase *el horizonte de sucesos* del agujero negro, puede escapar de este, haciéndolo por lo tanto invisible. Nótese la escala correspondiente a una galaxia en comparación a la escála del horizonte de eventos de un agujero negro en la Figura S.12. Sin embargo, cuando este agujero negro es activo y absorve grandes cantidades de materia, justo antes de que la materia atraviese este horizonte la gravedad crea un disco de acreción de esta materia.La immensa energía cinética de este disco de acreción puede producir el evento más luminoso y energético de emisión constante en el universo, llamado núcleo galáctico activo (en comparación con la supernova, que es el evento más luminoso pero de corta duración). Estos núcleos galácticos son por sí mismos fenómenos multi-onda y producen emisión a través de todo el espectro electromagnético. La emisión originada directamente en la acreción, y por lo tanto más energética, se exhibe como emisión ultravioleta y rayos-x, mientras que la emisión secundaria, es emitida en longitudes de onda infrarojas y ondas de radio.

Un nuevo método para caracterizar la emición multi-onda de galaxias y agujeros negros

Uno de los métodos más eficientes para extraer información sobre las propiedades físicas de las galaxias y agujeros negros es mediante el modelado de la emisión multionda, sintetizada como su distribución de energía espectrall (SEDs, por las siglas en inglés, spectral energy distributions). En el capítulo 2 de esta tesis, hemos desarrollado un software llamado AGNFITTER, para modelar consistentemente la emisión multi-onda de galaxias y agujeros negros. AGNFITTER aplica estadística Bayesiana para ajustar los SEDs observados, construidos con observaciones desde ultravioletas hasta el submilimétrico, usando modelos teóricos y semi-empíricos de diferentes componentes físicos. El método que presentamos es innovativo pues recupera la funciones de densidad de probabilidad de parámetros físicos fundamentales de galaxias y AGN, tal como las masas totales de las poblaciones de estrellas, las tazas de formación estelar, las luminosidades totales del los núcleos galácticos activos, correlacionados con las masas de los agujeron negros y obscuración por polvo, tratando de manera confiable los márgenes de error y la distribución inhomegénea de las observaciones multi-onda. AGNFITTER es un algoritmo escrito en el lenguaje Python, es modular y público, y en los dos últimos años ha brindado importantes aportes a al menos 25 proyectos diferentes de grupos de investigación de galaxias y AGN alrededor del mundo. En el capítulo 2 hemos también

evaluado y validado este método contruyendo los SED multi-onda de un conjunto de ∼ 2000 núcleos galácticos activos, seleccionados por su emisión en rayos-x, cuya emisión se origina en la época en la que el Universo tenía un quinto de su edad actual, es decir 3 giga-años después del Big Bang. Nuestra investigación revela que el modelado de las distribuciones de energía espectral, usando observaciones desde el infrarrojo lejano al ultravioleta de estos objetos, puede recuperar paralelamente los parámetros que gobiernan la emisión de galaxias y AGN, a pesar de la gran diferencia en las escalas que estos representan (al rededor de 10 ordenes de magnitud, Figura S.11).

Una nueva ventana hacia la física de las galaxias y agujeros negros

Gracias a la combinación única del campo de visión, resolución y sensibilidad del telescopio radio LOFAR (Low Frequency ARray), en la colaboración LOFAR Surveys estamos dando un paso importante hacia el uso de la emisión de radio de baja frecuencia para decifrar la propiedades del crecimiento de galaxias, tal como la taza de formación estelar en el Universo temprano. En el Capitulo 3 hemos conducido el primer estudio de la evolución de galaxias y AGN desde la perpectiva radio de baja frecuencia. Hemos caracterizado las propiedades físicas de galaxias de alta formación estelar y de AGNs seleccionados por su emisión radio, que habitan épocas de Universo equivalentes a corrimientos al rojo de 2.5, aproximadamente cuando el Universo tenía un quinto de la edad actual. Hemos construido la librería más profunda de espectros de radio, aplicando una técnica cuidadosa de extracción de fuentes, y técnicas de calibración de flujo para observaciones de diversos telescopios radio, incluyendo LOFAR (Países Bajos), VLA (USA), WSRT (Países Bajos) and GMRT (India). Enfocándonos en galaxias de alta formación estelar y con contribución negligible de acreción de agujeros negros, es decir cuya emisión radio está dominada por la emision de estrellas jóvenes masivas, hemos investigado una propiedad característica de estas galaxias, la correlación entre el infrarrojo y el radio continuo. Los resultados presentados en el capítulo 3 revelaron que la correlación infrarrojo-radio, tanto a alta como a baja frecuencia radio, no es constante, como lo sugiere la literatura, sino evoluciona en función del tiempo cósmico. Más importante, hemos encontrado una conexión entre la emisión de radio a baja frecuencia (150 MHz) de las galaxias y su formación estelar y hemos proporcionado la primera calibración de la emisión de radio a 150 MHz como diagnóstico de formación estelar.

Una nueva perspectiva a alta resolución del medio interestelar

El medio interestelar de galaxias alimenta tanto a la formación de estrellas como al crecimiento de agujeros negros en sus núcleos, y es por lo tanto un ingrediente fundamental en la formación y evolución de las galaxias en el Universo. Con la introducción del telescopio submilimétrico más grande del mundo, el Ataca Large (sub/)Millimeter Array (ALMA, Chile), podemos ahora investigar el medio interestelar en el Universo lejano en exquisito detalle. Comunmente, estudios del medio interestelar en el Universo temprano son conducidos observando las lineas de emisión de algunas de las partículas que lo componen. En particular, se observan la emisión de las transiciones rotacionales de la molécula de monóxido de carbono (CO). la linea de estructura fina [CII] , y la emisión del continuo emitido por las partículas de polvo. Sin embargo, el uso de estas lineas implica someterse a supocisiones sobre las condi-

ciones físicas del gas y el polvo, tales como la profundidad óptica, la temperatura y la densidad del gas, y la razón entre las cantidades de gas y polvo. Estas suposiciones pueden introducir grandes incertidumbres y llevarnos a conclusiones erroneas sobre las propiedades del medio interestelar. En los capítulos 4 y 5, hemos usado el telescopio ALMA para acercarnos a la solución de este problema, caracterizando la emisión de la tercera transición del monóxido de carbono CO(3-2), y la emission de [CII] a alta resolución para un grupo de galaxias a alto corrimiento al rojo, seleccionadas por su emisión en el submilimetrico. Estas galaxias se denominan SMGs por sus siglas en inglés (submillimeter galaxies). Para caracterizar los campos de velocidad que modelan esta galaxia, hemos ajustado modelos cinemáticos y dinámicos a los datos. Encontramos que la emisión de CO en nuestras galaxias SMGs son consistentes con un disco de rotación ordenado, a pesar de presentar una morfología perturbada en las imágenes ópticas, que por el contrario sugerirían que la galaxia acaba de coaliscionar o fusionarse con otra galaxia. Esta observación sugiere que los discos de gas molecular se pueden reformar rápidamente despues de un evento de fusión galactica. Finalmente, nuestro estudio paralelo de [CII] y el infrarrojo lejano (emisión continua del polvo) en el capítulo 5 demostró que las galaxias SMG que estudiamos presentan un gran déficit en la razón entre las emisiones de [CII] y el infrarrojo, en comparación con los valores que se espera en base a predicciones teóricas. Comparaciones entre nuestras observaciones con modelos de regiones fotolíticas [9] demuestran que este déficit es originado probablemente por la saturación térmica de niveles de [CII], y/o por una reducción significativa del calentamiento del gas por medio del efecto fotoeléctrico.

Una nueva perspectiva en alta resolución de la emisión multi-onda de galaxias

Una caracterización objetiva de la física de galaxias requiere estudios multi-onda, y esto se aplica también a estudios a alta resolución. Sin embargo, considerando que solo pocos telecopios pueden observar en las altas resoluciones requeridas para estudios del Universo lejano (correspondientes a elementos de resolución menores a un arcosegundo), el estudio a alta resolución del Universo temprano es muy difícil. En los capítulos 4 y 5, hemos combinado nuestras observaciones con el telescopio ALMA con observaciones a alta resolución del telescopio espacial *Hubble* para estudiar la emisión de las poblaciones de estrellas, de la distribuciones de polvo, del gas molecular de monóxido de carbono, y finalmente de la linea de estructura fina de carbono [CII]. Estas observaciones se han enfocado en las galaxias SMG que habitan el Universo temprano presentadas previamente. Luego de aplicar correciones astrométricas fidedignas basadas en observaciones con el telescopio espacial *GAIA* (especializado en mediciones precisas de distancias), nuestro trabajo reveló que las distribuciones de la emisión de polvo y gas molecular pueden estar completamente desalineadas de la emisión de las estrellas en estas galaxias. Esta observación pone a prueba suposiciones usadas comúnmente sobre el balance energético entre la emisión estelar y de polvo. Esta observación, a su vez, subraya el gran potencial del uso en paralelo de los telescopios *Hubble* y ALMA para ampliar nuestro conocimiento sobre la física de las galaxias a alto corrimiento al rojo. Finalmente, hemos conducido un análisis estadístico basado enla técnica de 'stacking'.[10] Hemos combinado las observaciones de diferentes galaxias par obtener los tamaños promedio de la emisión de polvo, gas molecular y estrellas. Nuestro trabajo revela que tanto la emisión de gas molecular como

[9] regiones fotolíticas (PDR, por sus siglas en inglés, photodissociation regions) son regiones en las que los enlaces químicos en el medio interestelar se rompen por causa de radiación

[10] Stacking (apilar) es una técnica observacional basada en sumar o promediar diferentes observaciones para de esta forma conseguir una señal/propiedad promedio.

la emisión estelar en estas galaxias, son en promedio claramente más extensas que la emisión del polvo o [CII] por un factor de > 2. Para entender el significado de esta observación, y si las diferencias de tamaño reflejan diferencias físicas y no aparentes, hemos aplicado un modelado de transporte radiativo a los perfiles radiales observados en nuestras galaxias. Nuestro trabajo revela que esta aparente diferencia entre los tamaños de las distribuciones de gas y polvo puede estar originada en cambios de temperatura y profundidad óptica a través de la galaxia, y que esta observación no implica necesariamente una diferencia física entre la distribución de estos materiales.

Publications

First and second author

1. Resolving the ISM at the peak of cosmic star formation with ALMA - The distribution of CO and dust continuum in z =2.5 sub-millimetre galaxies
Calistro-Rivera, Gabriela; Hodge, J. A.; Smail, Ian; Swinbank, A. M.; Weiss, A.; Wardlow, J. L.; Walter, F.; Rybak, M.; Chen, Chian-Chou; Brandt, W. N.; Coppin, K.; da Cunha, E.; Dannerbauer, H.; Greve, T. R.; Karim, A.; Knudsen, K. K.; Schinnerer, E.; Simpson, J. M.; Venemans, B.; van der Werf, P. P. 2018, *ApJ*, 863, 56C.

2. The LOFAR window on star forming galaxies and AGNs - curved radio SEDs and IR-radio correlation at $0 < z < 2.5$,
Calistro-Rivera, Gabriela; Williams, W. L.; Hardcastle, M. J.; Duncan, K.; Röttgering, H. J. A.; Best, P. N.; Brüggen, M.; Chyzy, K. T.; Conselice, C. J.; de Gasperin, F.; Engels, D.; Gürkan, G.; Intema, H. T.; Jarvis, M. J.; Mahony, E. K.; Miley, G. K.; Morabito, L. K.; Prandoni, I.; Sabater, J.; Smith, D. J. B.; Tasse, C.; van der Werf, P. P.; White, G. J. 2017, *MNRAS*, 469, 3468C.

3. AGNfitter: A Bayesian MCMC Approach to Fitting Spectral Energy Distributions of AGNs,
Calistro-Rivera, Gabriela; Lusso, Elisabeta; Hennawi, Joseph F.; Hogg, David W., 2016, *ApJ*,833, 98C.

4. Resolved [CII]/CO/FIR continuum multi-tracer study of two $z = 3$ dusty, star-forming galaxies
Rybak, Matus; **Calistro-Rivera, Gabriela**; Hodge J. A. Smail I.; Walter F.; van der Werf, P. E. da Cunha; Chian-Chou Chen; Dannerbauer H. ; Ivison R. J. ; Karim A. ; Simpson J. M.; Swinbank A. M. and Wardlow A. M. et al. 2018, *ApJ*, submitted.

5. LOFAR-Boötes: Properties of high- and low-excitation radio galaxies at $0.5 < z < 2.0$, Williams W. L. ; **Calistro-Rivera, Gabriela**; Best, P. N.; Hardcastle, M. J.; RÃ¶ttgering, H. J. A.; Duncan, K. J.; de Gasperin, F.; Jarvis, M. J.; Miley, G. K.; Mahony, E. K.; Morabito, L. K.; Nisbet, D. M.; Prandoni, I.; Smith, D. J. B.; Tasse, C.; White, G. J.et al. 2018, *MNRAS*, 475, 3429W.

Contributing author

6. The Far-Infrared Radio Correlation at low radio frequency with LOFAR/H-ATLAS, Read, S.C. et al. (including **Calistro-Rivera, Gabriela**) 2018, *MNRAS*, 480, 5625R

7. LOFAR/H-ATLAS: the low-frequency radio luminosity-star formation rate relation, Gürkan, G. et al. (including **Calistro-Rivera, Gabriela**) 2018, *MNRAS*, 475, 3010G

8. A Spatially Resolved Study of Cold Dust, Molecular Gas, H II Regions, and Stars in the z = 2.12 SMG ALESS67.1,
Chen, Chian-Chou et al.(including **Calistro-Rivera, Gabriela**) 2017, *ApJ*, 846, 108C

9. The LOFAR Two-metre Sky Survey. I. Survey description and preliminary data release, Shimwell, T. W. et al. (including **Calistro-Rivera, Gabriela**) 2017, *MNRAS*, 598A, 104S

10. The Lockman Hole project: LOFAR observations and spectral index properties of low-frequency radio sources,
Mahoney, E.K et al. (including **Calistro-Rivera, Gabriela**) 2016, *MNRAS*, 463.2997M

11. LoTSS/HETDEX: Optical quasars -I. Low-frequency radio properties of optically selected quasars
Gürkan, G et al. (including **Calistro-Rivera, Gabriela**) 2018, *A&A*, in press

12. The LOFAR Two-metre Sky Survey. II. First data release
Shimwell, T. W., et al. (including **Calistro-Rivera, Gabriela**) 2018, *A&A*, in press

13. Overdensity of SMGs around the z= 2.3 MAMMOTH-1 nebula – The environment and the powering of an ELAN
Arrigoni Battaia F., et al. (including **Calistro-Rivera, Gabriela**) 2018, *A&A*, in press

14. LoTSS/HETDEX: Disentangling star formation and AGN activity in lensed radio-quiet quasars
Stacey H. R., et al. (including **Calistro-Rivera, Gabriela**) 2018, *A&A*, in press

15. ALMA reveals evidence for spiral arms, bars and rings in high-redshift submillimeter galaxies
Hodge, J. et al. (including **Calistro-Rivera, Gabriela**) 2018, *ApJ*, submitted

Selected non-refereed publications:

16. Resolving the Interstellar Medium at the Peak of Cosmic Star Formation
Calistro-Rivera, Gabriela & Hodge, Jacqueline 2018, *Published in The Messenger (ESO), No. 173 (Sept 2018*)

17. Fitting Spectral Energy Distributions of AGN - A Markov Chain Monte Carlo Approach
Calistro-Rivera, Gabriela 2014, *Published in Proceedings of the IAU Symposia, IAU S304*

Curriculum Vitae

I was born on 24 March, 1990 in Huacho, a small coast city two hours away from Lima, the capital of Perú. I was raised by my grandparents in a peaceful neighbourhood right in front of the ocean. I went to my first school years here, to the Maria Auxiliadora primary school. At the age of 8, I moved with my parents to the capital city, Lima, and at the age of 10, I was accepted in the Peruvian-German School Alexander von Humboldt. There, I had the opportunity to learn several languages and was educated within a multicultural system with excellent Peruvian and German teachers in both STEM and humanities areas. Throughout my childhood, my father often shared with me his fascination for the enigmatic phenomena in the Universe, such as black holes and special relativity, and these stories woke up my curiosity for the Cosmos from early on. Although in most high-school years I had a preference for literature and arts, the last school years gave me the opportunity to attend inspiring Physics and Maths classes. The physics lectures by Herr Edgar Droll gave me the opportunity to learn about more advanced topics in Physics, introducing me to my first science magazines (Spektrum der Wissenschaft) and Physics TV-shows (Alpha-Centauri), reinforcing in this way my interest for the challenging aspects of Physics and Astronomy.

After graduating from the German Abitur in the Fall of 2007, I decided to study Physics. I was offered a full scholarship by the German Academic Exchange Service (DAAD) to move to Germany to embark my Bachelor studies. This scholarship was given to a group of high-school students selected among German-international schools from 120 different countries. This gave me the opportunity to start my undergraduate studies in the fall of 2008 in the Faculty of Physics and Astronomy of the University of Heidelberg. My first Bachelors research project was the morphological study of Ultra Compact Dwarf Galaxies under the supervision of Dr. Thorsten Lisker (Astronomisches Recheninstitut, Heidelberg). I graduated in 2012, with a thesis project on theoretical cosmology titled 'The Lensed Temperature Anisotropy of the CMB', as part of the group led by Prof. Matthias Bartelmann (Institute for Theoretical Astrophysics, Heidelberg). In the fall of 2012, I was awarded a DAAD full scholarship to pursue my Masters of Science degree in Physics at the Heidelberg University. In 2013, I joined the Max Planck Institute for Astronomy to conduct my Master thesis project on the spectral energy distributions of AGN under the supervision of Dr. Joseph Hennawi and Dr. Elisabeta Lusso. In this period, I had the opportunity to join observing trips to the La Silla ESO observatories, in Chile, and to present the results of my thesis in Germany, Armenia, and Australia.

In 2014, I was offered a PhD position at the Leiden Observatory. My PhD work focused on the panchromatic emission of star forming galaxies and active galactic nuclei across cosmic time, focusing on the characterization of fundamental properties for the evolution of galaxies such as star formation and black hole growth. Here, I worked as part of the low-frequency radio group led by Prof. Huub Röttgering and the dusty galaxies group, led by Dr. Jacqueline Hodge. As a PhD student, I became a member of two major collaborations studying radio and the sub-mm emission of galaxies, the LOFAR Surveys and the ALESS collaboration. During my PhD, I was able to participate in observing runs in La Palma, Spain, and to give invited and contributed talks on my research in numerous conferences and institutions, including Argentina, Colombia, France, Germany, Italy, the Netherlands, Japan, Spain, UK and USA. During my PhD, I had the opportunity to be teaching assistant to the course 'Galaxies: Structure and Dynamics' given by Dr. Rychard Bouwens and to develop and supervise three undergraduate projects.

Acknowledgments

There is a long list of people who have inspired, motivated, and accompanied me in the last years, making my path towards the end of my education as an astrophysicist one of the most exciting parts of my life.

Going back to the beginning, this story would have not started without my exceptional and inspiring Physics and Maths teachers during high-school. Vielen Dank an Herrn Droll, Herrn Lanzendörfer und Herrn Biernoth. Moving to Germany and carrying out my undergraduate studies at the Heidelberg University would have not been possible without the support of the DAAD program. I would like to thank the DAAD for giving me this unique opportunity. In this period, I was also lucky to meet the Willmann family. My Gasteltern, Valentin and Ortrud Willmann, were always there for me as I started my life as an independent adult. Lieber Valentin und liebe Ortrud, vielen Dank für eure Unterstützung in diesen Jahren und ich hoffe wir bleiben in Kontakt in die Zukunft. Through my University years in Heidelberg they were many great professors and supervisors I have learn so much from, and I am thankful to all of them. I would like to especially thank Prof. Matthias Bartelmann, who inspired and motivated me to persevere through the difficult parts of my career, always with an extremely contagious passion for science and unique wisdom and modesty. Lieber Matthias, vielen Dank für die wunderbare Vorlesungen, Rate und Unterstützung. Liebe Physiker Freunde in Heidelberg, ohne euch hätte ich die Analysis-zetteln und die harte Bar3/Bar133/ Küche Nächte nicht überleben/erleben können, vielen Dank für die viele wunderbare Jahre. Pingüis, con ustedes me llegó la familia a Alemania. Gracias por hacerse querer tanto, por darle color a nuestra época de maestría y ser la mejor compañía de esas que sabes que no se acaban. Sofi y Elena, muchísimas gracias por la hermandad y las mil aventuras que compartimos durante estos años, y espero que vengan muchas más.

My research career in observational astronomy started as part of the ENIGMA group at MPIA in Heidelberg. Thanks to all my ENIGMates from whom I learned so much and who welcomed me and made me feel part of the group from the first moment. Beta Lusso, grazie per avermi aiutato a formare le basi per la mia ricerca e per essere ancora sempre disponibile per me. Spero di poter rimanere la tua collaboratrice anche nel futuro. Joe Hennawi, my career would have been half as it is without having you as my supervisor. Thank you so much for teaching me how to conduct good science, for always motivating and valuing my work, and for being a truly caring and generous supervisor to me. Thank you as well for all your support to my future career, and I hope to have the pleasure to have you as a collaborator in future projects.

My years as a PhD student at the Leiden Sterrewacht has given me the opportunity to meet many wonderful people. I am very grateful to Xander Tielens, whose support was crucial throughout my PhD. Thank you, Xander, for your advice and all your efforts to help me construct the best environment possible for my research. I cannot express my gratitude enough to Jacqueline Hodge for welcoming me in her group, introducing me to the ALMA research and teaching me so much about the scientific career. I feel very lucky to be your first PhD student and I hope we remain close collaborators in the future. I would also like to thank Huub Röttgering for giving me the opportunity to embark a PhD, for welcoming in the LOFAR group, and for giving me his trust to choose my own research path.

All work in research is a collaborative work, and the chapters presented here would have not been possible without the LOFAR and ALESS collaborations. Thanks to all members of these collaborations, to those in Leiden and around the world, who have contributed with many insightful comments and suggestions to this thesis. I would like to specially thank Ian Smail and Martin Hardcastle, for their crucial guidance throughout the projects carried out in this thesis and their support and valuable advice for my future career.

Life in Leiden would have been half as happy, without the wonderful friends and colleagues who accompanied me in these years. Thanks to all the members the LOFAR group and Dusty Galaxies groups at the Sterrewacht for the interesting and fun group-meetings. Special thanks go to my co-supervisees Hiddo Algera and Dieuwertje van den Kamp, for helping me with the Dutch translation of the summary of this thesis. Wendy Williams, it has been a pleasure to have you as a collaborator. Thank you for your company both in Leiden and Hertforshire and for your contributions to the development of AGNfitter. Matus Rybak, thank you for the many interesting conversations about science and life, and for all your support in this last period of my PhD. I have been very lucky to have you as a close collaborator and friend, and I hope we remain in contact. I would like to thank all my Leiden colleagues and friends for the many interesting and fun scientific and non-scientific discussions and useful advice on different topics, especially Jarle Brinchman, Rychard Bouwens, Michael Maseda, Allison Hill, Corentin Schreiber, Yannik Bahe, Julius Donnert, Alexandra Candian and Themiya Nanayakkara. I would like to thank as well the ALLEGRO team, Luke Maud, Liz Gomez, Yanett Contreras, Carmen Toribio and Daniel Harsono, for your technical advice on my ALMA research and fun lunch conversations. Leo Burtscher, es hat mich sehr gefreut, dass Du in Leiden angekommen bist und wir unsere AGN Begeisterung zusammen ausdrücken konnten. Vielen Dank für deine motivierende Wörter und die viele interessante Diskussionen über alles Mögliche, von der gemeinsamen Entwicklung von Galaxien und AGN, bis boodschappen doen op de markt.

I would like to thank the Leiden PhDs from the earlier generations, Irene San José García, Matteo Brogi, Mattia Fumagalli, Renske Smit, Thanja Lamberts, Berenice Pila Díez, Monica Turner, Bernard van Heck, Andra Stroe, and Alex Rimoldi, who quickly welcomed me to the PhD community and shared with me their wisdom on this process. I'm very glad I overlapped with you even if only for a short time. Mattia, I also had the pleasure to be you office-mate and even house-mate for short but memorable times (and even musical partner for a day). Thanks to you and Anna for all the adventures and friendship! Andra and Renske, thank you both so much for all your support in the last period of my PhD. You are great examples to follow as scientists and I feel very lucky to have you as friends.

I would also like to thank all my fellow PhD students that embarked in this adventure together with me. Andrew, Ann-Sophie, Chris, Eva, Jorryt, Mike, Mason, Edwin, thanks for the fun conversations during coffee breaks, the parties and the shared adventures. I really cherish the days back to the 11th floor, and would like to thank the gang, Aayush, Mieke and Eleonora, for the great time we shared in that office, that luckily kept us together till this date. Thanks so much to the 'mostly' italian crew, Maria Cristina, Alberto, Tomasso, Valeria, Francesco, Gabriella, Kim, Christos, Soumajit, for the fun dinners and evenings. Caro Fra, grazie per tutte le serate insieme e le storie divertenti. Sono molto contenta che la nostra amicizia sia sopravvisuta alla distanza. A mis queridos latino/hispanos, Santi, Pablo, Igone, Poshito, Pedro, Jorge, Lina, Francisca, gracias por todos los borrels, fiestas, e infinitas risas, y por ser una mini-latinoamérica entera dentro del STRW. Kathy, gracias por los viajes inolvidables y sobre todo por la peruanidad que me trajiste, que hizo mis últimos dos años del doctorado muchísimo más rico. Josh, Luis, Aurelien, it was a pleasure to share an office with you and I wish I had been less busy as an officemate to get to know you better.

Ken, you are not only my paranymph on the defense day, but you have been it since you arrived at the STRW. Thank you so much for being the friend I could share my SED enthusiasm with, for all the fun, and for your help and advice, in science and life. Cristi, tu llegada a Leiden hizo de mi doctorado mil veces más feliz. Ya lo logramos dos veces, pero quisiera poder ser tu colega de grupo para siempre. Pero aunque eso nos pueda fallar en el futuro, estoy segura que nuestra amistad sí quedará intacta hasta que seamos viejitas.

A mis chicas de la vida entera, Pamela, Nicole, Francis, Adri, Marianne, Christel, Alejandra, Andrea, Yael, aunque las he tenido lejos, a algunas más que a otras, su amistad siempre me ha acompañado y fortalecido en todos estos años. Las quiero y siempre las tengo presentes. Un agradecimiento especial para Adriana Verán por leer y corregir pacientemente la ortografía oxidada de la versión original del resumen en castellano. Cari Angela, Robi e Leo, grazie per avermi sempre fatto sentire a casa. Sono molto grata che questi anni non solo mi abbiano dato il mio compagno ma anche a un'intera bellissima famiglia che ho sentito subito come la mia stessa. Abuelita Engracia, tía Gloria, tío Aldo, André y Melysa, les agradezco todo el cariño que nos brindan siempre.

Nada de esto hubiera sido posible sin el apoyo incondicional de mi familia. Tío Toño, gracias por todas las buenas recomendaciones de libros, y por estar siempre allí pendiente, para mí y para Leo. Mamá Chela, fue contigo y papá José que aprendí mis primeros números y letras, y resolví mis primeras sumas y restas. Fue allí que comenzó todo. No hay palabras suficientes para agradecer todo lo que has hecho por mí, mamita. Leo, tenerte como hermano es una de las cosas más bonitas en mi vida. Estoy muy orgullosa de ti, admiro tu talento, tu sentido del humor, tu pasión por las cosas que te gustan y estoy muy agradecida por ser tan cercana a ti, a pesar de la distancia. Mamá y papá, sin su esfuerzo constante, la confianza que me tienen, y el ejemplo que me dan, yo no sería nada. Este doctorado es de ustedes. Es el fruto de todo lo que me han enseñado y de todo lo que han sacrificado para poder darme las mejores oportunidades posibles. Gracias sobre todo por el amor que nos brindan, que me ha hecho crecer como una persona completa y felíz. Mami, la fuerza y perseverancia que ha sido vital para terminar este doctorado, la he heredado de ti. Gracias por ser el ejemplo de mujer fuerte e inteligente que yo aspiro a ser. Papi, tus cuentos de agujeros negros y gemelos de edades diferentes son los responsables de esta historia. Gracias por creer tan ciegamente en tus hijos, por querernos tanto, y por habernos enseñado a soñar siempre en grande. Leo y yo somos muy afortunados de tenerlos como papás.

Marco, averti conosciuto é il miglior regalo che l'astronomia mi abbia portato. Il tuo potere di farmi sempre ridere ha reso questi ultimi anni i piú felici, e la tua intelligenza e determinazione mi ispirano per diventare anche io sempre migliore. Grazie per essere stato la mia forza constante durante i periodi difficili di questo dottorato. Senza la tua compagnia e il tuo consiglio, questo percorso sarebbe stato molto grigio. Grazie per essere il compagno perfetto per me, per i viaggi e le storie del futuro, e benvenuti siano tutte le sfide impossibili, inverni pioggiosi e i jetlags terribili, che sono belli mentre li viviamo insieme.